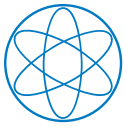

Dissertation

Searches for R-Parity Violating Supersymmetry in Multilepton Final States with the ATLAS Detector

von

Maximilian Emanuel Goblirsch-Kolb

eingereicht an der

Fakultät für Physik

der

Technischen Universität München

erstellt am

Max-Planck-Institut für Physik
(Werner-Heisenberg-Institut)

München

Juni 2015

MAX-PLANCK-GESELLSCHAFT

TECHNISCHE UNIVERSITÄT MÜNCHEN

Max-Planck-Institut für Physik
(Werner-Heisenberg-Institut)

Searches for R-Parity Violating Supersymmetry in Multilepton Final States with the ATLAS Detector

Maximilian Emanuel Goblirsch-Kolb

Vollständiger Abdruck der von der Fakultät für Physik der Technischen Universität München zur Erlangung des akademischen Grades eines

Doktors der Naturwissenschaften (Dr. rer. nat.)

genehmigten Dissertation.

Vorsitzender: Univ.-Prof. Dr. A. Ibarra
Prüfer der Dissertation:

1. Priv.-Doz. Dr. H. Kroha
2. Univ.-Prof. Dr. L. Oberauer
3. Univ.-Prof. Dr. G. Herten (schriftliche Beurteilung), Albert-Ludwigs-Universität Freiburg

Die Dissertation wurde am 15.06.2015 bei der Technischen Universität München eingereicht und durch die Fakultät für Physik am 08.07.2015 angenommen.

Abstract

This thesis presents two searches for signs of R-parity-violating supersymmetry (SUSY) through decays of the lightest supersymmetric particle (LSP) into two charged leptons and one neutrino. The searches are performed with the ATLAS experiment at the Large Hadron Collider (LHC) using a data set of pp collisions at $\sqrt{s} = 8$ TeV recorded during the 2012 LHC run, corresponding to an integrated luminosity of 20.3fb^{-1}.

As a prerequisite for these studies, which rely heavily on efficient reconstruction of charged leptons, a tag-and-probe method based on $Z \to \mu\mu$ decays is developed to measure the muon reconstruction efficiency of the ATLAS experiment with an accuracy of 0.1% and validate the predictions made by the detector simulation.

If the decay of the LSP occurs with a lifetime of less than about 1 mm/c, the standard reconstruction of leptons within ATLAS is efficient. A search for anomalous events with at least four charged leptons is presented. Since processes with four or more charged leptons are rare in the Standard Model, a very low level of background is achieved. A special effort is made to provide sensitivity to decays of an LSP that is very light compared to the initially produced supersymmetric particles. No sign of a signal is observed, and strong exclusion limits in the parameter space defined by the supersymmetric particle masses are derived.

A second search targets scenarios where the LSP lifetime is much greater than 1 mm/c, using the signature of a high-mass displaced vertex with two associated charged leptons. The reconstruction of such displaced vertices requires a non-standard event reconstruction. Signal vertices do not occur naturally in the Standard Model, leading to a negligible level of background. A novel technique is developed to estimate the dominant residual background from lepton tracks that randomly cross inside the tracking volume. No signal vertices are observed, in agreement with the background prediction, and upper limits on the number of supersymmetric particle decays in the data set and the production cross-sections within simplified SUSY models are set as a function of the LSP lifetime. The results of the four-lepton search are also extrapolated as a function of the LSP lifetime and included in the study to enhance sensitivity at short LSP lifetimes.

Acknowledgments

I am deeply grateful to Hubert Kroha for giving me the opportunity to be part of the MPI team, first as a diploma student and then as a PhD student, for supporting me and my work in every conceivable way, and especially for the enormous effort invested in helping improve my thesis over the last few months. My thanks also go to Sandra and Oliver Kortner, who originally motivated me to enter high energy physics and were always available to answer my many questions.

Related to my work in the SUSY analysis team, I wish to thank Nick Barlow, Abi Soffer, Helen Hayward and Nimrod Taiblum for the fruitful collaboration in the displaced vertex search. Thanks to Tina Potter and Estel Perez, Steve Farrell, Zara Grout, Lukas Marti, Basil Schneider and especially Federico Sforza for a great time in the four-lepton analysis team. And I particularly wish to thanks all the people deeply enjoyed working with in the Muon CP group, especially Massimo Corradi, Niels van Eldik, Gabriella Sciolla and Max Bellomo who, as conveners, created a pleasant and productive working environment.

The last years were a great time especially due to the amazing colleagues I had the honour of working with. Marco Vanadia taught me physics analysis, Sebastian Stern taught me fundamental truths about beer, money, statistics and the role of high energy physics in professional football, and Sebastian Nowak told me all the things I never wanted to know about my lunch. Thank you to Philipp Schwegler and Johanna Bronner for many an entertaining coffee break. And thanks especially to Johannes Junggeburth and Rainer Röhrig who, as my office mates during the busy last months, did not just have to endure my moaning but who helped me proof-read the thesis and find all those nasty little bugs so easy to miss. And to Nicolas Köhler who, busy with looking for stops and measuring efficiencies, still found the time to read proofs.

I am deeply grateful to my parents Holger and Maria Goblirsch-Kolb for supporting me over all the years.

Finally, I wish to express my deepest gratitude to Mike Flowerdew, who was the best day-to-day advisor I could wish for. Thank you very much for all the fruitful discussions in the course of our various analysis projects, the invaluable technical and scientific expertise and of course all the help with improving the thesis.

Contents

Chapter 1

Introduction

The predictions of the Standard Model of particle physics, developed in the second half of the 20^{th} century, have been successfully tested by precision measurements at several generations of accelerator experiments. In 2012, the ATLAS and CMS experiments [1, 2] at the Large Hadron Collider (LHC) [3] at CERN announced the discovery of a scalar boson with properties as predicted by the Higgs mechanism of the Standard Model, the last missing piece of the theory to be discovered. This mechanism is responsible for electroweak gauge symmetry breaking and the generation of the fundamental particle masses in the Standard Model.

However, several compelling arguments suggest that the Standard Model is not the final theory of elementary particle physics. A quantum theory of gravity is not part of the Standard Model and, according to cosmological observations [4], the matter described by the Standard Model only constitutes about 5% of the energy density of the universe. About 25% is due to so-called dark matter [5], so far only recognisable through gravitational effects, and about 70% arises from so-called dark energy [4], which is of a completely unknown nature. In addition, the enormous difference in the energy scales of the Standard Model (10^3 GeV) and of gravity (10^{19} GeV) leads to a hierarchy problem. The Higgs boson mass receives loop corrections from all massive particles that couple to the Higgs field, with contributions that scale quadratically with the particle masses and with the energy cut off scale of the theory. Consequently, validity of the Standard Model up to very high energy scales or the existence of new massive particles beyond the Standard Model lead to a fine-tuning problem of the observed Higgs boson mass of $m_H = 125.09$ GeV [6].

Supersymmetry [7], a new symmetry relating fermions and bosons, leads to a cancellation of the radiative corrections to the Higgs boson mass from fermion and boson loops. The particles of the Standard Model obtain superpartners with spins differing by 1/2, doubling the particle content of the Standard Model. As none of the superpartners have been observed to date, they must be heavier than their Standard Model partners and supersymmetry must be broken. In this case, the neutral and charged spin-1/2 sparticles mix to their mass eigenstates, the neutralinos and charginos, respectively. Supersymmetry still provides a solution to the hierarchy problem if the masses of the superpartners (at least of the ones that couple the strongest to the Higgs bosons, like the top squark) are not larger than a few TeV.

Experiments at the Large Hadron Collider, which collides protons at centre-of-mass-energies of up to 14 TeV, should be able to find signatures of supersymmetric particle production if supersymmetry solves the hierarchy problem. Most searches for supersymmetry performed at the LHC up to now assume the conservation of an additional quantum number, R-parity, which prevents rapid proton decay via the exchange of supersymmetric particles. It also requires the lightest supersymmetric particle (LSP) to be stable, making it an attractive candidate for dark matter. However, R-parity-conservation is not required for supersymmetry, nor is it the only mechanism that can ensure the stability of the proton. Giving up the requirement of R-parity-conservation opens up a new class of supersymmetric extensions of the Standard Model with R-parity-violation (RPV), which has been less extensively studied up to now. If R-parity is violated, the LSP can decay into Standard Model particles, leading to new experimental signatures that may have been missed in conventional supersymmetry searches.

In this thesis, a particular class of R-parity-violating models is investigated, where a neutralino $\tilde{\chi}_1^0$ as LSP decays due to lepton-number and R-parity-violating couplings to a pair of charged leptons and a neutrino. Constraints are set on these models using collision data recorded by the ATLAS experiment at the LHC at $\sqrt{s} = 8$ TeV in 2012.

As the LSP is produced in pairs at the LHC by R-parity-conserving mechanisms, the signal events contain four charged leptons and two neutrinos. If the average decay lengths of the LSP are small compared to the detector resolution, a search for four charged leptons originating from the primary proton-proton interaction vertex is sensitive to this signature, as processes producing four charged energetic leptons are rare in the Standard Model. This background is estimated using a combination of Monte Carlo simulation and data-driven techniques. No excess over the background prediction is observed and upper limits are set on the magnitude of a possible signal using a set of

simplified supersymmetric models. The signal sensitivity depends on the masses of the LSP and of the next-to-lightest supersymmetric particle, the NLSP, the type of the NLSP and the flavours of the final state leptons.

If the LSP decay length exceeds about 1 mm, the LSP decay can be reconstructed as a secondary vertex of two charged leptons with a high invariant mass displaced from the primary interaction point. Such processes do not occur in the Standard Model. The only background is due to instrumental effects or random intersections of lepton tracks and can be suppressed considerably making use of the expected vertex properties. In order to reconstruct the displaced decay vertices, a dedicated track and vertex reconstruction procedure had to be used. The combinatorial background due to random crossings of lepton tracks is estimated using a new data-driven technique. No displaced dilepton vertices satisfying all selection criteria are observed, consistent with the expectation from this method, and upper limits on a possible signal are derived as a function of the LSP lifetime. This search has been performed for the first time with the ATLAS data and considerably expands the sensitivity range of the RPV supersymmetry searches.

Chapter 2

The Supersymmetric Extension of the Standard Model

The Standard Model of particle physics (SM) describes the known elementary particles and their interactions. It has been remarkably successful in predicting experimental observations with high precision. In this chapter, the main features of the Standard Model are summarised, based on a detailed description in Ref. [8]. In spite of its successes, there is strong evidence that the Standard Model alone is insufficient to fully explain all phenomena. As one example, the hierarchy problem is discussed. Supersymmetry (SUSY) is one possible approach to extend the Standard Model in order to solve some of its insufficiencies. An overview of its principles is given.

In the following, natural units ($\hbar = c = 1$) are used. Fermion fields are described by two-component Weyl spinors rather than Dirac spinors - this is useful for introducing the supersymmetric notation used to extend the Standard Model.

2.1 The Standard Model

The Standard Model of particle physics was developed during the second half of the 20^{th} century. In the framework of relativistic quantum field theory, it describes all of the known elementary particles and fundamental forces, with the exception of gravity.

2.1.1 Principles of the Standard Model

In the Standard Model, the matter constituents are spin-1/2 fermions.

A major achievement is the introduction of interactions between the fermions by a unifying principle requiring invariance of the action under local gauge transformations [9] which correspond to local phase transformations of the fermion fields ψ,

$$\psi \longrightarrow \exp\left[i\alpha^a(x^\mu)T_a\right]\psi, \tag{2.1}$$

with scalar phase parameters $\alpha^a(x^\mu)$ corresponding to the generators T_a $(a = 1,\ldots,n)$ of the Lie groups of the unitary gauge transformations which are the charge operators of the interactions. Invariance of the action under gauge transformations is ensured by the introduction of spin-1 vector gauge fields A^a_μ transforming as

$$A^a_\mu \longrightarrow A^a_\mu + \frac{1}{g}\partial_\mu\alpha^a(x^\mu) + f_{abc}A^b_\mu\alpha^c(x^\mu), \tag{2.2}$$

where g is the gauge coupling strength parameter and f_{abc} $(a,b,c = 1,\ldots,n)$ are the structure constants of the group, fulfilling the commutation relation

$$[T_a,T_b] = if_{abc}T_c.$$

The gauge fields A^a_μ are introduced into the action via covariant derivatives

$$\partial_\mu \longrightarrow D_\mu = \partial_\mu - \frac{1}{2}igT_aA^a_\mu \tag{2.3}$$

in the kinetic terms which generate couplings between the fermion and gauge fields mediating the interactions.

The gauge symmetry group of the Standard Model is the direct product

$$\mathrm{SU}(3)_C \times \mathrm{SU}(2)_L \times \mathrm{U}(1)_Y$$

of the three simplest special unitary Lie groups. The eight charges of the $\mathrm{SU}(3)_C$ symmetry are called colour charges and are the sources of the strong interaction described by quantum chromodynamics (QCD) [10, 11]. The electroweak interactions [12–16] are described by the $\mathrm{SU}(2)_L \times \mathrm{U}(1)_Y$ symmetry. Charges associated with the $\mathrm{SU}(2)_L$ symmetry are described by weak isospin $\vec{I}$. The $SU(2)_L$ gauge fields couple exclusively

to left-handed fermions, leading to maximum parity violation by the charged weak interaction. The charge of the $\mathrm{U}(1)_Y$ group is the weak hypercharge Y, which is related to the electric charge Q via the Gell-Mann–Nishijima relation [17] $Y = 2(Q - I_3)$, where I_3 is the third component of the weak isospin. These three local gauge symmetries predict massless gauge fields, and the local $\mathrm{SU}(2)_L$ symmetry requires the fermions to be massless, too.

2.1.2 Field Content

Quarks and Leptons

The Standard Model contains three generations of quarks and leptons as elementary fermions (see Table 2.1). As quarks participate in the strong interactions, the quark fields are colour charge triplets under the fundamental representation of $SU(3)_C$:

$$q = \begin{pmatrix} q_r \\ q_g \\ q_b \end{pmatrix}.$$

Each fermion generation i ($i = 1,2,3$) contains a quark and lepton doublet Q_i and L_i, respectively, of $SU(2)_L$, where $I_3 = \pm 1/2$ distinguishes up- and down-type fermions. Each $SU(2)_L$ lepton doublet contains a left-handed neutrino and an electrically charged lepton. In addition, there are $SU(2)_L$ singlet states $u_i^\dagger$, $d_i^\dagger$, $e_i^\dagger$ of right-handed up- and down-type quarks and right-handed charged leptons. The Standard Model contains no right-handed neutrinos. Leptons do not participate in the strong interaction and are colour singlets.

Free massless fermion fields, expressed as a Weyl spinors χ, are described by terms

$$\mathcal{L}_{\text{fermion}} = \chi^\dagger \bar{\sigma}^\mu \partial_\mu \chi$$

in the Lagrangian density, where $\bar{\sigma}^\mu = g^{\mu\nu}\sigma_\nu = (\mathbb{1}, -\vec{\sigma})$, and $\vec{\sigma}$ are the Pauli matrices, acting on the spinor components.

Gauge Bosons

In addition to the fermions, the Standard Model contains the spin-1 gauge fields of the symmetry group listed in Table 2.2. The strong interaction is mediated by an octet of gluon fields, G_μ^a ($a = 1,\ldots,8$) corresponding to the eight generators of $SU(3)_C$. The

Table 2.1: Matter fields of the Standard Model in the fundamental representations of the gauge symmetries [8]. The three colour components of each quark field are not shown.

Quarks	$SU(3)_C$	$SU(2)_L$	Y
$Q_i = \begin{pmatrix} u_L \\ d_L \end{pmatrix}, \begin{pmatrix} c_L \\ s_L \end{pmatrix}, \begin{pmatrix} t_L \\ b_L \end{pmatrix}$	**3**	**2**	$+\frac{1}{3}$
$u_i^\dagger = u_R^\dagger, c_R^\dagger, t_R^\dagger$	$\bar{\mathbf{3}}$	**1**	$-\frac{4}{3}$
$d_i^\dagger = d_R^\dagger, s_R^\dagger, b_R^\dagger$	$\bar{\mathbf{3}}$	**1**	$+\frac{2}{3}$
Leptons			
$L_i = \begin{pmatrix} \nu_e \\ e_L \end{pmatrix}, \begin{pmatrix} \nu_\mu \\ \mu_L \end{pmatrix}, \begin{pmatrix} \nu_\tau \\ \tau_L \end{pmatrix}$	**1**	**2**	-1
$e_i^\dagger = e_R^\dagger, \mu_R^\dagger, \tau_R^\dagger$	**1**	**1**	$+2$

gluons themselves carry colour charge due to the non-Abelian nature of the $SU(3)_C$ group. The three generators of the $SU(2)_L$ gauge symmetry correspond to three gauge boson fields W_μ^a ($a = 1,2,3$), which are charged under the non-Abelian $SU(2)_L$ group, forming a triplet representation of the weak isospin, while the $U(1)_Y$ symmetry produces one singlet gauge field, B_μ.

Table 2.2: Gauge boson fields of the Standard Model in the adjoint representations of the gauge symmetries [8].

Gauge bosons	$SU(3)_C$	$SU(2)_L$	Y
G_μ^a	**8**	**1**	0
W_μ^a	**1**	**3**	0
B_μ	**1**	**1**	0

With the field strength tensor

$$V_{\mu\nu}^a = \partial_\mu V_\nu^a - \partial_\nu V_\mu^a + g f_{abc} V_\mu^b V_\nu^c, \tag{2.4}$$

for a gauge boson field V_μ^a ($V = G, W, B$), the free gauge field term in the Lagrangian density is

$$\mathcal{L}_{\text{gauge}} = -\frac{1}{4} V_{\mu\nu}^a V_a^{\mu\nu}. \tag{2.5}$$

In the case of the Abelian $U(1)$ group with $f_{abc} \equiv 0$, the last term of Eq. (2.4) is missing, like it is the case for the electromagnetic interaction. When present, the term leads to a self-coupling of the gauge bosons. In the strong interaction, the gluon self-coupling is responsible for the effect of confinement [18] of the coloured quarks and gluons inside colour-neutral mesons and baryons. At short distances inside the hadrons, quarks and gluons behave as free particles, an effect called asymptotic freedom [19]. One important consequence for hadron collider experiments is that quarks or gluons produced with high energies in the interaction hadronise and are observable as jets of mesons and baryons.

According to Eq. (2.3), the coupling of gauge bosons to the fermions of the Standard Model is obtained by replacing the ordinary derivative by the covariant derivative in the Lagrangian density:

$$\partial_\mu \longrightarrow D_\mu = \partial_\mu \underbrace{-\frac{1}{2} i g_s \lambda_a G_\mu^a}_{SU(3)_C} \underbrace{-\frac{1}{2} i g_W \sigma_\alpha W_\mu^\alpha}_{SU(2)_L} \underbrace{-i g_Y \frac{Y}{2} B_\mu}_{U(1)_Y},$$

where λ_a ($a = 1, \ldots, 8$) are the Gell-Mann matrices, the generators of $SU(3)$, σ_α ($\alpha = 1, 2, 3$) are the Pauli matrices, the generators of $SU(2)$, and $g_{s/W/Y}$ are the gauge coupling strengths of the strong, weak and hypercharge interactions.

2.1.3 Electroweak Symmetry Breaking

The gauge symmetries of the Standard Model require fermions and gauge bosons to be massless. Particle masses are instead generated by the spontaneous breaking of the local $SU(2)_L \times U(1)_Y$ symmetry [20–22]. To achieve this, an additional complex scalar $SU(2)_L$ doublet field ϕ with $I_3 = \pm 1/2$ and $Y = 1$, the Higgs field, is introduced in the Standard Model Lagrangian density:

$$\mathcal{L}_{\text{Higgs}} = \underbrace{\left(D_\mu \phi\right)^\dagger \left(D^\mu \phi\right)}_{T_{\text{Higgs}}(\phi, \phi^\dagger)} - \underbrace{\left(\mu^2 \phi^\dagger \phi + \frac{\lambda}{4} \left(\phi^\dagger \phi\right)^2\right)}_{V_{\text{Higgs}}(\phi, \phi^\dagger)}. \tag{2.6}$$

The scalar potential $V_{\text{Higgs}}(\phi, \phi^\dagger)$ contains a quadratic mass and a quartic self-coupling term. For $\mu^2 < 0$, it has a set of degenerate minima for non-zero values of the Higgs field

$$|\phi| = \sqrt{-\frac{2\mu^2}{\lambda}} =: \frac{v}{\sqrt{2}}.$$

While the set of minima is still $SU(2)_L \times U(1)_Y$ invariant, the realisation of one particular vacuum expectation value spontaneously breaks the $SU(2)_L \times U(1)_Y$ symmetry of the electroweak vacuum. In the unitary gauge, which eliminates massless Goldstone excitations of the vacuum, the field ϕ may be written

$$\phi = \frac{1}{\sqrt{2}} \begin{pmatrix} 0 \\ v + H(x) \end{pmatrix}, \tag{2.7}$$

where $H(x)$ is a massive excitation, the Higgs boson with mass $m_H = \sqrt{-\mu^2}$. A candidate for this neutral scalar Higgs boson with mass of $m_H = 125.09$ GeV [6] has been discovered in 2012 by the ATLAS and CMS experiments at CERN [1,2]. With Eq. (2.7), the kinetic term T_{Higgs} in Eq. (2.6) contains terms evaluating to

$$T_{\text{Higgs}}^{\text{gauge mass}} = \frac{1}{8} g_W^2 v^2 \left(\left(W_\mu^1\right)^2 + \left(W_\mu^2\right)^2 \right) + \frac{1}{8} v^2 \begin{pmatrix} W_\mu^3 \\ B_\mu \end{pmatrix}^T \begin{pmatrix} g_W^2 & -g_W g_Y \\ -g_W g_Y & g_Y^2 \end{pmatrix} \begin{pmatrix} W_\mu^3 \\ B_\mu \end{pmatrix}, \tag{2.8}$$

which act as mass terms for the electroweak gauge bosons invariant under local $SU(2)_L$ gauge transformations, and further terms that introduce couplings between the gauge bosons and the Higgs boson.

The mass eigenstates of the electroweak gauge bosons, the massive, electrically charged W boson fields $W_\mu^\pm$, the massive, neutral Z_μ boson field and the massless, neutral photon field A_μ, are obtained by the transformations

$$W_\mu^\pm = \frac{1}{\sqrt{2}} \left(W_\mu^1 \mp i W_\mu^2 \right), \qquad \begin{pmatrix} Z_\mu \\ A_\mu \end{pmatrix} = \begin{pmatrix} \cos\theta_W & \sin\theta_W \\ -\sin\theta_W & \cos\theta_W \end{pmatrix} \begin{pmatrix} W_\mu^3 \\ B_\mu \end{pmatrix},$$

with the Weinberg angle θ_W defined by

$$\cos\theta_W = \frac{g_W}{\sqrt{g_W^2 + g_Y^2}}. \tag{2.9}$$

The masses of the weak gauge bosons are given by

$$m_W = \frac{g_W v}{2}, \qquad m_Z = \frac{g_W v}{2\cos\theta_W}.$$

The vacuum expectation value defining the electroweak symmetry breaking scale is

related to the weak Fermi coupling constant G_F by

$$v = \left(\sqrt{2}G_F\right)^{-\frac{1}{2}} = 246.2 \text{ GeV}. \tag{2.10}$$

The massless photon does not couple to the Higgs field, corresponding to the unbroken $U(1)_Q$ gauge symmetry of the electromagnetic interaction.

Mass terms of the quarks and the charged leptons in the three generations $i = 1,2,3$ (see Table 2.1) are introduced in the Standard Model via $SU(2)_L \times U(1)_Y$ invariant Yukawa coupling terms to the Higgs fields ϕ,

$$\mathcal{L}_{\text{Yukawa}} = -y_L^{ij} e_i^\dagger L_j \phi - y_u^{ij} u_i^\dagger Q_j i\sigma_2 \phi^* - y_d^{ij} d_i^\dagger Q_j \phi + h.c., \tag{2.11}$$

with the Pauli matrix σ_2.

The Yukawa coupling matrices y_{ij} in Eq. (2.11) are in general non-diagonal. The mass eigenstates of the fermions are mixtures of the electroweak eigenstates. In the quark sector, the resulting mixing matrix is known as the Cabibbo-Kobayashi-Maskawa (CKM) Matrix [23, 24].

2.1.4 Limitations of the Standard Model

The experiments at the LEP and SLC electron-positron colliders, at the Tevatron $p\bar{p}$ collider and of the Large Hadron collider LHC (see Chapter 3.1) have performed precision tests of the electroweak and strong interactions at the one-loop level in perturbation theory leading to precise predictions for the masses of the W boson, the top quark and Higgs bosons, which agree with direct measurement (see Figure 2.1) within two standard deviations [25].

Figure 2.2 gives an overview of cross-section measurements of Standard Model processes by the ATLAS experiment at the Large Hadron Collider, which are in excellent agreement with the Standard Model predictions over 14 orders of magnitude [26]. The Standard Model is the most precisely tested theory to date.

Nevertheless, there are strong indications that the Standard Model alone is not sufficient to describe the fundamental particles and their interactions.

Besides the fact that gravity is not included in the Standard Model as a quantum field theory, astrophysical observations indicate the existence of so-called dark matter [5],

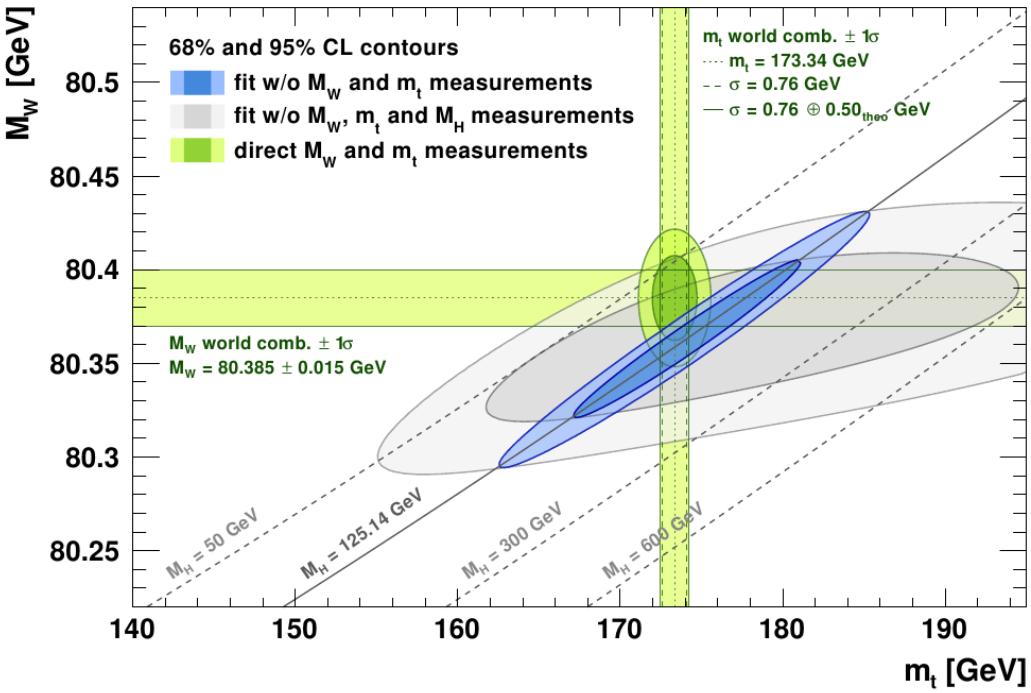

Figure 2.1: Comparison of direct measurements of the W boson and top quark masses with the prediction from precision measurements of the electroweak interaction LEP, SLD, Tevatron and the LHC [25].

assumed to be a new type of weakly interacting particle not described by the Standard Model which, so far, has only been detected by its gravitational attraction and appears to make up for about 25% [4] of the energy density of the universe, while only 5% consist of Standard Model particles.

Further observations of cosmological origin not explained by the Standard Model are the remaining 70% of the energy density of the universe in the form of so-called dark energy [4] and the apparent asymmetry between matter and anti-matter which requires much stronger baryon number and CP violation in the early universe than predicted by the Standard Model [27].

On the theoretical side, the Standard Model cannot explain the smallness of the Higgs boson mass compared to the Planck scale under radiative corrections as discussed in the next section.

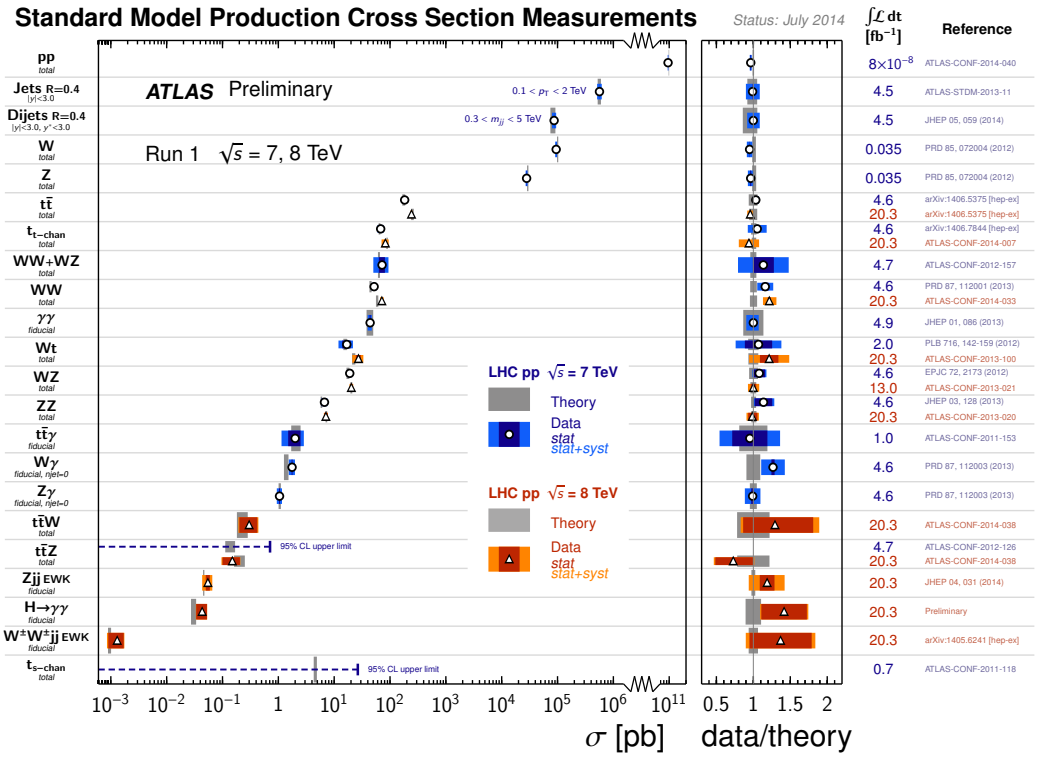

Figure 2.2: Overview of measured cross-sections and Standard Model predictions for a range of physics processes observed at the LHC with the ATLAS experiment [26].

2.1.5 The Hierarchy Problem

Figure 2.3a shows the leading radiative corrections to the Higgs boson mass due to virtual fermion loops in the Standard Model. The corrections diverge quadratically with the cutoff scale Λ_{UV} of the virtual particles in the loops up to which the Standard Model is valid. This kind of quadratic divergence is unique for a fundamental scalar boson. Analogous corrections to fermion and gauge boson masses only scale logarithmically with the cutoff energy Λ_{UV}. If the Standard Model is to be valid up to the Planck scale $m_{\mathrm{Pl}} = \sqrt{\hbar c G^{-1}} \approx 10^{19}$ GeV where quantum gravity effects need to be taken into account, fermion corrections to the square of the Higgs mass

$$\mathrm{m}_H^2 = -\mu^2 + \Delta m_H^2 = -\mu^2 - \frac{\Lambda_{\mathrm{UV}}^2}{8\pi^2} \sum_f \lambda_f^2 \approx (125.09\ \mathrm{GeV})^2 \tag{2.12}$$

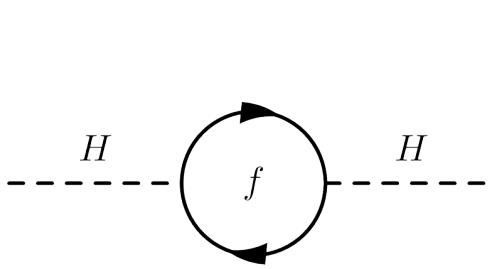

$$\Delta m_{\mathrm{H}}^2 = -\frac{\lambda^2}{8\pi^2}\Lambda_{\mathrm{UV}}^2 + m_f^2 \cdot O\left(\ln \Lambda_{\mathrm{UV}}\right) + \dots$$

(a)

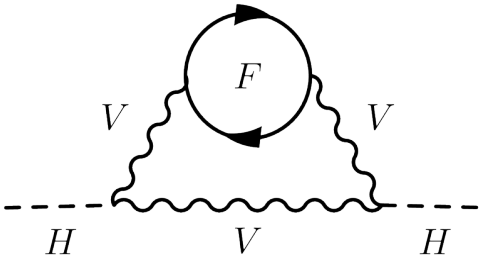

$$\Delta m_{\mathrm{H}}^2 \propto \frac{g^4}{(16\pi^2)^2} m_F^2 \cdot O\left(\ln \frac{\Lambda_{\mathrm{UV}}}{m_F}\right) + \dots$$

(b)

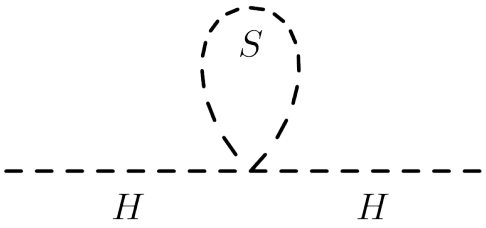

$$\Delta m_{\mathrm{H}}^2 = \frac{\lambda_S}{16\pi^2}\Lambda_{\mathrm{UV}}^2 - m_S^2 \cdot O\left(\ln \Lambda_{\mathrm{UV}}\right) + \dots$$

(c)

Figure 2.3: Radiative corrections to the squared Higgs mass for a single fermion in the Standard Model coupling directly to the Higgs field (a), a potential new heavy fermion coupling indirectly via electroweak vector bosons V (b) and a scalar particle S (c).

need to cancel with the mass parameter μ^2 in the Higgs potential with a precision of $m_H^2/\Lambda_{UV}^2 = m_H^2/m_{\mathrm{Pl}}^2 \approx 10^{-36}$, implying a fine-tuning over more than thirty orders of magnitude. The fine-tuning problem arising from the hierarchy of the electroweak symmetry breaking scale relative to the Planck scale becomes even more apparent when considering the effect of potential new heavy particles to the squared Higgs mass, which scales with the square of their masses (see Figure 2.3b) even when the new particles do not couple directly to the Higgs boson but only with mediation of gauge bosons.

2.2 Supersymmetry

A possible solution to the energy hierarchy problem for the stabilisation of the Higgs boson mass at the electroweak scale is a cancellation of the loop corrections from fermions

by scalar particles, as fermions and scalars lead to corrections of opposite sign to m_H^2 (see Figs. 2.3b, 2.3c). In order to achieve this, there must be a corresponding scalar particle for each Standard Model fermion and the two particles should have similar masses.

Supersymmetry (SUSY) [7] provides a mechanism for this, relating fermion and boson states. An introduction to supersymmetric extensions of the Standard Model based on Ref. [28] is given below.

2.2.1 Concept of Supersymmetry

The SUSY Algebra

The generators Q of supersymmetry mediate a transform fermions into bosons and vice versa:

$$Q\,|\text{boson}\rangle = |\text{fermion}\rangle\,, \qquad Q\,|\text{fermion}\rangle = |\text{boson}\rangle\,, \tag{2.13}$$

changing the spin by 1/2. The SUSY the generators therefore must be spinors and obey the anticommutation relations

$$\left\{Q_\alpha, Q_\beta\right\} = \left\{Q^\dagger_{\dot\alpha}, Q^\dagger_{\dot\beta}\right\} = 0, \tag{2.14}$$

$$\left\{Q_\alpha, Q^\dagger_{\dot\alpha}\right\} = 2\sigma^\mu_{\alpha\dot\alpha} P_\mu, \tag{2.15}$$

where α, β are left-handed and $\dot\alpha, \dot\beta$ right-handed Weyl spinor indices. According to Eq. (2.15), there is a nontrivial connection to space-time symmetries. The SUSY generators commute with the four-momentum, the generator of space-time translations:

$$\left[P^\mu, Q_\alpha\right] = \left[P^\mu, Q^\dagger_{\dot\alpha}\right] = 0. \tag{2.16}$$

The Haag-Sohnius-Lopuszánski generalisation [29] of the Coleman-Mandula theorem [30] states that the SUSY algebra defined in Eqs. 2.15-2.16 is the only nontrivial extension of the Poincaré algebra in renormalisable quantum field theory with massive particles.

Supermultiplets

In a supersymmetric theory, every particle has a superpartner under SUSY transformations in a common fundamental supermultiplet. Eq. (2.16) implies that the masses of

the superpartners in a supermultiplet must be equal. To preserve the gauge symmetries of the Lagrangian density, the superpartners must also have the same charge quantum numbers [31].

Two kinds of supermultiplets are required to formulate a supersymmetric extension of the Standard Model:

- Each *Chiral supermultiplet* consists of a complex scalar ϕ, and a Weyl spinor ψ. The fermions of the Standard Model belong to chiral supermultiplets with scalar superpartners, the sfermions. Scalar Higgs bosons form chiral supermultiplets with spin-1/2 higgsinos as superpartners.
- *Vector supermultiplets* are real fields. In the Wess-Zumino gauge, which eliminates unphysical auxiliary fields, a vector supermultiplet consists of a vector field A^a_μ and a Weyl spinor λ^a. The gauge boson fields of the Standard Model belong to vector supermultiplets with their fermionic superpartners, the gauginos.

Supersymmetry Breaking
The prediction of superpartners with the same masses as the Standard Model particles is in contradiction with the experimental observation. Therefore, supersymmetry, if realised in nature, must be broken and the superpartners too massive to be accessible to previous accelerator experiments. In order to provide a solution to the hierarchy problem, the masses of the superpartners must not be too large, no more than a few TeV. Several mechanisms of supersymmetry breaking have been proposed. Their effect is parametrised in a set of *soft* supersymmetry breaking terms, which lead to corrections to the squared Higgs mass that scale at most logarithmically with the SUSY mass scale.

2.2.2 The Minimal Supersymmetric Standard Model

The minimal supersymmetric Standard Model (MSSM) is the supersymmetric extension of the Standard Model with minimal particle content. Each Standard Model particles acquires a superpartner. In addition, two Higgs doublets H_u and H_d are needed to give masses to the up- and down-type fermions of the Standard Model, respectively. A single doublet as in the Standard Model would lead to gauge anomalies due to the non-zero hypercharge of the spin-1/2 higgsino.

Table 2.3 summarises the chiral multiplets of the MSSM with the fermions and Higgs

Table 2.3: Chiral supermultiplets of the MSSM in the three generations $i = 1,2,3$ [28] in the fundamental representations of the Standard Model gauge symmetries. The three colour charge components of each quark supermultiplet are not shown. $\alpha = 1,2$ is the index of the $SU(2)_L$ doublets.

Multiplet ($i = 1,2,3$)	Sfermions ϕ_i (spin-0)	Fermions ψ_i (spin-1/2)	$SU(3)_C$	$SU(2)_L$	Y
$\mathbf{Q_i^\alpha}$	$\tilde{Q}_i^\alpha = \begin{pmatrix}\tilde{u}_L\\ \tilde{d}_L\end{pmatrix}, \begin{pmatrix}\tilde{c}_L\\ \tilde{s}_L\end{pmatrix}, \begin{pmatrix}\tilde{t}_L\\ \tilde{b}_L\end{pmatrix}$	$Q_i^\alpha = \begin{pmatrix}u_L\\ d_L\end{pmatrix}, \begin{pmatrix}c_L\\ s_L\end{pmatrix}, \begin{pmatrix}t_L\\ b_L\end{pmatrix}$	$\mathbf{3}$	$\mathbf{2}$	$\frac{1}{3}$
$\mathbf{\bar{U}_i}$	$\tilde{u}_i^* = \tilde{u}_R^*, \tilde{c}_R^*, \tilde{t}_R^*$	$u_i^\dagger = u_R^\dagger, c_R^\dagger, t_R^\dagger$	$\bar{\mathbf{3}}$	$\mathbf{1}$	$-\frac{4}{3}$
$\mathbf{\bar{D}_i}$	$\tilde{d}_i^* = \tilde{d}_R^*, \tilde{s}_R^*, \tilde{b}_R^*$	$d_i^\dagger = d_R^\dagger, s_R^\dagger, b_R^\dagger$	$\bar{\mathbf{3}}$	$\mathbf{1}$	$+\frac{2}{3}$
$\mathbf{L_i^\alpha}$	$\tilde{L}_i^\alpha = \begin{pmatrix}\tilde{\nu}_e\\ \tilde{e}_L\end{pmatrix}, \begin{pmatrix}\tilde{\nu}_\mu\\ \tilde{\mu}_L\end{pmatrix}, \begin{pmatrix}\tilde{\nu}_\tau\\ \tilde{\tau}_L\end{pmatrix}$	$L_i^\alpha = \begin{pmatrix}\nu_e\\ e_L\end{pmatrix}, \begin{pmatrix}\nu_\mu\\ \mu_L\end{pmatrix}, \begin{pmatrix}\nu_\tau\\ \tau_L\end{pmatrix}$	$\mathbf{1}$	$\mathbf{2}$	-1
$\mathbf{\bar{E}_i}$	$\tilde{e}_i^* = \tilde{e}_R^*, \tilde{\mu}_R^*, \tilde{\tau}_R^*$	$e_i^\dagger = e_R^\dagger, \mu_R^\dagger, \tau_R^\dagger$	$\mathbf{1}$	$\mathbf{1}$	$+2$
Multiplet	Higgs fields ϕ (spin-0)	higgsino fields ψ (spin-1/2)			
$\mathbf{H_u^\alpha}$	$H_u^\alpha = \begin{pmatrix}H_u^+\\ H_u^0\end{pmatrix}$	$\tilde{H}_u^\alpha = \begin{pmatrix}\tilde{H}_u^+\\ \tilde{H}_u^0\end{pmatrix}$	$\mathbf{1}$	$\mathbf{2}$	1
$\mathbf{H_d^\alpha}$	$H_d^\alpha = \begin{pmatrix}H_d^0\\ H_d^-\end{pmatrix}$	$\tilde{H}_d^\alpha = \begin{pmatrix}\tilde{H}_d^0\\ \tilde{H}_d^-\end{pmatrix}$	$\mathbf{1}$	$\mathbf{2}$	-1

fields and their sfermion and higgsino superpartners. In Table 2.4, the vector supermultiplets of the MSSM containing the gauge fields of the electroweak and strong interactions and their spin-1/2 gaugino superpartners are shown.

The Lagrangian density of the MSSM is constructed as the supersymmetric equivalent of the Standard Model Lagrangian. This includes the kinetic part

$$\begin{aligned}\mathcal{L}_{\text{MSSM}}^{\text{kinetic}} = &- \sum_{\phi=\tilde{Q},\tilde{L},\tilde{u}^*,\tilde{d}^*,\tilde{e}^*,} \left(D^\mu \phi^{\dagger i} D_\mu \phi_i\right) + \sum_{\psi=Q,L,u^\dagger,d^\dagger,e^\dagger,} \left(D^\mu \psi^{\dagger i} \bar{\sigma}^\mu D_\mu \psi_i\right) \\ &- \sum_{\phi=\mathrm{H_u},\mathrm{H_d}} \left(D^\mu \phi^\dagger D_\mu \phi\right) + \sum_{\psi=\tilde{\mathrm{H}}_\mathrm{u},\tilde{\mathrm{H}}_\mathrm{d}} \left(D^\mu \psi^\dagger \bar{\sigma}^\mu D_\mu \psi\right) \\ &- \frac{1}{4} B_{\mu\nu} B^{\mu\nu} - \frac{1}{4} W_{\mu\nu}^b W_b^{\mu\nu} - \frac{1}{4} G_{\mu\nu}^a G_a^{\mu\nu} \\ &+ i\tilde{B}^\dagger \bar{\sigma}^\mu D_\mu \tilde{B} + i\tilde{W}_b^\dagger \bar{\sigma}^\mu D_\mu \tilde{W}^b + i\tilde{g}_a^\dagger \bar{\sigma}^\mu D_\mu \tilde{g}^a\end{aligned} \tag{2.17}$$

Table 2.4: Vector supermultiplets of the MSSM in the adjoint representations of the Standard Model gauge symmetries [28].

Multiplet	Gaugino λ^a	Gauge Boson A^a_μ	$SU(3)_C$	$SU(2)_L$	Y
$\mathbf{G}^a$	$\tilde{g}^a$	G^a_μ $(a = 1,\ldots,8)$	**8**	**1**	0
$\mathbf{W}^a$	$\tilde{W}^b$	W^b_μ $(b = 1,2,3)$	**1**	**3**	0
$\mathbf{B}$	$\tilde{B}$	B_μ	**1**	**1**	0

with kinetic terms for the fermions and sfermions, the Higgs fields and higgsinos, and the gauge fields and gauginos in the first, second, third and fourth lines, respectively. The covariant derivative of the gaugino fields in vector supermultiplets of non-Abelian gauge symmetries has the form

$$D_\mu \lambda_a = \partial_\mu \lambda_a + g f_{abc} A^b_\mu \lambda^c \tag{2.18}$$

required by supersymmetry. The supersymmetric version of the standard model Yukawa coupling terms is obtained using the *superpotential* defined by the scalar fields of the MSSM,

$$W_{\text{MSSM}} = -y^u_{ij}\tilde{u}^*_i \tilde{Q}^\alpha_j H^\beta_u \epsilon_{\alpha\beta} - y^d_{ij}\tilde{d}^*_i \tilde{Q}^\alpha_j H^\beta_d \epsilon_{\alpha\beta} - y^e_{ij}\tilde{e}^*_i \tilde{L}^\alpha_j H^\beta_d \epsilon_{\alpha\beta} + \mu H^\alpha_u H^\beta_d \epsilon_{\alpha\beta} \qquad (i,j = 1,2,3) \tag{2.19}$$

with the Yukawa coupling parameters y^u, y^d and y^e and the Higgs boson mass parameter μ.

Couplings between scalars and fermions are introduced into the MSSM Lagrangian density using the derivatives

$$W_u = \frac{\partial}{\partial \phi_u} W_{\text{MSSM}} \tag{2.20}$$

and

$$W_{uv} = \frac{\partial^2}{\partial \phi_u \phi_v} W_{\text{MSSM}} \tag{2.21}$$

of the superpotential, where the indices u, v run over all the sleptons, squarks and Higgs fields in the MSSM, in the form

$$\mathcal{L}^{\text{matter}}_{\text{MSSM}} = -\frac{1}{2} W^{uv}\psi_u \psi_v + h.c. - W_u W^{u*}. \tag{2.22}$$

The first term in Eq. (2.22) yields the Yukawa couplings between the Standard Model fermions and the Higgs bosons, as well as respective couplings of fermions, sfermions

and higgsinos. It also contains a higgsino mass term $\mu\left(\tilde{H}_u^\dagger \tilde{H}_d\right) + h.c.$ The second contribution in Eq. (2.22) results in mass terms for the squarks and sleptons as required by supersymmetry, the Higgs boson mass term $\mu^2\left(|H_u|^2 + |H_d|^2\right)$ as well as three- and four-scalar couplings.

Additional gauge interaction terms between fermions, sfermions and gauginos and a quartic sfermion coupling are required by supersymmetry in correspondence to the gauge couplings of the Standard Model fermions:

$$\begin{aligned}\mathcal{L}_{\text{MSSM}}^{\text{Gauge}} = &-\sqrt{2}\left[g_s\left(\phi_u^\dagger \lambda_a \psi^u\right)\tilde{g}^a + g_W\left(\phi_u^\dagger \sigma_b \psi^u\right)\tilde{W}^b + g_Y\left(\phi_u^\dagger \psi^u\right)\tilde{B}\right] + h.c. \\ &-\frac{1}{2}\left|g_s \phi_u^\dagger \lambda_a \phi^u\right|^2 - \frac{1}{2}\left|g_W \phi_u^\dagger \sigma_b \phi^u\right|^2 - \frac{1}{2}\left|g_Y \phi_u^\dagger \phi^u\right|^2,\end{aligned} \tag{2.23}$$

where the index u runs through all chiral supermultiplets in the MSSM.

The final contribution to the MSSM Lagrangian density are additional mass terms for the squarks, sleptons, gauginos and Higgs bosons, resulting from the breaking of supersymmetry:

$$\begin{aligned}\mathcal{L}_{\text{SUSY breaking}} = &-\frac{1}{2}\left(M_3 \tilde{g}_a \tilde{g}^a + M_2 \tilde{W}_b \tilde{W}^b + M_1 \tilde{B}\tilde{B} + h.c.\right) \\ &-\left(a_{ij}^u \tilde{u}^i \tilde{Q}^j H_u - a_{ij}^d \tilde{d}^i \tilde{Q}^j H_d - a_{ij}^e \tilde{e}^i \tilde{L}^j H_d + h.c.\right) \\ &-\left(m_Q^2\right)^{ij} \tilde{Q}_i^\dagger \tilde{Q}_j - \left(m_L^2\right)^{ij} \tilde{L}_i^\dagger \tilde{L}_j \\ &-\left(m_u^2\right)^{ij} \tilde{u}_i^* \tilde{u}_j - \left(m_d^2\right)^{ij} \tilde{d}_i^* \tilde{d}_j - \left(m_e^2\right)^{ij} \tilde{e}_i^* \tilde{e}_j \\ &- m_{H_u}^2 H_u^\dagger H_u - m_{H_d}^2 H_d^\dagger H_d - \left(b H_u H_d + c.c.\right),\end{aligned} \tag{2.24}$$

where i,j are generation indices ($i, j = 1, 2, 3$). The coefficients of the terms in Eq. (2.24) contribute a total of 105 additional free parameters due to the unknown SUSY breaking mechanism.

Electroweak Symmetry Breaking

The supersymmetry breaking term bH_uH_d (see Eq. (2.24)) is necessary to guarantee a nontrivial minimum of the scalar Higgs potential in the MSSM. Hence, electroweak supersymmetry breaking necessarily implies that SUSY must be broken [28].

The two complex Higgs doublets in the MSSM have a total of eight degrees of freedom. After spontaneous symmetry breaking, three are transformed into the longitudinal polarisation states of the W and Z bosons, as in the Standard Model. The remaining five

Table 2.5: Higgsino and gaugino states with spin-1/2 - eigenstates of the gauge symmetries and the corresponding mass eigenstates. The gluinos do not mix with the other gauginos due to their colour charge. The neutralino and chargino mass eigenstates are ordered according to increasing mass.

Eigenstates of the gauge symmetries	Mass eigenstates
2 neutral higgsinos $\tilde{H}_u^0$, $\tilde{H}_d^0$ 1 neutral wino $\tilde{W}_3$ 1 neutral bino $\tilde{B}$	4 neutralinos $\tilde{\chi}_1^0$, $\tilde{\chi}_2^0$, $\tilde{\chi}_3^0$, $\tilde{\chi}_4^0$
2 charged higgsinos $\tilde{H}_u^+$, $\tilde{H}_d^-$ 2 charged winos $\tilde{W}^\pm$	4 charginos $\tilde{\chi}_1^\pm$, $\tilde{\chi}_2^\pm$
8 gluinos $\tilde{g}_a$	8 gluinos $\tilde{g}_a$

degrees of freedom result in five massive Higgs bosons: two neutral scalars h^0 and H^0, a neutral pseudoscalar A^0, and two charged scalars $H^\pm$.

The couplings between the Higgs fields, the spin-1/2 higgsinos and spin-1/2 gauginos contained in the first line of Eq. (2.23) result in a mixing between the higgsinos and gauginos after electroweak symmetry breaking. The two neutral higgsinos mix with the bino and the neutral wino, and the two charged winos mix with the two charged higgsinos, resulting in four neutralinos $\tilde{\chi}_i^0$ ($i = 1 \ldots 4$) and four charginos $\tilde{\chi}_i^\pm$ ($i = 1 \ldots 2$), respectively (see Table 2.5). The gluinos do not mix due to their colour charges. The couplings of the neutralinos and charginos and their mass hierarchy depend on the parameters introduced by SUSY breaking.

2.2.3 R-Parity

The MSSM requires conservation of an additional quantum number, R-parity

$$P_R = (-1)^{3(B-L)+2s}\,, \tag{2.25}$$

with baryon number B, lepton number L and the spin s in order to prevent additional terms in the superpotential

$$W_{\Delta B,\Delta L} = \lambda_{ijk}\tilde{L}_i^\alpha \tilde{L}_j^\beta \tilde{e}_k^* \epsilon_{\alpha\beta}\epsilon_{ij} + \lambda'_{ijk}\tilde{L}_i^\alpha \tilde{Q}_j^\beta \tilde{d}_k^* \epsilon_{\alpha\beta} + \lambda''_{ijk}\tilde{u}_i^* \tilde{d}_j^* \tilde{d}_k^* \epsilon_{jk} + \kappa_i \tilde{L}_i^\alpha H_u^\beta \epsilon_{\alpha\beta}, \tag{2.26}$$

with coupling parameters λ_{ijk}, λ'_{ijk}, λ''_{ijk} and κ_i, where $i,j,k \in \{1,2,3\}$ are generation indices and $\alpha,\beta \in \{1,2\}$ are $SU(2)_L$ doublet indices. These terms would otherwise be allowed by supersymmetry, renormalisability and gauge symmetry requirements, and lead to lepton number (λ_{ijk},λ'_{ijk},κ_i) and baryon number (λ''_{ijk}) violation [32].

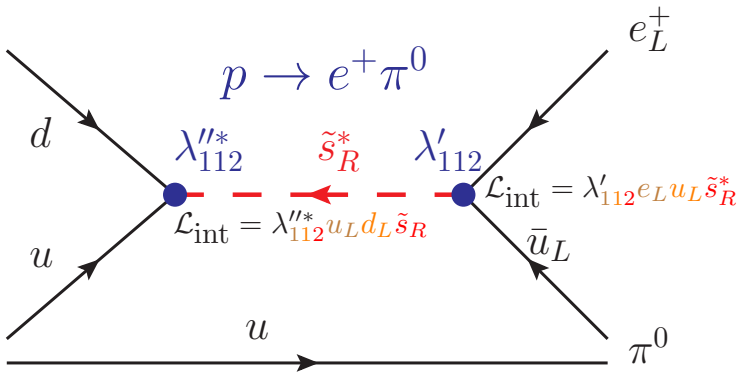

Figure 2.4: Proton decay process mediated by a combination of λ' and λ'' couplings.

Based on the field content, the first trilinear term in Eq. (2.26) is also referred to as the LLE term, the second as the LQD term and the third as UDD. Strong experimental bounds on the proton decay rate [33] forbid a significant simultaneous lepton and baryon number violation, which would result in rapid proton decay mediated by virtual sfermions as illustrated in Figure 2.4.

All Standard Model particles have positive R-parity, while the as-yet undiscovered superpartners have negative R-parity. R-parity-conservation (RPC) as in the MSSM has profound consequences:

- Superpartners are produced in even numbers from Standard Model particles.
- The lightest superpartner (LSP) cannot decay into Standard Model particles and thus has to be stable.
- Baryon and lepton number are both conserved and SUSY particles do not mediate proton decay.

If the stable LSP is the lightest neutralino $\tilde{\chi}^0_1$, it is an excellent candidate for a cold dark matter constituent [34].

It should be stressed that, while R-parity-conservation is one way to prevent rapid proton decay which also leads to an attractive dark matter candidate, proton decay can also be suppressed by other symmetries allowing for some of the terms in Eq. (2.26). For example, the baryon triality symmetry [35] allows for lepton number violation, but forbids baryon number violation. In such a scenario, the lepton number violating term $\kappa_i \tilde{L}_i^{\alpha} H_u^{\beta} \epsilon_{\alpha\beta}$ can generate neutrino masses through mixing of neutrinos and neutralinos [36].

An overview of the experimental signatures of R-parity-conserving and R-parity-violating (RPV) supersymmetry is given in Chapter 5.

2.3 Proton-Proton Interactions

As discussed in Section 2.2, in order to provide a solution to the hierarchy problem, superpartners must not be heavier than a few TeV. The Large Hadron Collider (LHC) at CERN, which collides protons at centre-of-mass energies of up to 14 TeV, therefore is the ideal accelerator for searches for supersymmetry. A proton-proton interaction at the LHC consists of several components. The hard scattering process with high momentum transfer between colliding constituents of the protons (quarks and gluons) and possible production of new particles can be described by perturbation theory [37]. Accompanying lower energy interactions of the proton remnants form the so-called underlying event that, in general, cannot be described by perturbation theory. Instead, phenomenological models are used which need to be tuned to the collision data [38].

According to factorisation theorems [39], the proton-proton collision cross-section $p_1\ p_2 \to X$ can be expressed by the hard scattering cross-section $ab \to X$ of partons a, b convoluted with the measured [40–43] parton distribution functions f_a and f_b in the protons:

$$\sigma(p_1 p_2 \to X) = \sum_{a \in p_1, b \in p_2} \int dx_a dx_b f_a\left(x_a, \mu_F^2\right) f_b\left(x_b, \mu_F^2\right) \cdot \hat{\sigma}_{ab\to X}\left(x_a, x_b, \mu_R^2\right). \quad (2.27)$$

Here, x_a and x_b are the momentum fractions of free partons a and b in the proton. The expression in Eq. (2.27) contains two energy scales [37] - the factorisation scale μ_F, which describes the boundary between hard and soft processes, and the renormalisation scale μ_R resulting from the perturbative calculation of the parton-level cross-section.

The sensitivity of the result to these scales usually decreases when higher-order correc-

tions are included. Varying the values of μ_F and μ_F of the scales can give an estimate of the theoretical uncertainty of the calculation.

Chapter 3

The ATLAS Detector at the Large Hadron Collider

3.1 The Large Hadron Collider

The Large Hadron Collider (LHC) [3] is a circular particle accelerator of 26.7 km circumference located at CERN, the European Centre for Particle Physics near Geneva. It collides proton beams at centre-of-mass energies up to 14 TeV. In 2010 and 2011, the LHC was operated at a centre-of-mass energy of $\sqrt{s}$ = 7 TeV, and in 2012 at $\sqrt{s}$ = 8 TeV [44]. Following a consolidation campaign in 2013-14, data-taking has recommenced in June 2015 at $\sqrt{s}$ = 13 TeV.

The LHC is installed in the tunnel formerly occupied by the LEP electron-positron collider. Experiments are located at four interaction points. There are the multi-purpose detectors ATLAS [45] and CMS [46] measuring highest energy processes, the LHCb B-physics experiment [47] and the ALICE heavy ion collision experiment [48]. The LHCf [49] and TOTEM [50] experiments, dedicated to physics in forward scattering of the protons, share the interaction regions with the ATLAS and CMS detectors, respectively. MoEDAL [51] will share the interaction region with LHCb. Figure 3.1 shows the layout of the LHC ring.

At nominal operation, the LHC proton beams consist of bunches of about $1.2 \cdot 10^{11}$ protons [3]. Passing through a chain of pre-accelerators from the LINAC 2 linear accelerator through a booster ring, the Proton Synchrotron (PS) and the Super Proton Synchrotron (SPS), the protons are accelerated to the injection energy of 450 GeV and

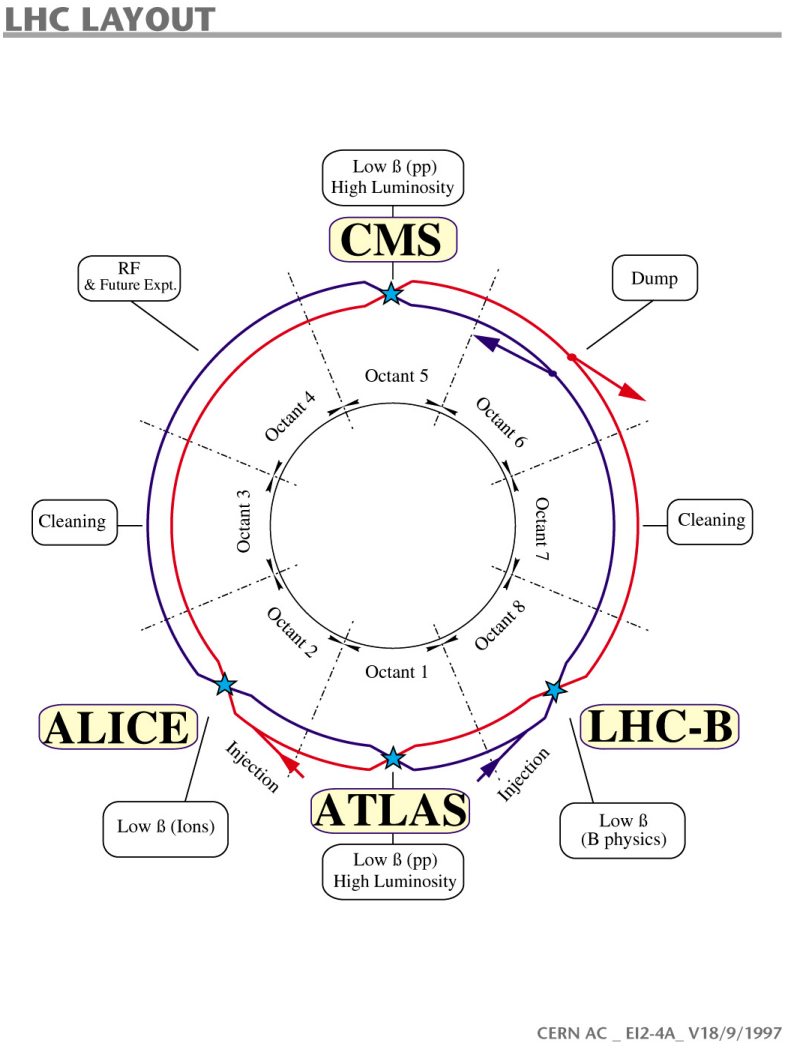

Figure 3.1: Layout of the LHC ring [52].

injected into the LHC in opposite directions in trains of up to 72 bunches with a bunch spacing of 25 ns, where they are accelerated to the final energy. At the design luminosity of 10^{34} cm^{-2}s^{-1}, the LHC is filled with a total of 2808 bunches per beam. Gaps between the bunch trains to allow for beam injection and dumping by kicker magnets. The full accelerator complex at CERN is illustrated in Figure 3.2. The operating parameters during LHC Run 1 were different from these nominal values [54] corresponding to the design luminosity. Apart from the lower beam energies, a bunch spacing of 50 ns in trains of up to 36 bunches was used, and up to 1396 bunches per beam. The lower energies and greater bunch spacing allowed for a larger bunch size of up to $1.7 \cdot 10^{11}$

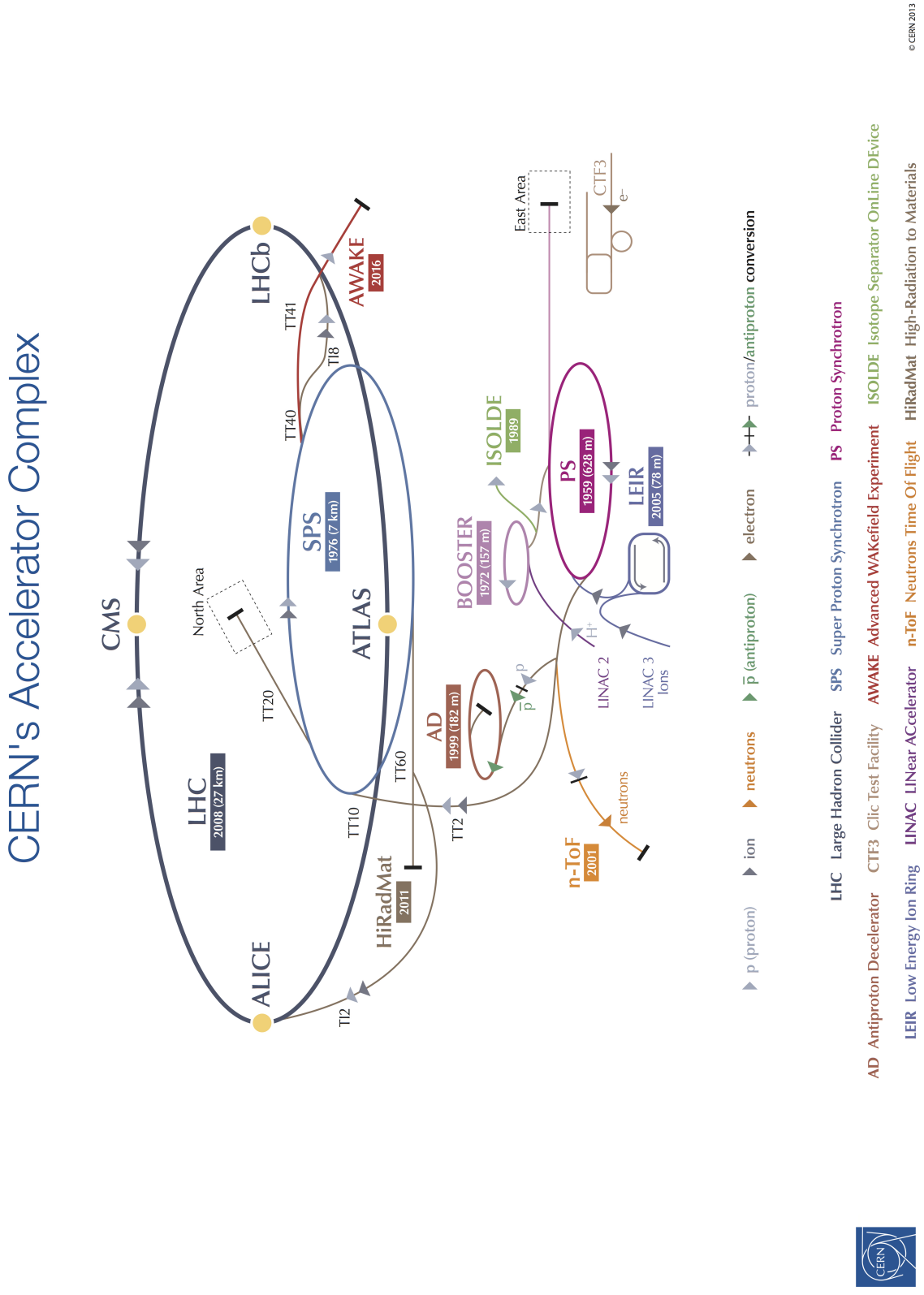

Figure 3.2: Overview of the accelerator chain at CERN [53].

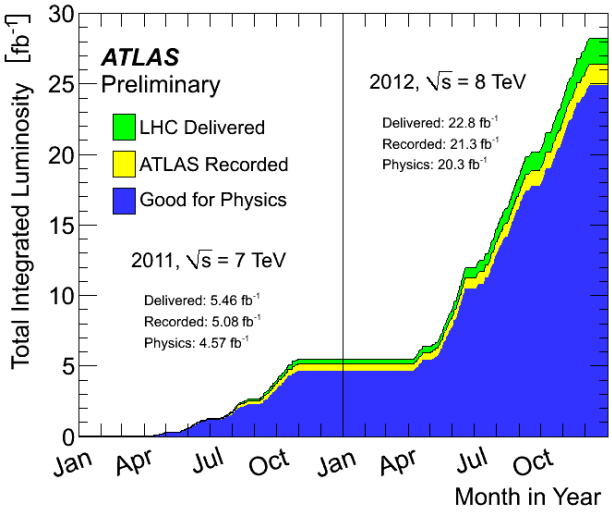

Figure 3.3: Integrated luminosity accumulated the ATLAS experiment in the years 2011-12 [56] as delivered by the LHC (green), recorded by the ATLAS detector (yellow) and accepted for physics analyses with all detector components operational (blue).

protons per bunch to increase the number of collisions per revolution. For the upcoming LHC Run 2, operation with nominal 25 ns bunch spacing is foreseen [55].

The rate of proton-proton interactions in the experiments is determined by the collider parameters via the instantaneous luminosity [44]

$$\mathcal{L} = \frac{N_p^2 n_b f}{4\pi\sigma_x^*\sigma_y^*} F = \frac{N_p^2 n_b f \gamma}{4\pi\beta^*\epsilon_n} F, \tag{3.1}$$

where N_p is the number of protons per bunch, n_b the number of bunches per beam, f the revolution frequency of the protons, $\sigma_{x,y}^*$ the transverse beam sizes at the interaction point and F a geometrical factor determined by the crossing angle of the beams [44]. In the alternative parametrisation, ϵ_n is the normalised transverse emittance, β^* the amplitude of the transverse beam oscillations around the nominal orbit at the interaction point, and γ the relativistic gamma factor. The rate of a process with the cross-section σ is given by

$$\frac{dN}{dt} = \sigma \cdot \mathcal{L}. \tag{3.2}$$

The LHC is designed to deliver an instantaneous luminosity of 10^{34} cm^{-2}s^{-1}. In LHC Run 1, a peak value of $7.7 \cdot 10^{33}$ cm^{-2}s^{-1} was achieved, close to the design value [44].

The total number of expected events N of a given process in a given time interval is determined by the integrated luminosity L over this time period

$$N = \sigma \int \mathcal{L} dt = \sigma \cdot L. \tag{3.3}$$

Figure 3.3 shows the integrated luminosity delivered to and recorded by the ATLAS experiment during the 2011 and 2012 data-taking periods. The data sets comprise 4.6 fb^{-1} in 2011 at $\sqrt{s}$ = 7 TeV and 20.3 fb^{-1} in 2012 at $\sqrt{s}$ = 8 TeV.

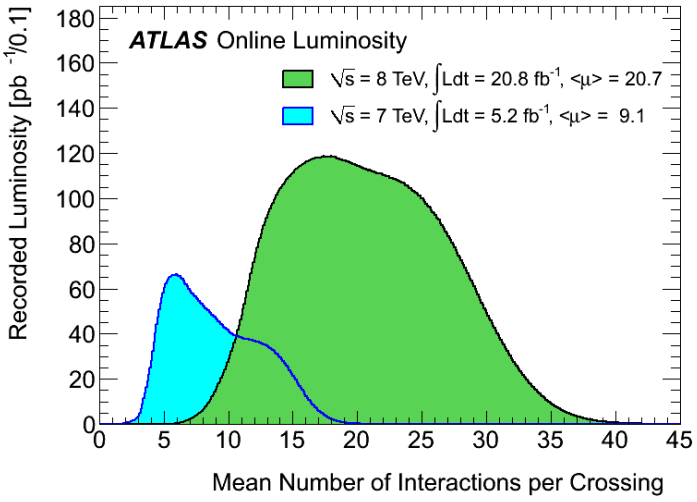

Figure 3.4: Distribution of the mean number of inelastic proton-proton interactions per bunch crossing for the 2011 (blue) and 2012 (green) data sets (see text) [57].

The strong focusing of the beams at the interaction point required to maximise the instantaneous luminosity in Run 1 increased the number of inelastic proton-proton interactions per bunch crossing μ. The total inelastic proton-proton interaction cross-section at $\sqrt{s}$ = 7 TeV was measured to be 60 mb [58]. Using Eq. (3.1) and (3.2), the expected number N_{bx} of inelastic interactions per bunch-crossing is given by

$$N_{bx} = \sigma_{\text{inel}} \cdot \frac{\mathcal{L}}{n_b \cdot f} = \sigma_{\text{inel}} \frac{N_p^2 \gamma}{4\pi\beta^* \epsilon_n} F. \tag{3.4}$$

For the typical beam parameters of the ATLAS and CMS interaction points at the highest luminosity during the LHC Run 1 [54] of $\epsilon_n \approx 2.5$ μm, $\beta^* \approx 0.6$ m, $N_p \approx 1.6 \cdot 10^{11}$,

$\gamma = 4.3 \cdot 10^3$ and $F \approx 1$, one obtains from Eq. (3.4) the estimate

$$N_{bx} = 6 \cdot 10^{-30}\ \mathrm{m}^2 \cdot \frac{\left(1.6 \cdot 10^{11}\right)^2 \cdot 4.3 \cdot 10^3}{4\pi \cdot 0.6\ \mathrm{m} \cdot 2.5 \cdot 10^{-6}\ \mathrm{m}} \approx 40.$$

The highest numbers of parasitic interactions, also called pile-up of events in the detector, occur at the start of a data-taking run before the beams lose intensity due to collisions. Additional pile-up activity can significantly degrade the experimental resolution. This will be further discussed in Section 3.3. Figure 3.4 shows the distribution of the mean number of inelastic proton-proton interactions per bunch crossing for the 2011 and 2012 LHC runs, averaged over typical data taking periods of one minute [43].

3.2 The ATLAS Detector

The ATLAS (**A** **T**oroidal **L**HC **A**pparatu**s**) detector [45] is one of two multi-purpose experiments at the LHC. It covers almost the entire solid angle around the interaction point. The following overview of the detector is based on Refs. [45, 59, 60].

3.2.1 Geometric Definitions

ATLAS uses a right-handed coordinate system (see Figure 3.5) with the origin of the nominal interaction point. The z axis points along the beam line, the x axis towards the centre of the LHC ring and the y axis upwards. For the data analysis, polar coordinates are commonly used, with the azimuthal angle ϕ, polar angle θ and radial distance r, defined as

$$\phi = \arctan \frac{y}{x}, \tag{3.5}$$

$$\theta = \arctan \frac{z}{\sqrt{x^2 + y^2}} \tag{3.6}$$

and

$$r = \sqrt{x^2 + y^2}. \tag{3.7}$$

The pseudorapidity

$$\eta = -\ln\left(\tan \frac{\theta}{2}\right) \tag{3.8}$$

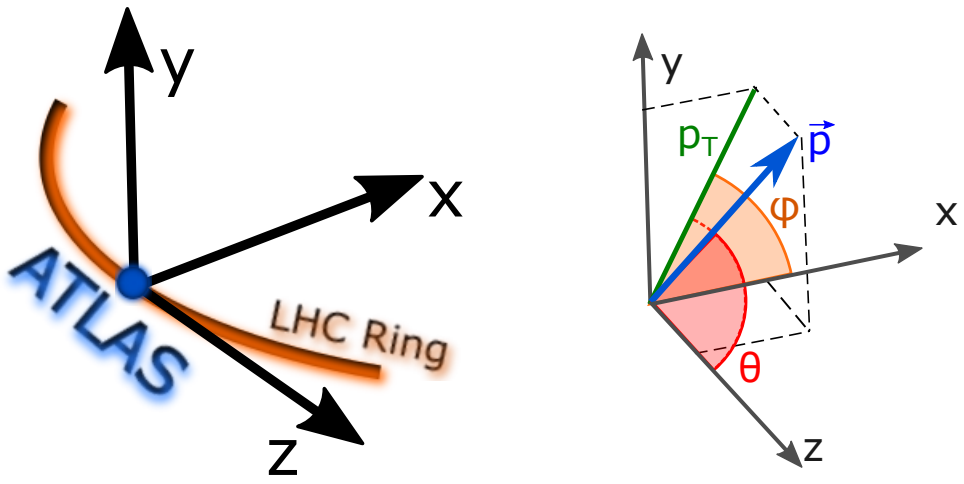

Figure 3.5: Left: Illustration of the ATLAS coordinate axes in relation the global coordinates. Right: Illustration of the commonly used polar notation of momenta in the ATLAS coordinates.

is frequently used instead of the polar angle. *Forward* and *central* refer to processes at high and low values of the pseudorapidity, respectively. Four-momenta of particles are described by the variables $[p_T, \eta, \phi, m]$ or $[p_T, \eta, \phi, E]$ (see Figure 3.5), with the transverse momentum

$$p_T = \sqrt{p_x^2 + p_y^2} = |\vec{p}| \cdot \sin\theta = |\vec{p}| \cdot \frac{1}{\cosh\eta}. \tag{3.9}$$

The angular distance between two vectors from the interaction point is measured by

$$\Delta R = \sqrt{(\Delta\eta)^2 + (\Delta\phi)^2}. \tag{3.10}$$

Charged particle tracks in the ATLAS magnetic fields are described by 5 parameters $\left[d_0, z_0, \theta, \phi, \frac{q}{p}\right]$ [61]. The charge of the particle is q, and the momentum vector at the point of closest approach is (p, θ, ϕ). The transverse and longitudinal signed impact parameters d_0 and z_0 describe the point of closest approach of the trajectory to the local z axis in the given frame of reference (see Figure 3.6). Commonly, either the nominal or the reconstructed primary interaction point (vertex) is used as reference point.

The ATLAS detector, shown in Figure 3.7, has a cylindrical geometry with a so-called barrel region and two endcaps. Detector components in the barrel are arranged in concentric cylinders around the beam pipe, while in the endcaps the arrangement is

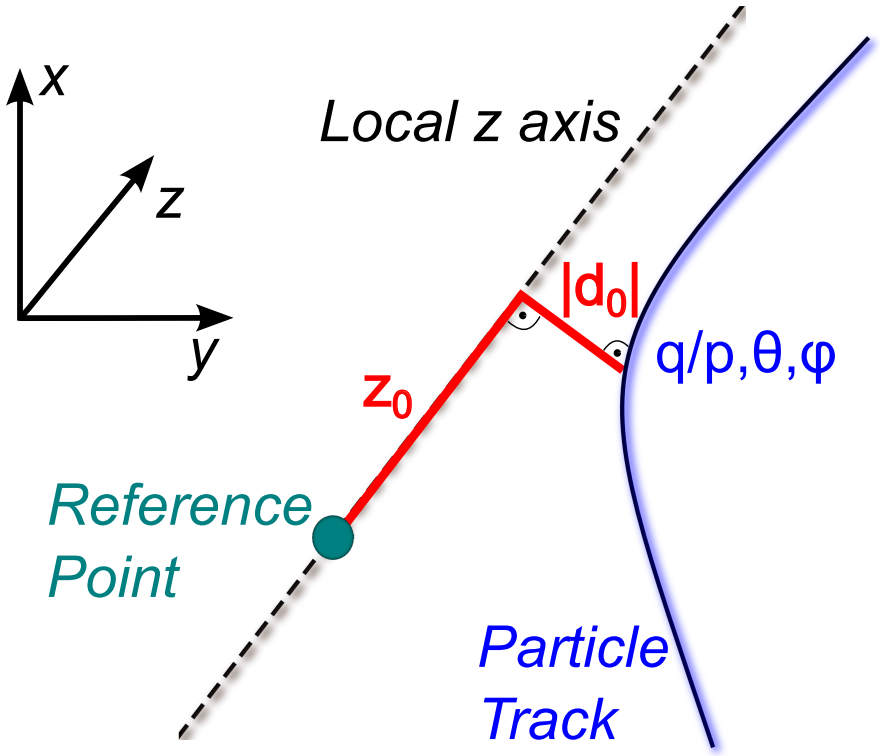

Figure 3.6: Parameters of charged particle tracks. d_0 and z_0 are the signed transverse impact parameter and longitudinal impact parameter, respectively. q is the particle charge and (p, θ, ϕ) the momentum vector in polar coordinates at the point of closest approach to the local z axis.

in circular wheels perpendicular to the beam pipe. The detector consists of three main subdetectors: The inner tracking detector, the calorimeters and the Muon Spectrometer.

3.2.2 The Inner Tracking Detector

The first detector component traversed by particles emerging from the interaction point is the Inner Detector (ID). It precisely measures the trajectories of charged particles produced in the interactions and allows for the reconstruction of the primary interaction point and possible secondary vertices from particle decays or pile-up interactions.

The ATLAS Inner Detector is surrounded by a superconducting solenoid magnet [63]

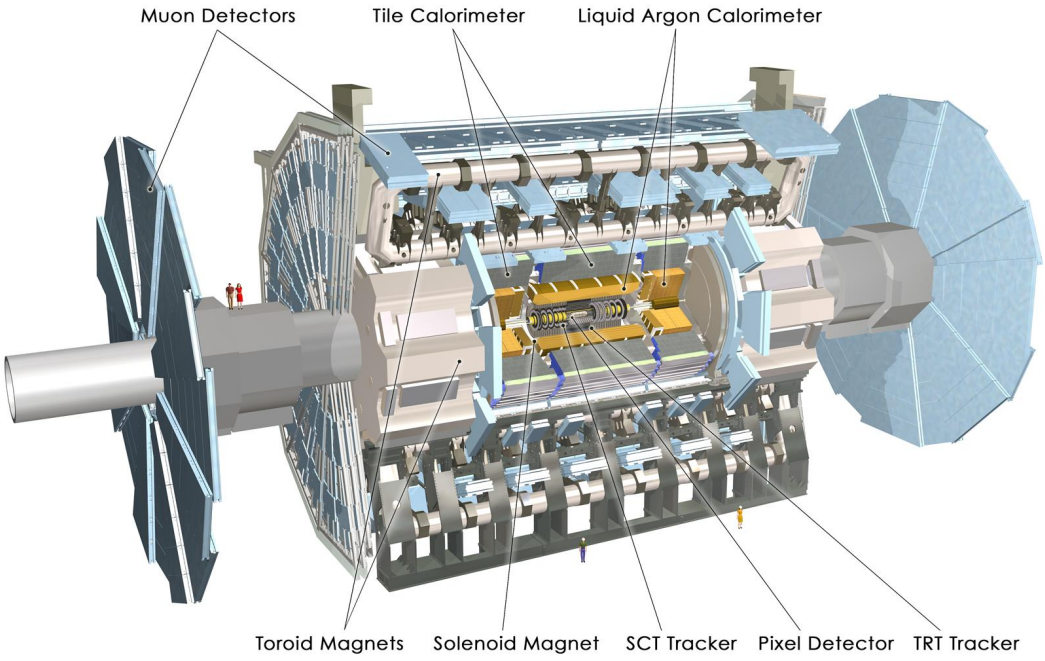

Figure 3.7: Illustration of the ATLAS detector [62].

which provides a homogeneous magnetic field in z direction with flux density of 2T. Charged particle tracks are bent in the plane perpendicular to the beam axis, allowing for the measurement of the particle momentum and charge.

Several thousand particles are produced per bunch crossing in the detectors of the LHC [45]. In order to resolve all particle tracks above typically 0.5 GeV, as well as production and decay vertices in an event, the ATLAS Inner Detector has to provide high granularity and spatial resolution and high rate capability. At the same time, the amount of material traversed by the outgoing particles must be kept at a minimum in order to prevent degradation of the spatial resolution due to multiple scattering and radiation. This is achieved by using silicon trackers near the interaction point surrounded by a straw drift tube detector.

Pixel Detector [64]

The layers of the Inner Detector closest to the beam pipe consist of silicon pixel sensors. The Pixel Detector with its high granularity is crucial for the precise reconstruction of production and decay vertices, pattern recognition and the identification of b-quark

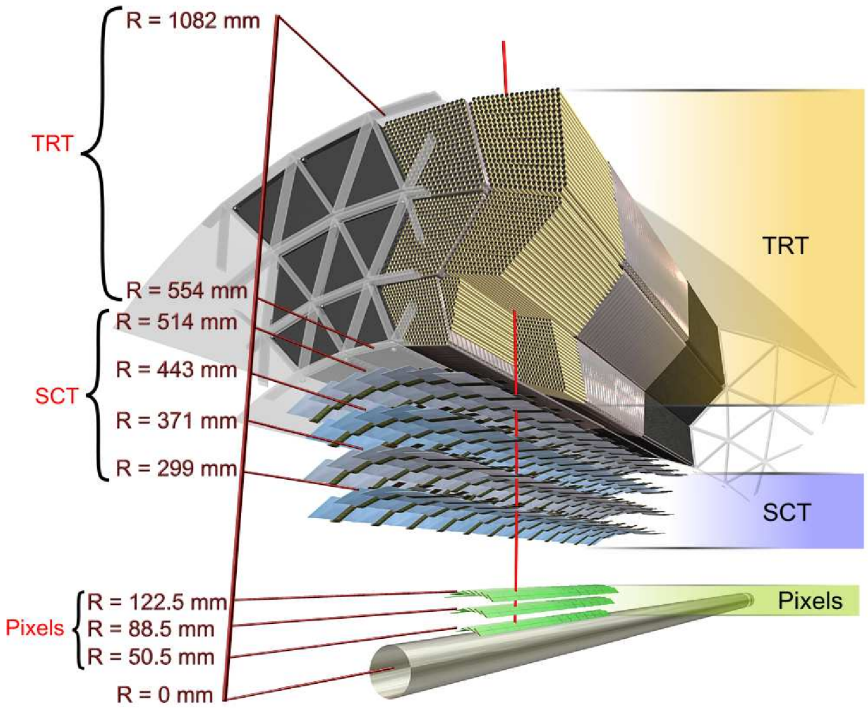

Figure 3.8: Layout of the ATLAS Inner Detector in the barrel region [45]. Three layers of pixel sensors are followed by four SCT layers and 36 layers of TRT straw tubes.

jets via the relatively long B meson lifetime of about 0.5 mm/c [65]. In the barrel part of the detector, three concentric cylindrical layers of pixel sensors are installed at radii of approximately 50.5 mm, 88.5 mm and 122.5 mm. In the endcaps, the pixel modules are mounted on three disks on either side of the interaction point, at $z = \pm 495$ mm, ± 580 mm and ± 650 mm. The Pixel Detector covers a pseudorapidity region of $|\eta| < 2.5$ with three layers of sensors, with a position resolution of 10 μm transverse and of 115 μm longitudinal to the beam axis in the barrel. The endcap modules have comparable resolutions in the longitudinal and radial directions, respectively.

Semiconducting Tracker (SCT)

The next layer of the tracking detector consists of four cylindrical layers of silicon microstrip sensors [66] in the barrel and nine layers in each endcap. To obtain two-dimensional hit position information in each layer, two sensors are mounted back-to-

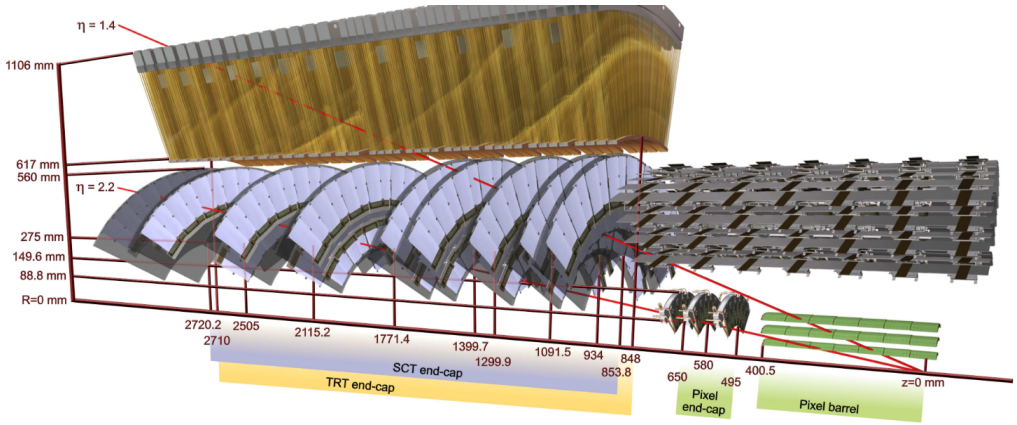

Figure 3.9: Layout of the ATLAS Inner Detector in the endcap region [45]. Three pixel disks and nine SCT disks are mounted on either side of the barrel.

back on each module with a small stereo angle of 40 mrad. In the barrel region, the strips point in the z direction, to measure with highest precision the $r\phi$ coordinates perpendicular to the magnetic field lines. The SCT layers are located at radii of 299 mm, 371 mm, 443 mm and 514 mm in the barrel. In the endcap disks, the strips are aligned in radial direction. The z coordinate of the nine endcap modules are between ±853 mm and ±2.72 m. Each particle from the interaction point hits at least four SCT sensor layers, each with a spatial resolution of 17 μm transverse and of 580 μm longitudinal to the beam axis in the barrel. The endcap modules have similar resolutions in the longitudinal and radial directions, respectively. The SCT and the Pixel Detector cover the pseudorapidity region $|\eta| < 2.5$.

Transition Radiation Tracker (TRT) [67]

The third component of the Inner Detector, the Transition Radiation Tracker (TRT), uses straw drift tubes with a diameter of 3 mm filled with a $Xe/CO_2/O_2$ gas mixture. Each straw tube has a spatial resolution of 130 μm in the plane perpendicular to the magnetic field. In addition, this subdetector is capable of contributing to the electron identification by detecting transition radiation emitted by the electrons passing through the interleaved polypropylene radiator material between the tubes. In the barrel region, the TRT tubes are oriented parallel to the beam line, with a length of 1.4 m. The sense wires are split in the centre to reduce occupancy, creating a small insensitive region of about 2 cm in length. In the endcaps, the TRT tubes are oriented radially. The TRT

extends to a pseudorapidity of $|\eta| < 2.0$. The coordinate along the TRT wire direction is not measured and therefore the TRT does not provide η-information.

3.2.3 The Calorimeter System

After passing through the Inner Detector, the particles enter the calorimeters (see Figure 3.10), which measure their energies by absorbing them (with the exception of neutrinos and muons). In order to accurately measure missing the transverse momentum (see Section 3.3), maximum solid angle coverage by the calorimeters is desirable. Furthermore, high energy resolution for particles and jets is required. The depth of the calorimeters must be large enough to fully contain the showers produced by incident particles. This is also important because particles emerging from the calorimeters ('punch-through') can enter the Muon Spectrometer (see Section 3.2.3.1) and be misidentified as muons. The calorimeters are finely segmented in three dimensions for angular measurements of showers, for matching them to tracks in the Inner Detector, and for the identification of electrons, photons, muons, hadrons and jets. Separate electromagnetic

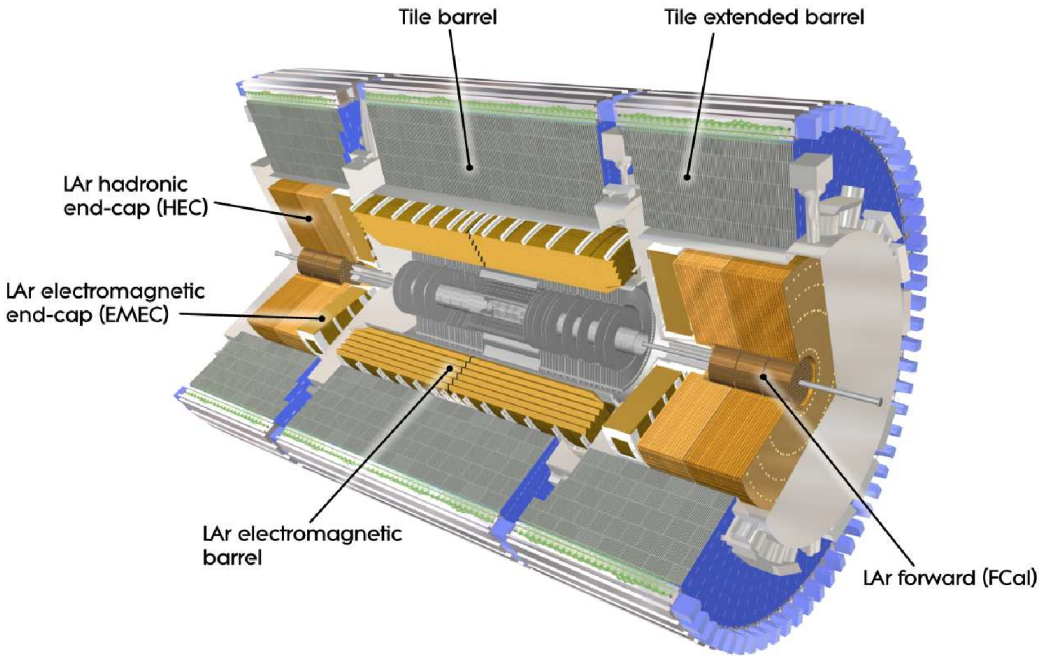

Figure 3.10: Layout of the ATLAS Calorimeter system [45]. Separate electromagnetic and hadronic calorimeters are installed, and different calorimeter technologies are used depending on the detector region.

and hadronic sampling calorimeters are used (see Figure 3.10). The total depth of the calorimeter system is about 10 interaction lengths.

The Electromagnetic Calorimeter

The Electromagnetic Calorimeter measures the electromagnetic showers and the energy of electrons and photons. It covers a pseudorapidity range of $|\eta| < 3.2$ and consists of a barrel section and two endcaps. Lead is used as absorber material in the form of accordion shaped plates. The active medium in the gaps between the lead plates is liquid argon which is ionised by the shower particles. Electrodes in the centre of the gaps collect the ionisation charges. The liquid argon calorimeter is housed in a cryostat which it shares with the superconducting solenoid magnet for the Inner Detector. In the endcaps, the cryostats are shared with the liquid argon Hadronic Calorimeter. The read-out electrodes are segmented in the η and ϕ directions and there are three segments in depth with different η–ϕ-granularity in order to reconstruct the electromagnetic shower shape [45]. A finely segmented pre-shower layer placed in front of the calorimeter is used to correct for the energy loss of the particles in material in front of it.

The Hadronic Calorimeter

The second calorimeter layer is the Hadronic Calorimeter, which is optimised for the precise energy measurement of strongly interacting particles that escape the Electromagnetic Calorimeter. The segmentation is coarser than in the Electromagnetic Calorimeter. In the barrel region, extending to $|\eta| = 1.7$, a sampling calorimeter with scintillating tiles in a steel absorber matrix is used. The tiles are read out using optical fibres coupled to photomultipliers. Segmentation is achieved by coupling several tiles to the same photomultiplier.

In the forward region of the detector, the Hadronic Endcap Calorimeter (HEC) covers the region $1.5 < |\eta| < 3.2$. It uses liquid argon as the active material and flat copper absorber plates oriented perpendicular to the beam line. Close to the beam line in the region $3.2 < |\eta| < 4.9$, the liquid argon forward calorimeter (FCal) completes the solid angle coverage. Again, liquid argon is used as active material filling longitudinal holes in a copper and tungsten absorber matrix.

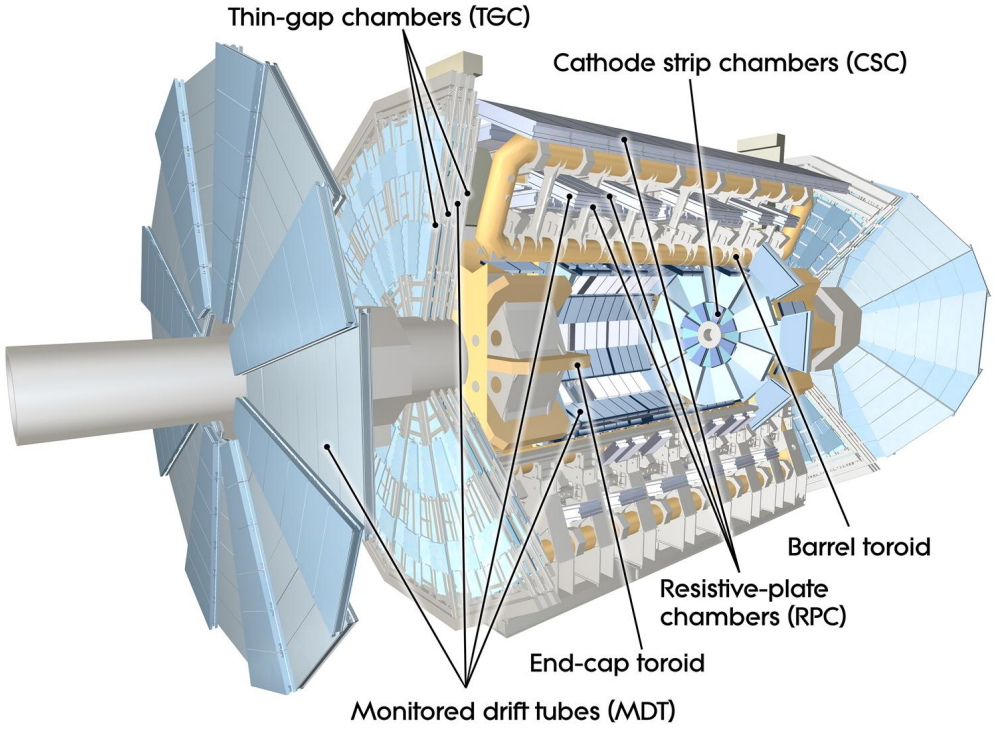

Figure 3.11: Illustration of the ATLAS Muon Spectrometer [68]. The barrel and endcap toroid coils are shown in brown while the three layers of barrel muon chambers and the three endcap wheels are shown in blue.

3.2.3.1 The Muon Spectrometer

Muons are the only charged particles of the Standard Model that pass through the calorimeters without being absorbed. The Muon Spectrometer surrounding the calorimeters (see Figure 3.11) is used for identification of muons and the precise measurement of their momenta in the toroidal magnetic field of a dedicated superconducting magnet system.

Air-core toroid magnets are used, one in the barrel and two in the endcaps, consisting of eight coils, in order to minimise multiple scattering. Each toroid consists of eight coils. The average flux density is 0.5 T in the barrel and about 1 T in the endcaps.

Muon chambers are split into two groups, those used for precision tracking and those used for triggering.

Precision Tracking Chambers

Muons with 1 TeV transverse momentum have a track saggita of 0.5 mm in the toroidal magnetic field. To measure the momentum with 10% precision, the saggita has to be measured with an accuracy better than 50 μm. Three layers of Monitored Drift Tube (MDT) chambers are used for this purpose. These precision muon tracking chambers provide a spatial resolution of 35 μm.

Each chamber contains 2×3 or 2×4 (in the innermost chamber layer) layers of drift tubes. The tubes are oriented tangential to the magnetic field lines, measuring the track curvature in the bending plane containing the beam axis. In the barrel region, three concentric cylindrical layers of chambers are mounted on the magnet coils at distances of 5 to 10 m from the beam line. In the central pseudorapidity region $|\eta| < 0.1$, the spectrometer only partially instrumented with chambers to allow for the passage of services for the Inner Detector and the calorimeters, leading to a loss of muon acceptance in this region. In the endcap regions at $|\eta| \gtrsim 1.05$, muon chambers are mounted on three wheels oriented perpendicular to the beam line at distances between 7.4 m and 21.5 m from the interaction point. In the inner endcap layer close to the beam pipe at $|\eta| > 2.0$, Cathode Strip Chambers (CSC) are used because of the higher radiation background in this region. CSCs are multiwire proportional chambers with segmented cathode planes providing two-dimensional coordinate measurement. The highest spatial resolution of 40 μm obtained in the wire direction corresponds to the η measurement. The resolution in the ϕ coordinate is 5 mm, sufficient for the momentum direction measurement.

Trigger Chambers

The maximum drift time of ionisation electrons in the drift tubes of the MDT chambers is about 700 ns while the bunch crossing time interval of the LHC is 25 ns (50 ns in Run 1). This means that an assignment of a muon to a particular bunch crossing is not possible using the MDT chambers alone. The latter is necessary for correct event reconstruction and drift time measurement in the MDT tubes as the LHC bunch crossing clock provides the start signal for the drift time measurement. Fast trigger chambers with a time resolution of a few ns but reduced spatial resolution are combined with the MDT chambers for this purpose. Resistive Plate Chambers (RPC) with 1.5 ns time resolution are installed on the MDT chambers in the middle and outer layers of the barrel. A spatial resolution of about 1 cm in two coordinates is obtained using segmented cathode planes. The RPCs provide the second (ϕ) coordinate of muon hits along the MDT tubes. In the endcaps, thin gap chambers (TGC), multiwire proportional chambers

with thin gas gaps, are used. These provide a spatial resolution of a few mm in both the η and ϕ coordinates and a time resolution of 4 ns. Three layers of TGC chambers in the middle endcap wheel are used for the endcap muon trigger.

3.2.4 Trigger and Data Acquisition

The high bunch crossing rate of 40 MHz (20 MHz in LHC Run 1), with up to 40 inelastic interactions per bunch crossing, presents a challenge for the ATLAS data acquisition system. A collision event contains approximately 1 MB of information. Recording every collision would mean a data rate of several tens of Terabytes per second, while only a small fraction of the collision events is of interest for further analysis. The processes of interest at the LHC, for example top quark production, electroweak processes or Higgs boson production have cross-sections many orders of magnitude smaller than the total inelastic p–p cross-section (see Figure 3.12).

A trigger system, illustrated in Figure 3.13, is used [70] to drastically reduce the recorded event rate. The first trigger stage, Level 1 (L1), is a hardware trigger with only 2.5 μs latency. Input to the L1 decision is provided by the muon trigger chambers with an approximate momentum measurement, and the calorimeters, read out in trigger towers with coarser segmentation. The Level 1 trigger accepts potentially interesting events with highly energetic muons or calorimeter clusters. It reduces the event rate from 40 MHz to about 100 kHz.

The second trigger stage is the Level 2 (L2) trigger which runs simplified reconstruction algorithms on a computing farm outside the detector. The reconstruction is only carried out in η–ϕ *Regions of interest* (RoIs) selected by the Level 1 trigger. Only a small fraction of the total event information is needed, speeding up the decision. The L2 trigger algorithms also use Inner Detector information and combine information from different subdetectors for particle identification. The Level 2 trigger has to make a decision within 40 ms, and reduces the event rate to a few kHz.

Finally, the Event Filter (EF) performs a full reconstruction of the events accepted by the L2 trigger. It is run on a computing farm, similar to the L2 trigger, and has a latency of several seconds. The EF uses reconstruction algorithms and detector calibration constants close to the ones used in the offline reconstruction as well as the complete event information. This allows for a further reduction of the event rate to a few hundred Hz which is then written to disk for later analysis. The L2 and EF triggers are together

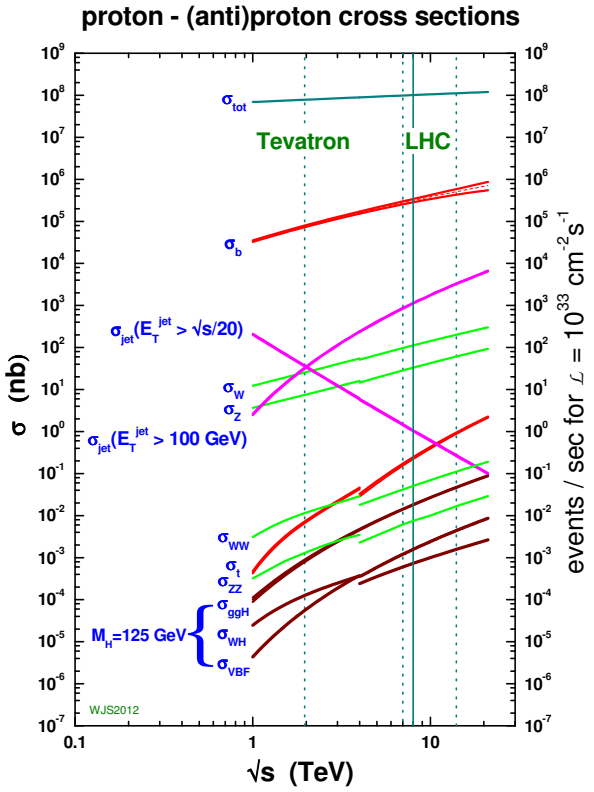

Figure 3.12: Cross-sections of Standard Model processes in pp (LHC) and $p\bar{p}$ (Tevatron) collisions as a function of the centre-of-mass energy $\sqrt{s}$ and corresponding event rates at an instantaneous luminosity of 10^{33} cm^{-2}s^{-1} [69].

referred to as the High Level Trigger (HLT).

The ATLAS *trigger menu* [70] selects a wide range of signatures of interest while staying within the rate limits imposed by the available storage capacity and bandwidth. The signatures include highly energetic charged leptons, jets and photons as well as large missing transverse momentum.

3.3 Particle Reconstruction

Particle identification is an essential part of the event reconstruction. Different particles leave different signatures in the detector referred to as *physics objects*, like charged leptons,

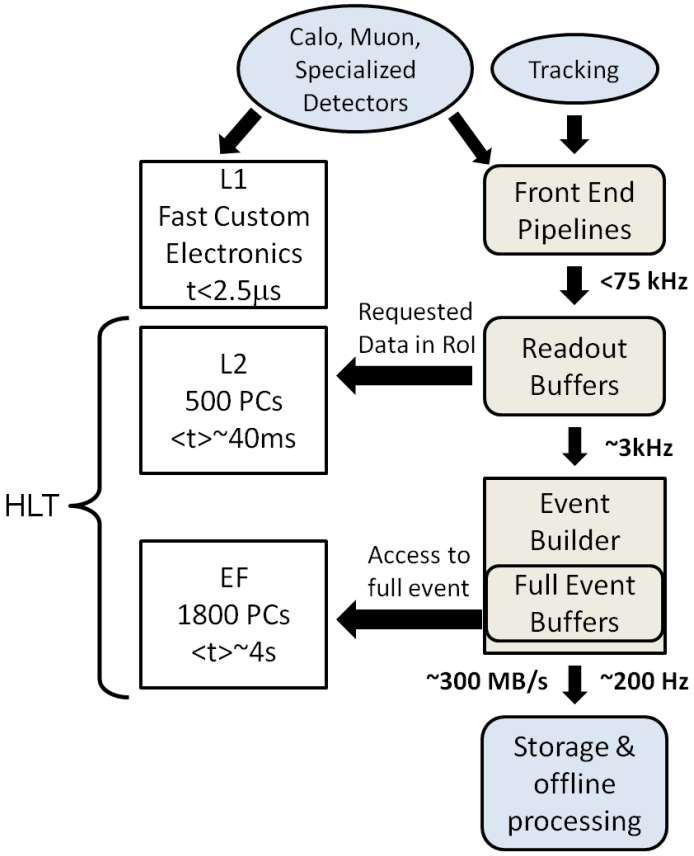

Figure 3.13: Illustration of the ATLAS trigger system [70].

photons and jets.

3.3.1 Track Reconstruction

Inner Detector tracks are required for charged lepton and jet reconstruction. They are reconstructed from the hits in the tracking detectors (silicon and TRT) with two methods [71]. The primary approach is the so-called *silicon-seeded* reconstruction which starts from space-points in the Pixel Detector and the innermost SCT layer and extends the resulting track candidates through the remaining SCT and the TRT. The standard implementation of the this algorithm only searches for tracks with a transverse impact parameter $|d_0|$ of less than 10 mm.

A second approach is used to gain efficiency for tracks that do not originate from the primary interaction vertex. Track segments are formed from TRT hits and extended inwards and matched to hits in the silicon detectors using only hits not already associated to track candidates from the silicon-seeded method. A maximum transverse impact parameter of $|d_0| = 100$ mm is allowed in this case. While the restriction in the impact parameter speeds up the execution and prevents misidentifications, it is a limitation to long-lived particle searches, as will be discussed in Chapter 7. A stand-alone tracking procedure is also performed in the Muon Spectrometer, where the hits in the chambers are combined to form track segments. At a later stage these are combined with Inner Detector tracks (see Section 3.3.6).

3.3.2 Vertex Finding

Reconstructed tracks are then used to locate the primary and secondary interaction vertices. For the identification of one or more primary vertices, tracks with similar longitudinal impact parameters are selected. For secondary vertex reconstruction, a more complex approach described in Section 7.4.2 is used. The compatibility of the selected tracks with the assumption of a common origin in a vertex position $\vec{V}$ [72] is evaluated with a χ^2 test with

$$\chi^2 = \sum_i^{\text{tracks}} \left(\vec{x}_i - \vec{f}(\vec{V},\vec{p}_i)\right)^T \mathbf{C}_i^{-1} \left(\vec{x}_i - \vec{f}(\vec{V},\vec{p}_i)\right), \tag{3.11}$$

where $\vec{x}_i = \left[d_0^i, z_0^i, \theta^i, \phi^i, q^i/|\vec{p}^i|\right]$ is the track parameter vector (see Section 3.2.1) and $\mathbf{C}_i$ the associated track parameter covariance matrix. The function $\vec{f}(\vec{V},\vec{p})$ describes the track parameter vector for a particle emerging from the vertex position $\vec{V}$ with momentum $\vec{p}$. Best fit values for $\vec{V}$ and $\vec{p}_i$ for all tracks in the set are determined by minimising the χ^2 function in Eq. (3.11) [73].

A crucial prerequisite for this procedure is accurate propagation of tracks through the detector, to determine $\vec{f}(\vec{V},\vec{p})$. A Runge-Kutta technique is used [61] that correctly accounts for interactions with the detector material and inhomogeneities in the magnetic field. Under the assumptions of a homogeneous field and no material interactions, an analytic description of the trajectory in the form of a helix is possible, which will be used in Section 7.7.

Using tracks reconstructed in the Inner Detector and the Muon Spectrometer as well

as energy deposits in the calorimeters, the physics objects are identified as illustrated in Figure 3.14. The objects include electrons, photons, jets, τ-jets (hadronic τ decays) and muons.

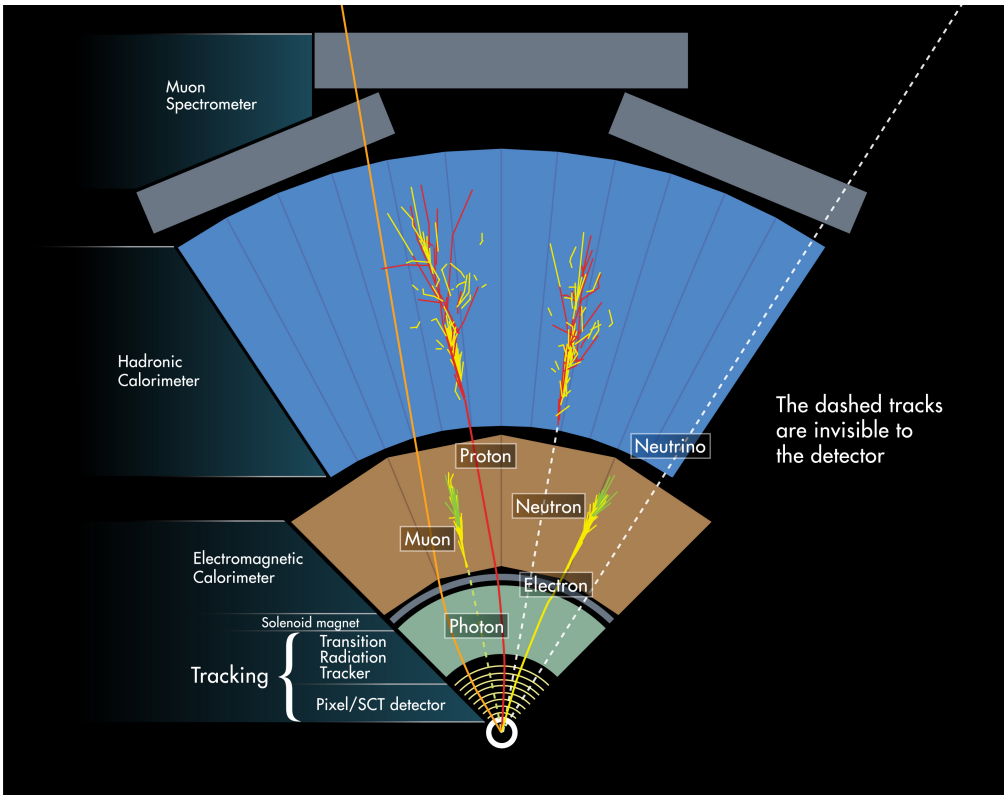

Figure 3.14: Schematic illustration of particle signatures in the ATLAS detector [74].

3.3.3 Electron and Photon Identification

Electrons and photons are absorbed in the Electromagnetic Calorimeter (ECAL), leading to the characteristic signature of electromagnetic showers in the ECAL without significant energy deposits in the Hadronic Calorimeter (HCAL). An electron object is formed from an ECAL cluster with a matching Inner Detector track [75]. A photon object consists of an ECAL cluster either without a matching track or with a track that is consistent with a photon conversion [76]. To separate electrons and photons from $\pi^0 \to \gamma\gamma$ decays and other sources of misidentification, additional requirements are made using information such as the track quality and ECAL shower shapes [76]. Three levels of electron and

photon identification, differing in the strictness of the requirements, are used. *Loose* criteria provide the maximum efficiency, but also the highest misidentification rate. The *Medium* and *Tight* criteria are stricter, trading efficiency against purity [75]. Figure 3.15

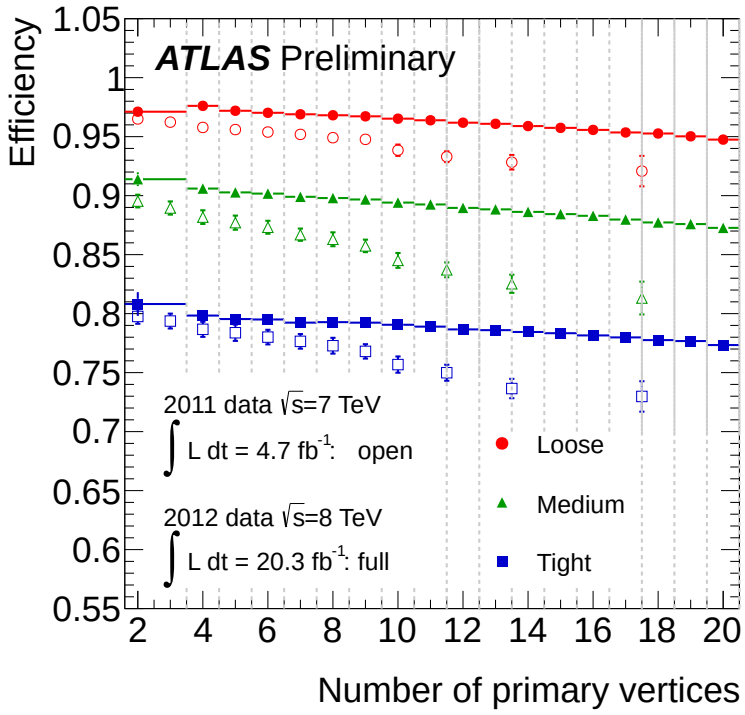

Figure 3.15: Electron reconstruction and identification efficiency as a function of the number of reconstructed pile-up vertices for the three quality levels measured in 2011 (open markers) and 2012 (filled markers) collision data [77].

shows the reconstruction and identification efficiency in collision data for the different quality levels depending on the amount of pile-up. Efficiencies of between 70% and 97% are reached. The energy of the candidates is most precisely measured using the calorimeter cluster. For electrons, the direction of flight is determined using the Inner Detector track [45]. Vertex assignment is performed using the Inner Detector track for electrons and converted photons. For non-converted photons, an estimate of the direction of flight is obtained from the calorimeter shower direction using the radial segmentation of the calorimeter and presampler information.

3.3.4 Jet Reconstruction

Jets consist of energy deposits in both the ECAL and the HCAL, associated with tracks in the Inner Detector. Different jet finding algorithms are used in the ATLAS event reconstruction. The standard method is the anti-k_{T} [78,79] algorithm, applied to topological clusters of η–ϕ cells of the calorimeters [71]. To take into account energy losses in insensitive material, energy deposits not included in the jet reconstruction and the different response to electromagnetic and hadronic interactions, the measured jet energy is corrected using a jet energy scale (JES) parameter [80] derived from simulated events.

Additional quality criteria [81] are imposed to reject backgrounds due to calorimeter noise spikes and pile-up events. These include the distribution of the jet energy among the different calorimeter cells, the value of the energies deposited in the HCAL and ECAL, the association with Inner Detector tracks and the time of the energy deposit compared to the bunch crossing time.

Jets originating from b quarks are identified based on the relatively long lifetime of B hadrons leading to an average decay length of order $c\tau \approx 0.5$ mm [65]. Dedicated b-jet tagging algorithms [82] search for secondary vertices inside reconstructed jets.

3.3.5 Hadronic τ Decays

Tau lepton production is an important signature of many new physics processes. Tau leptons decay into final states with an odd number of charged (mostly 1 or 3) and additional neutral hadrons with a branching ratio of 65% [65]. In this case, the signature in the detector is similar to that of a QCD jet with 1–3 tracks pointing towards the calorimeter shower. Accordingly, the hadronic τ decay identification starts from jets reconstructed with the anti-k_{T} algorithm with a distance parameter $R = 0.4$ [83]. Multivariate algorithms [84] are used to discriminate τ-jets from QCD jets and electrons using the kinematic properties of the τ decay and the expected shower shape in the calorimeters. Again, three different quality levels of τ jets, *Loose*, *Medium* and *Tight*, with increasing purity and decreasing efficiency, are defined.

Even at the lowest purity, hadronic τ reconstruction has a lower efficiency and higher misidentification rate than muon and electron reconstruction [85]. The reconstruction efficiency is between 20% and 70%, depending on the number of tracks associated with the τ candidate and the quality level, corresponding to background rejection rates of between 10^3 and 10 (see Figure 3.16).

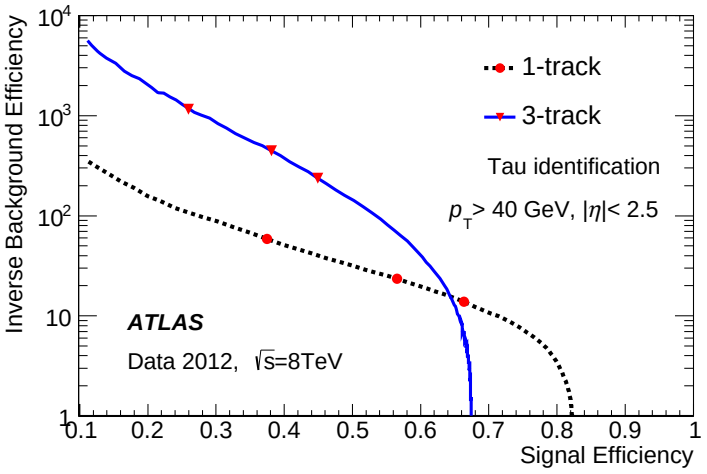

Figure 3.16: Measured background rejection rate versus efficiency for the identification of hadronic τ decays [85]. The red markers indicate the Loose, Medium and Tight identification criteria.

By convention for the reconstructed physics objects, τ *lepton* always refers to a hadronically decaying τ identified as a τ-jet. Leptonic τ decays to an electron or muon are classified as electron or muon objects.

3.3.6 Muon Identification

The signature of a muon in the detector is a pair of matching tracks in the Inner Detector and in the Muon Spectrometer, with small energy deposits in the calorimeters compatible with a minimum ionising particle. Even if one of the tracks is missing, the muon can still be identified. Four methods [86] are used to identify muons (see Figure 3.17):

- *Combined muons* are formed if a track in the Inner Detector and a track in the Muon Spectrometer are compatible. The information of both tracks is statistically combined, enhancing the precision of the track parameter determination. This category has the highest purity and precision, and most muons reconstructed by ATLAS are combined muons.

- *Segment-tagged muons* recover low-momentum muons which do not penetrate the whole Muon Spectrometer and thus do not leave a complete track there. In this case, an Inner Detector track is identified as a muon if there is a track segment

in the Muon Spectrometer along the extrapolated track. The purity of segment-tagged muons is reduced compared to combined muons as rejection of secondary muons from $\pi^{\pm}/K^{\pm} \to \mu^{\pm}\nu$ decays is more difficult without an independent Muon Spectrometer track.

- *Calorimeter-tagged muons* are used to recover muons in the region $|\eta| < 0.1$, where the Muon Spectrometer is only partially instrumented. Here, Inner Detector tracks are identified as muons if the energy deposit in the calorimeters along the projected track is consistent with a minimum ionising particle. The purity of calorimeter-tagged muons is reduced compared to combined muons for the same reason as in the case of segment-tagged muons.

- *Standalone muons* are tracks in the Muon Spectrometer without a corresponding Inner Detector track. They are especially useful to extend the muon reconstruction into the high-pseudorapidity region $2.5 < |\eta| < 2.7$, which is covered by precision muon tracking chambers but not the Inner Detector.

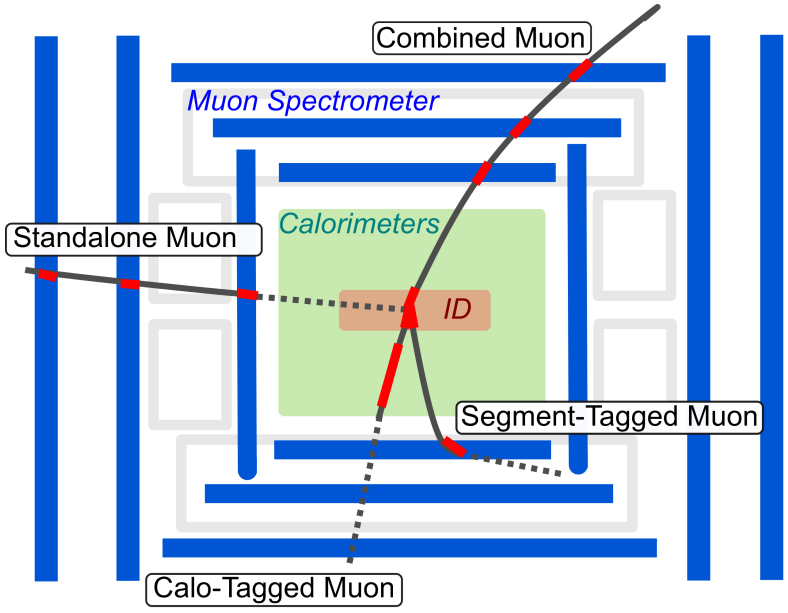

Figure 3.17: Illustration of the different types of muon reconstruction in the ATLAS detector. Measurements on the track used for the reconstruction are marked in red.

3.3.7 Missing Transverse Momentum

Neutrinos and hypothetical weakly interacting new particles, for example the lightest SUSY neutralino if R-parity is conserved (see Section 2.2), escape the detector and are not directly reconstructed. Instead, their presence is inferred from the momentum balance in the detector in the transverse plane. While the transverse momentum of the colliding partons and, therefore, of their collision products, is negligible, the boost of the final state particles in the beam direction is not known a priori and is difficult to reconstruct. The components of the missing transverse momentum due to escaping particles are given by the inverse of the visible transverse momenta of reconstructed objects [87]:

$$E_{x,y}^{\text{miss}} = -\left[\sum_{\text{electrons}} E_{x,y} + \sum_{\text{photons}} E_{x,y} + \sum_{\text{jets}} E_{x,y} + \sum_{\text{muons}} E_{x,y} + \sum_{\text{clusters}} E_{x,y}\right]. \tag{3.12}$$

In addition to electrons, photons, muons and jets entering the calculation, calorimeter deposits not associated to these objects are also taken into account. To avoid double counting, tracks or showers reconstructed as several different objects (which is allowed) are corrected in the so-called *overlap removal*. The energy deposits of reconstructed muons in the calorimeter are removed as well.

A frequently used quantity is the scalar missing transverse energy

$$E_{\text{T}}^{\text{miss}} = \sqrt{\left(E_x^{\text{miss}}\right)^2 + \left(E_y^{\text{miss}}\right)^2}. \tag{3.13}$$

3.4 Simulation of Collision Events

For precise predictions of expected signals from new physics and the background contributions, a detailed simulation of the different physics processes in the ATLAS detector is used [88]. The simulation procedure, illustrated in Figure 3.18, includes event generation and full simulation of the interactions of the particles produced in the collision with the detector components as well as of the electronics response of the detectors, followed by the same reconstruction algorithms used for collision data.

The first step is the generation [89] of the physics process under study. This includes the simulation of the hard interaction, the hadronisation of final state quarks and gluons, as well as the underlying event (Section 2.3).

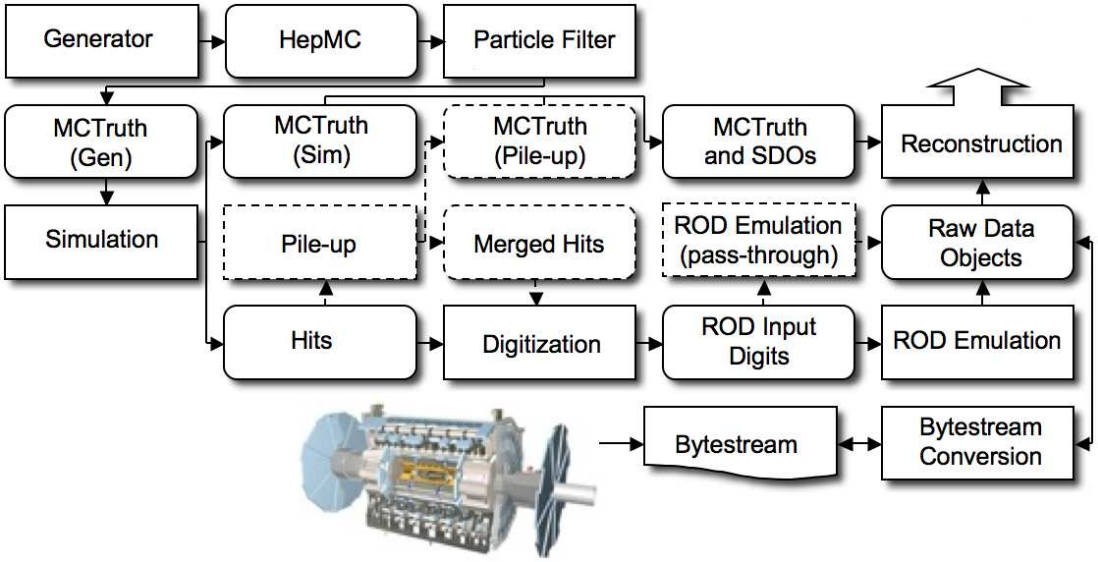

Figure 3.18: Schematic illustration of the ATLAS Simulation framework [88].

Many different event generators are used in ATLAS. PYTHIA 6/8 [90,91], SHERPA [92] and HERWIG(++) [38,93] are multi-purpose generators at leading order in perturbation theory which take into account all of the above processes. In addition, the specialised leading-order generators ALPGEN [94] and MadGraph 4/5 [95,96] are used to generate processes with additional jets, but are unable to perform hadronisation or to simulate the underlying event. Finally, the generators POWHEG [97,98] and MC@NLO [99] provide predictions of hard processes at next-to-leading order. Pile-up interactions (Section 3.1) are taken into account by merging the generated events with separately simulated inelastic proton-proton scattering events. The generated events are often filtered in order to select the ones with the desired properties of the produced particles (high transverse momentum leptons, for example) in order to reduce the number of events to be processed in the following steps.

Following the generation and filtering steps, a detailed detector simulation based on the GEANT4 package [100] is used, which propagates the final state particles through the detector. Interactions with the detector material as well as the response of the detectors and their electronics are simulated in detail. As this full simulation is computationally expensive, especially for the simulation of the calorimeters, an alternative fast simulation [101] based on parametrised response models [102] and a fast track simulation in the Inner Detector and Muon Spectrometer [103] is used wherever possible to save

processing time. In both cases, the output is passed through the same reconstruction algorithms as used for the collision data, described in Section 3.3.

Chapter 4

Measurement of the Muon Reconstruction Efficiency

In this thesis, searches for supersymmetric processes producing many leptons are discussed. For this purpose, a detailed understanding of the lepton reconstruction performance both in collision data and Monte Carlo simulation is essential. In particular, the muon reconstruction is discussed in the following. A so called *tag-and-probe* method has been developed in order to measure the muon reconstruction efficiency in comparison with the ATLAS detector simulation [86]. The results are used to derive corrections to the simulation, which are a necessary input for the analyses discussed in Chapters 6 and 7.

4.1 The Tag-and-Probe Method

Goal of the tag-and-probe measurement is to determine the *reconstruction efficiency* ϵ, the probability that a muon in the detector is correctly reconstructed, using muon pairs originating from $Z \to \mu\mu$ decays. The two muons in the pair are designated *tag* and *probe*. The tag muon is a reconstructed muon physics object satisfying additional quality criteria. The probe track is a reconstructed track in the Inner Detector, or in the Muon Spectrometer, or both. It is not required to be a muon physics object. The muon reconstruction efficiency is estimated as the ratio

$$\epsilon = \frac{N_{\text{match}}}{N_{\text{probes}}} \tag{4.1}$$

between the amount N_{match} of probe tracks *matched* with a nearby reconstructed muon physics object within a cone of size $\Delta R = 0.05$ (see Section 3.2.1) in the η–ϕ plane and the total number of probe tracks N_{probes}.

When using Inner Detector probe tracks to measure the efficiency of the combined and segment-tagged reconstruction methods (see Section 3.3.6), the result is corrected for the efficiency of the Inner Detector track reconstruction, obtained in an auxiliary measurement using Muon Spectrometer tracks as probes.

4.2 Selection of Tag-and-Probe Pairs and Background Estimation

4.2.1 Selection Strategy

Tag-and-probe muon pairs are selected in the data by applying a series of requirements which discriminate between $Z \to \mu\mu$ decays and background processes.

The tag muon is required to have been reconstructed using the combined method and to satisfy the kinematic criteria listed in Table 4.1. It must also satisfy a single muon trigger with a momentum threshold of 24 GeV to ensure the recording of the event independently of the probe track.

Table 4.1: Criteria for selecting tag muons in the tag-and-probe method.

Tag muon selection criteria	
Transverse momentum	$p_{\text{T}} > 25$ GeV
Pseudorapidity	$\lvert\eta\rvert < 2.4$

Table 4.2: Criteria for the probe object selection in the tag-and-probe method.

Probe selection criteria	
Transverse momentum	$p_{\text{T}} > 10$ GeV
Pseudorapidity	$\lvert\eta\rvert < 2.5$
Transverse opening angle with probe	$\Delta\Phi(\text{tag}, \text{probe}) > 0.2$
Invariant mass of tag-probe system	$\lvert m_Z - m_{\ell\ell}\rvert < 10$ GeV
Opposite charge to tag	$q_{\text{tag}} \cdot q_{\text{probe}} < 0$

The probe tracks need to satisfy requirements listed in Table 4.2, including a minimum transverse momentum. Inner Detector probe tracks must additionally be identified as

calorimeter-tagged muons in order to enhance their purity. Additional criteria on the opening angle and the invariant mass are applied on the tag and probe pair to ensure consistency with a $Z \to \mu\mu$ decay. Finally, the tag and probe tracks are required to have opposite charges.

4.2.2 Backgrounds

While tag-and-probe pairs in the collision data predominantly arise from $Z \to \mu\mu$ decays, a small fraction of the pairs originates from background processes in which the probe track is not necessarily a muon, causing a deviation of the efficiency estimated according to Eq. (4.1) from the actual muon reconstruction efficiency. This is corrected by subtracting the estimated background contributions B_{matches} and B_{probes} from the respective numbers of probes in the data in the numerator and denominator of Eq. (4.1).

$$\epsilon = \frac{N_{\text{matches}} - B_{\text{matches}}}{N_{\text{probes}} - B_{\text{probes}}}. \tag{4.2}$$

Irreducible backgrounds with two leptons from the hard interaction include top quark pair production, diboson production and $Z \to \tau\tau$ decays and are predicted using Monte Carlo simulation. Top quark pair production is simulated using the MC@NLO generator [99], while POWHEG [97,98] interfaced to PYTHIA 8 [91] and HERWIG [93] are used to simulate Z boson decays to leptons and diboson production, respectively.

The *reducible* background comprises probe tracks that do not originate from the hard interaction. These can be secondary leptons from decays of b-mesons, in-flight decays of pions or kaons or hadrons misidentified as calorimeter tagged muons. As the charge of probe tracks from reducible sources is not correlated with the tag muon charge, this contribution is estimated using a data-driven method based on a control sample of probe tracks that have the same charge as the tag muon.

After subtracting residual contributions from irreducible backgrounds and $Z \to \mu\mu$ decays using Monte Carlo simulation, the numbers $B^{\text{SC}}_{\text{probes/matches}}$ of probes in this same-charge (SC) control sample are scaled to yield an estimate of the reducible background $B^{\text{red.}}_{\text{probes/matches}}$ in the opposite charge sample,

$$B^{\text{red.}}_{\text{probes/matches}} = B^{\text{SC}}_{\text{probes/matches}} \cdot (1 + \theta), \tag{4.3}$$

using the transfer factor

$$\theta = \frac{B^{\mathrm{OC}}_{\mathrm{probes/matches}}(\mathrm{MC}) - B^{\mathrm{SC}}_{\mathrm{probes/matches}}(\mathrm{MC})}{B^{\mathrm{SC}}_{\mathrm{probes/matches}}} \tag{4.4}$$

obtained from the predicted amounts $B^{\mathrm{OC}}_{\mathrm{probes/matches}}(\mathrm{MC})$ and $B^{\mathrm{SC}}_{\mathrm{probes/matches}}(\mathrm{MC})$ of opposite- and same-charge tag-and-probe pairs according to the Monte Carlo simulation of the reducible background processes. The processes considered when determining the transfer factor include $b\bar{b}$ and $c\bar{c}$ pair production simulated using PYTHIA 6 [90] and W boson production simulated using POWHEG [97,98] interfaced to PYTHIA 8 [91].

4.2.3 Data Sample for the 2012 LHC Run

Figure 4.1 shows the pseudorapidity distribution of the probe tracks in the 2012 LHC data set taken at $\sqrt{s} = 8$ TeV. The expected contribution from the process of interest $Z \to \mu\mu$ is indicated in red. A green contribution shows the estimated reducible background, while the irreducible background processes of diboson, top quark pair and $Z \to \tau\tau$ production are indicated in blue, orange and grey, respectively.

The purity of the selected probes is observed to be very high, with a signal to background ratio of more than $100 : 1$, stronger in the case of Muon Spectrometer probe tracks due to the lower misidentification rate of these objects. The sample amounts to more than 5 million recorded Z boson decays, allowing for an efficiency measurement with high statistical precision.

4.2.4 Systematic Uncertainties

Several systematic error sources affect the precision of the efficiency determination.

The transfer factor θ in Eq. (4.4) used to estimate the reducible background contribution is a obtained using Monte Carlo simulation and assigned a 100% uncertainty to account for potential inaccuracies in the description of soft processes by the simulation. This results in an error on the measured efficiencies of less than 0.5 permill for most of the phase space - only at very low and very high muon momenta, values of up to 3 permill are attained.

The size of the angular cone used to determine if a probe is matched to a muon physics object is chosen based on Monte Carlo simulation of the $Z \to \mu\mu$ process. The result of a

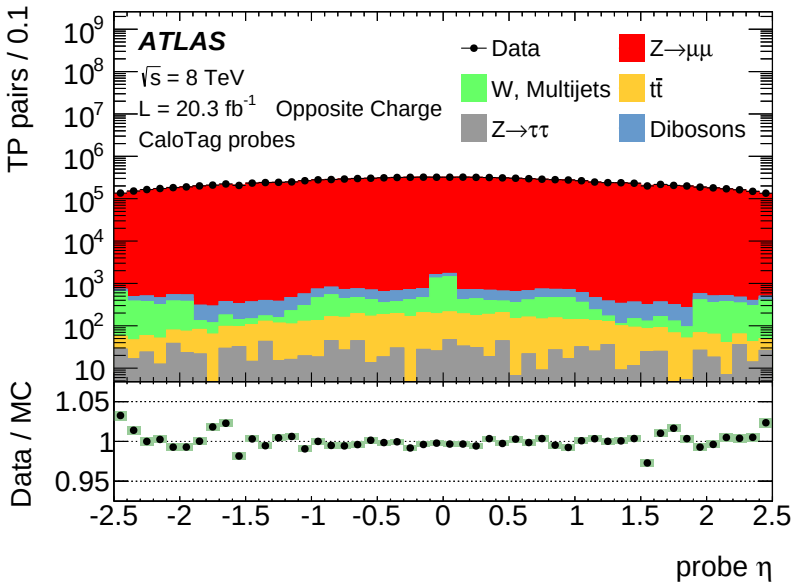

(a)

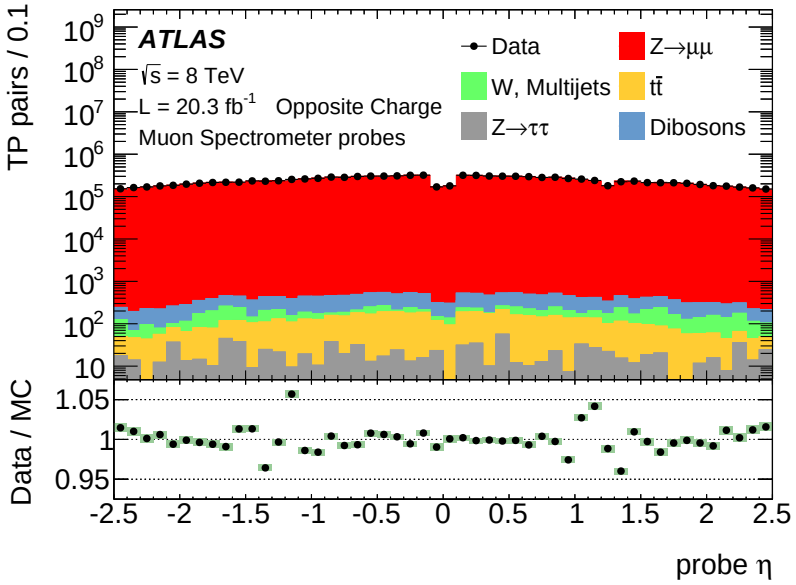

(b)

Figure 4.1: Pseudorapidity distribution of the Inner Detector (a) or Muon Spectrometer (b) probe tracks used in the tag-and-probe analysis. The bottom panel shows the ratio between observed and expected counts.

cone size variation by 50% in both directions is propagated to the efficiency results to account for inaccuracies in the simulated ΔR distributions, resulting in an error on the efficiency of about 1 permill which increases to up to 0.8% for $p_{\mathrm{T}} < 15$ GeV.

The measured efficiency can deviate from the real muon reconstruction efficiency if the selection criteria of the analysis affect the probability for a probe track to be matched, for example through the selection of a particular phase-space region or through probe quality criteria. The resulting systematic error on the efficiency measurement is estimated by comparing the outcome of the Tag&Probe measurement in the Monte Carlo simulation to the reconstruction efficiency in the same sample determined as the fraction of event-generator-level muons reconstructed by the detector, resulting in an error on the efficiency on an order of 1 permill. In the central pseudorapidity region $|\eta| \approx 0$, larger values of up to 1% are observed.

As the differential distributions of probes observed in the data show small deviations from the prediction (see Figure 4.1), a further systematic error is obtained by comparing the nominal result of the efficiency measurement to a result obtained if the probe distribution in the simulation is weighted to match the one in the data. This results in a negligible additional error on the efficiencies of less than 0.1 permill.

Finally, a small fraction of muons with high momenta has a significant energy loss in the calorimeters, which leads to a mismatch between the momentum measurements in the Inner Detector and the Muon Spectrometer, causing the combined muon reconstruction to fail. Based on a Monte Carlo simulation of high momentum single muons, an energy dependent systematic uncertainty of 0.42% per TeV of muon momentum is applied.

Figure 4.2 depicts the systematic uncertainty on the measured efficiency as a function of the pseudorapidity and the transverse momentum for the combination of combined and segment-tagged reconstruction methods. The total error is smaller than three permill with the exception of the central pseudorapidity region and dominated by the choice of the ΔR matching cone size illustrated in dark green and possible biases of the tag-and-probe measurement drawn in blue. The uncertainty on the background estimation is marked in red and only contributes significantly at low momenta. Due to the fine axis binning permitted by the number of recorded Z bosons, the uncertainty due to the differential kinematic distribution of probe muons (light green) is negligible.

In addition to the systematic error sources, the statistical precision in the efficiency determination is limited by the number of Z bosons in the data set. However, in most of the kinematic phase space, the corresponding error is smaller than one permill and

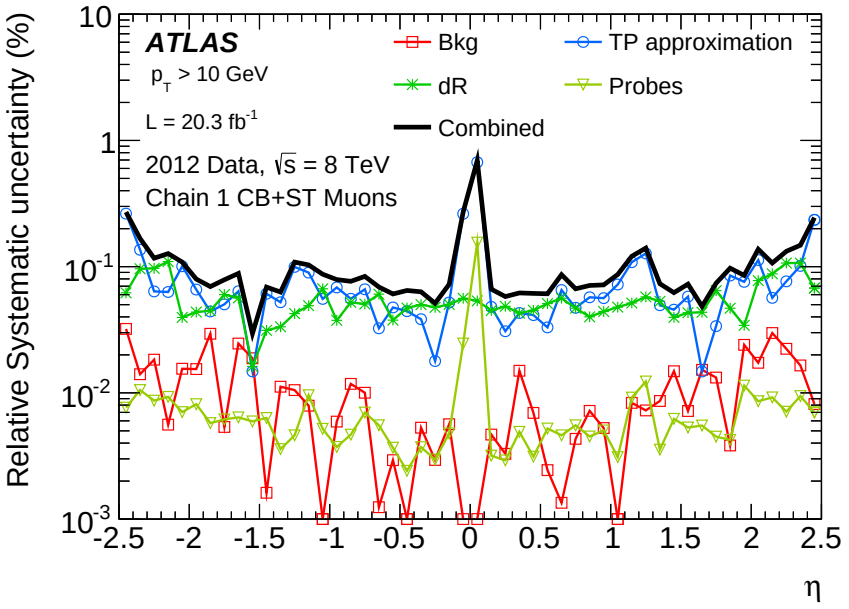

(a)

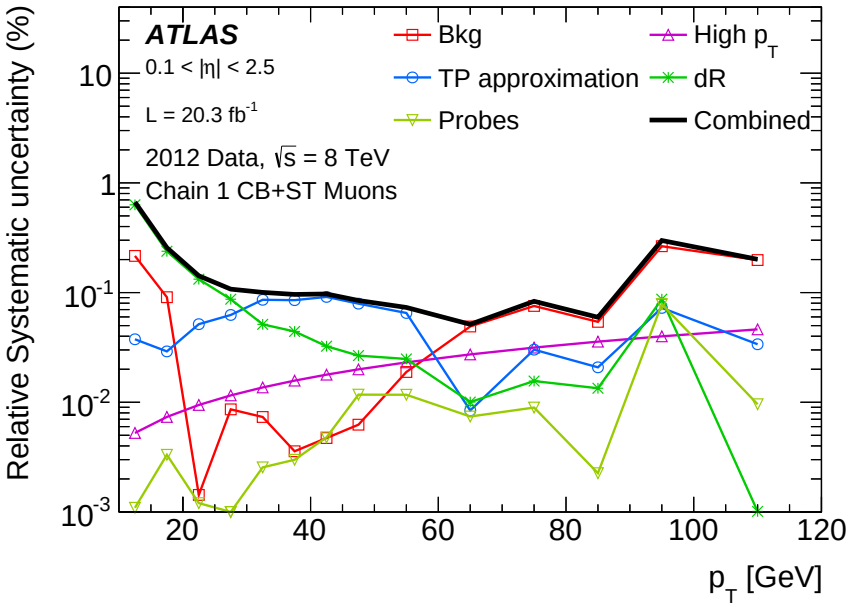

(b)

Figure 4.2: Systematic uncertainties on the efficiency measurement using the tag-and-probe method as a function of the pseudorapidity (a) and the muon transverse momentum (b). The overall uncertainty is indicated as a thick black line.

the systematic uncertainty dominates. Only at high transverse momenta $p_T > 80$ GeV, the limited number of available probe tracks from Z boson decays results in a statistical error on the efficiency of up to 1%.

4.3 Results for the 2012 Data Set

Figure 4.3 shows the reconstruction efficiency for combined (CB) muons (red, black) and the combination of combined and segment-tagged (CB+ST) muons (blue) as a function of the pseudorapidity. Solid dots indicate the efficiency obtained in collision data, while open circles indicate the efficiency predicted by the simulation. The ratio between the observation and prediction is shown in the bottom panel.

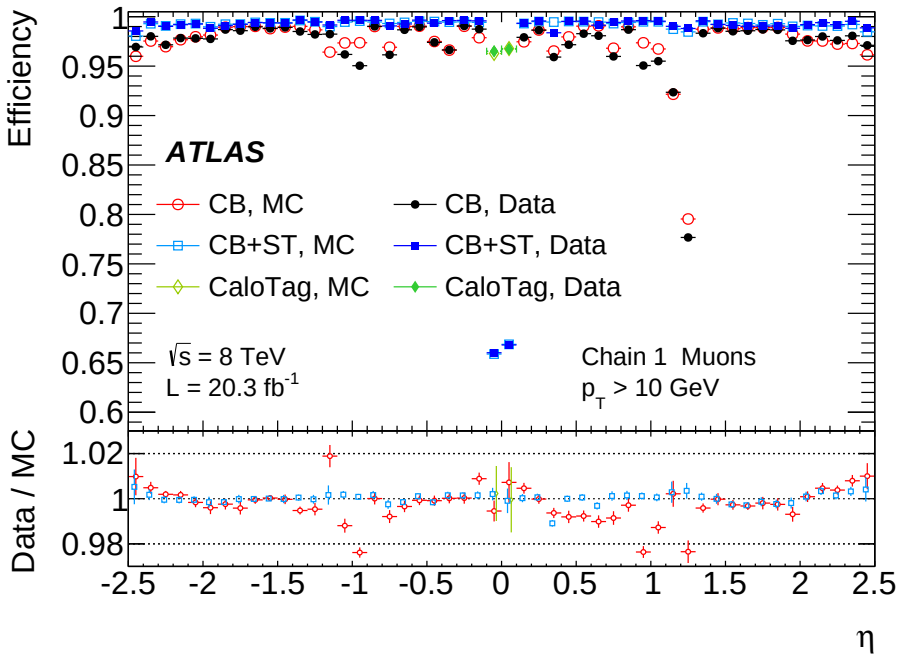

Figure 4.3: Muon reconstruction efficiency as a function of the pseudorapidity for combined muons (red/black) and the combination of combined and segment-tagged muons (blue). For the central pseudorapidity region, the efficiency of Calorimeter-tagged muons is shown in green.

For the combined muon reconstruction, high efficiencies beyond 95% are observed. The efficiency is reduced in the region of the transition between barrel and endcap muon spectrometer near $|\eta| = 1$, in the forward region of $|\eta| > 2$ and in the central detector

region around $|\eta| = 0$, where the muon spectrometer is only partially instrumented (see Section 3.3.6). The simulation predicts the combined muon reconstruction efficiency measured in the data to within 1% with the exception of the transition region, where the agreement is at a level of about 2%. Combining combined with segment-tagged muons enhances the efficiency to above 99%, and recovers all inefficiencies apart from the central detector region. The agreement between simulation and real data also improves, and is generally better than 1%. The remaining inefficiency in the central region can be recovered using calorimeter-tagged muons, indicated by green dots, at the price of a reduced purity.

In the following, the efficiencies for the combination of combined and segment-tagged muons, as commonly used in ATLAS analyses, are further explored.

Figure 4.4 shows the efficiency for this combination as a function of the transverse muon momentum and the mean number $< \mu >$ of inelastic proton-proton interactions per bunch-crossing. To be sensitive to transverse momenta below 10 GeV, an auxiliary measurement using $J/\Psi \rightarrow \mu\mu$ decays described in Ref. [86] is included. After reaching a plateau value for transverse momenta above 5 GeV, the reconstruction efficiency is observed to be uniform at a high value of about 99% and independent of the transverse momentum. The simulation predicts this result correctly to within one permill. In addition, the efficiency is observed to be nearly independent of the level of pile-up. A slight inefficiency for very high values of $< \mu >$ is caused by the layer of endcap MDT chambers closest to the beam pipe, which is affected by a high rate of background hits.

The large number of recorded $Z \rightarrow \mu\mu$ decays allows a study of the efficiency within the η–ϕ plane with a very fine granularity. Figure 4.5 illustrates the high level of precision achieved. The inefficiency in the central pseudorapidity region observed earlier is now resolved to be periodic in the ϕ coordinate, consistent with the locations of uninstrumented sectors in the muon spectrometer. Deviations of the efficiency in the real data from the prediction can be finely localised. In the example shown, an inactive portion of an MDT chamber at $(\eta, \phi) \approx (0.4, -1.2)$ can be identified. Inoperable sensors in the pixel detector cause a less significant disagreement at $(\eta, \phi) \approx (1.8, 2.4)$.

The precise determination of the efficiency in data and simulation allows for a correction of the simulation by weighting simulated reconstructed muons with the ratio between observed and predicted efficiencies as depicted in Figure 4.5b, also referred to as the *efficiency scale factor*. This correction is used in the searches for supersymmetry discussed in Chapters 6 and 7.

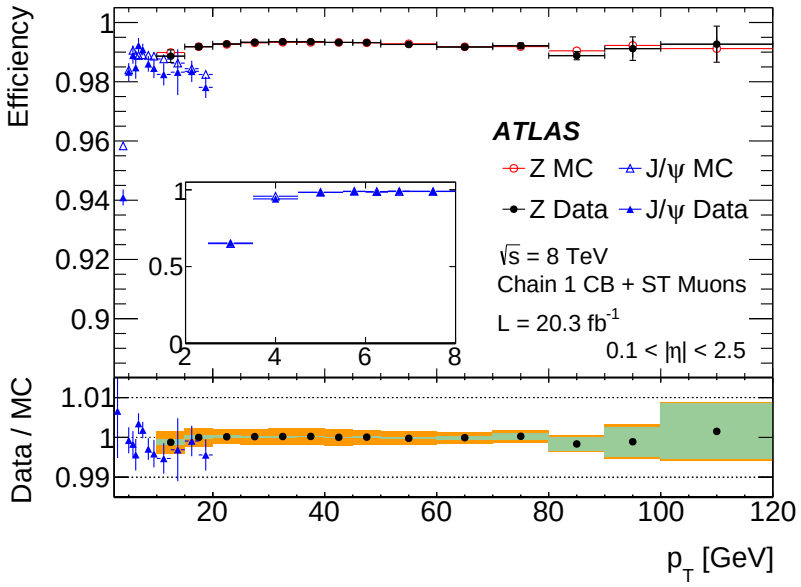

(a)

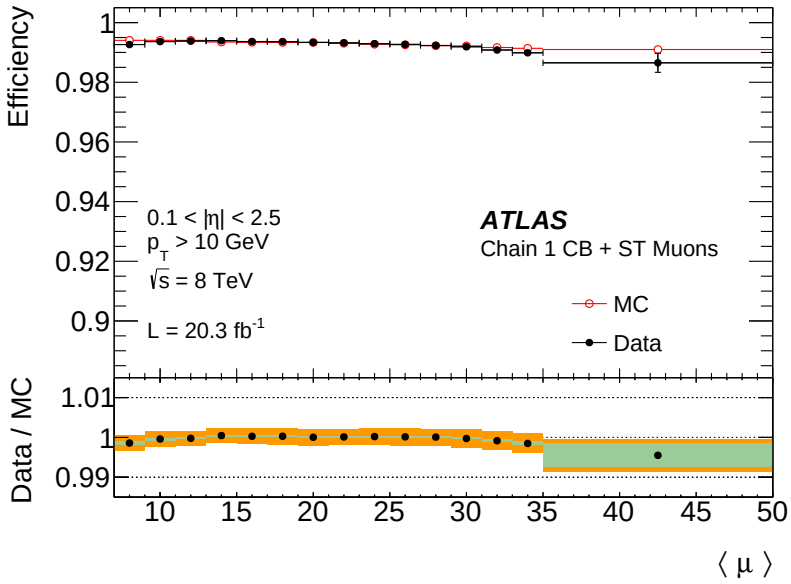

(b)

Figure 4.4: Reconstruction efficiency for the combination of combined and segment-tagged muons as a function of the transverse momentum (a) and the mean number of inelastic proton-proton interactions per bunch-crossing (b).

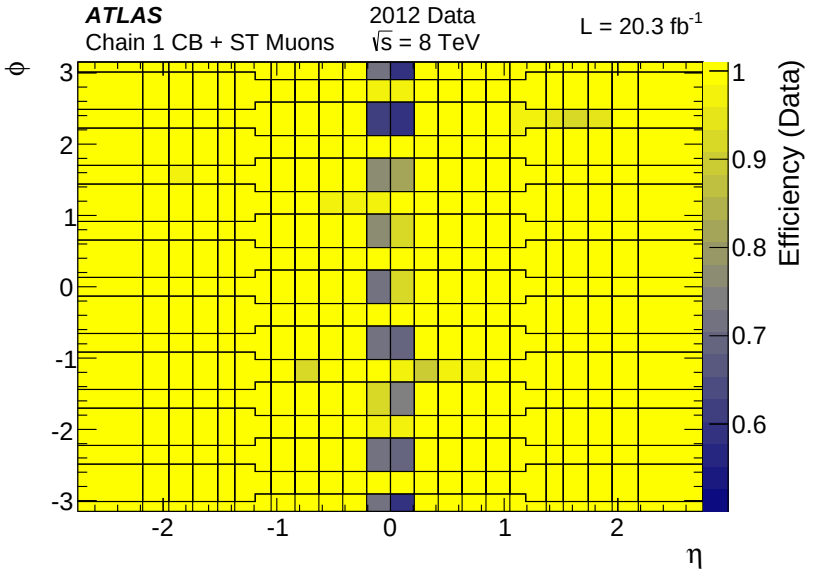

(a)

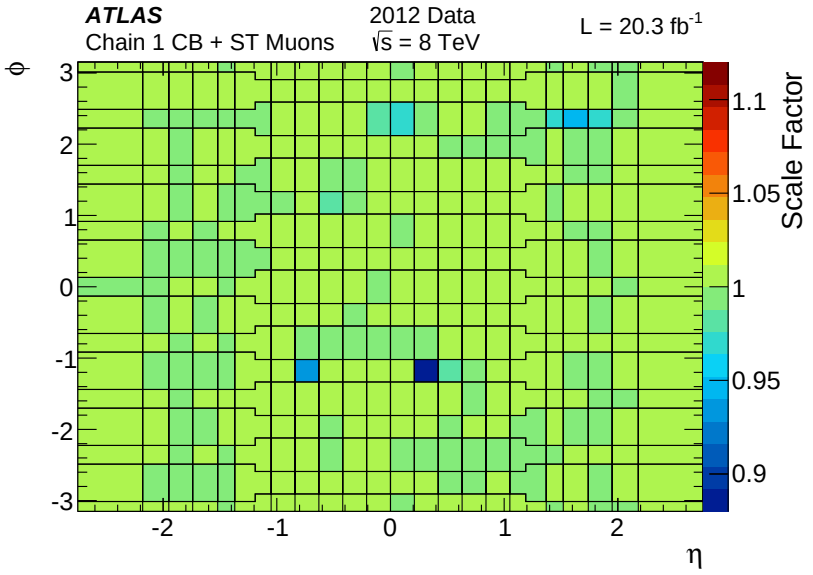

(b)

Figure 4.5: Muon reconstruction efficiency measured in the data (a) and ratio between the efficiency results in data and simulation (b) from the tag-and-probe method within the η–ϕ plane.

Chapter 5

Signatures of Supersymmetry at the Large Hadron Collider

As preparation for the searches for Supersymmetry described in Chapters 6 and 7 of this thesis, experimental signatures of supersymmetric particle production both in the case of R-parity-conservation (RPC) and -violation (RPV) are discussed in this chapter. A simplified SUSY model used for the development and interpretation of the measurements in this thesis is described. The shorthand $l_i \equiv L_i^2$ and $\nu_i \equiv L_i^1$ $(i = 1,2,3)$ is used to refer to left-handed charged leptons and neutrinos, while $\ell_i^\pm$ $(i = 1,2,3)$ is used to refer to charged lepton flavours regardless of helicity ($\ell_1^\pm = e^\pm$, $\ell_2^\pm = \mu^\pm$, $\ell_3^\pm = \tau^\pm$).

5.1 R-Parity-Conserving-Supersymmetry

If R-parity is conserved, superpartners are only produced at the LHC in even numbers from incoming quarks and gluons. The production cross-sections depend on the masses of the superpartners and in the case of electroweak neutralinos and charginos also on the mixing parameters (see Section 2.2.2). Example cross-sections dependent on the average mass of the produced SUSY particles, calculated at next-to-leading order precision using the PROSPINO [104–107] program, are given in Figure 5.1.

If the mass of the squarks and gluinos is below about 1.5 TeV for a centre-of-mass energy of $\sqrt{s} = 8$ TeV, they are produced at significant rates via the strong interaction, due to the coloured initial state. Figure 5.2 shows examples of this strong production of squarks and gluinos.

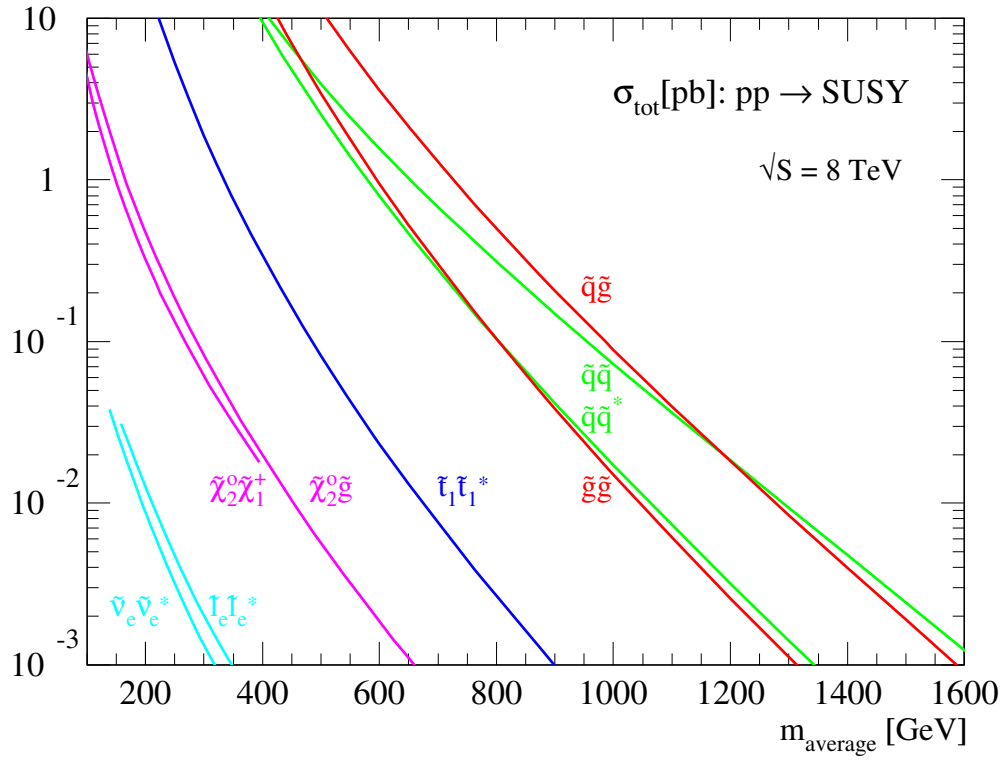

Figure 5.1: Predicted production cross-sections for supersymmetric particles as a function of their average mass [104–107].

Sleptons, sneutrinos, neutralinos and charginos can be directly produced via electroweak interactions (see Figure 5.3). The chargino and neutralino production mechanisms depend on the gaugino and higgsino content of the mass eigenstates, which determines their couplings.

The superpartners that are produced decay in cascades, with branching fractions determined by the mixing parameters and the mass hierarchy. The cascades end when only the lightest supersymmetric particle (LSP) and particles of the Standard Model remain.

In R-parity-conserving scenarios, the LSP does not decay and escapes the detector. This leads to the signature of highly energetic Standard Model particles (leptons, photons or jets) and large missing transverse momentum due to the escaping LSP in the final state. Figure 5.4 shows some examples of such cascade decay signatures. In Figure 5.4a, a pair of strongly-produced gluinos decays via intermediate squarks, yielding a four-jet final state with large missing transverse momentum. A search for this signature is described

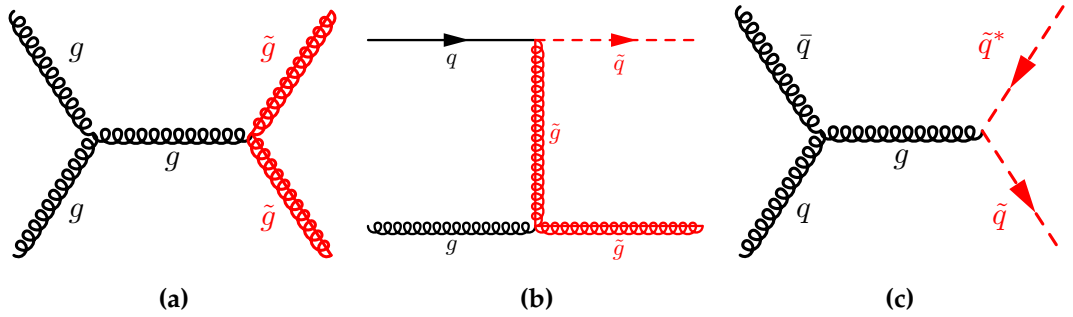

Figure 5.2: Examples of squark and gluino production via the strong interaction at a hadron collider.

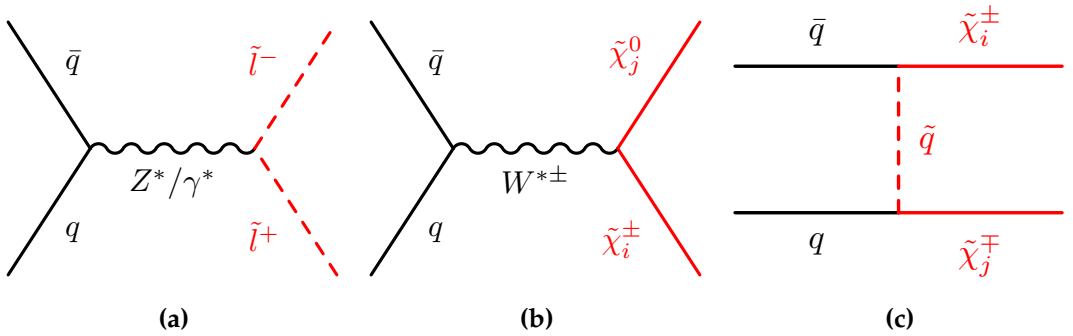

Figure 5.3: Examples of slepton, neutralino and chargino production via the electroweak interaction at a hadron collider.

in Ref. [108]. Figure 5.4b shows electroweak production of two charginos, which decay via intermediate sleptons. The final state contains two charged leptons and missing transverse momentum [109]. Figure 5.4c shows the production of two top squarks, each of which decays into a top quark and a neutralino LSP. This channel is of great interest due to the high top Yukawa coupling - if supersymmetry is to solve the hierarchy problem, this coupling hints that the top squark should be relatively light ($m_{\tilde{t}} \lesssim 1$ TeV). An experimental search for this signature is outlined in Ref. [110]. The common feature of the searches for R-parity-conserving supersymmetry is the requirement of large missing transverse momentum in the final state.

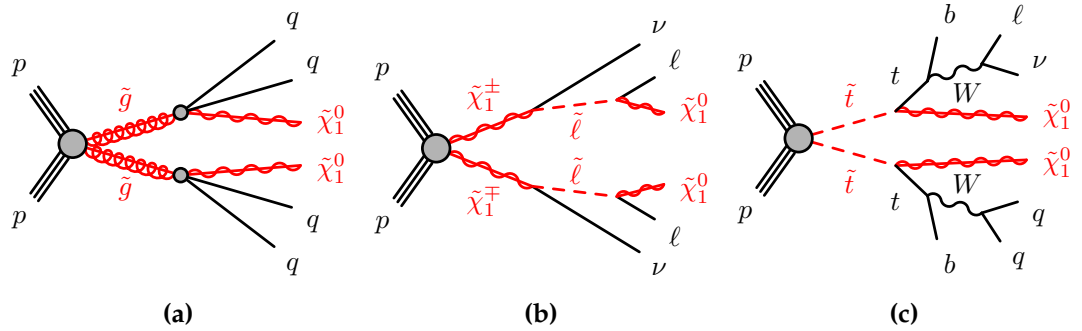

Figure 5.4: Examples for R-parity-conserving cascade decays of pair produced supersymmetric particles in pp collisions: Gluinos decaying into two jets and the LSP [108] (a), charginos decaying into a charged lepton, a neutrino and the LSP [109] (b) and top squarks decaying into a top quark and the LSP (c), with two possible top quark decay modes [110].

5.2 R-Parity-Violating-Supersymmetry

Allowing R-parity-violating terms in the MSSM Lagrangian has profound consequences for the expected experimental signatures. Inserting the contents of Eq. (2.26) into the term $W^{uv}\psi_u\psi_v + h.c$ of the MSSM Lagrangian (see Eq. (2.22)) yields new couplings, including ones between a slepton, a lepton and a neutrino or two leptons and a sneutrino:

$$\mathcal{L}_{\mathrm{LLE}} = \lambda_{ijk}\left(\tilde{e}_k^* L_i^\alpha L_j^\beta + \tilde{L}_i^\alpha L_j^\beta e_k^\dagger + \tilde{L}_j^\beta L_i^\alpha e_k^\dagger\right)\epsilon_{\alpha\beta}\epsilon_{ij} + h.c., \tag{5.1}$$

$$\mathcal{L}_{\mathrm{LQD}} = \lambda'_{ijk}\left(\tilde{d}_k^* L_i^\alpha Q_j^\beta + \tilde{L}_i^\alpha Q_j^\beta d_k^\dagger + \tilde{Q}_j^\beta L_i^\alpha d_k^\dagger\right)\epsilon_{\alpha\beta} + h.c., \tag{5.2}$$

$$\mathcal{L}_{\mathrm{UDD}} = \lambda''_{ijk}\left(\tilde{d}_k^* u_i^\dagger d_j^\dagger + \tilde{u}_i^* d_j^\dagger d_k^\dagger + \tilde{d}_j^* u_i^\dagger d_k^\dagger\right)\epsilon_{jk} + h.c., \tag{5.3}$$

$$\mathcal{L}_{\mathrm{bilinear}} = \kappa^i L_i^\alpha \tilde{H}_u^\beta \epsilon_{\alpha\beta} + h.c., \tag{5.4}$$

where $i,j,k \in \{1,2,3\}$ are generation indices and $\alpha,\beta \in \{1,2\}$ doublet indices of $SU(2)_L$. Examples of vertices resulting from the LLE couplings are shown in Figure 5.5. Analogous vertices result from the two other trilinear RPV superpotential terms (LQD, UDD), while the bilinear term introduces a coupling between left-handed leptons or neutrinos and the $\tilde{H}_u$ higgsino which can introduce neutrino masses through mixing with the

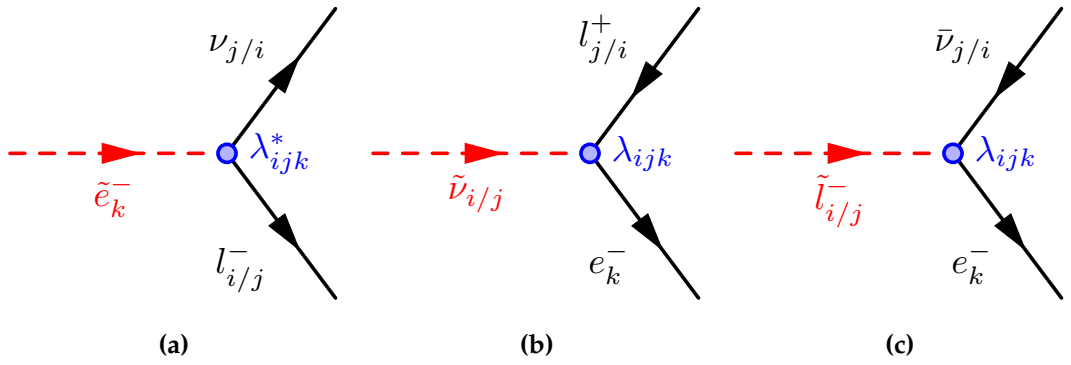

Figure 5.5: Examples of lepton-flavour- and lepton-number-violating couplings due to an R-parity-violating LLE term in the superpotential. The conjugate processes are also possible. The indices i, j, k indicate lepton flavours. The charged left handed leptons are denoted as $l_i \equiv L^2_i$, the neutrinos as $\nu_i \equiv L^1_i$.

neutralinos.

Figure 5.6 shows examples of decays of SUSY particles mediated by such RPV couplings. Figure 5.6a shows the same gluino pair production process as Figure 5.4a, but with an additional R-parity-violating decay of the neutralino LSP into three quarks via intermediate squarks under a UDD coupling, resulting in a ten-jet final state without missing transverse momentum. This topology is not covered by searches for 4-jet final states with large missing transverse momentum produced in the case of R-parity-conservation. A dedicated search for events with high jet multiplicities [111] is sensitive to such a process. Figure 5.6b shows the RPV equivalent to the RPC process in Figure 5.4c with pair production of top squarks. A non-zero UDD coupling lets the top squark decay into two quark jets, leading to a four-jet final state without leptons or missing transverse momentum, which is again not covered by searches for the corresponding R-parity-conserving process. In the case of a non-zero LQD coupling, the two stops would each decay into a lepton or neutrino and a quark instead, leading to a final state with jets, between zero and two charged leptons and possibly missing transverse energy [112].

R-parity-violation also gives rise to new sparticle production processes not present in the MSSM. Figure 5.6c shows resonant sneutrino production from initial-state quarks via the LQD term with a subsequent decay of the sneutrino into charged leptons via the LLE term as an example where both the production and decay of the superpartners proceeds via R-parity-violating processes. The signature in this case is a dilepton resonance with

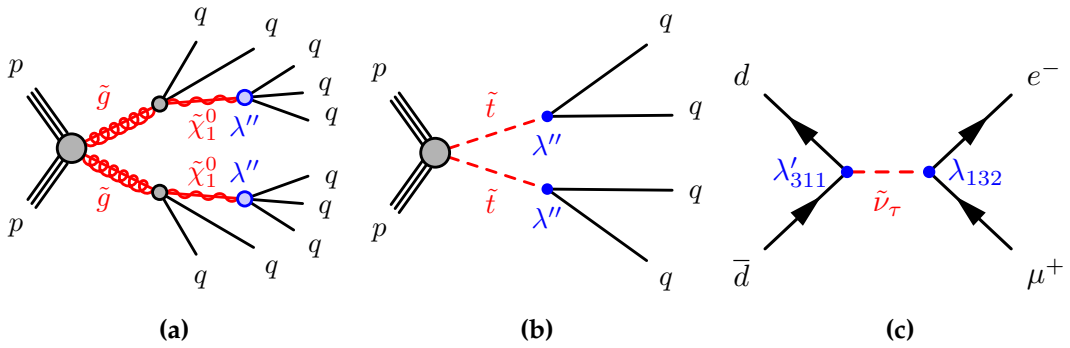

Figure 5.6: Examples of R-parity-violating decays of supersymmetric particles: A gluino decaying via an intermediate squark (not shown) and UDD couplings [111] (a), a top squark pair decaying into quark pairs via UDD couplings leading to a 4-jet final state (b) and flavour violating dilepton resonance from sneutrino decay with non-zero LQD and LLE couplings [113] (c).

different lepton flavours [113].

Such RPV signatures require dedicated searches. In this thesis, RPV processes with a non-zero LLE coupling are studied.

5.3 The LLE Coupling with Neutralino LSP

5.3.1 Simplified Models

For the study of supersymmetric LLE couplings simplified models are used that allow only one particular RPV process with 100% branching fraction. For this purpose, two superpartners, the next-to-lightest supersymmetric particle (NLSP) and the LSP are assigned masses within reach of the LHC with $\sqrt{s} = 8$ TeV. All other superpartners are effectively decoupled with high masses of 4.5 TeV. The LSP is always a bino-like neutralino $\tilde{\chi}_1^0$, ensuring flavour-independent coupling to leptons of both helicities, whereas a higgsino would preferentially couple to τ leptons and a wino only to left-(right)-handed (anti)leptons. The NLSP may be a wino-like chargino $\tilde{\chi}_1^\pm$, a slepton, a sneutrino or, to explore strong production processes, a gluino. In the cases of a slepton or a sneutrino NLSP, all three flavour states are assumed to be degenerate in mass, and *L-slepton* $\tilde{L}_i^2$ and *R-slepton* $\tilde{e}_i^*$ NLSPs are considered separately due to their different coupling behaviour. Only one particular LLE coupling parameter λ_{ijk} takes a non-zero

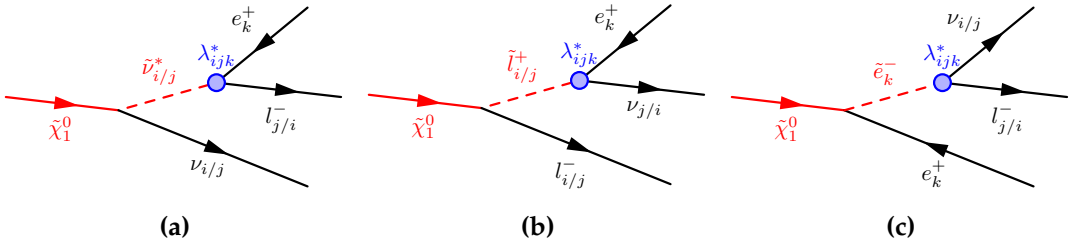

Figure 5.7: Decays of a neutralino LSP into two charged leptons and a neutrino via the R-parity-violating LLE coupling λ_{ijk}. i, j, k are generation indices. The decay is mediated either by a virtual sneutrino (a), a virtual L-slepton (b) or a virtual R-slepton (c). The conjugate of every process is also possible.

value at a time. No assumption is made on the exact value, instead the decay width of the LSP is set by hand. The LLE coupling does not affect the dominant SUSY production processes at the LHC for the NLSP choices under study. Therefore, the first step of each process is always pair production of the NLSP, with cross-sections as predicted with R-parity-conservation (see Table A.2). In the cases of a wino, sneutrino or slepton NLSP, weak production as illustrated in Figs. 5.3a and 5.3c dominates, while the gluino NLSP is produced via the strong process illustrated in Figure 5.2a or a t-channel process with a virtual gluino.

The NLSP pairs undergo cascade decays until the LSP is reached. In contrast to RPC SUSY, the RPV LLE coupling causes the LSP to decay into Standard Model charged leptons and neutrinos via an intermediate virtual slepton or sneutrino as illustrated in Figure 5.7. Ignoring helicity, lepton charge and the neutrino flavour, two different charged lepton flavour final states are possible: $\tilde{\chi}_1^0 \to \ell_i \ell_k \nu$ and $\tilde{\chi}_1^0 \to \ell_j \ell_k \nu$ (with $\ell_1 = e, \ell_2 = \mu, \ell_3 = \tau$). For a single active coupling and mass-degenerate sleptons, as assumed in the models, these occur with a branching fraction of 50% each. Figure 5.8 shows the resulting signatures for different NLSP choices considered in the simplified models.

The choice of non-zero λ_{ijk} coupling determines the lepton flavour configurations in the final state. Table 5.1 lists the LSP decay modes for the different choices. There are nine variations, as antisymmetry in the left-handed lepton indices in the superpotential [28] requires $\lambda_{ijk} = -\lambda_{jik}$. The four coupling parameters λ_{121}, λ_{122}, λ_{133} and λ_{233} marked in red in Table 5.1 are studied in the simplified models. These correspond to the extreme cases in terms of τ lepton multiplicity - the λ_{121} and λ_{122} couplings lead to final states

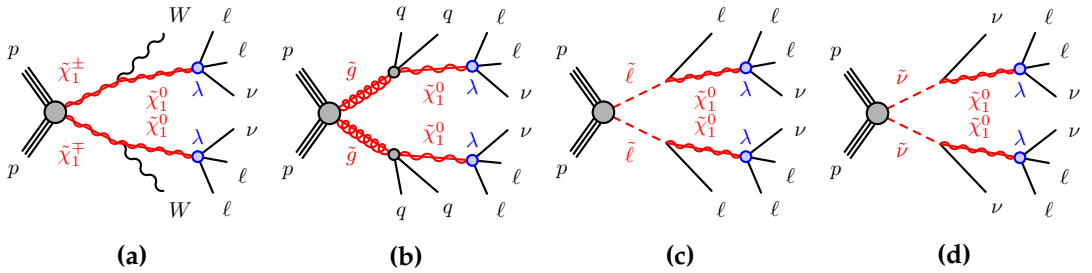

Figure 5.8: NLSP choices considered in the simplified models with an LLE RPV coupling: wino NLSP (a), gluino NLSP (b), slepton NLSP (c) and sneutrino NLSP (d). Both R-slepton and L-slepton NLSPs, corresponding to left- and right-handed Standard Model leptons, are considered. The LSP is always a bino-like neutralino $\tilde{\chi}_1^0$

Table 5.1: Possible decay modes for a $\tilde{\chi}_1^0$ LSP decaying via a single, R-parity-violating LLE coupling. i, j, k are the flavour indices defined by the choice of the non-zero λ_{ijk} coupling. The cases marked red are studied here.

	$ij = 12$	$ij = 13$	$ij = 23$
$k = 1$	$ee\nu_\mu / e\mu\nu_e$	$ee\nu_\tau / e\tau\nu_e$	$e\mu\nu_\tau / e\tau\nu_\mu$
$k = 2$	$e\mu\nu_\mu / \mu\mu\nu_e$	$e\mu\nu_\tau / \mu\tau\nu_e$	$\mu\mu\nu_\tau / \mu\tau\nu_\mu$
$k = 3$	$e\tau\nu_\mu / \mu\tau\nu_e$	$e\tau\nu_\tau / \tau\tau\nu_e$	$\mu\tau\nu_\tau / \tau\tau\nu_\mu$

Table 5.2: Final-state charged lepton flavour configurations for a pair of $\tilde{\chi}_1^0$ LSP decaying via a single, R-parity-violating LLE coupling for the coupling choices studied in this thesis.

Active Coupling	Charged lepton flavour configurations					
λ_{121}	$eeee$	(25%)	$eee\mu$	(50%)	$ee\mu\mu$	(25%)
λ_{122}	$ee\mu\mu$	(25%)	$e\mu\mu\mu$	(50%)	$\mu\mu\mu\mu$	(25%)
λ_{133}	$ee\tau\tau$	(25%)	$e\tau\tau\tau$	(50%)	$\tau\tau\tau\tau$	(25%)
λ_{233}	$\mu\mu\tau\tau$	(25%)	$\mu\tau\tau\tau$	(50%)	$\tau\tau\tau\tau$	(25%)

without any τ leptons, while the λ_{133} and λ_{233} couplings lead to at least one τ lepton per LSP decay. Because of their decays (see Section 3.3.5), τ leptons are reconstructed with lower efficiency and purity than muons or electrons. Therefore, the sensitivity of searches decreases with increasing numbers of τ leptons in the final state.

Since the NLSP and hence LSP are pair produced, two neutralino decays occur in every event, resulting in final states with four charged leptons and two neutrinos from the LSP decays and additional particles from the NLSP decay. Table 5.2 lists the possible flavour configurations of the four leptons from the LSP decays for the different choices of non-zero λ_{ijk} coupling investigated here.

For one choice of λ_{ijk} coupling and NLSP type, the only free parameters within the simplified models are the masses of the NLSP and the LSP and the lifetime of the LSP decay. For fixed lifetime, this results in a two-dimensional parameter space defined by the two masses. A systematic investigation of this parameter space is performed by simulating a grid of mass combinations, the so-called *mass points*, in the plane and interpolating between them.

5.3.2 Existing Experimental Constraints before the LHC

The parameter space of the models has been constrained by previous experiments. At the LEP electron-positron collider, lower limits for the slepton and sneutrino masses of about 90 – 100 GeV were obtained [114–118], depending on the LSP mass and the active R-parity-violating LLE coupling and with a small variation between the experiments (see Figure 5.9). The D0 experiment reported a lower limit of about 200 – 220 GeV (150 – 180 GeV) [119] on the mass of a Wino-like chargino decaying via a $\lambda_{121/122}$ (λ_{133}) LLE coupling similar to the scenario considered in this study, depending on the LSP mass and the active R-parity-violating LLE coupling (see Figure 5.10).

Limits on the strength of a single active λ_{ijk} coupling on the order of $0.03 - 0.05 \cdot \left[\frac{100\text{ GeV}}{m_{\tilde{\ell}/\tilde{\nu}}}\right]$, shown in Table 5.3, follow from precision measurements of the leptonic partial decay widths of the τ lepton, CKM mixing parameters and atomic parity-violation in caesium-133 [120] (see Table 5.3). However, these have little impact on this work, as couplings below these limits still allow the LSP decay under study to take place both promptly or with a measurable lifetime for all considered NLSP-LSP mass combinations.

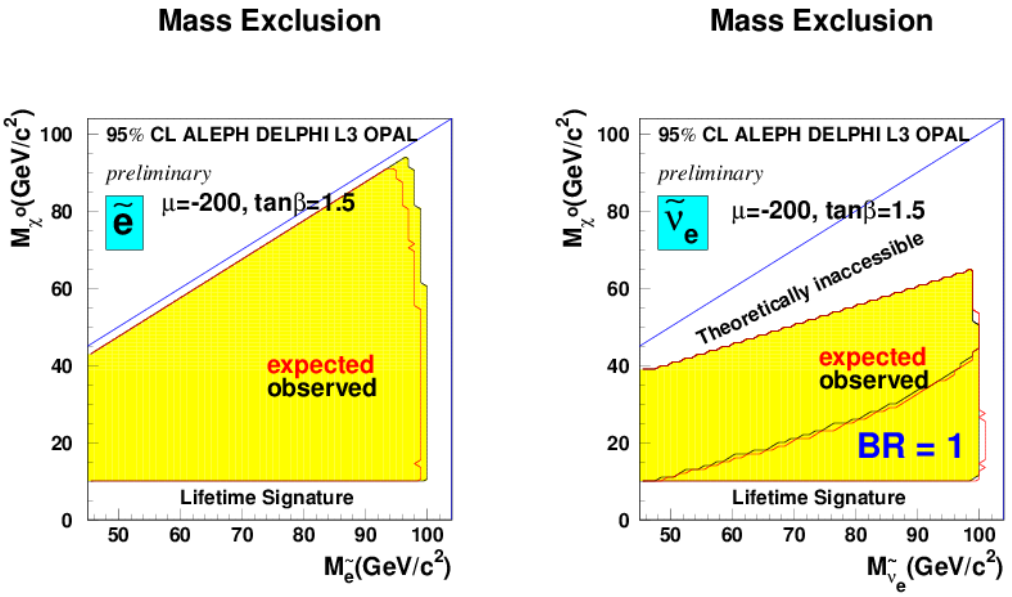

(a) **(b)**

Figure 5.9: Region of the selectron-neutralino (a) and sneutrino-neutralino (b) mass planes excluded by the LEP2 experiments for R-parity-violating decays via an LLE coupling [114–118].

Table 5.3: Upper limits on the magnitude of the R-parity-violating LLE couplings from precision measurements of muon and τ decay widths, CKM mixing parameters and atomic parity-violation [120]. For each coupling, the most stringent limit is given.

Coupling	2σ upper limit on $\lvert\lambda_{ijk}\rvert \frac{m_{\tilde{\ell}/\tilde{\nu}}}{100\ \text{GeV}}$ [120]	source
λ_{12k}	0.03	CKM parameter V_{ud}
λ_{13k}	0.05	τ decay
λ_{23k}	0.05	τ decay

5.3.3 Effect of the NLSP and LSP Masses

Besides the determination of the production cross-sections, the NLSP and LSP mass combination also influence the final state kinematics. Figure 5.11 shows the relativistic $\beta\gamma$ factor of the LSP for the example of the RPV model with a gluino NLSP. Figure 5.11a gives the dependence of the mean value on the NLSP-LSP mass combinations. An LSP that is light compared to the NLSP is produced with high boost. This is further illustrated in Figure 5.11b for the three cases of $m_{\tilde{\chi}_1^0} = 10$, 200 and 1090 GeV for $m_{\tilde{g}} = 1.1$ TeV. While

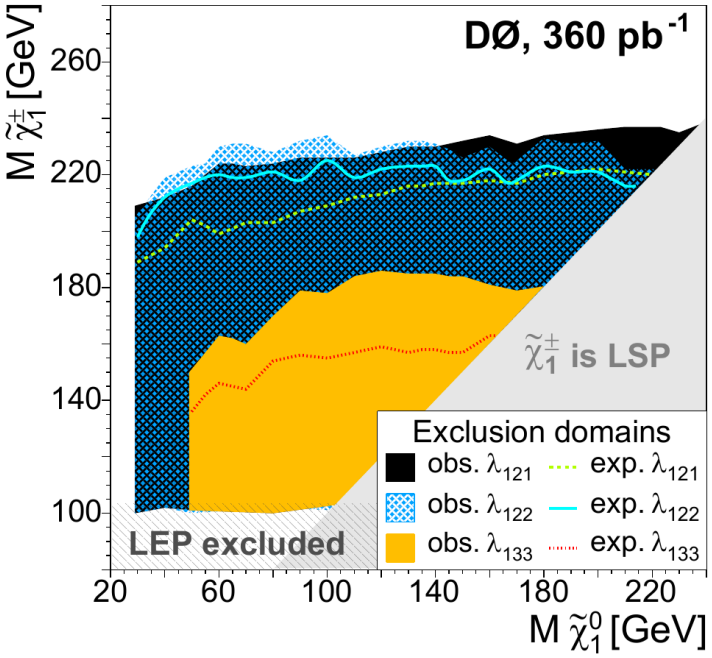

Figure 5.10: Region of the wino-neutralino mass plane excluded by the D0 experiment at the Tevatron $p\bar{p}$ collider for R-parity-violating decays via an LLE coupling [119].

the $\beta\gamma$ factor for the case $m_{\tilde{\chi}_1^0} \approx m_{\tilde{g}}$ is small for kinematic reasons, it reaches up to 200 for a very light LSP.

In the R-parity-violating model with LLE coupling studied, the LSP decays into two charged leptons and a neutrino. Figure 5.12 shows the mean separation ΔR (see Section 3.2.1) between the pair of charged leptons from an LSP decay as a function of the NLSP-LSP mass combinations in the gluino model and the ΔR distributions for three LSP masses in the mass grid for $m_{\tilde{g}} = 1.1$ TeV. For a very light LSP the angular separation of the leptons is small due to the boost of the decaying particle, while the angular spread becomes wider for a heavy LSP. The strong collimation is challenging for the lepton reconstruction, as signatures can overlap. For example, if two electrons are very close, the calorimeter clusters can merge such that one or even both of the electrons fail the reconstruction.

In addition to the direction, also the momentum value of the final state leptons is affected by the different mass combinations. Figure 5.13 shows the final state lepton momenta for the example of a gluino NLSP. For a light LSP, the subleading lepton has on average small transverse momentum, and the p_T distribution favours very low momenta.

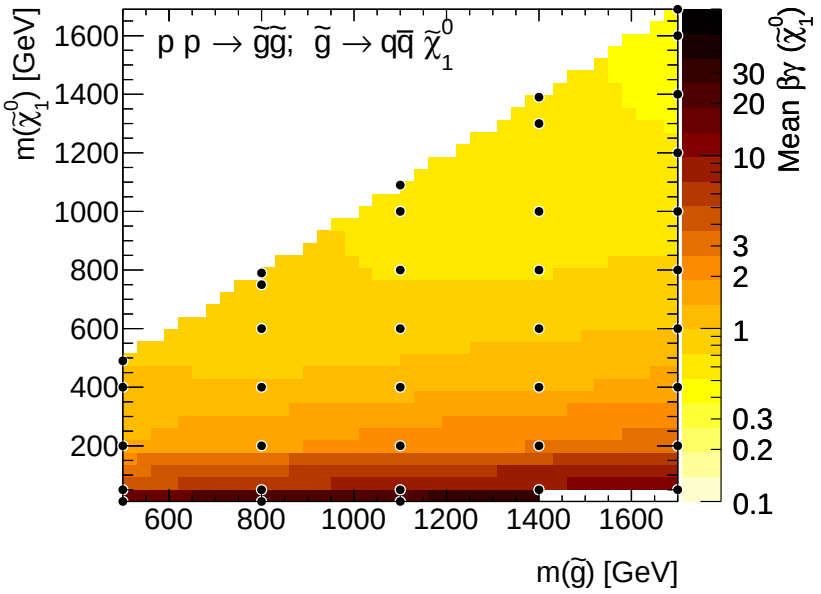

(a)

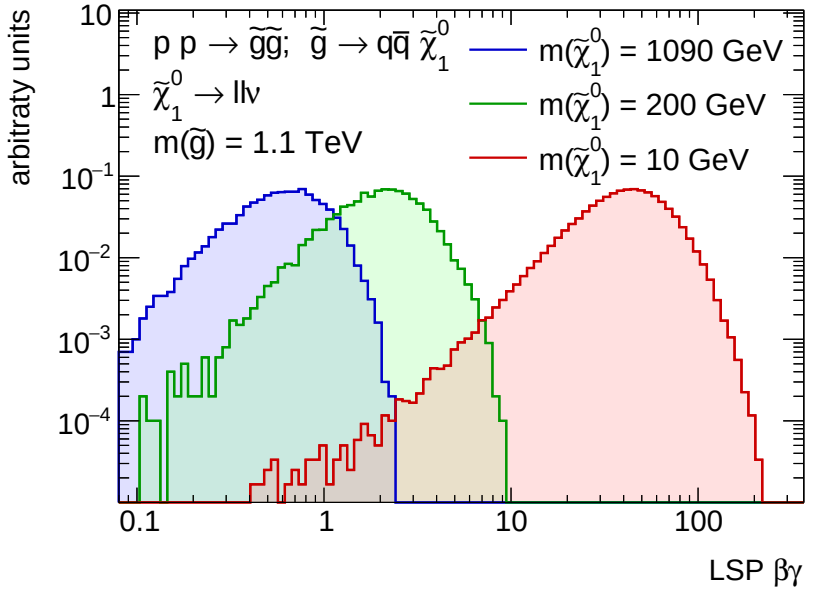

(b)

Figure 5.11: Relativistic $\beta\gamma$ factor of the neutralino LSP for the simplified LLE RPV model with gluino LSP. Mean value as a function of NLSP-LSP mass combinations (a) and differential distributions for the cases of $m_{\tilde{\chi}_1^0}$ = 10, 200 and 1090 GeV and a gluino mass of $m_{\tilde{g}}$ = 1.1 TeV (b) are shown.

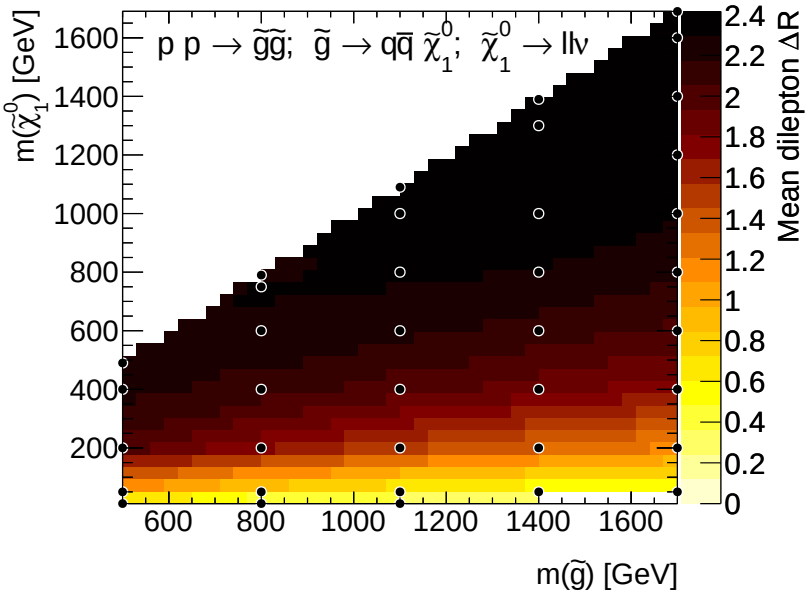

(a)

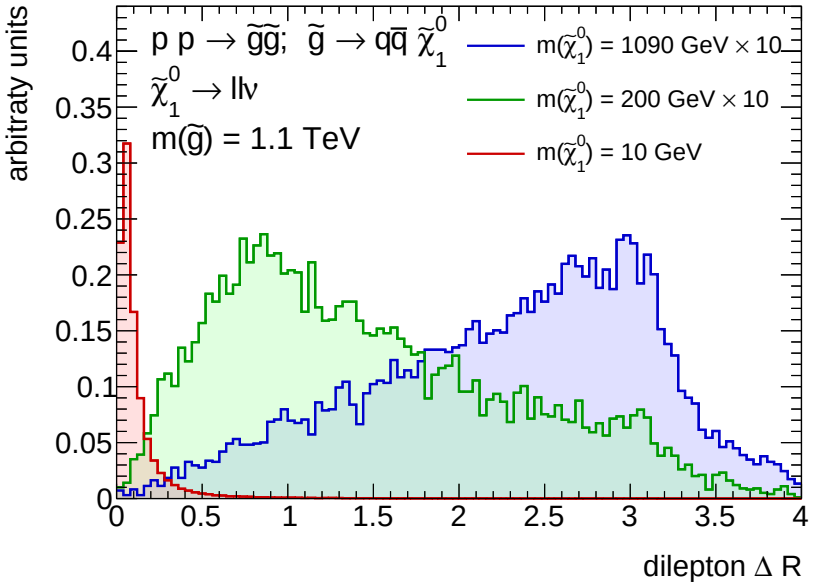

(b)

Figure 5.12: Separation ΔR in the η–ϕ plane between pairs of charged final state leptons in the simplified RPV LLE model with a gluino NLSP. Mean value depending on the NLSP-LSP mass combination (a) and distributions for the cases of $m_{\tilde{\chi}_1^0}$ = 10, 200 and 1090 GeV and a gluino mass of $m_{\tilde{g}}$ = 1.1 TeV (b) are shown. The distributions for $m_{\tilde{\chi}_1^0}$ = 200 GeV and $m_{\tilde{\chi}_1^0}$ = 1090 GeV are scaled by a factor of 10.

The conclusion of these studies is that the final state kinematics are strongly affected by the NLSP-LSP mass ratio. With decreasing ratio and LSP mass, the final state lepton momenta decrease and become more collimated around the LSP direction of flight. At the same time, the momenta of particles emitted in the cascade decay increase. Therefore, the region of low LSP masses is more difficult to probe experimentally, reducing the sensitivity to the model compared to the region of comparable NLSP and LSP masses.

5.3.4 Effect of the LSP Lifetime

The lifetime of the LSP is a further free parameter of the simplified models. For the case of a neutralino decaying via an RPV LLE coupling λ_{ijk} with an intermediate virtual sfermion $\tilde{f}$ (see Figure 5.7), the lifetime is given by [121]

$$\tau \simeq 10\ \text{ps} \cdot \frac{1}{\lambda_{ijk}^2} \cdot \left(\frac{m_{\tilde{f}}}{100\ \text{GeV}}\right)^4 \cdot \left(\frac{1\ \text{GeV}}{m_{\tilde{\chi}_1^0}}\right)^5 . \tag{5.5}$$

Three cases can be distinguished:

$c\tau \ll 1$ mm
For very short lifetimes, the decay vertices of the LSP can not be resolved from the primary vertex (Section 3.3). The experimental signature then consists of four charged leptons from the primary vertex in addition to particles from the cascade, also referred to as the prompt decay scenario.

1 mm $\lesssim c\tau \lesssim$ 1 m
With increasing LSP lifetimes, the LSP decay vertex becomes more separated from the primary vertex, but is still within the detector. The signature consists of cascade particles from the primary vertex and secondary dilepton decay vertices of the two LSPs. If these secondary vertices are located within the Inner Detector (Section 3.2.2), they can be reconstructed. This reconstruction is also possible for decays beyond the Inner Tracker, if both charged leptons leave tracks in the Muon Spectrometer.

$c\tau \gg 1$ m
For very large LSP lifetimes, the decay takes place outside the detector. For a neutral LSP, the resulting signature is identical to the one for R-parity-conserving supersymmetry,

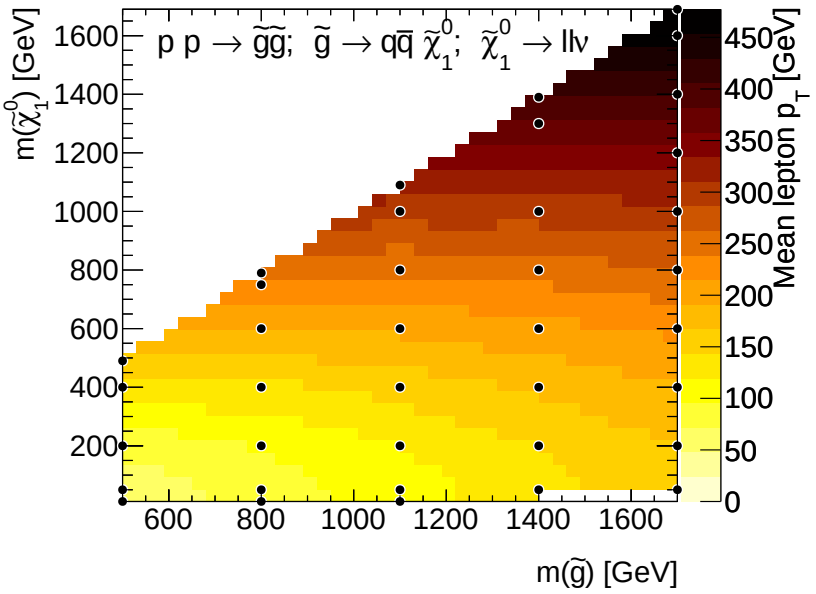

(a)

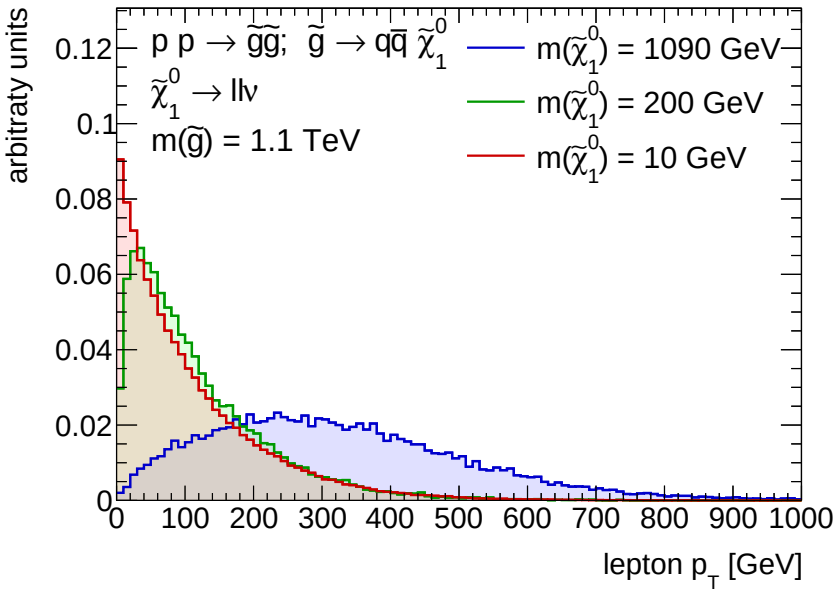

(b)

Figure 5.13: Transverse momentum of the charged leptons for the simplified RPV LLE model with a gluino NLSP. Mean value depending on the NLSP-LSP mass combinations (a) and distributions for the cases of $m_{\tilde{\chi}_1^0}$ = 10, 200 and 1090 GeV and a gluino mass of $m_{\tilde{g}}$ = 1.1 TeV (b) are shown.

with cascade particles and significant missing transverse momentum due to the escaping LSPs. If the LSP is charged, it can be reconstructed in the Inner Detector and, if it is not absorbed in the calorimeters, in the Muon Spectrometer [122] and identified through its slow speed compared to Standard Model particles.

As the last scenario is already covered by already performed searches for R-parity-conserving supersymmetry, the emphasis of this thesis is on dedicated search for the first two scenarios.

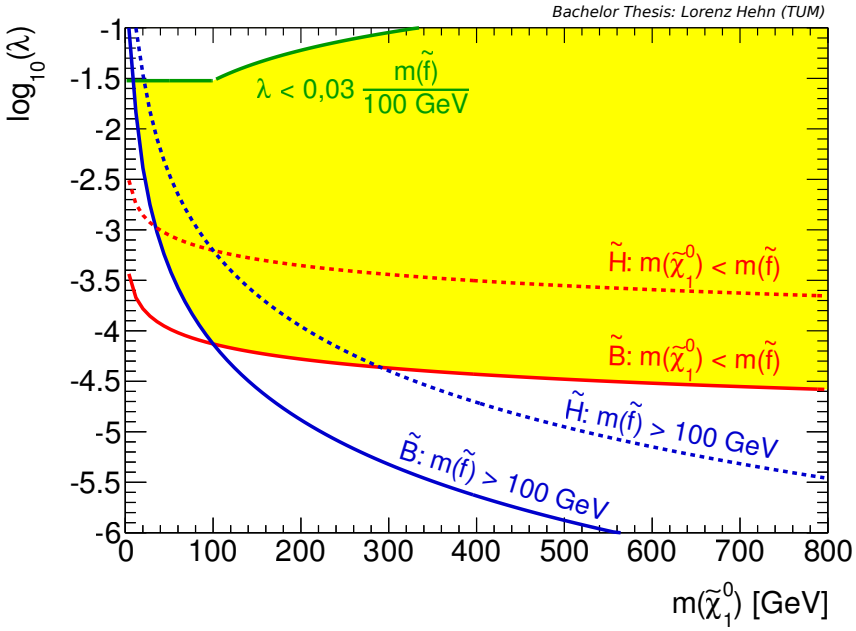

Figure 5.14: Region (yellow) in the $m_{\text{LSP}} - \lambda$ plane where prompt decays (with lifetimes less than 1 ps) of the LSP are possible for an RPV LLE coupling [123]. The blue solid line corresponds to the LEP lower bounds on the slepton and sneutrino masses. The green line indicates existing upper limits on the magnitude of the λ coupling. The red solid line marks the border to the region where the slepton or sneutrino mass would have to be below the LSP mass to yield prompt decays according to Eq. (5.5).

Figure 5.14 shows the region in the $m_{\text{LSP}} - \lambda$ plane where Eq. (5.5) yields a valid result with $\tau < 1$ ps [123]. Its boundaries are defined by constraints on the slepton or sneutrino mass (blue line) and the λ parameter (green line) described in Section 5.3.2 and by the requirement that the sleptons and sneutrinos must not be lighter than the LSP (red line). For small LSP masses below about 50 GeV, short-lived decays are only possible in a small interval of the λ coupling. As the LSP mass increases, a wider range of coupling

parameters spanning more than four orders of magnitude can generate prompt decays. Therefore, both the short and the medium lifetime scenarios are interesting for RPV SUSY searches, as both are possible for all LSP masses above 10 GeV.

If the LSP lifetime is negligible, a search for events with four charged leptons is effective, as such a high lepton multiplicity is rare in Standard Model processes. This search is described in Chapter 6.

A dedicated search for displaced decay vertices of high-mass charged lepton pairs targeting medium LSP lifetimes is discussed in Chapter 7. Such vertices do not occur in Standard Model processes, leading to very low expected background.

Chapter 6

RPV Decays of a Short-Lived LSP in Events with Four Leptons

As discussed in Section 5.3, decays of a short-lived neutralino via an R-parity-violating (RPV) LLE coupling result in a signature of four charged leptons emerging from the primary vertex location. In the following, a search [124] exploiting this signature is presented.

6.1 Analysis Strategy

To search for events with decays of supersymmetric particles, the number of events passing certain requirements on discriminating variables is compared to the number of Standard Model events expected to pass those selection criteria. These criteria are also called *signal regions* in the discriminating variable space, and are optimised for maximum sensitivity to the new processes.

In the search for prompt neutralino LSP decays via LLE couplings, the main selection requirement is the presence of four charged leptons. Electrons and muons are in the following referred to as *light leptons*, to distinguish them from hadronic τ decays. Final states with more than two hadronic τ decays are not considered because of the less efficient τ reconstruction (Section 3.3.5).

Final state leptons are classified into two categories, depending on their origin. Leptons originating from a hard interaction, including the signal process, are referred to as *prompt*

leptons. On the other hand, leptons from secondary Standard Model particle decays ($b \to c\mu^- \bar{\nu}_\mu$, for example) or misidentified leptons (a converted photon misidentified as an electron, for example), are designated as *fake leptons*.

Standard Model processes with four prompt leptons in the final state are rare. They include $ZZ^{(*)}/Z\gamma^*$ diboson production, various different Higgs boson production and decay processes, top quark pair production in association with vector bosons and triple gauge boson production (ZWW, ZZZ). These backgrounds are called *irreducible*, because they do not involve fake leptons. The small numbers of expected events and the similarity to the signal prohibit purely data-driven techniques for background estimation, therefore Monte Carlo simulation are used to predict the irreducible background.

Processes with fewer than four prompt leptons in the final state and additional fake leptons contribute to the *reducible* background. Fake leptons can be rejected by lepton identification criteria. Contributions to this source of background are $WZ \to 3\ell 1\nu$ diboson production as well as $Z \to \ell\ell$ and top quark pair production. The reducible background is estimated using a data-driven technique.

Reducible background is rejected by requirements on the four final state leptons. Further event-level selection criteria suppress the irreducible background as well as remaining reducible contributions. These requirements include moderate missing transverse momentum, because of neutrinos in the final state for the signal (see Section 5.3), and large effective mass, defined as the scalar sum of the momenta of all leptons and jets in the event passing certain selection criteria. The effective mass is sensitive to the masses of the initially produced particles. Finally, on-shell leptonic Z boson decays are rejected.

The charged lepton and signal region selection criteria are explained in Section 6.2. In Section 6.3 the resulting expected signal yields are discussed. The estimation of the Standard Model background is described in Section 6.4. Systematic uncertainties in the signal prediction and background estimate are summarised in Section 6.5. In Section 6.6 the statistical methods for the interpretation of the analysis result are discussed. These are applied to the four-lepton search in Section 6.7.

6.2 Event Selection

6.2.1 Trigger and Preselection

Only data taken with fully operational detector is used. A well-reconstructed primary vertex with at least 5 associated tracks to which the leptons can be associated is required. Every recorded event has to satisfy at least one trigger condition. The lepton triggers used for the four-lepton analysis are listed in Table 6.1. At least one of these eight triggers is required to have accepted the event. The combination of single and dilepton triggers is expected to be highly efficient in four-lepton events.

Table 6.1: Trigger requirements of the four-lepton analysis at event-filter level. At least one of the listed trigger conditions has to be satisfied. Additional isolation and reconstruction quality requirements on the trigger objects are not listed.

Trigger	Momentum thresholds
Single muon	24 GeV
Single electron	24 GeV
Symmetric dielectron	12 GeV, 12 GeV
Asymmetric dielectron	24 GeV, 7 GeV
Symmetric dimuon	13 GeV, 13 GeV
Asymmetric dimuon	18 GeV, 8 GeV
Electron+muon	12 GeV(e), 8 GeV(μ)
Muon+electron	18 GeV(μ), 7 GeV(e)

6.2.2 Lepton and Jet Selection

The first step of the event selection is the collection of all leptons and jets to be considered. To facilitate the data-driven background estimation, the selection of leptons and jets consists of two stages.

Baseline Selection

Electrons and muons with transverse energy or momentum above 10 GeV within the acceptance of the Inner Detector are used (see Table 6.2), ensuring reliable reconstruction and low fake rates. Table 6.3 lists the selection criteria for baseline τ leptons.

Table 6.2: Baseline selection criteria for electrons and muons in the four-lepton analysis.

Baseline muon requirements		Baseline electron requirements	
Muon type	Combined or segment-tagged	Identification criteria	*Medium*
Transverse momentum	$p_{\mathrm{T}} > 10$ GeV	Transverse energy	$E_{\mathrm{T}} > 10$ GeV
Pseudorapidity	$\lvert\eta\rvert < 2.5$	Pseudorapidity	$\lvert\eta\rvert < 2.47$

Table 6.3: Baseline selection criteria for τ leptons in the four-lepton analysis. The pseudorapidity requirement is applied to both the calorimeter cluster and the inner detector track with the highest momentum.

Baseline τ lepton requirements	
Transverse momentum	$p_{\mathrm{T}} > 20$ GeV
Pseudorapidity	$\lvert\eta\rvert < 2.47$
Number of charged tracks	1 or 3
Total charge	± 1

Table 6.4: Baseline selection criteria for jets in the four-lepton analysis.

Baseline jet requirements	
Algorithm	Anti-k_{T}, $\Delta R = 0.4$
Transverse momentum	$p_{\mathrm{T}} > 20$ GeV
Pseudorapidity	$\lvert\eta\rvert < 4.5$

Table 6.4 lists the baseline jet selection criteria for jets to be considered in the following analysis steps, including the effective mass calculation.

Removal of Overlaps

At this stage, there are still ambiguities in the object reconstruction. For example, electrons and τ leptons passing the kinematic criteria of the jet reconstruction are in general also reconstructed as baseline jets. Electrons and muons may additionally be reconstructed as baseline τ leptons. Leptons within jets are regarded as fakes. Bremsstrahlung from a muon can result in an additional reconstructed electron.

For this reason, an iterative overlap removal procedure is applied to close-by baseline objects, resolving ambiguities and removing secondary objects. In each step, combinations of different close-by objects (electrons, muons, τ leptons or jets) are considered. If two objects are closer than a certain minimum separation ΔR_{min}, one of the two objects, or both, are discarded according to the rules listed in Table 6.5. The final step is applied to τ leptons passing the additional *Medium* quality requirements, as otherwise genuine jets misidentified as τ leptons would be removed.

Table 6.5: Overlap removal procedure of baseline objects in the four-lepton analysis.

Step	Close-by objects	Maximum separation ΔR_{min}	Object removed
1	Two electrons	0.05	lower energy electron
2	Electron and jet	0.2	jet
3	Electron and τ	0.2	τ
4	Muon and τ	0.2	τ
5	Jet and muon	0.4	muon
6	Jet and electron	0.4	electron
7	Muon and electron	0.01	both
8	Two muons	0.05	both
9	Jet and *Medium* quality τ	0.2	jet

While this procedure is useful in removing misidentified or doubly identified objects, it can also harm the sensitivity to signals with strongly collimated leptons for neutralinos lighter than 50 GeV (see Figure 5.12b). Therefore, the minimum separation values ΔR_{min} used for the overlap removal between lepton pairs were optimised compared to the value of 0.1 applied in previous iterations of the search [125], significantly improving the acceptance of collimated lepton pairs (see Figure 6.1).

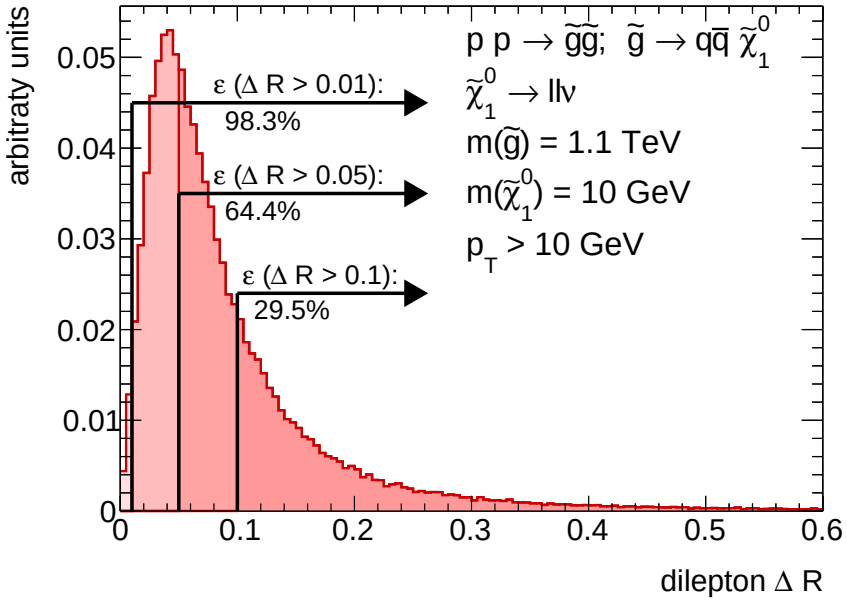

Figure 6.1: Separation ΔR in the η–ϕ plane between pairs of charged final state leptons in the simplified RPV LLE model with a gluino NLSP with $m_{\tilde{g}} = 1.1$ TeV decaying into a neutralino with $m_{\tilde{\chi}_1^0} = 10$ GeV and fraction of lepton pairs with $p_{\mathrm{T}} > 10$ GeV passing overlap removal criteria of $\Delta R_{\mathrm{min}} = 0.1$ as used in Ref. [125] and $\Delta R_{\mathrm{min}} = 0.01$ and 0.05 as used in this search.

Table 6.6: Additional selection criteria for signal muons in the four-lepton analysis. Corrected isolation variables are used (see text).

Signal muon requirements	
Track isolation	$p_{\mathrm{T}}^{\mathrm{cone},30} < 0.12 \cdot p_{\mathrm{T}}$
Transverse impact parameter significance	$\frac{\lvert d_0 \rvert}{\sigma(d_0)} < 3$
Longitudinal impact parameter	$\lvert z_0 \sin\theta \rvert < 1$ mm

Signal Leptons and Jets

After overlap removal, further selection criteria are applied to eliminate fake leptons almost completely, using requirements on track or calorimeter activity and the impact parameters as well as further object quality criteria. Leptons fulfilling these cuts are *signal leptons*, while those failing them are called *loose*. Loose leptons are used for the background estimation.

Table 6.7: Additional selection criteria for signal electrons in the four-lepton analysis. Corrected isolation variables are used (see text).

Signal electron requirements	
Track isolation	$p_{\mathrm{T}}^{\mathrm{cone},30} < 0.16 \cdot E_{\mathrm{T}}$
Calorimeter isolation	$E_{\mathrm{T}}^{\mathrm{cone},30} < 0.18 \cdot E_{\mathrm{T}}$
Transverse impact parameter significance	$\frac{\lvert d_0 \rvert}{\sigma(d_0)} < 5$
Longitudinal impact parameter	$\lvert z_0 \sin\theta \rvert < 0.4$ mm
Quality	Tight

Table 6.8: Additional selection criteria for signal jets in the four-lepton analysis.

Signal jet requirements	
Pseudorapidity	$\lvert\eta\rvert < 2.5$
Fraction of tracks coming from primary vertex	> 0.5 if $p_{\mathrm{T}} < 50$ GeV and $\lvert\eta\rvert < 2.4$

The additional requirements applied to electrons, muons and jets are listed in Tables 6.6–6.8, respectively. For τ leptons, only *Medium* quality criteria including an electron and muon veto are applied in addition. As this search is for prompt neutralino decays, the impact parameters of muons and electrons with relation to the primary vertex location are required to be small, rejecting fake leptons from B meson decays.

Isolation of the signal objects from close-by tracks and calorimeter clusters is required. The track and calorimeter isolation variables are defined as the sum of momenta or energies of inner detector tracks or calorimeter clusters within an η–ϕ cone around the lepton track,

$$p_{\mathrm{T}}^{\mathrm{cone},30} = \sum_{\substack{\mathrm{Tracks} \\ \Delta R < 0.3}} p_{\mathrm{T}} \qquad \text{and}$$

$$E_{\mathrm{T}}^{\mathrm{cone},30} = \sum_{\substack{\mathrm{CaloClusters} \\ \Delta R < 0.3}} E_{\mathrm{T}},$$

respectively. The isolation requirements are very effective in removing fake leptons produced in jets.

Correction to Lepton Isolation

For the four-lepton analysis, the standard definition of isolation variables as above is

not optimal, especially in the case of boosted decaying particles. If a lepton pair is sufficiently collimated that one of the four final state leptons enters the isolation cone of another ($\Delta R < 0.3$), the isolation for each lepton includes the energy or momentum of its neighbour. As a consequence, both would be regarded as non-isolated and rejected. This is expected to occur frequently for neutralino masses below about 50 GeV (see Section 5.3).

This effect is taken into account in the isolation variables used in the four-lepton search by subtracting the contribution of leptons in the isolation cone that pass the signal requirements apart from the isolation criteria. Figure 6.2 shows the effect of this correction for the example of electron track isolation in 1.1 TeV gluino NLSP pair production with a 10 GeV neutralino. The distribution of the default track isolation variables shows a long tail caused by close-by leptons. After the correction, the tail is mostly removed. For an electron track isolation requirement of 0.16, as applied in the event selection, the isolation efficiency for each electron improves from 35% to more than 80% after the correction. The effect on the event selection efficiency is illustrated in Figure 6.3, which shows the number of signal leptons identified in events with four baseline leptons surviving the overlap removal for the same decay scenario. Using corrected isolation variables enhances the fraction of such events in which all four leptons pass the signal lepton criteria by more than three orders of magnitude. This demonstrates that only the use of corrected isolation variables allows the search to be sensitive to LSP masses below 50 GeV.

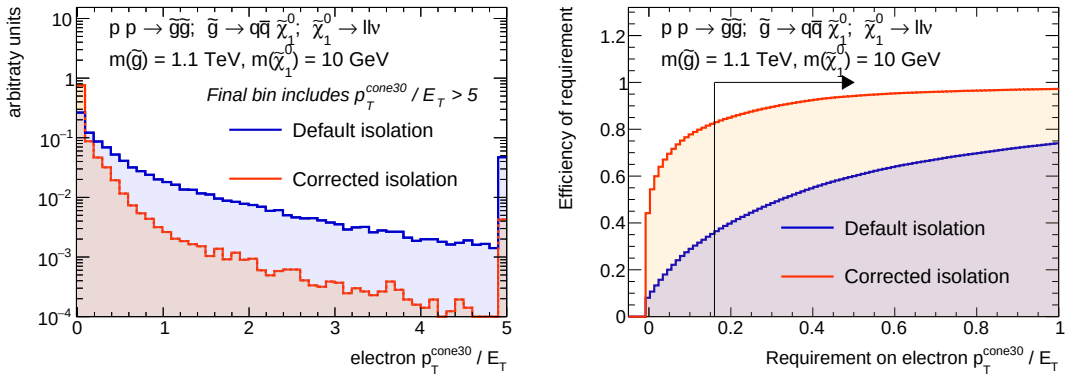

(a) **(b)**

Figure 6.2: Distribution of the electron track isolation variable with (red) and without (blue) correction for nearby leptons (a) and efficiency of the isolation requirements as a function of the cut value (b).

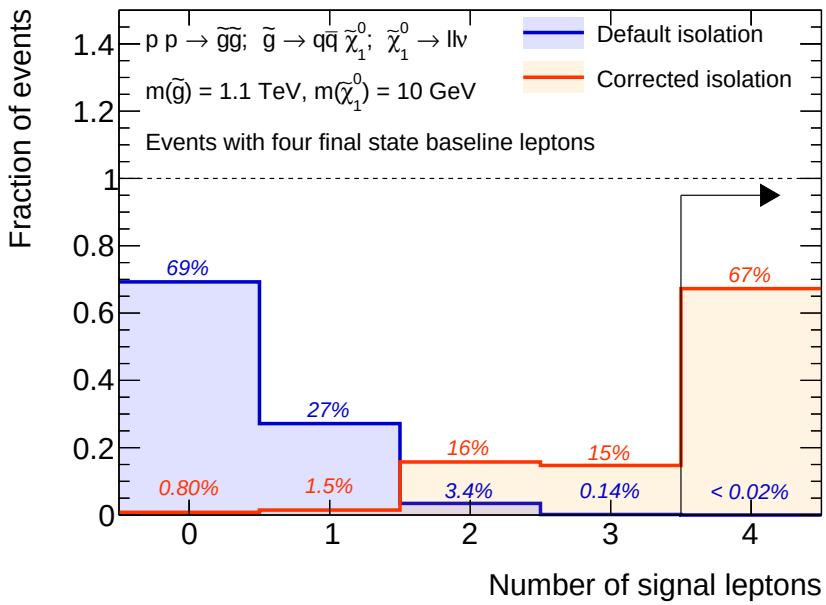

Figure 6.3: Distribution of the number of final state signal leptons using uncorrected (red) and corrected (blue) isolation variables for events with four baseline leptons and a gluino NLSP with $m_{\tilde{g}} = 1.1$ TeV decaying to a neutralino with $m_{\tilde{\chi}_1^0} = 10$ GeV and jets, where the neutralino subsequently decays via the RPV λ_{121} LLE coupling.

6.2.3 Signal Regions

Once the signal leptons and jets have been identified, the effective mass can be computed:

$$m_{\text{eff}} = \sum_{\text{Signal leptons}} p_{\text{T}} + \sum_{\substack{\text{Signal jets} \\ p_{\text{T}}>40 \text{ GeV}}} p_{\text{T}} + E_{\text{T}}^{\text{miss}}. \tag{6.1}$$

All signal regions require at least four signal leptons in the final state, which leads to a major suppression of reducible backgrounds. As τ leptons are reconstructed with a lower efficiency and higher background contamination than the lighter leptons, different signal regions are defined for events with 2, 3 and at least 4 light leptons (e,μ). The irreducible background is not expected to be affected by the requirement of four signal leptons. Therefore, additional criteria are used to suppress this contribution.

Two approaches are used, optimised for different signal topologies.

The first aims at cases where the effective mass is not an efficient discriminant. This

occurs for a low NLSP mass or scenarios with a lack of visible cascade particles. One example are sneutrino NLSPs, which decay into the LSP and produce only neutrinos as cascade particles. In this approach, discrimination against irreducible backgrounds is achieved by requiring a moderate amount of missing transverse energy. Such a signal region is defined for each light lepton multiplicity.

The second approach, complementary to the first, exploits the effective mass, which is especially effective for heavy NLSPs and visible cascade particles. One example is gluino NLSP production where the NLSP masses can reach beyond 1 TeV and the cascade includes several jets. For each light lepton multiplicity, one such signal region is defined, requiring high effective mass or large missing transverse energy.

Common to all signal regions is the veto against Z boson decays into same-flavour, opposite sign (SFOS) lepton pairs. In addition, three-lepton combinations of an SFOS pair and a further lepton as well as four-lepton combinations of two SFOS pairs are vetoed to take into account final state radiation and resonant $Z \to 4\ell$ production via internal conversion [126]. Events containing such signal lepton combinations with an invariant mass within 10 GeV of the Z boson mass (91.2 GeV) [65] are rejected.

The three light lepton multiplicity categories and two irreducible background suppression approaches lead to a total of six signal regions which are summarised in Table 6.9.

Reference [124] takes into account three additional signal regions with inverted Z veto. These target scenarios with conserved R-parity, where an on-shell Z boson is part of the signal signature. They are not relevant when searching for R-parity-violating decays.

Table 6.9: Signal regions for the four-lepton search. All veto Z boson decays ('noZ'). The analysis in Ref. [124] includes further signal regions optimised to detect R-parity-conserving signatures.

Signal region	Light leptons (e, μ)	τ leptons	$E_{\mathrm{T}}^{\mathrm{miss}}$ [GeV]		m_{eff} [GeV]
SR0noZa	≥ 4	≥ 0	> 50		
SR1noZa	3	≥ 1	> 50		
SR2noZa	2	≥ 2	> 75		
SR0noZb	≥ 4	≥ 0	> 75	or	> 600
SR1noZb	3	≥ 1	> 100	or	> 400
SR2noZb	2	≥ 2	> 100	or	> 600

6.3 Signal Expectation

6.3.1 Signal Simulation

Signal simulation grids generated according to the simplified models described in Section 5.3, covering a wide range of the NLSP-LSP mass combinations, are used to optimise the selection criteria and interpret the results. Five NLSP candidates are considered, the gluino, a wino-like chargino, an R- or L-slepton or a sneutrino. In the slepton and sneutrino cases, all flavours are degenerate in mass. The decay width of the bino-like neutralino LSP is fixed to 0.1 GeV, corresponding to a decay length of $\hbar c/\Gamma \approx 2 \cdot 10^{-12}$ mm which is far below the detector resolution and therefore leads to the considered prompt neutralino decay. Four choices for the RPV λ parameter, λ_{121}, λ_{122}, λ_{133} and λ_{233}, are considered in the analysis as discussed before (Section 5.3). Events are generated using the HERWIG++ generator [38, 93]. The number of generated events is determined based on the kinematic considerations discussed in Section 5.3, with the goal of obtaining a Monte Carlo statistical precision on the signal yields of better than 10%. For neutralino masses greater than 50 GeV, typically 5000 events are generated. For lower neutralino masses, up to $3 \cdot 10^5$ events are required to obtain a reliable efficiency estimate.

6.3.2 Signal Yields

The probability for a signal event to be accepted by the selection is determined by two factors, the acceptance and the efficiency.

The acceptance A is defined as the fraction of signal events accepted by an ideal detector, i.e. events with four leptons fulfilling the kinematic requirements applied in the analysis and passing the $E_{\mathrm{T}}^{\mathrm{miss}}$, Z-veto and effective mass cuts.

The efficiency ϵ is the ratio between the number of events N_{SR} actually selected in the signal region after full detector simulation and reconstruction and the number of events which satisfy the kinematic and signal region criteria at generator level. Using the acceptance A, the efficiency takes the form

$$\epsilon = \frac{N_{\mathrm{SR}}}{\sigma L A},$$

with the integrated luminosity L and the production cross-section σ. It includes fi-

nal state object identification and reconstruction efficiencies, energy and momentum resolutions.

Figure 6.4 shows the acceptance and efficiency of the SR0noZb signal region with four light leptons as a function of the chargino NLSP and neutralino LSP mass for the case of a wino-like NLSP and non-zero λ_{121} coupling (see also Section A.2). The acceptance is high in the top right corner of the signal grid, corresponding to high NLSP and neutralino masses. In this parameter space region, the final state leptons are mostly well separated and highly energetic. The acceptance decreases with the neutralino mass (see Section 5.3, Figs. 5.12 and 5.13) since the cascade particles carry away more momentum, leading to reduced final state lepton momenta. In addition, for very small neutralino masses, collimated lepton pairs are rejected by the overlap removal. There is an especially pronounced acceptance drop for LSP masses of 10 GeV. Furthermore, the acceptance increases with the NLSP mass because the effective mass scales with the mass of the initially produced NLSPs. The efficiency, on the other hand, is constant at about 70% across most of the grid. There is only a decrease for very light neutralinos as a consequence of the difficult reconstruction of close-by leptons.

As another extreme case, Figure 6.5 shows the acceptance and efficiency of the SR2noZb signal region with two hadronically decaying τ leptons for the model with a gluino NLSP and a LSP decaying via the λ_{133} coupling (see also Section A.2). For this τ-rich signal region, the acceptance is far lower than for the SR0noZb case, only between 5% and 30%, in spite of the high gluino masses under study which make the effective mass cut highly efficient across the entire grid. One important reason for this low acceptance is the requirement of two light leptons and two hadronic τ decays in the final state. The LSP decay branching ratios in Table 5.2 for a λ_{133} coupling and the 65% hadronic branching fraction of the τ lepton [65] lead to an overall branching fraction of 41% of the neutralino decays into the selected final state with two light leptons and two hadronic τ decays which gives an upper limit on the acceptance. In addition, the minimum transverse momentum requirement for τ leptons is 20 GeVcompared to 10 GeV for the light leptons resulting in a more pronounced acceptance loss with a decreasing neutralino mass than in the case of four light leptons. Also, the signal loss due to lepton collimation in the overlap removal procedure sets in earlier than for light leptons. The efficiency is also far below the one in the four light lepton case due to the rather low τ reconstruction efficiency and overlapping decays at low neutralino masses.

Figure 6.6 shows an intermediate case, SR1noZb with three light leptons and one hadronic τ lepton decay for the same model as in the SR2noZb example (see also

Section A.2). As only approximately 26% of the neutralino decays via the λ_{133} coupling lead to final states with three light leptons and one hadronic τ decay, the acceptance with values between 1% and 15% is lower than in SR2noZb. The kinematic effects are similar to the ones discussed for SR2noZb. The efficiency is slightly higher than for the SR2noZb signal region (about 10–15% compared to 7–12%), as only one hadronic τ decay has to be reconstructed.

The total fraction of the selected signal events over most of the mass plane is 10% to 50% for the SR0noZ regions and λ_{12X} couplings, i.e. final states with only light leptons, while it drops below 10% for small neutralino masses. For the slepton model with additional cascade leptons, the overall signal acceptance and efficiency reaches up to 70%.

For the SR1noZb and SR2noZb signal regions with τ-rich final states due to λ_{X33} couplings, the selection efficiencies are lower, peaking at values of approximately 10% and reaching down below 1% especially for sneutrino and gluino NLSPs, where there are no additional light leptons from the cascade.

The expected signal yield for a process with production cross-section σ (see Table A.2) at integrated luminosity L is given by:

$$N_{\text{Signal}}^{\text{exp.}} = A \cdot \epsilon \cdot \sigma \cdot L. \tag{6.2}$$

Figures 6.7 and 6.8 show the expected signal yields for a wino and a gluino NLSP. For each case, results for a signal region with four light leptons and a λ_{12X} coupling and for a τ-rich signal region assuming a λ_{X33} coupling are shown. The τ-enriched signal regions have a much smaller signal yield as expected, and, therefore, lower NLSP mass reach. For example, in SR2noZb for a gluino NLSP and a λ_{133} coupling, the line of 10 expected events occurs at a gluino mass more than 300 GeV lower than for SR0noZb and λ_{121} coupling.

A severe reduction of the expected yield for very low LSP masses below 50 GeV is also observed, consistent with the behaviour of the acceptance and efficiency. Therefore, the NLSP mass reach of the analysis is reduced for a very light LSP.

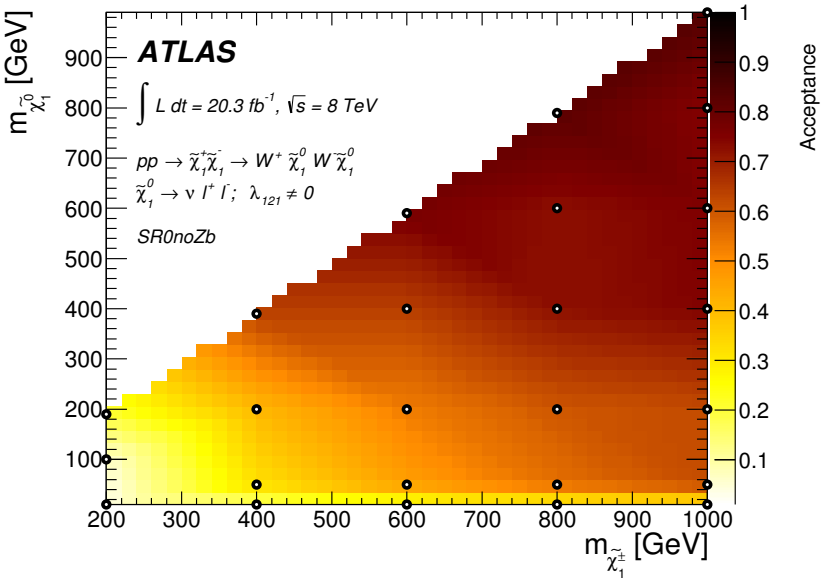

(a)

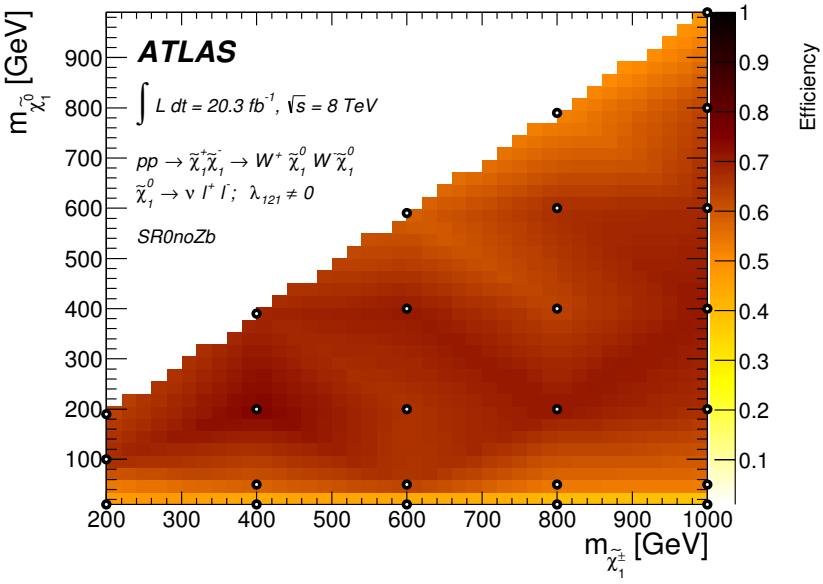

(b)

Figure 6.4: Acceptance (a) and efficiency (b) of the SR0noZb signal region for the simplified model with wino NLSP and active λ_{121} coupling in the wino-neutralino mass plane.

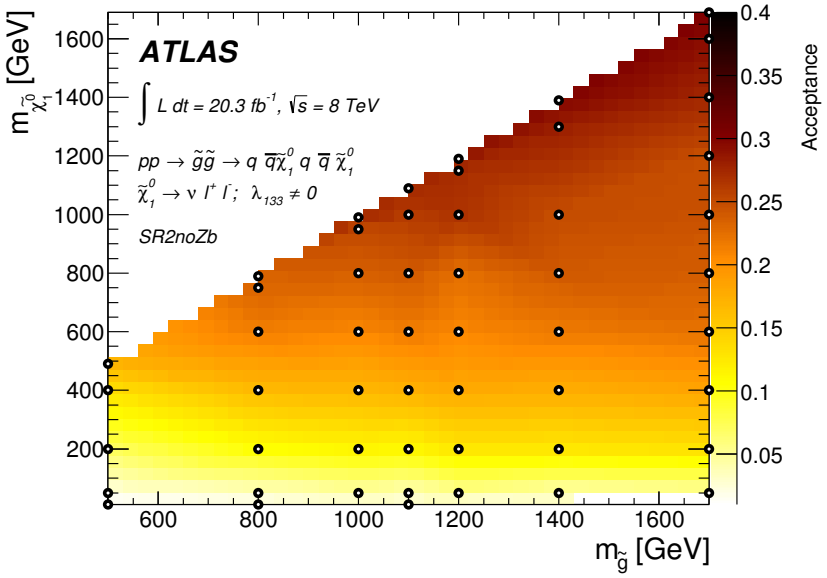

(a)

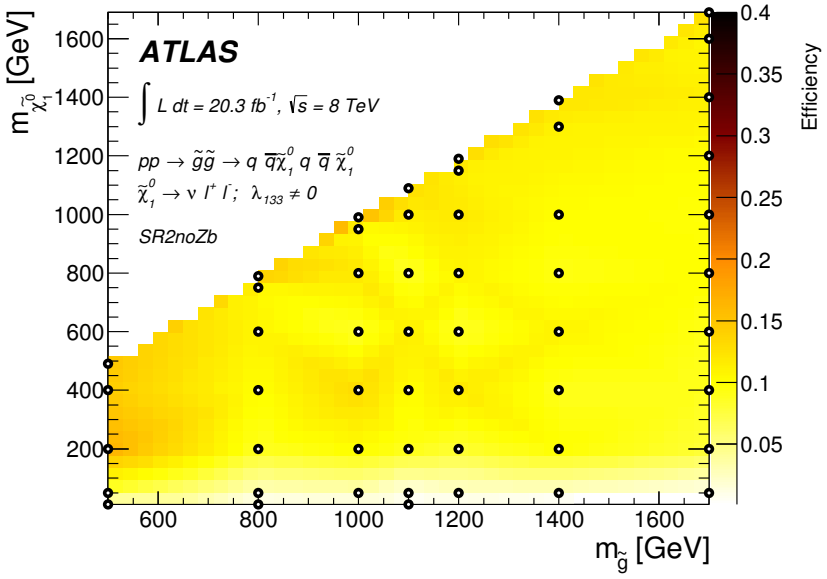

(b)

Figure 6.5: Acceptance (a) and efficiency (b) of the SR2noZb signal region for the simplified model with gluino NLSP and active λ_{133} coupling in the gluino-neutralino mass plane.

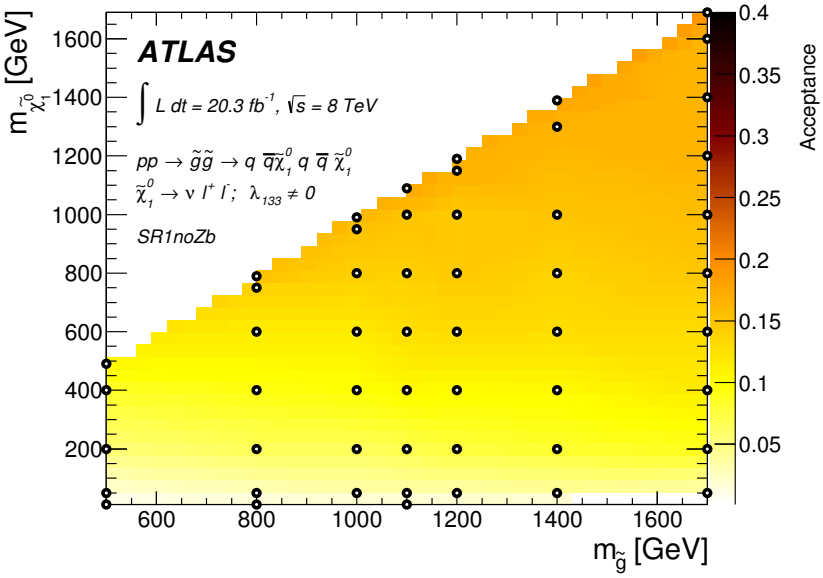

(a)

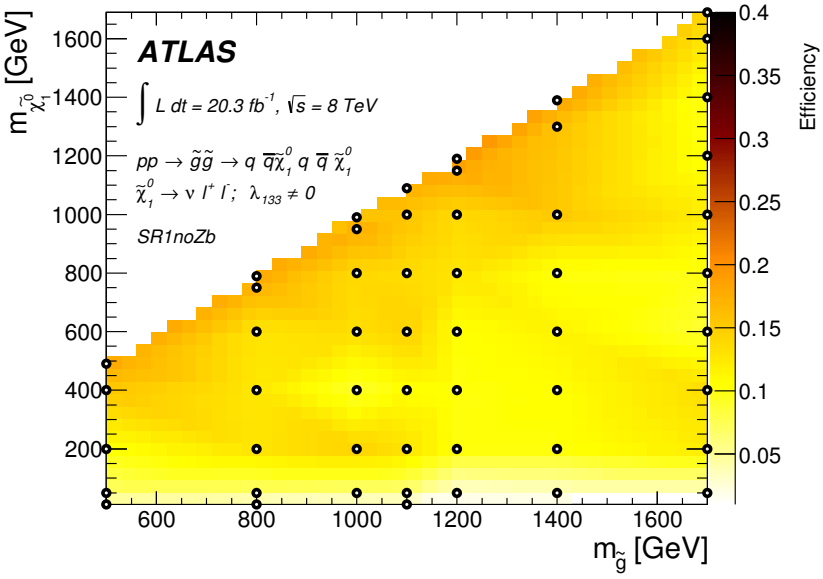

(b)

Figure 6.6: Acceptance (a) and efficiency (b) of the SR1noZb signal region for the simplified model with gluino NLSP and active λ_{133} coupling in the gluino-neutralino mass plane.

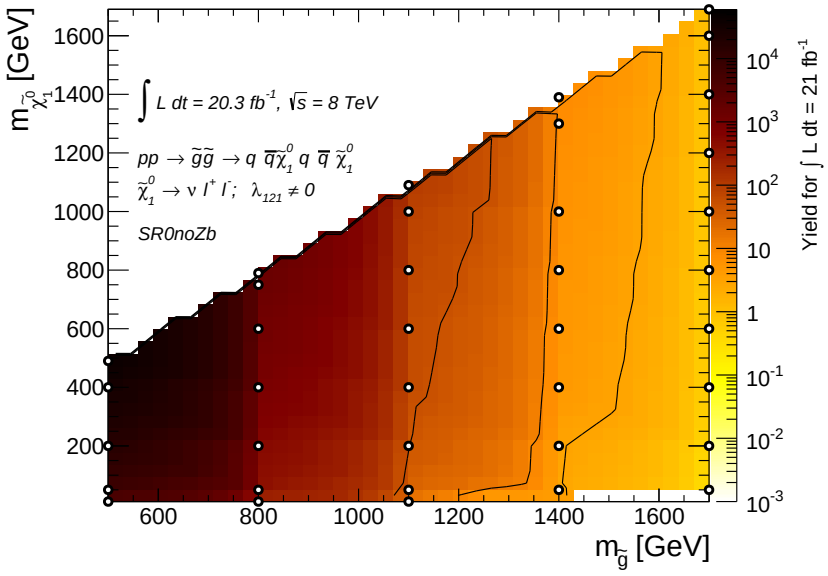

(a)

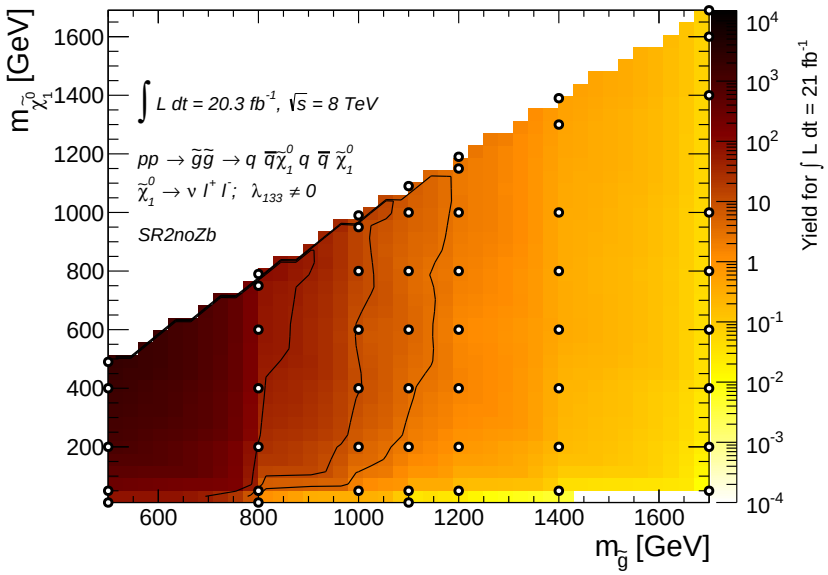

(b)

Figure 6.7: Expected signal yields for a gluino NLSP, in SR0noZb with an active λ_{121} coupling (a) or in SR2noZb for an active λ_{133} coupling (b). The black solid lines indicate contours of 5, 10 and 50 expected signal events (from right to left).

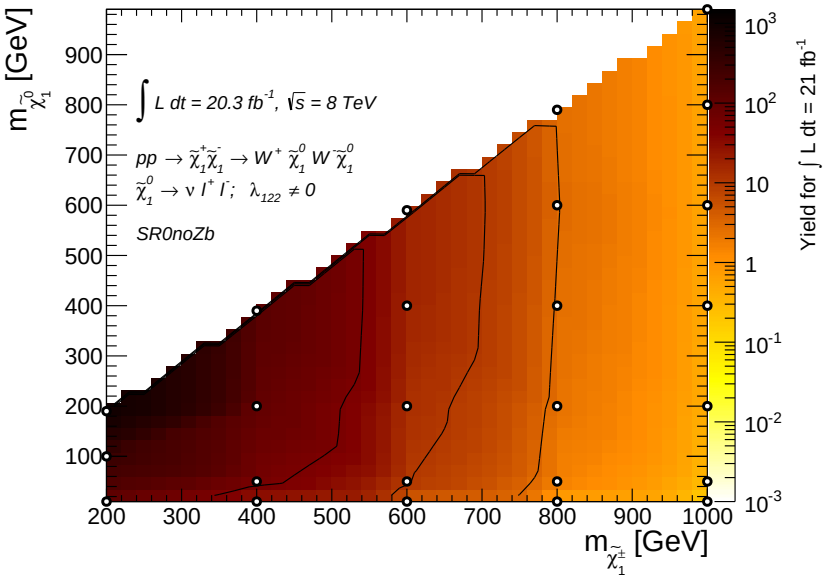

(a)

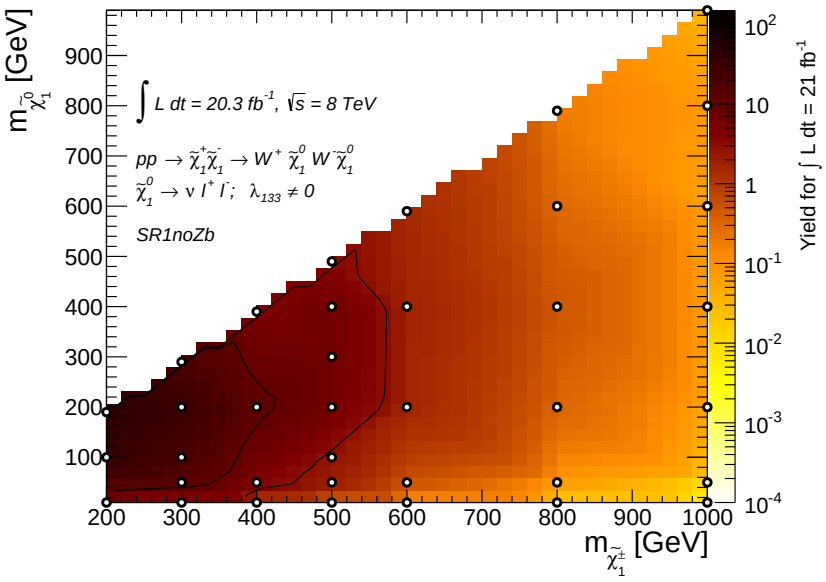

(b)

Figure 6.8: Expected signal yields for a wino NLSP, in SR0noZb with an active λ_{122} coupling (a) or in SR1noZb for an active λ_{133} coupling (b). The black solid lines indicate contours of 5, 10 and 50 expected signal events, from right to left.

6.4 Background Estimation

To estimate the remaining background of Standard Model processes in the signal regions, different methods are applied for the irreducible and for the reducible contributions, Monte Carlo simulation and a data-driven approach, respectively.

6.4.1 Irreducible Backgrounds

Background Processes

Irreducible backgrounds are estimated by means of Monte Carlo simulation. Figure 6.9 shows some of the dominant processes, all of which are rare. The four signal leptons in the final state are from decays of heavy particles produced in the hard interaction, which is reliably described by the Monte Carlo generators (see Table A.1).

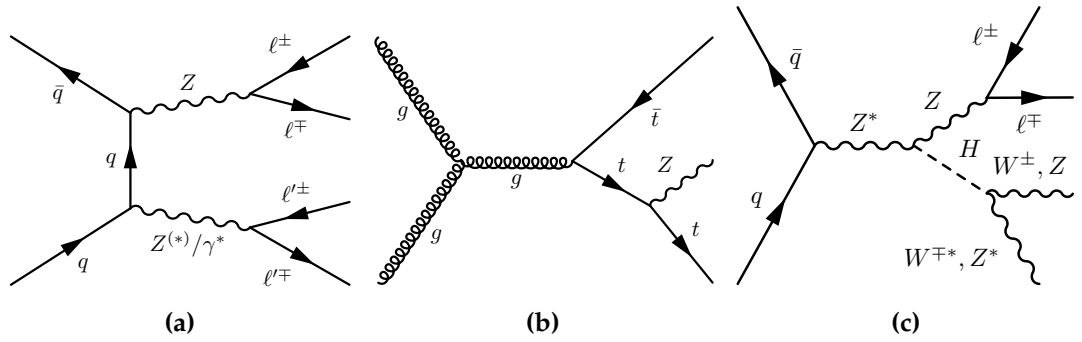

Figure 6.9: Examples for irreducible background processes with ZZ diboson production (a), $t\bar{t} + Z$ production (b) and $ZH \to ZWW$, $ZH \to ZZZ$ (c) with leptonic gauge boson decays.

The background in Figure 6.9 with the highest cross-section is $ZZ \to 4\ell$ production. This process is generated to next-to-leading order precision using the POWHEG [97,98] generator, interfaced to PYTHIA 8 [91] for parton shower simulation. The product of production cross-section and leptonic Z decay branching ratios is about 0.8 pb (see Table A.1). However, no missing transverse momentum is expected from the process and there is only small effective mass compared to the signal processes, since apart from the four leptons there are no other final state particles. Therefore, this background is efficiently suppressed by the $E_{\mathrm{T}}^{\mathrm{miss}}$ and m_{eff} cuts, as well as the Z veto which rejects decays with on-shell Z bosons. In addition to diboson events, triple gauge boson production (ZWW, ZZZ) has to be considered as irreducible background. The MadGraph [95,96]

generator is used to generate these processes at leading order perturbation theory, using again PYTHIA 8 for parton showering. Like the signal, these processes lead to final states with four charged leptons and additional neutrinos from leptonic W boson decays or jets from W or Z boson decays. While the product of production cross-section and decay branching ratios for these processes is very small, on the order of 1 fb (see Table A.1), the similarity of the signature to the signal enhances the probability that they pass the signal region requirements.

The third important irreducible background is the production of semileptonically decaying top quark pairs in association with a leptonically decaying Z boson, leading to a final state with four charged leptons, two neutrinos and two b-jets. ALPGEN [94] interfaced to HERWIG [38, 93] is used to generate this process. While the production cross-section times branching ratio for the decays into the final state is only about 3 fb (see Table A.1) for this process, it passes the signal region criteria with significantly higher probability than $ZZ^{(*)}/Z\gamma^*$events, for the same reasons as the triple gauge boson processes.

Finally, also Standard Model Higgs boson decays with four final state leptons are considered for $m_H = 125$ GeV, namely $H \to ZZ^*$ in all Higgs production modes, gluon fusion, vector boson fusion, Higgs radiation of W or Z bosons and associated production with top quark pairs, and $H \to WW^*$ and $H \to \tau\tau$ in the $t\bar{t}H$ and ZH production channels. The production processes in association with gauge bosons or top quarks have smaller cross-sections (see Table A.1), but the probability to be accepted by the signal region criteria is higher because of additional missing transverse energy and jets. Gluon fusion and vector boson fusion are generated using POWHEG interfaced with PYTHIA 6 [90], while all other processes are generated by PYTHIA 6.

Efficiency of Sgnal Region Requirements

Table 6.10 summarises the efficiencies of the Z veto and of the full signal region criteria for the four main irreducible backgrounds.

Due to the presence of one or two on-shell Z bosons in the final state, the $ZZ^{(*)}/Z\gamma^*$ contribution is strongly suppressed by the Z veto. Higgs boson decays like $ZH \to WW^*/\tau\tau$ pass the Z veto with higher probability as at most one final state Z boson can be on shell. In the ZWW and $t\bar{t} + Z$ processes, the single Z boson is either on-shell or off-shell, leading to the highest probability of passing the Z veto.

In the case with fewer than four light leptons, the rejection power of the Z veto decreases since at most one on-shell Z decays to two light leptons and processes without on-shell

Table 6.10: Efficiencies of the signal region cuts of the four-lepton analysis after the four-signal-lepton criterion for the irreducible backgrounds. The given errors are due to Monte Carlo statistics. The efficiency of the Z veto is shown separately.

Signal region requirement	$ZZ^{(*)}/Z\gamma^*$	$t\bar{t}+Z$	Tri-boson	Higgs
4 light leptons				
Z Veto	$(2.16 \pm 0.04)\%$	$(12.9 \pm 1.0)\%$	$(7.9 \pm 0.4)\%$	$(6.5 \pm 0.4)\%$
SR0noZa	$(0.15 \pm 0.01)\%$	$(10.5 \pm 0.9)\%$	$(4.4 \pm 0.3)\%$	$(3.8 \pm 0.3)\%$
SR0noZb	$(0.12 \pm 0.01)\%$	$(8.8 \pm 0.8)\%$	$(4.1 \pm 0.3)\%$	$(3.1 \pm 0.3)\%$
3 light leptons, $\geq 1\tau$				
Z Veto	$(15.4 \pm 0.3)\%$	$(22.4 \pm 1.6)\%$	$(26.7 \pm 1.3)\%$	$(40.0 \pm 1.2)\%$
SR1noZa	$(3.0 \pm 0.2)\%$	$(16.3 \pm 1.4)\%$	$(15.4 \pm 1.1)\%$	$(22.0 \pm 1.2)\%$
SR1noZb	$(1.5 \pm 0.1)\%$	$(17.4 \pm 1.4)\%$	$(10.3 \pm 0.9)\%$	$(17.2 \pm 1.2)\%$
2 light leptons, $\geq 2\tau$				
Z Veto	$(17.0 \pm 0.4)\%$	$(55.4 \pm 3.9)\%$	$(47.9 \pm 2.5)\%$	$(36.9 \pm 1.2)\%$
SR2noZa	$(1.3 \pm 0.1)\%$	$(22.9 \pm 3.3)\%$	$(16.6 \pm 1.9)\%$	$(13.4 \pm 1.1)\%$
SR2noZb	$(1.0 \pm 0.1)\%$	$(20.6 \pm 3.2)\%$	$(12.8 \pm 1.7)\%$	$(9.9 \pm 1.0)\%$

$Z \to ee/\mu\mu$ decays are also possible.

The lack of additional neutrinos and jets in the $ZZ^{(*)}/Z\gamma^*$process in combination with the suppression by the Z veto leads to a very small efficiency for the $ZZ \to 4\ell$ background. The other processes are accepted by the four light-lepton signal regions with higher probabilities between 3 and 11%.

As a consequence, the $ZZ^{(*)}/Z\gamma^*$process does not dominate the irreducible background, in spite of a relatively high cross-section (see Table 6.12).

6.4.2 Reducible Backgrounds

The reducible background consists of processes with fewer than four prompt leptons in the final state and additional fake leptons passing the signal lepton selection criteria defined in Section 6.2.2. As these criteria have been optimised to reject fake leptons, this happens with a low probability which strongly depends on the details of the events and their reconstruction in the detector. Also, simulation of these backgrounds with high statistical precision would require a very large number of simulated events.

For these reasons, backgrounds with fake leptons are estimated by reweighting collision data events in two *control regions* CR1 and CR2 defined for each of the six signal regions,

which apply the same cuts on effective mass, missing transverse energy and the same Z veto as the signal regions, but require the presence of only three or two signal leptons, and one or two loose leptons, respectively (see Table 6.11).

Table 6.11: Lepton multiplicity requirements of the signal regions and the control regions used to estimate the reducible background.

Region	Signal leptons	Loose leptons	Weight
Signal Region (SR)	≥ 4	≥ 0	
CR1	3	≥ 1	W(CR1)
CR2	2	≥ 2	W(CR2)

The probability of a fake lepton to pass the signal lepton criteria is called the *fake rate* f, which depends on the control region, the lepton flavour and track multiplicity (e, μ, 1-track-τ, 3-track-τ), the transverse momentum p_{T} and, for electrons and τ leptons, on the pseudorapidity η. The *rejection rate* $\bar{f} = 1 - f$ describes the probability that a fake lepton is properly rejected by the signal criteria and therefore categorised as a loose lepton.

The *signal lepton efficiency* ϵ is the probability of a prompt lepton to pass the signal lepton criteria, and the *signal lepton inefficiency* $\bar{\epsilon} = 1 - \epsilon$ the probability that a prompt lepton fails to satisfy the signal lepton cuts and is classified as a loose lepton. The rejection rate $\bar{f}$ and signal lepton efficiency ϵ are assumed to be large compared to the fake rate and signal inefficiencies, respectively.

For a reducible background event with three prompt leptons (P) and one fake lepton (F), the probability P^{3P1F} of passing the signal region (SR) requirement of four signal leptons is

$$P^{\mathrm{3P1F}}(\mathrm{SR}) = \epsilon_{P1}\epsilon_{P2}\epsilon_{P3}f_{F1},$$

where ϵ_{Pi} ($i = 1,2,3$) and f_{F1} are the signal lepton efficiencies for the three prompt leptons and the appropriate fake rate for the fake lepton, respectively. For the same event, the probability of obtaining three signal leptons and one loose lepton, leading to an observed event in the CR1 control region, is

$$P^{\mathrm{3P1F}}(\mathrm{CR1}) = \epsilon_{P1}\epsilon_{P2}\epsilon_{P3}\bar{f}_{F1} + O(\bar{\epsilon}\cdot f).$$

Thus, for a process with three prompt leptons P_1, P_2 and P_3 and one fake lepton F_1, the

rate of events in one of the signal regions is related via the *fake ratio*

$$R_{F1} \equiv \frac{P^{3P1F}(\text{SR})}{P^{3P1F}(\text{CR1})} \approx \frac{f_{F1}}{1 - f_{F1}} \tag{6.3}$$

to the rate of events in the respective CR1 region with the same lepton flavours and kinematics.

For events with two prompt leptons P_1 and P_2 and two fake leptons F_1 and F_2, the probabilities P^{2P2F} of observing an event in a signal region with four signal leptons, the respective CR1 control region with three signal leptons or the CR2 control region with two signal leptons (see Table 6.11) are given by

$$\begin{aligned} P^{2P2F}(\text{SR}) &= \epsilon_{P1}\epsilon_{P2} f_{F1} f_{F2}, \\ P^{2P2F}(\text{CR1}) &= \epsilon_{P1}\epsilon_{P2}\left(\bar{f}_{F1} f_{F2} + f_{F1}\bar{f}_{F2}\right) + O(\bar{\epsilon}\cdot f^2) \qquad \text{and} \\ P^{2P2F}(\text{CR2}) &= \epsilon_{P1}\epsilon_{P2}\bar{f}_{F1}\bar{f}_{F2} + O(\bar{\epsilon}\cdot f), \end{aligned}$$

respectively. Accordingly, the rate of events with two prompt leptons in the CR1 control region is related to the rate in the CR2 region by the factor

$$\frac{P^{2P2F}(\text{CR1})}{P^{2P2F}(\text{CR2})} \approx \frac{f_{F1}}{1 - f_{F1}} + \frac{f_{F2}}{1 - f_{F2}} = R_{F1} + R_{F2}, \tag{6.4}$$

and the rate of signal region (SR) events from this source scales with the ratio

$$\frac{P^{2P2F}(\text{SR})}{P^{2P2F}(\text{CR2})} \approx \frac{f_{F1}}{1 - f_{F1}} \cdot \frac{f_{F2}}{1 - f_{F2}} = R_{F1} \cdot R_{F2} \tag{6.5}$$

compared to the rate in the CR2 region.

Hence, the reducible background in each of the signal regions can be estimated by weighting collision data events observed in the respective CR1 and CR2 control regions using the fake ratios. Events in the CR1 region are weighted by the fake ratio R of the loose lepton (see Eq. (6.3)),

$$W(\text{CR1}) = R. \tag{6.6}$$

Events with more than one loose lepton (meaning more than four total leptons) are counted several times, once for each loose lepton. This correctly predicts the signal region contribution from processes with three prompt leptons.

For events from processes with only two prompt leptons and at least two fake leptons

F_1 and F_2, applying this weight in the CR1 region is, according to Eq. (6.4), equivalent to scaling the rate of events in the CR2 region with

$$\frac{P^{2\mathrm{P2F}}(\mathrm{CR1})}{P^{2\mathrm{P2F}}(\mathrm{CR2})} \cdot W(\mathrm{CR1}) = 2R_{F1} \cdot R_{F2},$$

which is twice the ratio of signal region and CR2 rates determined for these processes in Eq. (6.5). This is corrected by assigning a negative weight

$$W(\mathrm{CR2}) = -R_1 R_2, \tag{6.7}$$

compromised of the fake ratios R_1 and R_2 of the two loose leptons to events in the CR2 control region. Events with more than two loose leptons are again counted several times, once for every pair of loose leptons.

As the fake rates are small, especially for electrons and muons, the estimate neglects events with more than two fake leptons.

Events in the control regions can also come from the irreducible background or from a signal, if prompt leptons fail the signal lepton cuts. The estimate is corrected for this contamination by applying the same weighting technique on simulated control region events in the Monte Carlo simulation of the signal (Section 6.3) and the irreducible background (see Section 6.4.1) and subtracting the resulting yields from the result obtained using the data (see Figure 6.10).

Fake leptons can have several origins – light and heavy flavour jets and conversions (for electrons) are considered, as well as gluon jets for τ leptons. These may occur in different physics processes – $Z \to \ell\ell$ production and $t\bar{t}$ production with two prompt leptons as well as WZ and $t\bar{t}W$ production with three prompt leptons are the dominant contributors. To account for this, the fake ratios R^{ℓ}_{XR} for each lepton flavour $\ell = e, \mu, \tau$ in a given control region XR are determined as the average of the fake ratios R^{ℓ}_{op} for a specific fake lepton origin and physics process obtained in Monte Carlo simulation,

$$R^{\ell}_{XR} = \sum_{o}^{\substack{\text{Fake lepton}\\ \text{types}}} \sum_{p}^{\substack{\text{Physics}\\ \text{processes}}} w^{XR}_{op} R^{\ell}_{op} s^{\ell}_{o}, \tag{6.8}$$

where the weight w^{XR}_{op} is the fraction of fake leptons in the given control region XR with origin o from the physics process p. Inaccuracies in the detector simulation are corrected by a scale factor s^{ℓ}_{o}, obtained by comparing data and simulation in an auxiliary

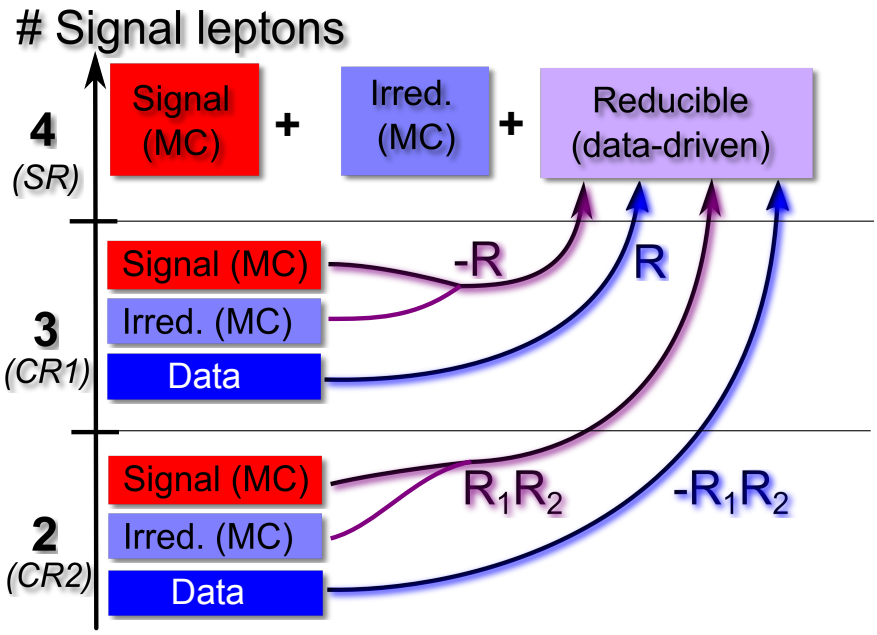

Figure 6.10: Illustration of the weighting technique used to estimate the reducible background in the four-lepton search.

measurement. W boson production in association with jet activity is used to obtain the correction for fakes from light flavour jets, $b\bar{b}$ pair production for heavy flavour jets and $Z/\gamma^* \to \mu\mu$ for conversion electrons from final state radiation.

The resulting average fake ratios R^{ℓ}_{XR} are a function of the transverse momentum and, for electrons and τ leptons, of the pseudorapidity. Typical values range between 1% and 15%.

6.4.3 Background Prediction in the Signal Regions

Table 6.12 summarises the estimated number of background events in the signal regions. Given the challenging nature of τ lepton reconstruction, the reducible background from fake τ leptons plays a major role in the SR1noZ and SR2noZ signal regions, while the SR0noZ regions with four light leptons are dominated by irreducible background, with a negligible reducible contribution. A high signal region acceptance makes $t\bar{t} + Z$ the most important individual process, in spite of a low production cross-section compared to $ZZ^{(*)}/Z\gamma^*$. The background estimation is tested using validation regions enriched in backgrounds (see A.4).

Table 6.12: Number of predicted background events in the signal regions of the four-lepton analysis.

	$ZZ^{(*)}/Z\gamma^*$	$t\bar{t}+Z$	VVV	Higgs	Reducible	**Exp. SM**
SR0noZa	0.29 ± 0.08	0.8 ± 0.4	0.19 ± 0.09	0.27 ± 0.23	$0.006^{+0.164}_{-0.006}$	$\mathbf{1.6 \pm 0.5}$
SR0noZb	0.19 ± 0.05	0.68 ± 0.34	0.18 ± 0.07	0.22 ± 0.20	$0.06^{+0.15}_{-0.06}$	$\mathbf{1.4 \pm 0.4}$
SR1noZa	0.52 ± 0.07	0.21 ± 0.08	0.14 ± 0.07	0.40 ± 0.33	$3.3^{+1.3}_{-1.1}$	$\mathbf{4.6^{+1.3}_{-1.2}}$
SR1noZb	$0.219^{+0.036}_{-0.035}$	0.17 ± 0.07	0.09 ± 0.04	0.30 ± 0.26	$2.1^{+1.0}_{-0.9}$	$\mathbf{2.9^{+1.0}_{-0.9}}$
SR2noZa	0.15 ± 0.04	0.13 ± 0.10	0.051 ± 0.024	0.20 ± 0.16	3.4 ± 1.2	$\mathbf{4.0^{+1.2}_{-1.3}}$
SR2noZb	$0.112^{+0.025}_{-0.024}$	$0.27^{+0.28}_{-0.27}$	0.040 ± 0.018	0.13 ± 0.12	$2.5^{+0.9}_{-1.0}$	$\mathbf{3.0 \pm 1.0}$

6.5 Systematic Uncertainties

6.5.1 Signal Prediction

A major source of systematic uncertainty in the expected signal yield is the theoretical prediction of the production cross-section, which is computed at next-to-leading order precision in the strong coupling constant and, for strong production, includes next-to-leading logarithmic accuracy in the resummation of soft gluon emission [104–107]. For electroweak processes, the uncertainty in this prediction ranges between 5% and 10%, increasing with the NLSP mass. If the NLSP is produced via the strong interaction, as in the gluino model, this uncertainty assumes values between 15% and 60%, again growing with the NLSP mass.

For the τ-rich signal regions SR1noZa/b and SR2noZa/b, the Monte Carlo statistical precision of the acceptance and efficiency determination is severely limited with the relative error in the signal yield reaching up to 25%. For the SR0noZa/b regions, which show higher acceptances and efficiencies, this systematic error is below 5% (see Section A.3).

While these two systematic uncertainties dominate, additional smaller effects have also been considered:

The acceptance and efficiency is affected by theoretical uncertainties in the description of the kinematics of the processes due to the modelling of initial and final state radiation as well as the parton density functions and the choice of the renormalisation and factorisation scales. These errors are small compared to the cross-section uncertainty.

Typical values are between 2% and 5%, reaching up to 10% when the neutralino mass approaches the NLSP mass (see Section A.3).

Finally, there are systematic errors due to detector effects, the energy calibration and resolution for electrons, muons, τ leptons and jets, which affect the efficiency of the lepton selection requirements and also the missing transverse energy and the effective mass determination. The simulated reconstruction and identification efficiencies of muons, electrons and τ leptons, as well as the trigger efficiency are a further source of uncertainty. Together, these contributions contribute less than 10% to the total systematic error (see Section A.3).

6.5.2 Background Estimation

As the irreducible background component is determined using Monte Carlo simulation, the systematic error of the prediction is dominated by the uncertainties in the event generation with two main contributions. First, the background normalisation depends on the total cross-section calculation with uncertainties dominantly from the strong interaction. In addition, predictions of the distributions of discriminating variables are important for the background estimate in the signal region. For $t\bar{t} + Z$ production, the theoretical uncertainty on the production cross-section is on the order of 30% [127]. The electroweak $ZZ^{(*)}/Z\gamma^*$diboson production cross-section is predicted with higher precision of about 5% [128], while the small triple gauge boson cross-sections have a high theoretical uncertainty of 50%. For Higgs boson production, the uncertainty on the production cross-section ranges between about 3% for the vector boson fusion process and 15% for gluon fusion [129].

For the $t\bar{t} + Z$ and $ZZ^{(*)}/Z\gamma^*$ processes, uncertainties in the differential cross-sections are studied by comparing different event generators. A comparison of the $t\bar{t} + Z$ prediction with the MadGraph [95,96] generator yields a $30-40$% uncertainty depending on the signal region. For $ZZ^{(*)}/Z\gamma^*$ production, a comparison with the generator aMC@NLO [99] yields an uncertainty between 5 and 20%, which is smaller as the $ZZ^{(*)}/Z\gamma^*$ process in both cases is computed to next-to-leading order in perturbation theory, while $t\bar{t} + Z$ is only known at leading order. Uncertainties on the signal region efficiency for Higgs boson production due to prediction of differential distributions are conservatively estimated to 20% for the electroweak WH/ZH and vector boson fusion processes, and 100% for gluon fusion process and associated production with top quark pairs by the strong interaction.

A further systematic uncertainty on the irreducible background prediction is the Monte Carlo statistical error in the prediction of the selection efficiency, in particular when the background rejection is strong. Especially for τ rich signal regions, the statistical error on the background prediction is up to 30%.

Uncertainties in the simulation of the detector response and the reconstruction, as discussed for the signal yields as well as in Section A.3, together contribute a systematic error in the background estimate of less than 10%.

The main uncertainties on the reducible background consist of limited statistics in the control regions and uncertainties on the average fake ratios. The total impact is up to 100% of the estimate for the case of four light leptons, and up to 50% for signal regions with at least one τ lepton.

6.6 Statistical Methods

For the statistical evaluation of the potential presence or the absence of a signal excess above the estimated background in the signal regions a frequentist profile likelihood ratio technique [130] is used. The predicted number of events n_{pred} in a signal region consists of the Standard Model background estimation of b events and an additional signal contribution of $\mu \cdot s$ events,

$$n_{\text{pred}}(\mu) = b + \mu \cdot s, \tag{6.9}$$

with the signal strength μ as free parameter scaling the nominal number of signal events predicted by the SUSY signal model. The Standard Model hypothesis of no signal corresponds to a signal strength $\mu = 0$, while $\mu = 1$ corresponds to the nominal signal hypothesis.

It is important to note that in the four-lepton analysis the reducible background estimate receives a correction for all contributions with four prompt leptons including a potential signal contribution. For this reason, the background yield $b = b(\mu)$ in signal regions with a non-negligible reducible background depends on the signal strength :

$$b(\mu) = \underbrace{b_{\text{irred}} + b_{\text{red}}^{\text{no signal}}}_{\text{Table 6.12}} - \mu \cdot b_{\text{red}}^{\text{signal}}, \tag{6.10}$$

where b_{irred} is the estimated irreducible background from Monte Carlo simulation

and $b_{\text{red}}^{\text{no signal}}$ the estimated reducible background as listed in Table 6.12. $b_{\text{red}}^{\text{signal}}$ is the result of obtaining the weighting technique described in Section 6.4.2 to the predicted signal events in the control regions. This is relevant for the SR1noZ and SR2noZ signal regions with one or two hadronically decaying τ leptons. The resulting variation of the background yield with the signal strength is however within 1σ of the background estimate. For the SR0noZ signal regions, the reducible background is negligible and set to zero with an uncertainty corresponding to the value estimated for zero signal.

Systematic uncertainties affecting the signal and background predictions are incorporated into the likelihood function as nuisance parameters $\theta = (\theta_1, \theta_2, \ldots)$ assumed to follow a normal distribution with width one and mean zero. Non-zero values of the nuisance parameters cause variations of the signal or background yields $x = s, b$ within the systematic uncertainties σ_i^{sys} using a linear approximation:

$$x(\theta) = x_{\text{nominal}} \cdot \prod_i \left(1 + \theta_i \cdot \sigma_i^{\text{sys}}\right) \qquad (x = s, b).$$

Applying this parametrisation, the likelihood function of observing n_{obs} events in a single signal region is given by

$$f_{\text{single}}\left(n_{\text{obs}}|\mu,\theta\right) = \mathcal{P}\left(n_{\text{obs}}|\lambda = b(\mu,\theta) + \mu \cdot s(\theta)\right) \cdot \prod_i \mathcal{G}\left(\theta_i|\alpha = 0, \sigma = 1\right), \tag{6.11}$$

where

$$\mathcal{P}\left(n|\lambda\right) = \frac{\lambda^n}{n!}\exp(-\lambda)$$

is the Poisson distribution with mean value λ and

$$\mathcal{G}\left(\theta|\alpha,\sigma\right) = \frac{1}{\sqrt{2\pi\sigma^2}}\exp\left[-\frac{1}{2}\left(\frac{\theta-\alpha}{\sigma}\right)^2\right]$$

is the normal distribution with mean α and width σ.

Several signal regions with yields $n_{\text{obs}}^k = (n_{\text{obs}}^1, n_{\text{obs}}^2, \ldots)$ and predicted signal and background yields $s_k(\theta)$, $b_k(\mu,\theta)$ are combined in a product of likelihoods with the same signal strength parameter μ:

$$f_{\text{comb}}\left(\mathbf{n}_{\text{obs}}|\mu,\theta\right) = \prod_k \mathcal{P}\left(n_{\text{obs}}^k|\lambda = b_k(\mu,\theta) + \mu \cdot s_k(\theta)\right) \cdot \prod_i \mathcal{G}\left(\theta_i|\alpha = 0, \sigma = 1\right). \tag{6.12}$$

When combining signal regions, the nuisance parameters representing instrumental ef-

fects and the theoretical description of the processes are common to all signal regions and are only included once in the likelihood of Eq. (6.12), while the Monte Carlo statistical uncertainties enter with an independent nuisance parameter for each signal region.

In the four-lepton analysis, the event yields in the two signal regions for each light lepton multiplicity SRXnoZa and -noZb ($X = 0, 1, 2$) are not statistically independent, as events can pass the selection criteria for both regions noZa and noZb simultaneously. Therefore, only one of the two signal regions noZa or noZb is included in the likelihood for each model, one SR0, one SR1 and one SR2 region. The choice between the regions is made separately for each mass point based on the expected sensitivity.

To obtain a test statistic for hypothesis testing, a profile likelihood ratio is defined using the likelihoods in Eq. (6.11) or (6.12):

$$\lambda_\mu = \begin{cases} \dfrac{f\left(\mathbf{n}_{\text{obs}}|\mu, \hat{\hat{\theta}}(\mu)\right)}{f\left(\mathbf{n}_{\text{obs}}|\hat{\mu}, \hat{\theta}\right)}, & \text{for } \hat{\mu} \geq 0 \\ \dfrac{f\left(\mathbf{n}_{\text{obs}}|\mu, \hat{\hat{\theta}}(\mu)\right)}{f\left(\mathbf{n}_{\text{obs}}|0, \hat{\hat{\theta}}(\mathbf{0})\right)}, & \text{for } \hat{\mu} < 0 \end{cases} , \tag{6.13}$$

where $\hat{\theta}$ and $\hat{\mu}$ are the unconditional maximum likelihood estimators for the nuisance parameters and the signal strength. This means that for positive $\hat{\mu}$, the denominator is the global maximum of the likelihood function. $\hat{\hat{\theta}}(\mu)$ is the conditional maximum likelihood estimator for the nuisance parameters if the signal strength is fixed to the value μ. By construction, λ_μ is always less or equal to 1. The signal strength is truncated at zero, as no negative signals (e.g. due to destructive interference) are expected in the SUSY models under investigation.

From this likelihood ratio, a test statistic q is derived. When testing the Standard Model (i.e. background only, $\mu \equiv 0$) hypothesis in order to search for a positive signal, it is defined as

$$q_0 = \begin{cases} -2 \ln \lambda_0, & \text{for } \hat{\mu} \geq 0 \\ 0, & \text{for } \hat{\mu} < 0 \end{cases} . \tag{6.14}$$

As negative signals are not considered in this analysis, the cut off of negative $\hat{\mu}$ ensures that a fluctuation of the background contribution in the data to lower values is not misinterpreted as a signal. Since the denominator of the likelihood ratio λ_μ is the global maximum of the likelihood function for positive $\hat{\mu}$, this test statistic is positive definite, and small values indicate a good compatibility of the observation with the

background-only hypothesis.

When testing a signal hypothesis $\mu \geq 0$ in order to exclude a signal (signal plus background hypothesis, $\mu \geq 0$), the test statistic is defined by,

$$q_\mu = \begin{cases} -2 \ln \lambda_\mu, & \text{for } \hat{\mu} \leq \mu \\ 0, & \text{for } \hat{\mu} > \mu \end{cases} . \tag{6.15}$$

A cut off for $\hat{\mu}$ above the hypothesised signal strength is applied to ensure a stronger than predicted signal contribution in the data does not disfavour the signal hypothesis. Similar to q_0, this test statistic is positive definite and small values of q_μ indicate good compatibility of the observation with the signal hypothesis.

The probability density function $f(q)$ of the test statistic is obtained by so-called toy Monte Carlo pseudo-experiments where the nuisance parameters are fixed to their conditional maximum likelihood estimates from data for a given signal strength parameter assumption. Random event yields n_{obs} are generated according to the likelihood function $f\left(\mathbf{n}_{\text{obs}}|\mu,\theta\right)$ defined in this way. The resulting distribution approximates the probability density function $p(q)$ for sufficient toy Monte Carlo statistics.

For testing the background-only hypothesis when searching for a signal and calculating its significance, the p-value p_0 of the test statistic q_0

$$p_0 = \int_{q_0^{\text{obs}}}^{\infty} f(q_0) dq_0, \tag{6.16}$$

where q_0^{obs} is the measured value of q_0, describes the probability of obtaining the observed event yield n_{obs} in the signal region in the absence of a signal. Large p-values indicate good agreement of the data with the background hypothesis, while small values signal an excess of events above the background prediction.

The significance Z_0 of the p-value p_0 is defined as the one-sided quantile of a normal distribution of unit width corresponding to p_0 (see Figure 6.11). A p-value of 0.05 corresponds a significance of $Z_0 = 1.645$ standard deviations. For claiming a signal, the background hypothesis is commonly required to be excluded with a probability $p_0 = 2.9 \cdot 10^{-7}$, corresponding to a signal significance of $Z_0 = 5$ standard deviations.

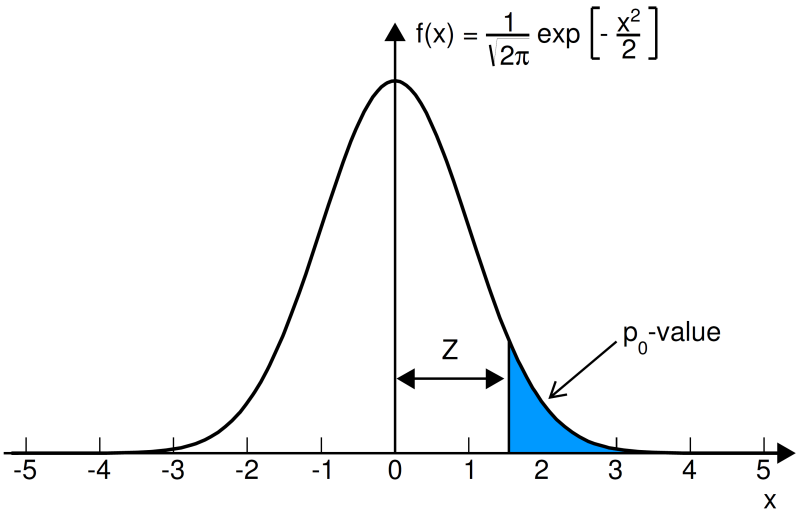

Figure 6.11: Definition of the p_0-value and significance Z_0 [131].

When attempting to exclude the signal hypothesis, the p-value p_μ of the test statistic q_μ

$$p_\mu = \int_{q_\mu^{\text{obs}}}^{\infty} f(q_\mu) dq_\mu \tag{6.17}$$

is used, describing the probability of obtaining at most the observed event yield n_{obs} in the signal region in the presence of a signal of strength $\mu \geq 0$. It is important to note that for $\mu = 0$, the p-values p_0 and $p_{\mu=0}$ are not the same, due to the difference between the test statistics.

To derive exclusion limits, the CL_s definition [132]

$$CL_s(\mu) = \frac{p_\mu}{p_{\mu=0}} \tag{6.18}$$

is used. Compared to the direct use of the p_μ-value, this adds an additional protection against false exclusion of a small signal in case of a downward fluctuation of the background, where $p_{\mu=0}$ (unlike p_0) decreases, increasing the CL_s probability. This conservative definition approaches the result with directly using p_μ for large signals.

Analogously to the p_0-value, a significance Z_{CL_S} is assigned to the CL_s value. $CL_s = 0.05$ corresponds to a 95% confidence level exclusion of the signal hypothesis, and is equivalent to a CL_s significance $Z_{\text{CL}_\text{S}} = 1.645$.

In both cases, determining signal significance or exclusion limits, the sensitivity of the analysis is estimated using toy Monte Carlo experiments. In each toy experiment, the number of observed events is randomly chosen around the predicted background yield according to the likelihood function in Eq. (6.11) or (6.12) and the p_0-value (for discovery potential) or the CL_s value (for expected exclusion limits) determined. In this way, a probability density function of p_0 or CL_s is obtained. The median of the distribution gives the expected p_0 or CL_s value while the 68% CL band gives the error on the expected result.

6.7 Results and Interpretation

6.7.1 Observations in the Signal Regions

Table 6.13 lists the number of data events observed in each signal region in comparison with the Standard Model (SM) expectation. In all signal regions, the observations are close to the expected values and show no signs of a significant excess in any region. The distributions of the missing transverse energy and effective mass are shown in Figures 6.12–6.14 together with an example for a potential signal. No sign of a signal is seen, especially at large missing transverse energy or effective mass. This is reflected in the corresponding observed p_0-values and significances Z_0. The smallest p-value is observed in signal region SR2noZb, with a significance of only one standard deviation. A model-independent upper limit $N^{95\%}_{\text{BSM}}$ on the number of expected events from an arbitrary signal is derived individually for each signal region by inserting the most general signal model possible, $s(\theta) \equiv 1$ with no systematic uncertainties, leading to the

Table 6.13: Expected and observed number of events in the signal regions of the four-lepton analysis. p_0 is truncated at 0.5.

	Exp. SM	**Data**	p_0	Z_0	$N^{95\%}_{\text{BSM}}$	$\sigma^{95\%}_{\text{vis}}$[fb]
SR0noZa	$\mathbf{1.6} \pm 0.5$	**3**	0.15	1.02	5.9	0.29
SR0noZb	$\mathbf{1.4} \pm 0.4$	**1**	0.50	-	3.7	0.18
SR1noZa	$\mathbf{4.6}^{+1.3}_{-1.2}$	**4**	0.50	-	5.7	0.28
SR1noZb	$\mathbf{2.9}^{+1.0}_{-0.9}$	**1**	0.50	-	3.5	0.17
SR2noZa	$\mathbf{4.0}^{+1.2}_{-1.3}$	**7**	0.13	1.14	9.2	0.45
SR2noZb	$\mathbf{3.0} \pm 1.0$	**6**	0.10	1.30	8.7	0.43

form

$$n_{\text{pred}} = \mu + b(\theta) \tag{6.19}$$

for the event yield in the signal region, while no signal contribution is subtracted from the reducible background estimate. The CL_s value is computed for different values of μ and interpolated between these values. The signal strength μ^{95} with $CL_s(\mu^{95}) = 0.05$ is interpreted as the 95% confidence level upper limit $N_{\text{BSM}}^{95\%}$ on the number of expected signal events consistent with the observation in the signal region. Using the integrated luminosity $L = 20.3\text{fb}^{-1}$, this upper limit is translated into an upper limit on the *visible cross-section*

$$\sigma_{\text{vis}}^{\text{max}} = \frac{1}{L} \cdot N_{\text{BSM}}^{95\%}. \tag{6.20}$$

This corresponds to a limit on the product of production cross-section σ, decay branching ration BR, signal region acceptance A and efficiency ϵ for a signal,

$$\sigma_{\text{vis}} = \sigma \cdot BR \cdot A \cdot \epsilon. \tag{6.21}$$

It allows arbitrary signal models to be tested against the analysis results by estimating the signal region acceptance and efficiency and comparing the resulting visible cross-section to the model-independent upper limit (see Table 6.13). Signal contributions between 3.7 and 9.2 expected events are excluded at 95% confidence level, depending on the signal region, corresponding to visible cross-sections of less than 0.5 fb.

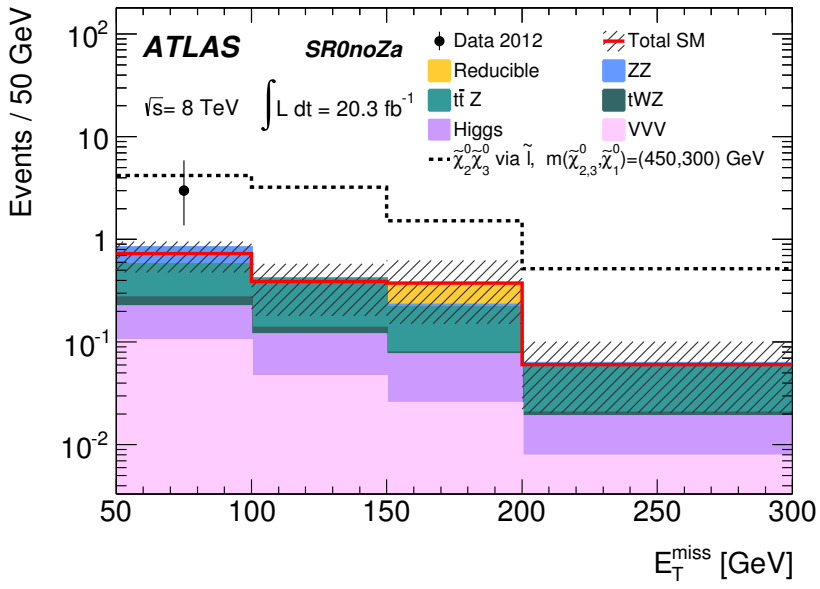

(a)

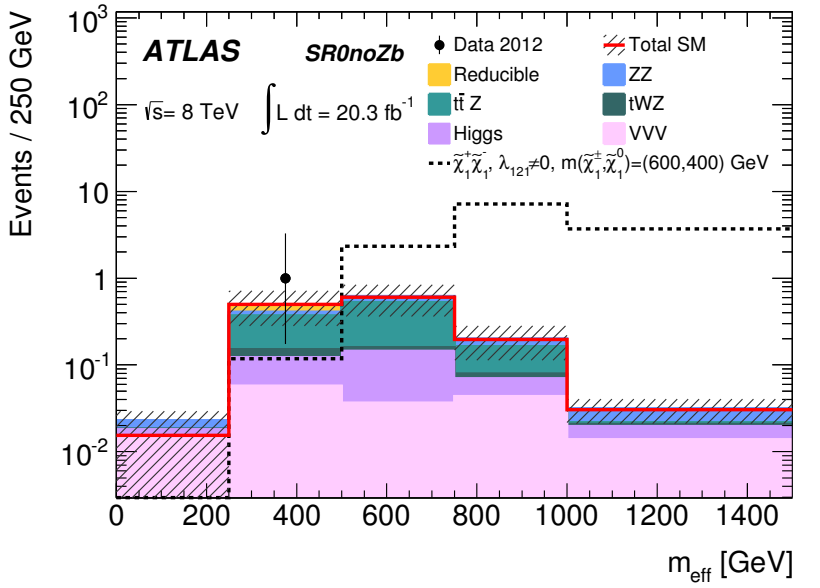

(b)

Figure 6.12: Predicted and observed distribution of the missing transverse energy in SR0noZa (a) and the effective mass in SR0noZb (b). The dashed line indicates an example signal of R-parity-conserving neutralino pair production [124] (a) or the simplified RPV model with a wino NLSP and a λ_{121} LLE coupling (b).

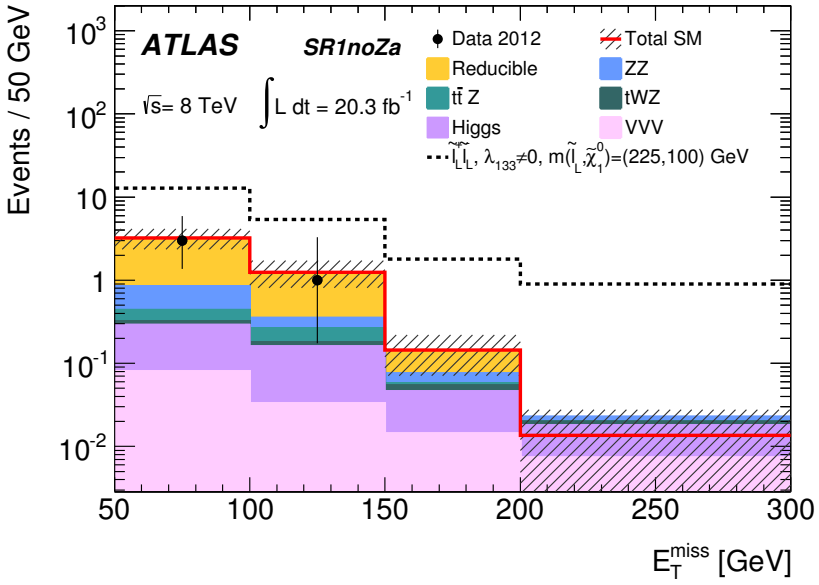

(a)

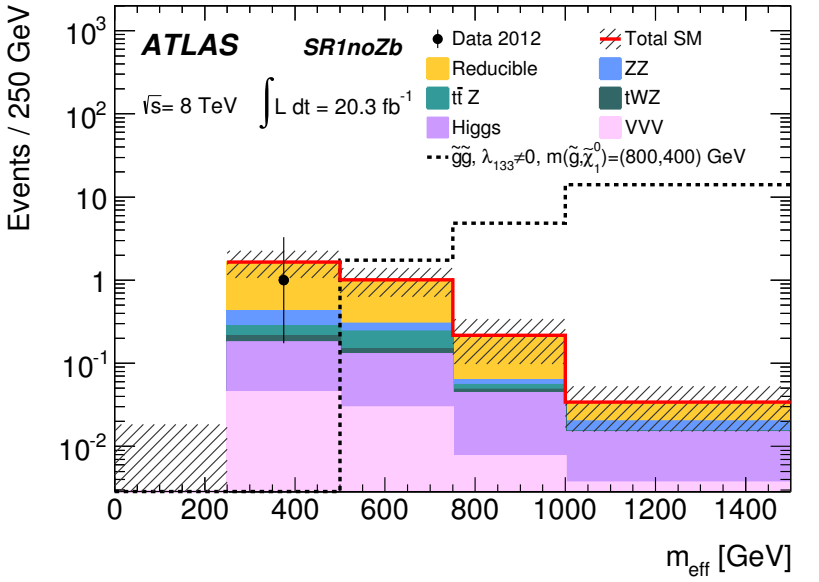

(b)

Figure 6.13: Predicted and observed distribution of the missing transverse energy in SR1noZa (a) and the effective mass in SR1noZb (b). The dashed line indicates an example signal from the simplified RPV model with an L-slepton NLSP and a λ_{133} LLE coupling (a) or the RPV simplified model with a gluino NLSP and a λ_{133} LLE coupling (b).

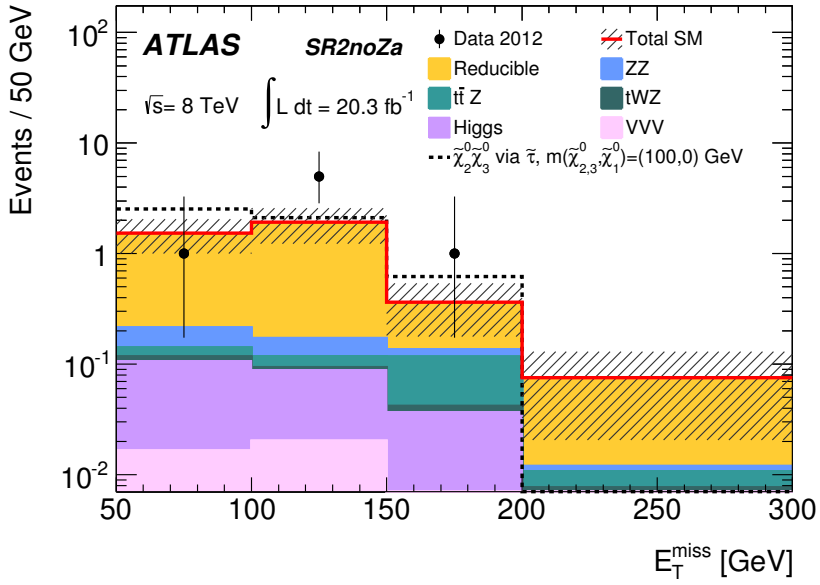

(a)

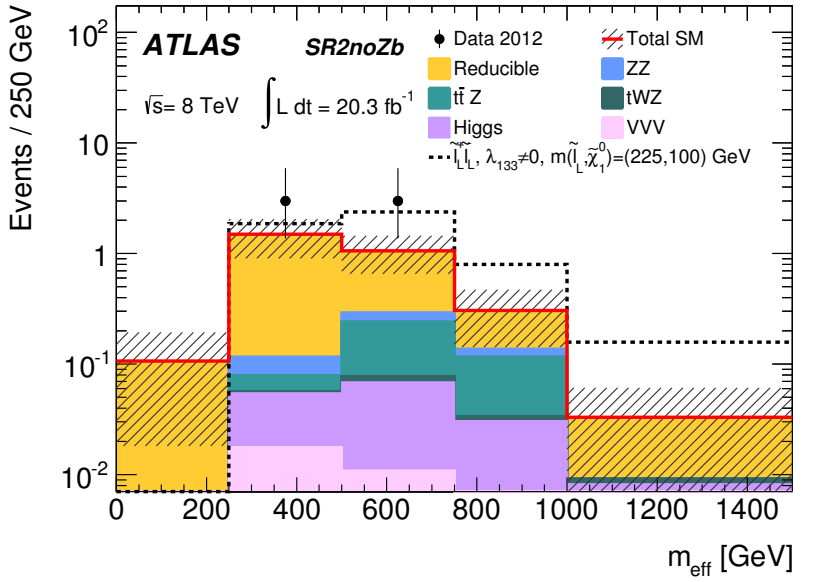

(b)

Figure 6.14: Predicted and observed distribution of the missing transverse energy in SR2noZa (a) and the effective mass in SR2noZb (b). The dashed line indicates an example signal of R-parity-conserving neutralino pair production [124] (a) or the RPV simplified model with an L-slepton NLSP and a λ_{133} LLE coupling (b).

6.7.2 Exclusion Limits for the Simplified Models

The parameter space of the NLSP and neutralino masses of the RPV SUSY models is constrained by testing the $\mu = 1$ hypothesis of each simulated mass configuration using the CL_s definition. Contours of constant $CL_s(\mu = 1) = 0.05$ (see Section 6.6) in the NLSP-LSP mass plane are determined by linear interpolation of the CL_s significance $Z_{\mathrm{CL_S}}$ between the simulated points. This procedure is illustrated in Figure 6.15 for the wino and gluino models with $\lambda_{121} \neq 0$. Mass points to the left of the contour $Z_{\mathrm{CL_S}} = 1.645$, equivalent to $CL_s \leq 0.05$, are excluded at 95% CL_s.

For these limits, the theoretical uncertainty on the signal production cross-section is not treated as a nuisance parameter. Instead, the exclusion contours determined for the nominal cross-section as well as for its $\pm 1\sigma$ upper and lower values leading to an exclusion band indicating the current theoretical uncertainty.

The signal regions SR0noZb, SR1noZb and SR2noZb are combined to set the limit for NLSP masses above 300 GeV, while for lower masses, the noZa regions relying on missing transverse energy become relevant as the effective mass is reduced (see Section 6.3.2).

Figures 6.17–6.16 show the resulting exclusion contours for the different models for all λ_{ijk} coupling parameters studied (see Table 5.1). For the wino model (see Figure 6.17a), chargino masses up to 750 GeV are excluded for neutralino masses above 50 GeV and λ_{12X} couplings leading to final states consisting exclusively of light leptons. For $\lambda_{X33} \neq 0$ with τ leptons in the final state, the highest chargino mass that can be excluded is 550 GeV for a neutralino mass of 300 GeV. The excluded gluino NLSP mass (see Figure 6.17b) is about twice as high as in the wino case due to the high strong production cross-sections. For LSP decays to light leptons, the exclusion reaches up to gluino masses of 1.35 TeV for a neutralino mass above 50 GeV, while in the τ-rich case masses up to about 1 TeV are excluded for neutralino masses above 200 GeV. For the L- and R-slepton NLSP production (see Figure 6.18), the mass limit for LSP decays into light leptons ranges between 400 GeV and 500 GeV for neutralino masses above 50 GeV. The limit is stronger for L- compared to R-sleptons due to the higher production cross-section enhanced by the $SU(2)_L$ coupling of the L-sleptons. For τ-rich decays, slepton masses between 300 GeV and 400 GeV are excluded for neutralino masses above 50 GeV. This exclusion is closer to the four light lepton case than for the other models as two additional leptons from the cascade enhance the acceptance, and populate the four-light-lepton signal regions even for τ-rich LSP decays. Sneutrino NLSP masses (see Figure 6.16) below

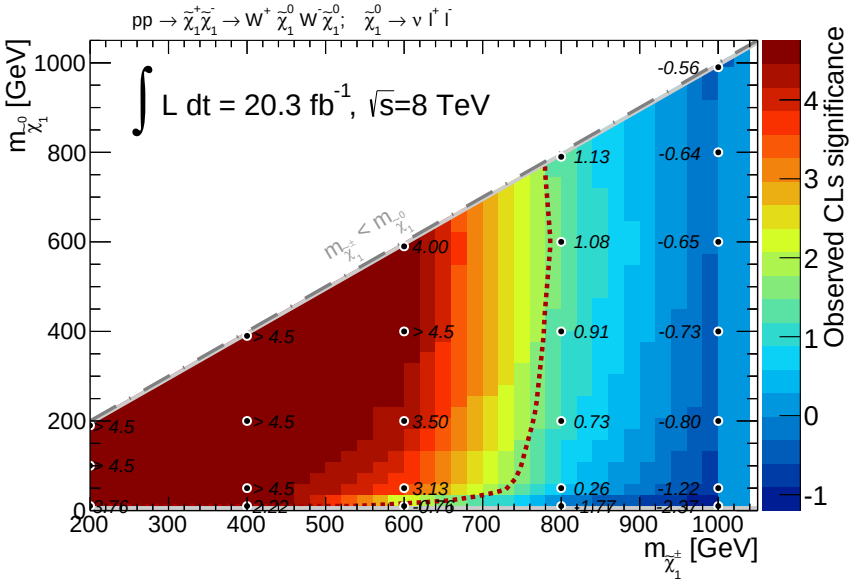

(a)

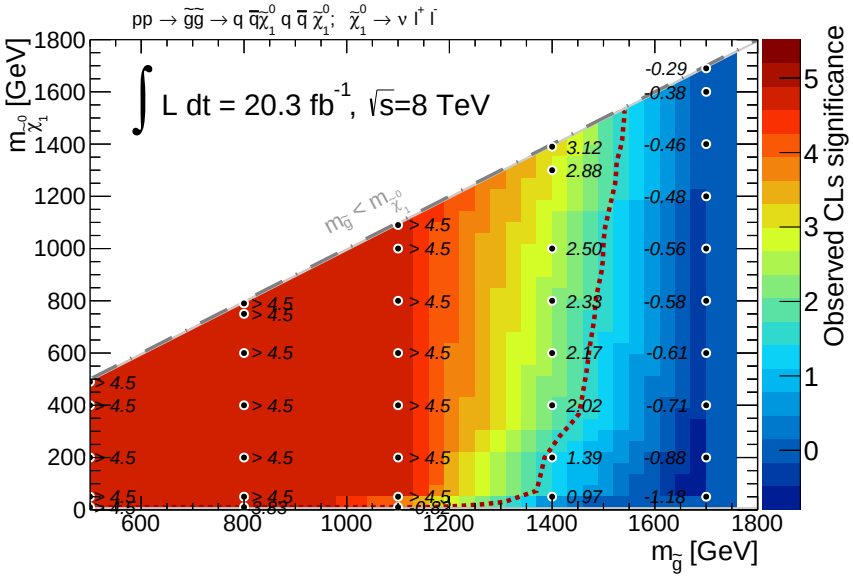

(b)

Figure 6.15: Interpolated significance $Z_{\mathrm{CL_S}}$ of CL_s and resulting 95% exclusion contour (see text) in the NLSP-neutralino mass plane for the wino (a) and gluino (b) simplified model with $\lambda_{121} \neq 0$. The black dots indicate the mass combinations for which CL_s values have been computed.

400 GeV are excluded for an LSP mass above 50 GeV if the LSP decays to light leptons. For τ-rich decays, only a small region of the sneutrino-LSP mass parameter space near $m_{\tilde{\nu}} = 75$ GeV and $m_{\tilde{\chi}_1^0} = 65$ GeV is excluded. The lack of visible cascade particles is responsible for this comparatively weak exclusion.

In general, the excluded NLSP mass is reduced by about 100 GeV in the challenging region of LSP masses below 50 GeV for LSP decays to light leptons, since the signal region acceptance and efficiency decrease with increasing LSP boost (see Section 6.3.2). The drop for τ-rich LSP decays is even more pronounced. Compared to previous iterations of the analysis [133], the correction of the electron and muon isolation variables (see Section 6.2.2) and the optimised overlap removal procedure yield a dramatic improvement of the analysis sensitivity in this region of the NLSP-LSP mass plane.

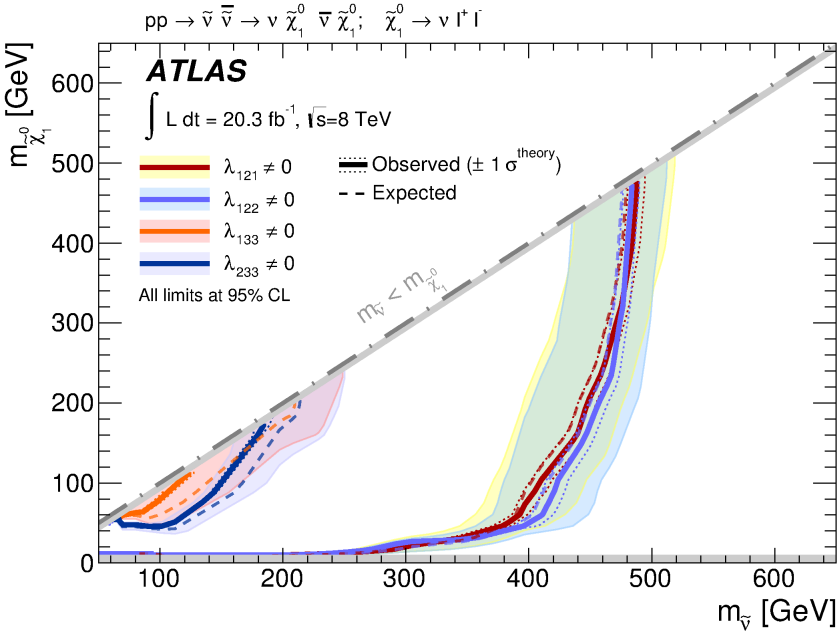

Figure 6.16: Exclusion contours in the NLSP-neutralino mass plane for the simplified RPV model with a sneutrino NLSP. The expected exclusion obtained from inserting the background prediction as observed yield is shown as shaded band with dashed median value. The solid lines are the observed limit contours. The light dashed lines indicate the uncertainties on the signal production cross-sections. Results are shown for the four benchmark couplings in Table 5.1, λ_{121} (dark red), λ_{122} (light blue), λ_{133} (orange) and λ_{233} (dark blue). The kinematic limit $m_{\text{NLSP}} \geq m_{\text{LSP}}$ is indicated as dashed-dotted line.

6.7.3 Validity of the Resulting Limits

The simplified models discussed in Section 5.3 and used for deriving exclusion limits make a specific set of assumptions on the nature of the LSP as a bino-like neutralino, the presence of a single dominant LLE coupling and on the (SUSY) particle masses. It is useful to also consider deviations from these assumptions, and their effect on the experimental sensitivity. For example, if the LSP is not a neutralino, the final state can be dramatically altered. In the case of a chargino LSP, either one or three charged leptons ($\tilde{\chi}_1^{\pm} \to \ell^{\pm}\nu\nu/\ell^{\pm}\ell^{\mp}\ell^{\pm}$) are produced in decays via virtual sleptons or sneutrinos, respectively, leading to a four-lepton final state only in a fraction of all events. The analysis is therefore still expected to be sensitive, to a degree depending on the decay branching ratios. If the LSP is a slepton, a direct $\tilde{\ell} \to \ell\nu$ decay takes place if allowed by the generation indices of the active λ_{ijk} couplings, resulting in a final state with two charged leptons and missing transverse energy. Searches for slepton and stau pair production in R-parity-conserving SUSY [134, 135] target this final state. If the R-parity-violating coupling does not allow a direct decay, indirect decays via intermediate neutralinos ($\tilde{\ell} \to \ell\ell\ell\nu$) or charginos ($\tilde{\ell} \to \ell\ell\ell\nu/\ell\nu\nu\nu$) lead to final state with between two and six charged leptons. The four-lepton analysis is highly sensitive to such scenarios [136]. A squark or gluino LSP must decay indirectly via a virtual neutralino ($\tilde{q} \to q\ell\ell\nu$, $\tilde{g} \to qq\ell\ell\nu$) or chargino ($\tilde{q} \to q\ell\ell\ell\nu/q\ell\nu\nu\nu$, $\tilde{g} \to qq\ell\ell\ell\nu/qq\ell\nu\nu\nu$), leading again to final states with between two and six charged leptons, such that the four-lepton search is again expected to be sensitive to at least a fraction of the decays.

Constraints from proton decay allow other lepton number violating RPV couplings as well as LLE (see Eq. (2.26)). If LQD couplings are present and non-negligible, they compete with the LLE coupling, allowing a neutralino LSP to decay into a pair of quarks and either a charged lepton or neutrino ($\tilde{\chi}_1^0 \to \ell qq/\nu qq$). If either of the two neutralino LSP decays takes place via this coupling, the event is lost to the four-lepton analysis. Therefore, the analysis acceptance is reduced by the square of the branching ratio to the $\ell\ell\nu$ final state.

Finally, the analysis assumes the neutralinos to have a negligible lifetime. If the neutralino decay length exceeds about 0.1 mm (see Section 5.3.4), the impact parameter requirements of the signal lepton selection start becoming inefficient. For even longer lifetimes, the track reconstruction efficiency of the Inner Detector will start to degrade. In the next chapter, this will be studied in more detail and a complementary analysis is performed for the case of longer neutralino lifetimes.

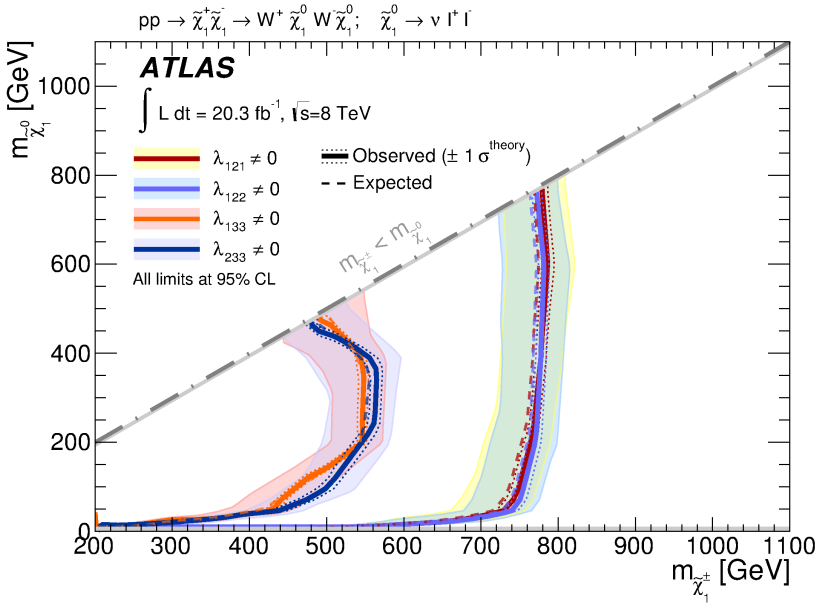

(a)

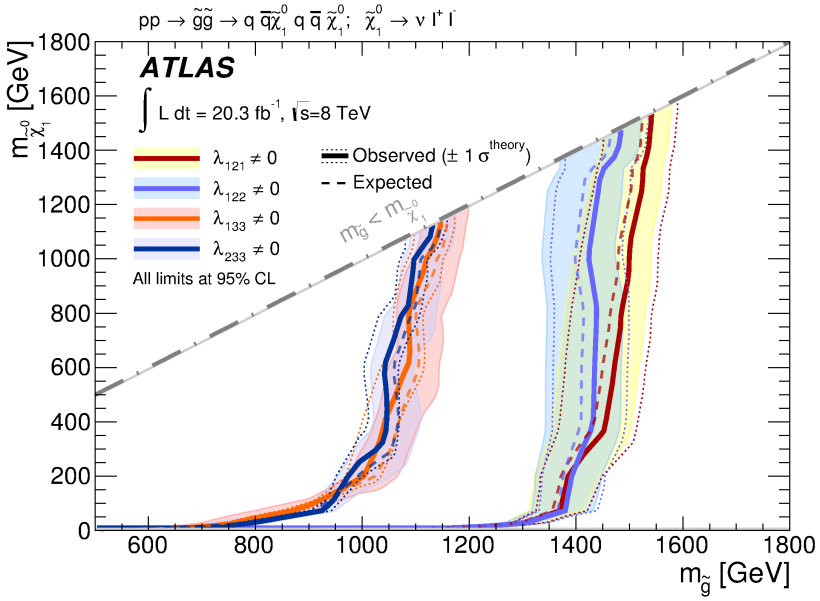

(b)

Figure 6.17: Exclusion contours in the NLSP-neutralino mass plane for the simplified RPV model with a wino (a) or gluino (b) NLSP. The expected exclusion obtained from inserting the background prediction as observed yield is shown as shaded band with dashed median value. The solid lines are the observed limit contours. The light dashed lines indicate the uncertainties on the signal production cross-sections. Results are shown for the four benchmark couplings in Table 5.1, λ_{121} (dark red), λ_{122} (light blue), λ_{133} (orange) and λ_{233} (dark blue). The kinematic limit $m_{\text{NLSP}} \geq m_{\text{LSP}}$ is indicated as dashed-dotted line.

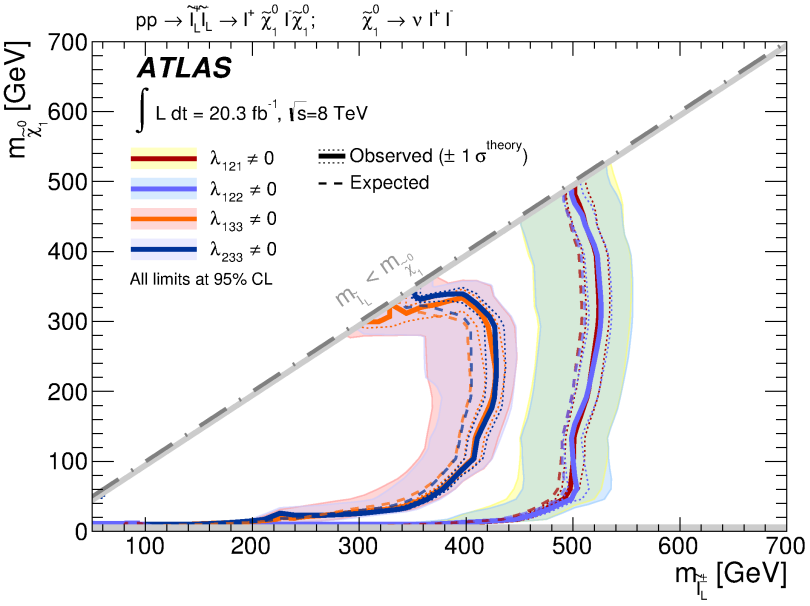

(a)

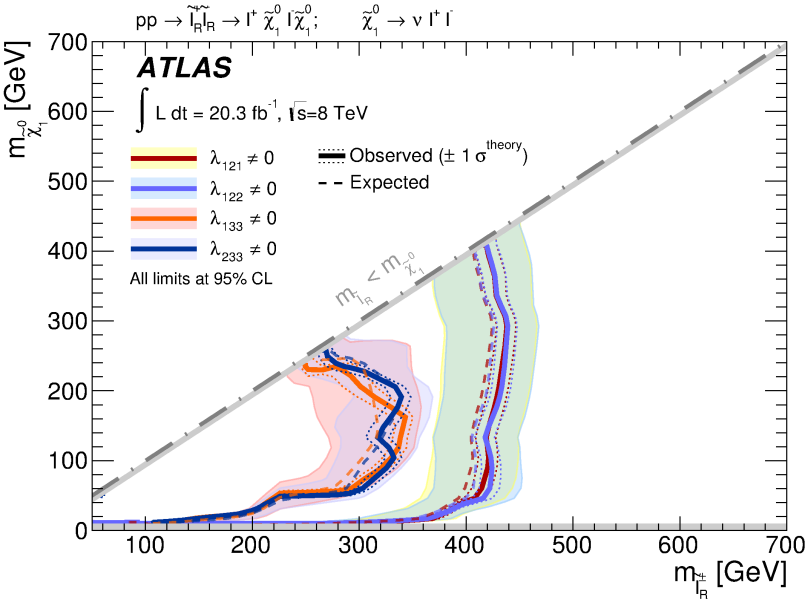

(b)

Figure 6.18: Exclusion contours in the NLSP-neutralino mass plane for the simplified RPV model with an L-slepton (a) or R-slepton (b) gluino NLSP. The expected exclusion obtained from inserting the background prediction as observed yield is shown as shaded band with dashed median value. The solid lines are the observed limit contours. The light dashed lines indicate the uncertainties on the signal production cross-sections. Results are shown for the four benchmark couplings in Table 5.1, λ_{121} (dark red), λ_{122} (light blue), λ_{133} (orange) and λ_{233} (dark blue). The kinematic limit $m_{\text{NLSP}} \geq m_{\text{LSP}}$ is indicated as dashed-dotted line.

Chapter 7

RPV Decays of Long-Lived Neutralinos into Lepton Pairs

7.1 Analysis Strategy

In the previous chapter, strong limits have been established on prompt R-parity-violating neutralino LSP decays into four-lepton final states. The event selection for this analysis relies on the assumption that all four leptons originate from the primary vertex. If the lifetime of the neutralino reaches about 1 ps, this assumption is no longer valid.

Figure 7.1 illustrates the two main challenges imposed by decays of a long-lived LSP. First, final state leptons produced at displaced decay vertices can have large transverse impact parameters $|d_0|$. For high neutralino masses, large $|d_0|$ are preferred, while the effect is weakened due to the smaller decay opening angle for a light boosted LSP. The impact parameter criteria in the signal lepton selection of the four-lepton search are thus inefficient for displaced decays. In addition, even if these criteria were modified, the reconstruction itself limits the achievable analysis sensitivity as the standard ATLAS track reconstruction algorithms do not reconstruct Inner Detector tracks with transverse impact parameters above $|d_0| = 10$ mm. Also, the LSP decays occur at larger radii as the lifetime increases. This reduces the number of tracking detector layers traversed by the decay leptons, deteriorating the reconstruction efficiency. This deterioration is exacerbated for a light LSP as the laboratory frame decay length $c\tau_{\text{lab}} = \beta\gamma c\tau$ is enhanced by the boost of the decaying particle.

At the same time, a powerful new approach for signal selection becomes available. The

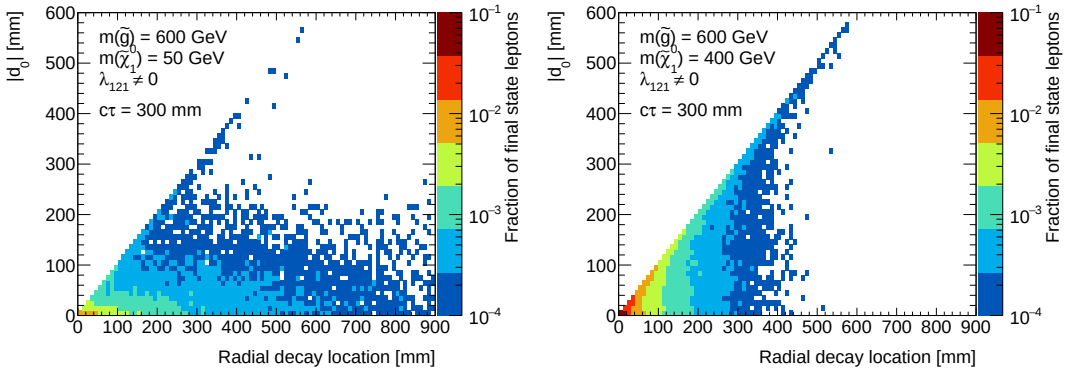

(a) **(b)**

Figure 7.1: Transverse impact parameter $|d_0|$ of final state leptons vs. the radial location of the neutralino decay vertex for the simplified RPV model with a gluino NLSP, $c\tau = 300$ mm, $m_{\tilde{g}} = 600$ GeV and a neutralino mass of $m_{\tilde{\chi}_1^0} = 50$ GeV (a) or $m_{\tilde{\chi}_1^0} = 400$ GeV (b).

individual neutralino decays can be resolved as separate displaced vertices with two emerging leptons (see Figure 7.2). The analysis [137] described in the following detects such vertices inside the detector volume up to the radius of the first layer of the SCT tracker, forming a cylinder around the beam line with length $z = \pm 300$ mm and radius $r = 300$ mm (see Figure 7.3). The vertices are required to be highly displaced, with a separation of at least 4 mm from the beam line.

One important conceptual difference to the four-lepton analysis described in Chapter 6 is that the search is for displaced dilepton vertices, instead of four-lepton events with two LSP decays. This greatly enhances the generality of the results, as no requirements are made on the number of displaced vertices in a single event or additional cascade particles. Any signal leading to at least one high mass displaced dilepton vertex is covered by the analysis, whether or not those signals have a supersymmetric origin. To achieve this generality, event-level observables like the effective mass or the missing transverse energy, which take into account features apart from the displaced vertex, cannot be used in the signal selection.

As the default ATLAS track reconstruction does not reconstruct tracks with $|d_0| > 10$ mm, it was necessary to rerun track reconstruction with loosened requirements. In order to perform this *re-tracking* procedure, additional information about Inner Detector hits was required which could only be kept accessible for analysis for about 1% of all events due to limitations in processing time and storage capacity. A filtering procedure based on

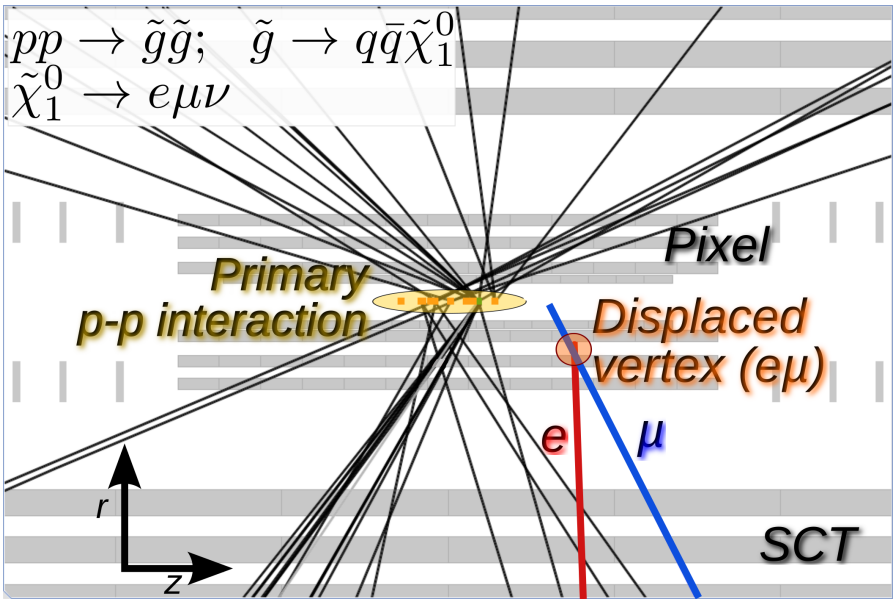

Figure 7.2: Simulated event in the simplified RPV model with a gluino NLSP, $\lambda_{121} \neq 0$ and a neutralino decay length $c\tau = 30$ mm, with a reconstructed displaced secondary vertex from a $\tilde{\chi}_1^0 \to e\mu\nu$ decay between the first and second layers of the pixel detector.

calorimeter deposits and Muon Spectrometer tracks described in Section 7.3 was applied for this purpose.

After reconstruction of the displaced vertex candidates from this filtered sample, a simple signal selection procedure is employed. The main requirement is the association of two charged leptons with a vertex candidate of high invariant mass.

No Standard Model particle has the right properties to produce such vertices without some sort of misreconstruction. However, a variety of background processes are considered as possible sources of high-mass displaced dilepton vertices.

- A cosmic ray passing through the detector can be reconstructed as a pair of collinear muons, with opposite charges as the reconstruction assumes that particles are travelling away from the interaction point. Due to the high transverse momenta of cosmic rays and the flat distribution of their transverse impact parameter, high-mass displaced vertices similar to the signal can occur.

- Misreconstructed prompt decays like $Z \to \ell\ell$ can lead to displaced vertices if both leptons appear to be displaced due to limited impact parameter resolution.

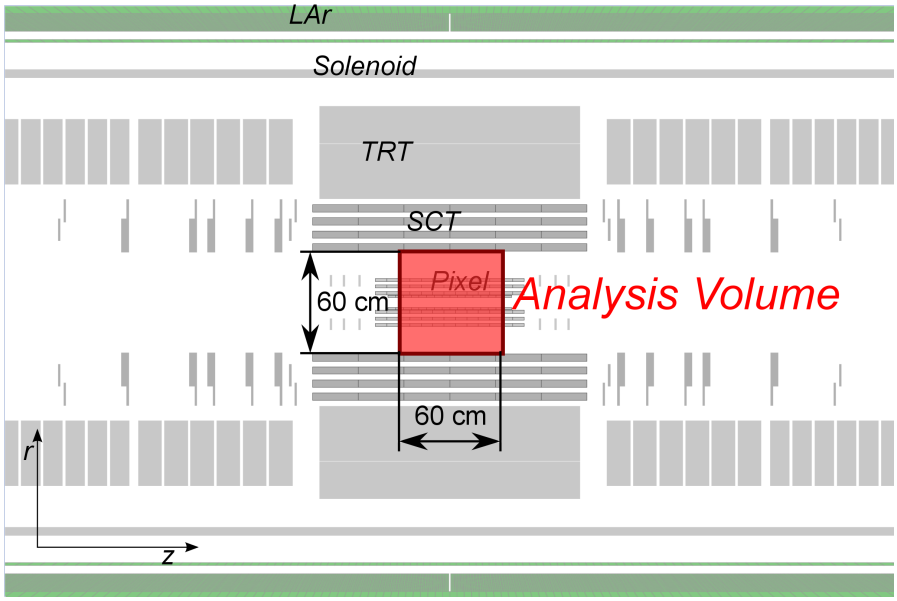

Figure 7.3: Detector volume considered for the search for displaced dilepton vertices.

- Lepton tracks can randomly cross within the tracking volume and form a displaced vertex, which can have high invariant mass due to the random dilepton opening angle.

As these sources are challenging to estimate with high precision and there is no precedent in ATLAS for their estimation, the selection strategy explicitly aims to suppress the backgrounds to negligible levels. The residual background components are estimated using dedicated data sets.

7.2 Signal Models

To guide the development of the search strategy and to provide a model for interpreting the results, four NLSP-LSP mass combinations (see Figure 7.4) from the simplified RPV gluino NLSP model with λ_{121} and λ_{122} couplings discussed in Section 5.3 are used. In this first iteration of the analysis, no couplings leading to τ leptons in the final state are considered.

Two mass points are placed in the region of the mass plane at $(m_{\tilde{g}}, m_{\tilde{\chi}_1^0}) = (600, 400)$ and $(1300, 1000)$ GeV, where the decaying neutralino is not significantly boosted. The other two points are have a relatively light neutralino, which gets a large boost: $(m_{\tilde{g}}, m_{\tilde{\chi}_1^0}) =$

(600,50) and (1300,50) GeV. In this way, the sensitivity of the analysis to the mass of the initially produced NLSP and to the boost of the decaying LSP is explored. As the search strategy is independent of the cascade particles, other NLSP choices need not be investigated.

For each of the four mass combinations, four lifetime values of the neutralino are simulated, $\tau_{\tilde{\chi}_1^0}$ = 10 ps, 100 ps, 1 ns and 10 ns, corresponding to decay lengths of between 3 mm and 3 m.

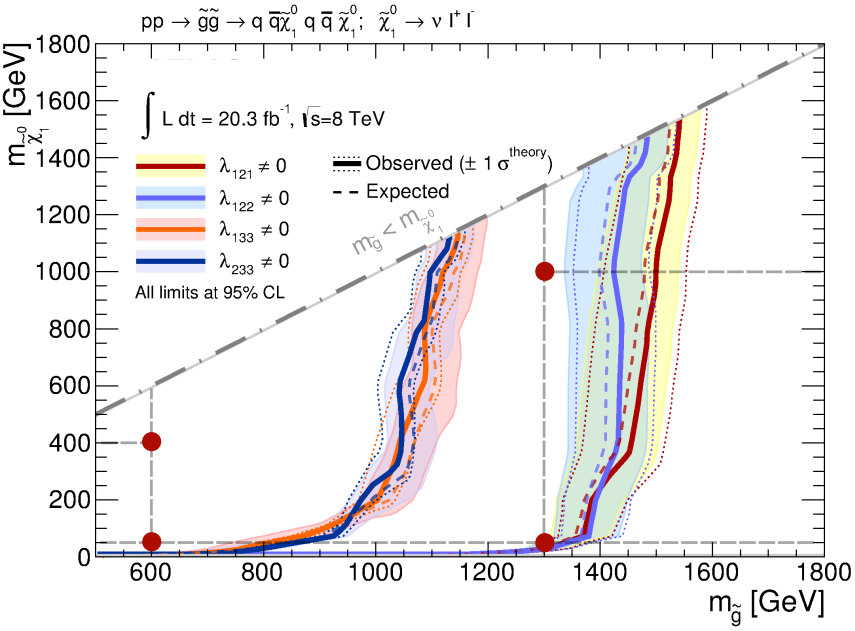

Figure 7.4: NLSP-LSP mass combinations in the simplified gluino NLSP model considered for the displaced dilepton vertex search (red dots) in the gluino-neutralino mass plane with the exclusion limits of the prompt four-lepton analysis for the same model overlaid (from Section 6.7.2).

7.3 Filtering of the Data for Re-Tracking

The track and vertex reconstruction of the ATLAS experiment (Section 3.3.1) is not optimised for the reconstruction of highly displaced decay vertices and of the associated tracks. To save processing time and storage capacity, tracks in the Inner Detector are only reconstructed if their transverse impact parameter is less than 10 mm. However, leptons from long-lived signal decays can have much larger impact parameters

such that their Inner Detector tracks are not reconstructed by the standard tracking software (see Figure 7.1).

For this reason, the track reconstruction is repeated with modified algorithms optimised for the detection of tracks from a displaced vertex in addition to the tracks already reconstructed by the standard tracking. Then, lepton and vertex reconstruction are repeated using the extended set of tracks.

The information necessary to carry out this procedure is not stored in the standard ATLAS event data format. Therefore, input data sets had to be generated from the raw data in a first step. The information content of the input data is significantly larger than the one of ordinary ATLAS data. Due to limited disk space, only about 1% of the triggered data could be stored in this way. Thus the data used in this search were preselected by a filter algorithm before the re-tracking procedure was performed.

The filtering procedure attempts to maximise the acceptance for events containing signal decays while reducing the number of background events by two orders of magnitude. As the filtering is performed before the re-tracking, Inner Detector tracks of leptons from highly displaced vertices may not be available for the preselection. Therefore, the single- and dilepton triggers described in the four-lepton analysis (Section 6.2) are not used. The decay leptons can only be reliably detected by exploiting their interactions with the detector components outside the Inner Detector. In the case of muons, a track in the Muon Spectrometer, providing a full momentum measurement, can be used. Energy deposits in the Electromagnetic Calorimeter caused by electrons can be reconstructed as photon candidates if no associated track is reconstructed. Figure 7.5 shows the electron and muon reconstruction efficiencies for leptonic neutralino decays from Monte Carlo simulation as a function of the transverse impact parameter $|d_0|$ of the simulated particle trajectories.

The efficiency for combined muon and for electron reconstruction shows a rapid decline with increasing $|d_0|$. Standalone muons (see Section 3.3.6) and photons however have high reconstruction efficiencies even for large $|d_0|$. The $|d_0|$-dependence of the electron and photon efficiencies is complementary, leading to a high efficiency above 50% if both are considered. Therefore, the filtering strategy relies on a combination of standalone muons, electrons and photons.

Only three triggers are available that are independent of the Inner Detector track reconstruction (see Table 7.1). A single standalone muon trigger requires one standalone muon in the barrel region of the detector with a high transverse momentum. The single

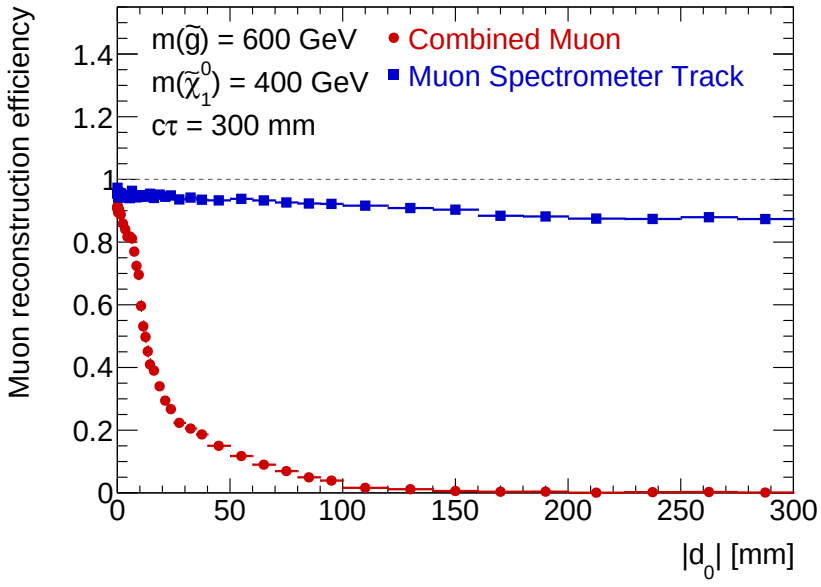

(a)

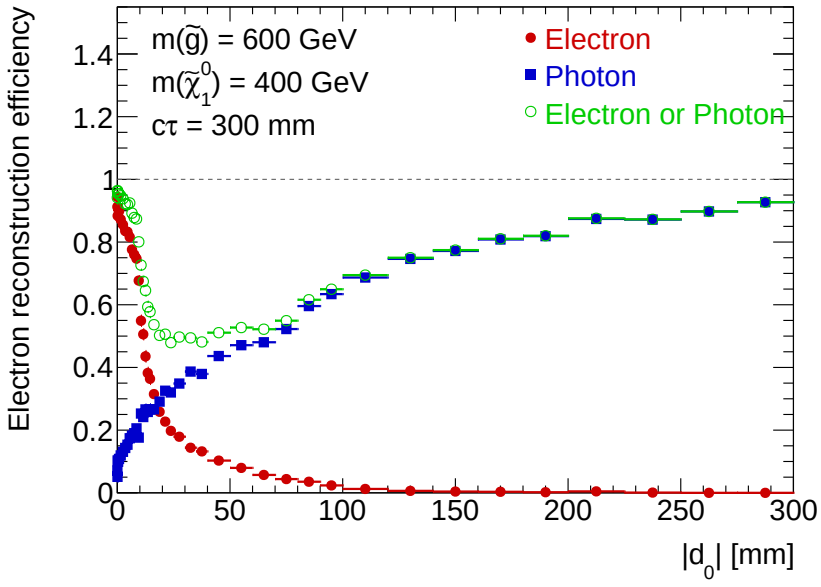

(b)

Figure 7.5: Reconstruction efficiency of muons (a) and electrons (b) from neutralino decays via $\lambda_{121/122}$ couplings for the gluino model with $m_{\tilde{g}} = 600\,\text{GeV}$, $m_{\tilde{\chi}_1^0} = 400\,\text{GeV}$ and $c\tau = 300\,\text{mm}$ as a function of the transverse impact parameter $|d_0|$ of the event-generator level particle trajectory. Statistical errors are shown.

Table 7.1: Triggers used for the displaced dilepton vertex search. No Inner Detector information is used by any of the triggers.

Trigger	Requirement
Single muon	Standalone muon with $p_{\mathrm{T}} \geq 50$ GeV in $\lvert\eta\rvert < 1.05$
Single photon	Photon with $E_{\mathrm{T}} \geq 120$ GeV
Diphoton	At least two photons with $E_{\mathrm{T}} \geq 40$ GeV each

photon trigger searches for one highly energetic photon candidate. As the Inner Detector is not considered by this trigger, there is no efficiency degradation at low transverse impact parameters as observed for the offline photon reconstruction in Figure 7.5, and no separate electron trigger is necessary. Finally, a diphoton trigger requires two photons (again without considering Inner Detector tracks) with a more moderate minimum transverse energy requirement. Standalone muons and photons reconstructed without Inner Detector information are affected by a higher rate of secondary decays and misidentifications than electrons and combined muons. Therefore, the kinematic requirements of all three triggers are more severe than the ones applied to the high-quality lepton candidates in the four-lepton search.

Table 7.2: Offline filter requirements for the displaced dilepton vertex search. The trigger associated with each filter is also indicated (see Table 7.1). At least one combination of trigger and filter requirements has to be satisfied in order to accept an event for the re-tracking procedure.

Trigger	Filter	Requirements
Single photon	Single photon	Photon with $E_{\mathrm{T}} \geq 130$ GeV
	Single electron	Electron with $\lvert d_0\rvert > 2.0$ mm and $E_{\mathrm{T}} \geq 120$ GeV
Diphoton	Two photons	At least two photons with $E_{\mathrm{T}} \geq 48$ GeV each
	Two electrons	At least two electrons, with $E_{\mathrm{T}} \geq 43$ GeV and $\lvert d_0\rvert > 2.5$ mm each
	Electron+photon 1	Electron with $E_{\mathrm{T}} \geq 39$ GeV and photon with $E_{\mathrm{T}} \geq 48$ GeV
	Electron+photon 2	Electron with $E_{\mathrm{T}} \geq 38$ GeV and $\lvert d_0\rvert > 2.0$ mm and photon with $E_{\mathrm{T}} \geq 39$ GeV
Single muon	Single muon	Combined or standalone muon in $\lvert\eta\rvert < 1.07$ with $p_{\mathrm{T}} \geq 50$ GeV and $\lvert d_0\rvert > 1.5$ mm

Events fulfilling one of the three trigger conditions are subjected to offline filtering criteria to further reduce the number of events. Table 7.2 lists the offline filter requirements. Three types of criteria are used, corresponding to the three triggers. Events passing the single photon trigger are required to contain at least one energetic reconstructed photon or electron. For electrons, it is necessary to additionally require a large transverse impact parameter to reduce the number of events with prompt leptons (e.g. $W \to \ell\nu$). If an event is accepted by the diphoton trigger, the presence of at least two reconstructed photons, at least two electrons or at least one photon and at least one electron is required. This combination of trigger and offline filters is used to recover acceptance to dielectron decays where no single highly-energetic object is present. Finally, events accepted by the single muon trigger are required to contain a reconstructed combined or standalone muon with high impact parameter and momentum matching the single muon trigger threshold.

Figure 7.6 shows the trigger and filter efficiency for individual neutralino decays into two electrons. For a small neutralino mass ($m_{\tilde{\chi}_1^0} = 50$ GeV), the single electron, single photon and two-object filters all have similar efficiency which is nearly constant for $r_{\text{DV}} > 40$ mm. At lower radii, the transverse impact parameter requirements and inefficiency of the offline photon selection (see Figure 7.5b) reduce the filter efficiency. For a larger neutralino mass ($m_{\tilde{\chi}_1^0} = 400$ GeV), the final state leptons have higher momenta (see Section 5.3 and 6.3) and are less collimated with the neutralino direction than for the small neutralino mass, and therefore can have relatively large transverse impact parameters up to the radius of the neutralino decay (see Figure 7.1). Both features increase the filter acceptance, leading to high efficiency of more than 60% for small radial vertex displacements where lepton tracks are successfully reconstructed by the default tracking algorithm but impact parameters are sufficiently large to be accepted by the electron filters. At larger radii the inclusion of offline photons in the filter selection increases the efficiency from below 10% to about 30%. In Figure 7.7, results for decays into one electron and one muon are shown. As the single muon filter transverse momentum requirement is much less stringent than for the single electron or photon filters, its efficiency is higher, which also increases the overall electron-muon selection efficiency compared to displaced decays into two electrons. Finally, Figure 7.8 shows the result for LSP decays into two muons, which are only selected by the single muon filter. Peak efficiencies are about 35% and 75% for low and high neutralino masses, respectively.

The data passing the filtering procedure are stored on disk and used as input to the re-tracking, described next.

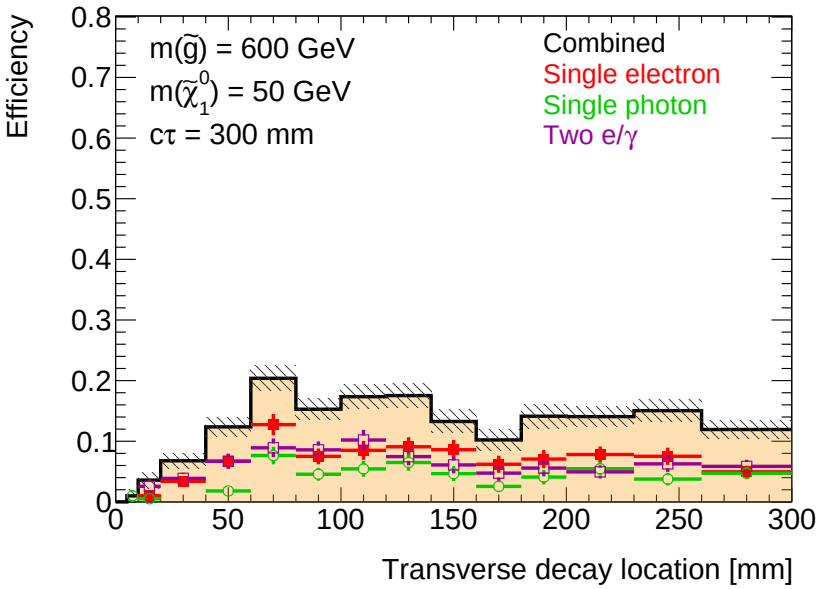

(a)

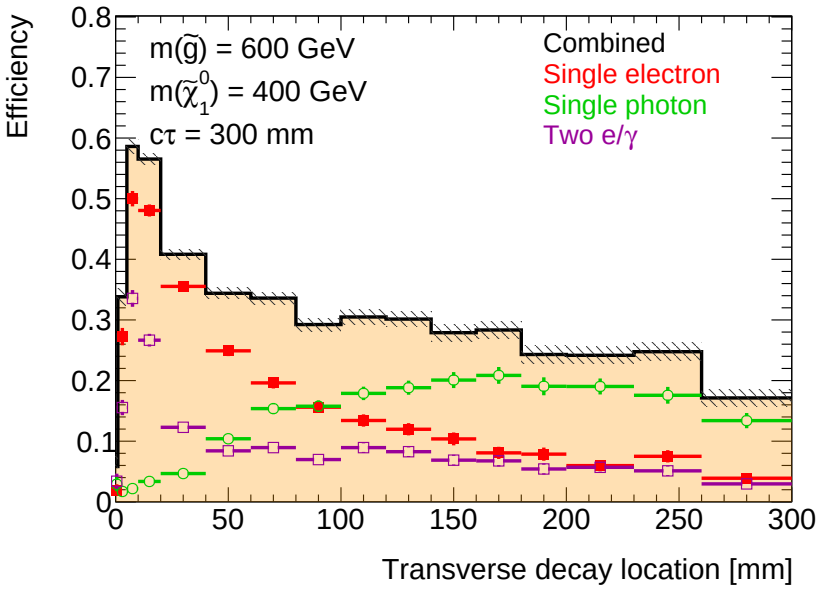

(b)

Figure 7.6: Combined and individual trigger and filter efficiencies for individual $\tilde{\chi}_1^0 \to eev$ decays with $c\tau = 300$ mm in the gluino model for $m_{\tilde{g}} = 600$ GeV and $m_{\tilde{\chi}_1^0} = 50$ GeV (a) or $m_{\tilde{\chi}_1^0} = 400$ GeV (b) as a function of the radial location of the neutralino decay. Statistical errors are given.

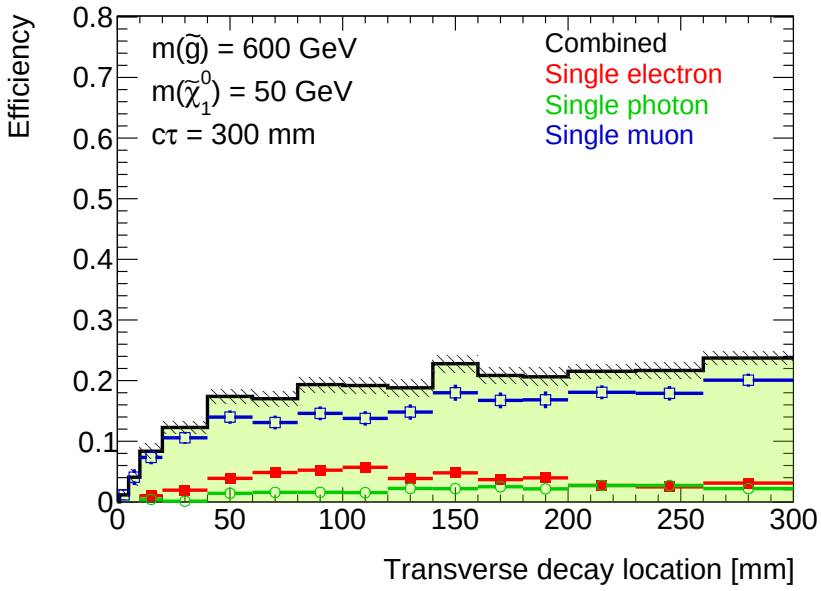

(a)

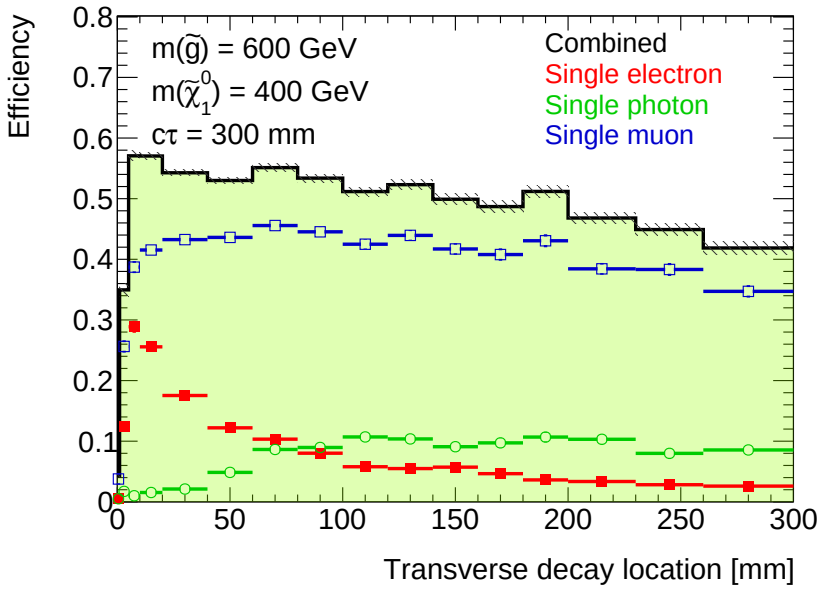

(b)

Figure 7.7: Combined and individual trigger and filter efficiencies for individual $\tilde{\chi}_1^0 \to e\mu\nu$ decays with $c\tau = 300$ mm in the gluino model for $m_{\tilde{g}} = 600$ GeV and $m_{\tilde{\chi}_1^0} = 50$ GeV (a) or $m_{\tilde{\chi}_1^0} = 400$ GeV (b) as a function of the radial location of the neutralino decay. Statistical errors are given.

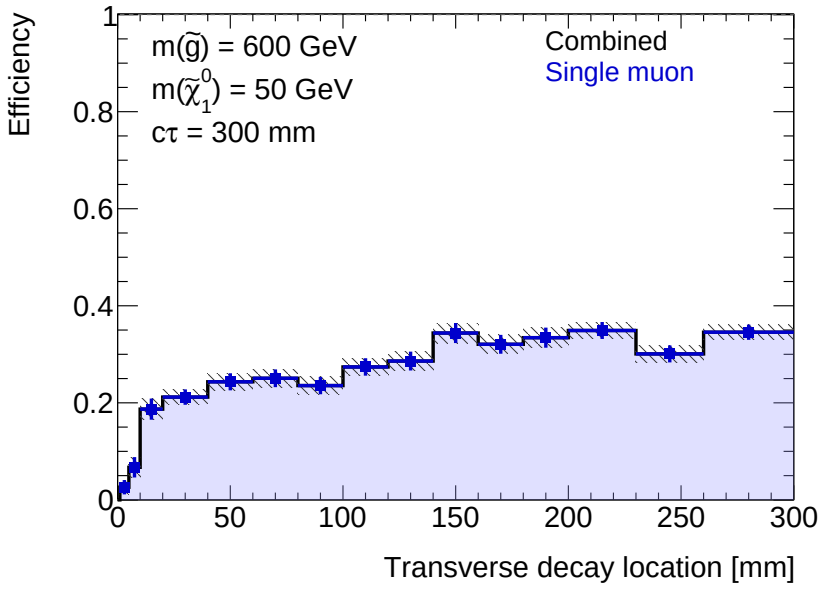

(a)

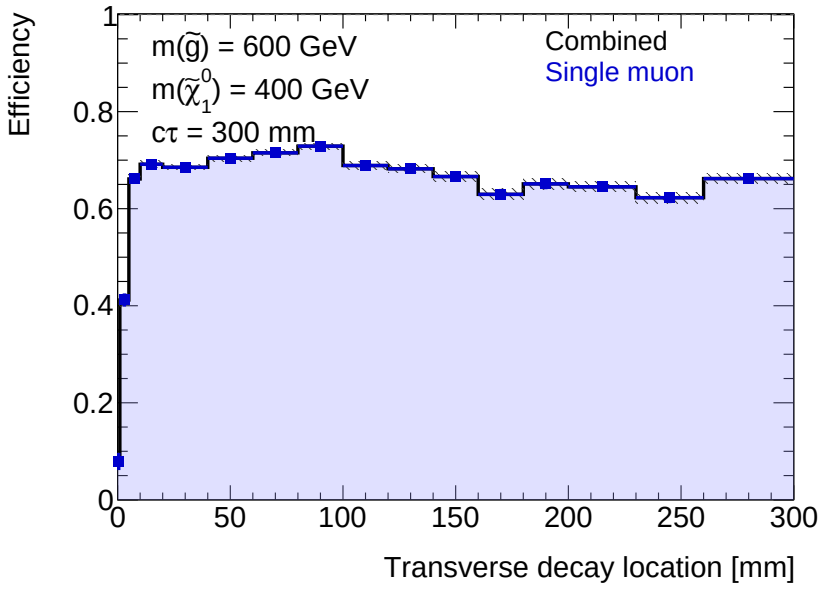

(b)

Figure 7.8: Combined and individual trigger and filter efficiencies for individual $\tilde{\chi}_1^0 \to \mu\mu\nu$ decays with $c\tau = 300$ mm in the gluino model for $m_{\tilde{g}} = 600$ GeV and $m_{\tilde{\chi}_1^0} = 50$ GeV (a) or $m_{\tilde{\chi}_1^0} = 400$ GeV (b) as a function of the radial location of the neutralino decay. Statistical errors are given.

7.4 Reconstruction of Displaced Vertices

7.4.1 Track and Lepton Reconstruction

Reconstruction of Inner Detector tracks with high impact parameters is carried out for the events accepted by the filtering procedure described above using a technique originally developed for other displaced vertex searches in ATLAS [137, 138]. The silicon-seeded track reconstruction (Section 3.3.1) is repeated using hits not yet associated with existing tracks. While the standard silicon-seeded reconstruction only searches for tracks with transverse impact parameters below 10 mm, the modified algorithm used for recovering highly displaced tracks extends coverage up to 300 mm. This includes all lepton tracks originating from decays within the fiducial tracking volume considered.

Subsequently, the lepton reconstruction is repeated. The new tracks are associated with Muon Spectrometer tracks and clusters in the electromagnetic calorimeter, promoting standalone muons and photons to combined muons and electrons, respectively. Figure 7.9 shows the vast increase in the signal lepton reconstruction efficiency due to the re-tracking procedure. The efficiencies are above 80% up to an impact parameter of 30 and 50 mm for electrons and muons, respectively, and even for the maximum considered value of $|d_0| = 300$ mm an efficiency of about 10% is retained.

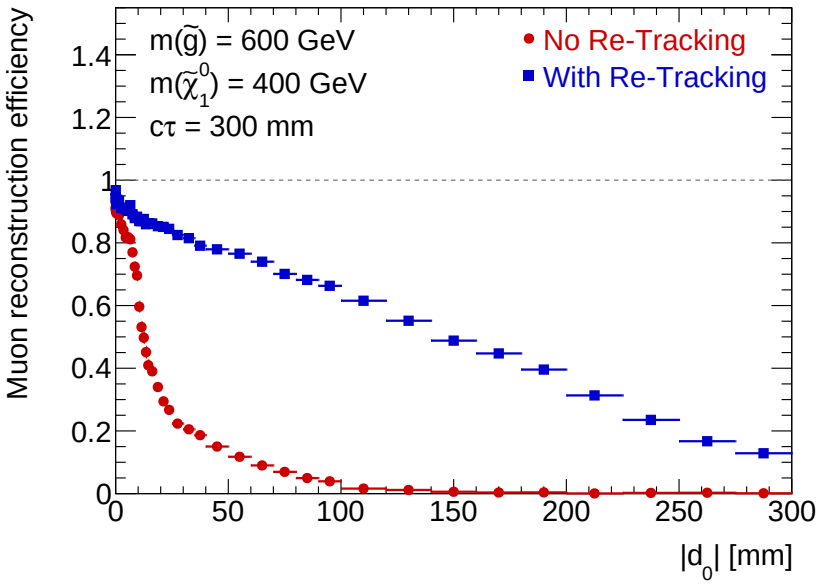

(a)

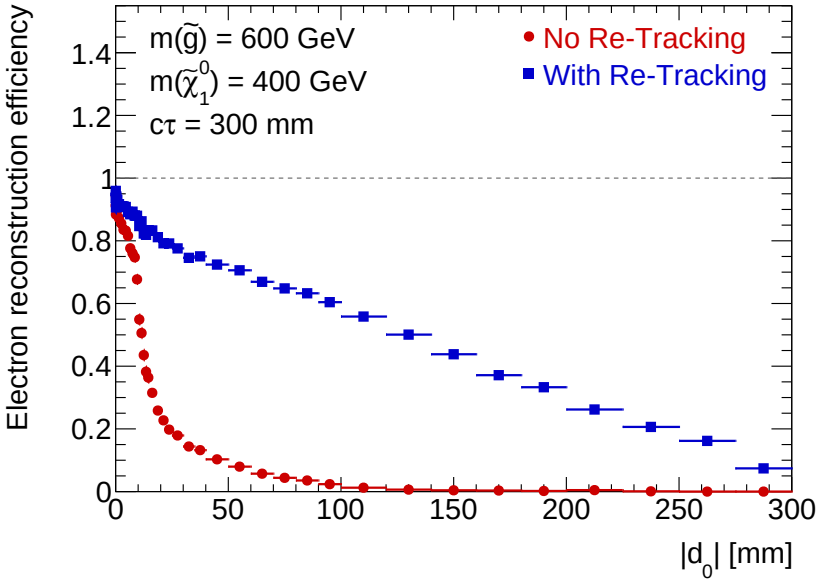

(b)

Figure 7.9: Reconstruction efficiency of combined muons (a) and *Loose* electrons (b) from neutralino decays via $\lambda_{121/122}$ couplings for the gluino model with $m_{\tilde{g}}$ = 600 GeV and $m_{\tilde{\chi}_1^0}$ = 400 GeV as a function of the transverse impact parameter $|d_0|$ of the event-generator level particle trajectory, before and after the re-tracking procedure. Statistical errors are given.

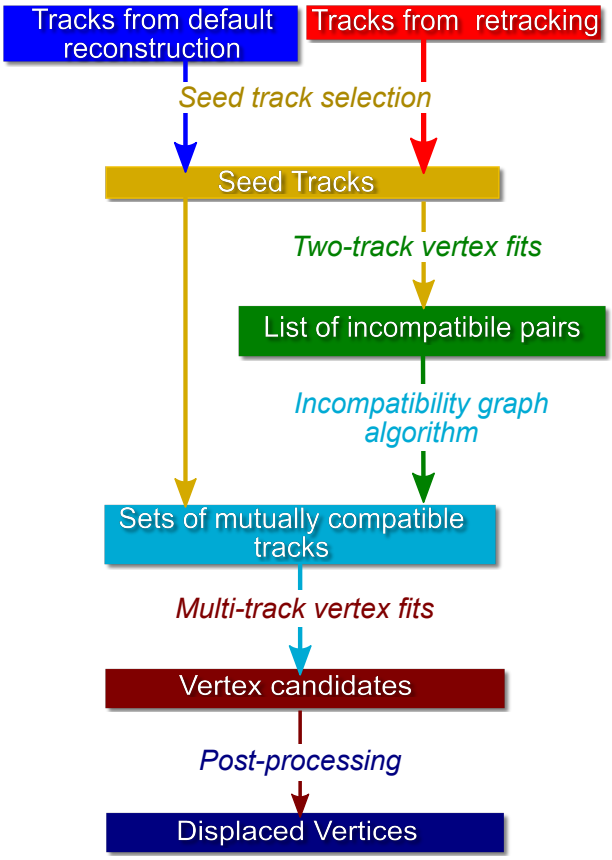

Figure 7.10: Flow diagram of the displaced vertex reconstruction procedure. The boxes indicate input and output data, the text in between the application of algorithms.

7.4.2 Displaced Vertex Reconstruction

After the new track and lepton reconstruction, displaced vertices are identified using Inner Detector tracks fulfilling the *seed track* requirements listed in Table 7.3. A flow diagram of the procedure is shown in Figure 7.10. These cuts, in particular the requirement of high transverse impact parameter, separate tracks from displaced decays from those originating from primary vertices [137, 138]. The contribution of tracks from pile-up interaction vertices and soft hadronic processes (the underlying event) is further reduced by a transverse momentum cut. To ensure a precise measurement of the impact parameter, a minimum number of hits in the silicon tracking detectors is required. Tracks with only SCT hits are rejected to suppress track misidentifications in the forward direction.

From the seed tracks, pairs are identified which can form common vertices. First, a two-track vertex fit is performed for every possible track pair, using the standard ATLAS

Table 7.3: Seed Track requirements used for the displaced vertex reconstruction [138].

Seed track requirements	
Transverse momentum	$p_{\mathrm{T}} > 1$ GeV
Impact parameter	$\lvert d_0 \rvert > 2$ mm
SCT hits on track	≥ 2
Pixel and TRT hits on track	at least one TRT hit or two pixel hits

Table 7.4: Requirements on two-track displaced vertices (DV) used as seed vertices [138].

Seed vertex requirements	
Fit quality	$\frac{\chi^2_{\mathrm{fit}}}{N_{\mathrm{d.o.f}}} < 5$
Inner hit veto	No silicon hits on tracks at $r < r_{\mathrm{DV}}$
Back pointing momentum veto	$(\vec{r}_{DV} - \vec{r}_{PV}) \cdot \frac{\vec{p}_{DV}}{\lvert\vec{p}_{DV}\rvert} > -20$ mm

vertex fitter (Section 3.3.1). Two tracks are considered compatible with a common vertex if the fit yields a *seed vertex*, a valid solution that passes additional requirements listed in Table 7.4 [138]. The *inner hit veto* rejects pairs where one of the tracks contains hits at radial locations r closer to the interaction point than the fitted radial vertex location r_{DV}, assuming that particles produced in the decay travel outward in the detector from their origin. The *back-pointing momentum veto* rejects vertex candidates where the track momentum sum points inwards to the interaction point.

The compatibility information obtained this way is translated into an incompatibility map listing pairs of incompatible tracks. This is used as input to the so called Incompatibility Graph algorithm [139], which finds sets of tracks mutually compatible with a common vertex. For each such track combination resulting from the Incompatibility Graph algorithm, a multi-track vertex fit is performed. Vertex candidates resulting from this procedure may still have tracks in common. Therefore, a post-processing step is carried out. If a track is associated to more than one displaced vertex candidate and the locations of the candidates are compatible with one another within 3σ and the track is well compatible with all vertex candidates ($\chi^2/N_{\mathrm{d.o.f}} < 6$), the candidates are merged into one and refit. Otherwise, the common track is removed from all vertices except the one with which it has the smallest χ^2 of the fit. Finally, also vertices closer than 1 mm are merged and refit. The resulting displaced vertices are used for further analysis.

While the displaced dilepton vertex signal is expected to yield vertices with only two tracks, performing the full multi-track reconstruction procedure ensures consistency

with other displaced vertex search channels [137] and correct reconstruction of potential signal vertices with higher track multiplicities from other sources than the RPV SUSY models studied in this thesis.

Figure 7.11 shows the efficiency of the displaced vertex reconstruction and its individual steps for signal LSP decays into two light leptons with $c\tau$ = 300 mm in the gluino NLSP model. To obtain a displaced vertex, the two decay leptons have to be reconstructed in the Inner Tracker by the standard reconstruction or the re-tracking. The corresponding efficiency is high but slowly decreases with increasing radius of the neutralino decay vertex. The seed track criteria reject a large fraction of signal decays with small radii in particular through the requirement of a large transverse impact parameter. This is especially pronounced for a light neutralino. For decay radii between 50 and 300 mm, these cuts show efficiencies between 40% and 50%. Between 50% and 80% of the decays with two identified seed tracks also have a successfully reconstructed displaced vertex. The efficiency of the displaced vertex reconstruction is rather stable with respect to the radial vertex displacement. For small neutralino mass, it is slightly higher than for higher mass, due to the smaller lepton track opening angle. The overall vertex reconstruction efficiency reaches a maximum value of about 40%.

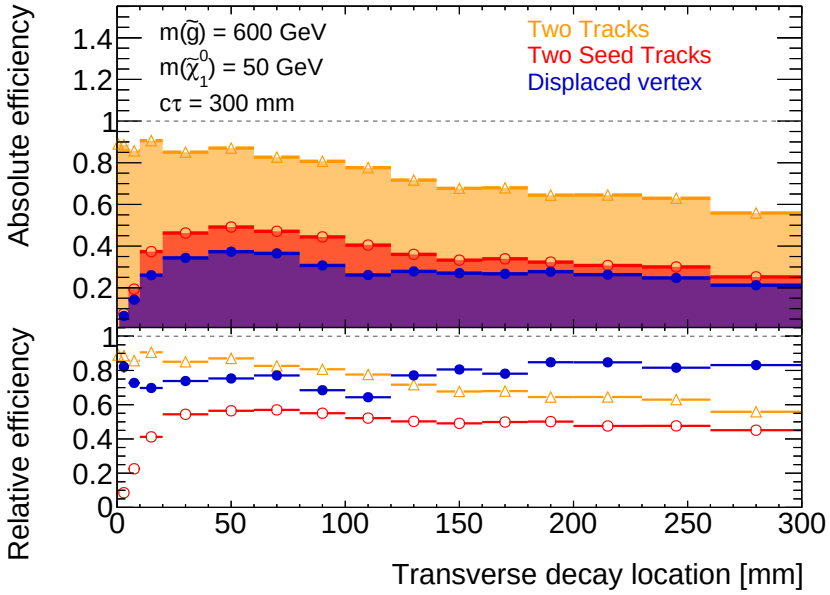

(a)

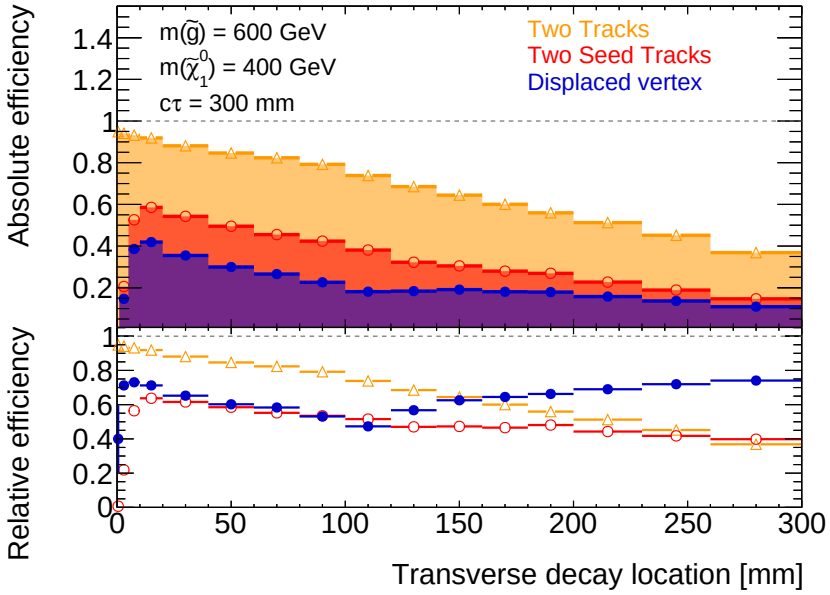

(b)

Figure 7.11: Efficiencies of the different steps of the displaced vertex reconstruction, the identification of two lepton tracks (orange), seed track selection requirements (red) and vertex finding (blue), as a function of the radial neutralino decay location for an active λ_{121} coupling in the gluino model with $m_{\tilde{g}} = 600$ GeV, $c\tau = 300$ mm and $m_{\tilde{\chi}_1^0} = 50$ GeV (a) or $m_{\tilde{\chi}_1^0} = 400$ GeV (b). Relative efficiencies are with respect to the previous step in the vertex reconstruction procedure.

7.5 Vertex Selection Criteria

Once displaced vertices have been reconstructed, further selection criteria are applied to reduce the backgrounds to negligible levels. The rarity of the displaced vertex signature allows to achieve a vanishing background.

7.5.1 Background Sources

Displaced vertices occur in Standard Model decay processes, in particular two-body meson and baryon decays like $K_S^0 \to \pi^+\pi^-$ with a decay length of $c\tau = 2.7$ cm [65], and can be strongly suppressed since the masses of the resulting vertices are small, below about 5 GeV (i.e. $B^\pm \to J/\psi\pi^\pm \to \mu\mu\pi^\pm$), and because only a small fraction of the decays lead to two final state leptons.

Other backgrounds are due to detector effects.

Cosmic ray muons traversing the detector are reconstructed as a pair of oppositely charged muon tracks pointing in exactly opposite directions from an, in general displaced, vertex which can be reconstructed by the vertex finding algorithm. The signature of two muon trajectories pointing in exactly opposite directions makes it possible to distinguish cosmic muons from the signal.

Displaced vertices can also originate from particle interactions with detector material. Such vertices can be recognised by their location in detector regions with material.

The dominant background source are random crossings of two lepton tracks in the detector satisfying the seed track and vertex requirements of the displaced vertex search, which too are rare but show no single specific signature which could distinguish them from the signal as effectively as the other backgrounds.

7.5.2 Vertex Selection

In the search for displaced dilepton vertices, three signal regions are defined depending on the flavours of the leptons, requiring at least two electrons (ee), at least one electron and at least one muon ($e\mu$) or at least two muons ($\mu\mu$) associated to the vertex. These may overlap, for example if a vertex has more than two associated leptons. Apart from the lepton flavour composition, the requirements for all signal regions are identical. For certain results like model-dependent cross-section limits, the three regions are combined

into one flavour-independent signal region which accepts displaced vertices with at least two light leptons (e, μ) of any flavour combination, the union of the three flavour-specific regions.

To ensure that a hard interaction took place, displaced vertex candidates are only considered if there is at least one primary vertex candidate with more than five associated tracks in the same event.

Displaced vertex candidates are restricted to the fiducial region in the Inner Detector with $0 < r_{\mathrm{DV}} < 300$ mm and -300 mm $< z_{\mathrm{DV}} < 300$ mm with respect to centre of the detector. In addition, displaced vertices are required to have a transverse distance

$$\Delta_{xy} = \sqrt{(x_{\mathrm{DV}} - x_{\mathrm{PV}})^2 + (y_{\mathrm{DV}} - y_{\mathrm{PV}})^2}$$

of at least 4 mm to each reconstructed primary vertex with coordinates $(x_{\mathrm{PV}}, y_{\mathrm{PV}})$ in the transverse plane, selecting only long-lived particle decays while strongly suppressing short-lived hadron decays with typical decay lengths of several hundred micrometers and misreconstructed prompt decays. To ensure a well-reconstructed vertex, the χ^2 of the final vertex fit for the displaced vertex candidate is restricted to less than five times the number of degrees of freedom in the vertex fit.

After these requirements, there is still a significant contribution from interactions of particles with the detector material. Figure 7.12a shows the locations of vertices identified by the procedure outlined in Section 7.4.2, after the above requirements. No requirements are made on the number of tracks associated with the vertex or their identification as leptons. The beam pipe (r = 29–36 mm), the three concentric layers of the pixel detector ($r = 51, 89, 122$ mm) and several layers of pixel detector support material (r = 75 mm, 110 mm, 190–210 mm, 230 mm and 260 mm) stand out with enhanced concentrations of identified vertices.

A material veto against vertices reconstructed in this detector material is constructed based on a three-dimensional map of the known locations of detector material including support structures, the beam pipe and the measured locations of individual pixel modules. Approximately 42% of the fiducial volume is discarded in this way, mostly at $r > 180$ mm. Surviving vertices are shown in Figure 7.12a.

The remaining displaced vertices are required to contain at least two light charged leptons, electrons or muons. For the ee, $e\mu$ and $\mu\mu$ signal regions, at least two electrons, one electron and one muon or two muons, respectively, are required to be associated

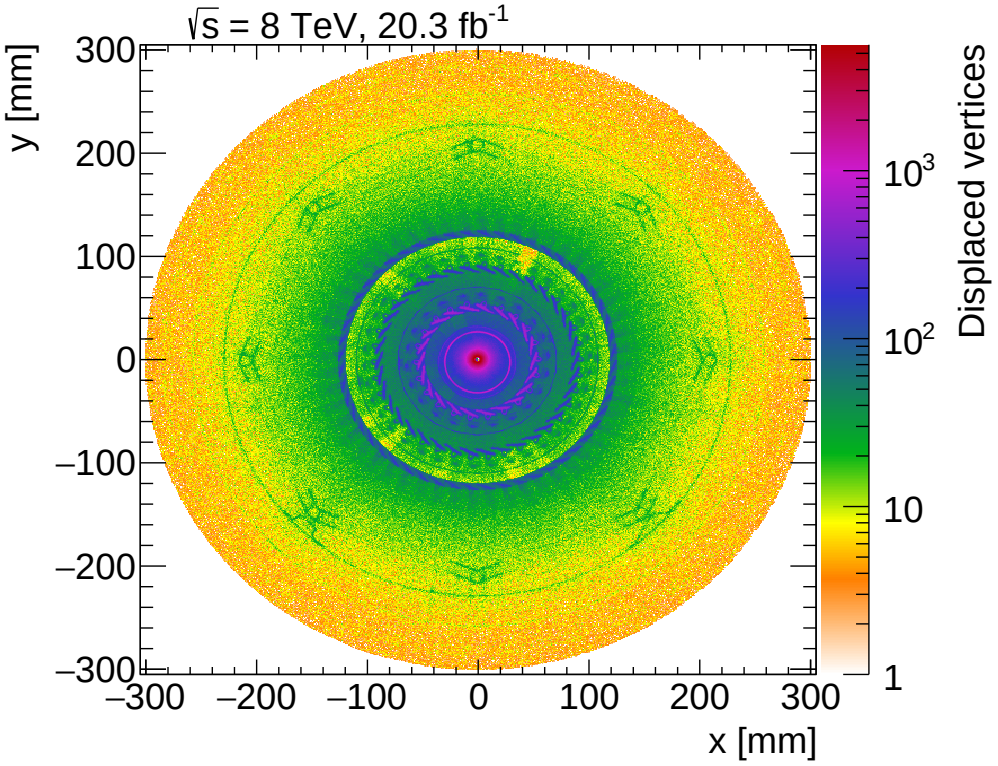

(a)

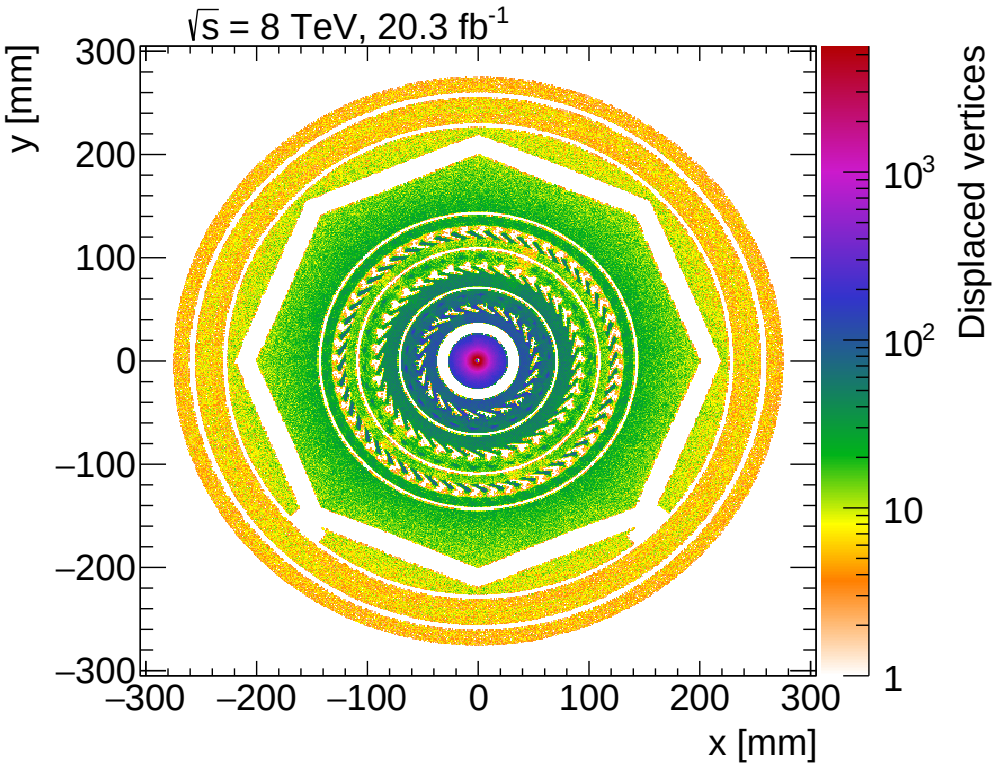

(b)

Figure 7.12: Location of displaced vertices in the tracker fiducial volume reconstructed in the 2012 data set (a) and accepted by the material veto (b). No requirements are made on the composition of the vertices or the invariant mass of the associated tracks and, especially, the presence of leptons.

to the vertex. Additional leptons of arbitrary flavour as well as non-lepton tracks are allowed to be associated to the vertex, in order to provide sensitivity to as wide a range of models as possible.

For leptons emerging from the vertex, a minimum transverse momentum of 10 GeV is required to suppress hadron decays and misidentified leptons. Muons are required to be reconstructed by the combined method (see Section 3.3.6), while electrons need to satisfy the *Loose* identification criteria, adapted for displaced decays by removing requirements on the number of silicon sensors crossed by the track and requesting instead a minimum number of high-threshold hits (see Section 3.2.2) in the TRT for tracks with $|\eta| < 2.0$ within the TRT acceptance [138]. An overlap removal procedure following Table 7.5 is applied to resolve cases where a track at a vertex is associated with two different reconstructed leptons.

Table 7.5: Overlap removal procedure for leptons sharing an Inner Detector track.

Overlap removal procedure		
Step	Objects sharing a track	Action
1	Two electrons	Remove lower E_{T} electron
2	Two muons	Remove lower p_{T} muon
3	Electron and muon	Remove both

Cosmic rays are suppressed by rejecting vertices containing a pair of leptons 1, 2 pointing in exactly opposite directions. The variable

$$\Delta R^{\mathrm{cosmic}} = \sqrt{(\Delta\phi - \pi)^2 + (\eta_1 + \eta_2)^2} \tag{7.1}$$

is used to quantify the deviation in the η–ϕ plane from the topology expected for cosmic rays, i.e. $\eta_1 = -\eta_2$ and $\Delta\phi = \pi$, requiring $\Delta R^{\mathrm{cosmic}} > 0.04$ to reject cosmic ray muons. As muons could also be misreconstructed as electrons, the cosmic veto takes into account combinations of electron and muon tracks or two electron tracks, and not only muon pairs.

Finally, to allow interpretation at the level of observed vertices, two leptons at the vertex must to satisfy one of the trigger and offline filter requirements of Section 7.3.

To suppress hadron decays with displacements sufficient to pass the Δ_{xy} cut, an invariant mass of the tracks at the vertex of $m_{\mathrm{DV}} \geq 10$ GeV is required. As the LSP decays into two

leptons of opposite charge in the models under consideration, the displaced vertices are also required to contain at least one lepton of each charge. The background of random track crossings is independent of charge and, therefore, reduced by a factor of two by this requirement. Table 7.6 summarises the selection criteria.

Table 7.6: Selection criteria of displaced dilepton vertices (DV).

Primary vertex	$n_{\text{Tracks}} > 5$
Cosmic muon veto	$\Delta R^{\text{cosmic}} > 0.04$ for all lepton pairs
Fiducial volume	$\lvert r_{\text{DV}}\rvert < 300$ mm, $\lvert z_{\text{DV}}\rvert < 300$ mm
Distance to any PV	$\Delta_{xy} > 4$ mm
Vertex fit quality	$\chi^2/N_{\text{d.o.f.}} \leq 5$
Material veto	Reject vertices in regions with known material
Dilepton decay	≥ 2 leptons at the vertex
Lepton transverse momentum	$p_{\text{T}}^{\text{ID}} > 10$ GeV for both leptons measured in the Inner Detector (ID)
Trigger and filter	Leptons at the vertex fulfil trigger and offline filter criteria
Dilepton charge	At least one lepton of each charge
Invariant vertex mass	$m_{\text{DV}} > 10$ GeV

Tables 7.7 to 7.9 show the expected number of LSP decay vertices accepted after each of the analysis selection requirements for an example signal model with $m_{\tilde{g}} = 600$ GeV, $m_{\tilde{g}} = 400$ GeV and $c\tau_{\text{LSP}} = 300$ mm. The first major efficiency loss is due to the reconstruction of a displaced vertex candidate. The material veto and the offline filter requirements are further causes for inefficiency. Apart from these unavoidable losses, all requirements applied in the analysis to suppress backgrounds are highly efficient on the signal. Therefore, no dedicated optimisation of the selection criteria (for example based on S/B) is performed. The total signal efficiency is close to 5% for decays into two electrons, 6% for decays into an electron and a muon and 8% for dimuon final states.

Table 7.7: Expected number N_{vtx} of displaced vertices of LSP decays into electron pairs and total (ϵ_{abs}) and relative (ϵ_{rel}) efficiencies at different stages of the vertex selection for $m_{\tilde{g}} = 600$ GeV and $m_{\tilde{\chi}_1^0} = 400$ GeV. The neutralino decay is assumed to occur via a λ_{121} coupling with a decay length of $c\tau = 300$ mm.

Requirement	N_{vtx}	ϵ_{rel} [%]	ϵ_{abs} [%]
LSP decays	$(2.604\pm0.022) \cdot 10^4$	0±0	100±0
Primary vertex	$(2.520\pm0.022) \cdot 10^4$	96.78±0.08	96.78±0.08
Reconstructed DV	$(4.00\pm0.08) \cdot 10^3$	15.87±0.30	15.36±0.29
Fiducial volume	$(3.87\pm0.08) \cdot 10^3$	96.68±0.35	14.85±0.29
$\Delta_{xy} > 4$ mm	$(3.79\pm0.08) \cdot 10^3$	98.02±0.29	14.55±0.29
$\chi^2/N_{\text{d.o.f.}} \leq 5$	$(3.79\pm0.08) \cdot 10^3$	100±0	14.55±0.29
Material veto	$(2.67\pm0.07) \cdot 10^3$	70.5±1.0	10.26±0.25
Two associated leptons	$(2.38\pm0.06) \cdot 10^3$	89.2±0.8	9.16±0.23
Lepton η, p_{T} requirements	$(2.28\pm0.06) \cdot 10^3$	95.7±0.6	8.76±0.23
Lepton quality criteria	$(2.11\pm0.06) \cdot 10^3$	92.3±0.8	8.09±0.22
Cosmics veto	$(2.10\pm0.06) \cdot 10^3$	99.53±0.20	8.05±0.22
Trigger and filter requirement	$(1.30\pm0.05) \cdot 10^3$	61.8±1.3	4.98±0.18
DV mass	$(1.29\pm0.05) \cdot 10^3$	99.90±0.10	4.97±0.17
Opposite di-lepton charge	$(1.29\pm0.05) \cdot 10^3$	99.38±0.20	4.94±0.17

Table 7.8: Expected number N_{vtx} of displaced vertices of LSP decays into an electron and a muon and total (ϵ_{abs}) and relative (ϵ_{rel}) efficiencies at different stages of the vertex selection for $m_{\tilde{g}} = 600\,\text{GeV}$ and $m_{\tilde{\chi}_1^0} = 400\,\text{GeV}$. The neutralino decay is assumed to occur via a λ_{121} coupling with a decay length of $c\tau = 300$ mm.

Requirement	N_{vtx}	ϵ_{rel} [%]	ϵ_{abs} [%]
LSP decays	$(2.604\pm0.022)\cdot10^4$	0±0	100±0
Primary vertex	$(2.500\pm0.022)\cdot10^4$	96.02±0.06	96.02±0.06
Reconstructed DV	$(4.88\pm0.09)\cdot10^3$	19.51±0.34	18.73±0.32
Fiducial volume	$(4.66\pm0.09)\cdot10^3$	95.5±0.4	17.89±0.32
$\Delta_{xy} > 4$ mm	$(4.59\pm0.09)\cdot10^3$	98.62±0.23	17.64±0.31
$\chi^2/N_{\text{d.o.f.}} \leq 5$	$(4.59\pm0.09)\cdot10^3$	100±0	17.64±0.31
Material veto	$(3.21\pm0.08)\cdot10^3$	69.9±0.9	12.33±0.27
Two associated leptons	$(2.92\pm0.07)\cdot10^3$	90.9±0.6	11.21±0.26
Lepton η, p_{T} requirements	$(2.83\pm0.07)\cdot10^3$	96.8±0.4	10.86±0.26
Lepton quality criteria	$(2.64\pm0.07)\cdot10^3$	93.5±0.7	10.15±0.25
Cosmics veto	$(2.62\pm0.07)\cdot10^3$	98.96±0.30	10.04±0.25
Trigger and filter requirement	$(1.63\pm0.05)\cdot10^3$	62.2±1.3	6.25±0.20
DV mass	$(1.63\pm0.05)\cdot10^3$	99.91±0.09	6.24±0.20
Opposite di-lepton charge	$(1.62\pm0.05)\cdot10^3$	99.72±0.12	6.23±0.20

Table 7.9: Expected number N_{vtx} of displaced vertices of LSP decays into a pair of muons and total (ϵ_{abs}) and relative (ϵ_{rel}) efficiencies at different stages of the vertex selection for $m_{\tilde{g}} = 600$ GeV and $m_{\tilde{\chi}_1^0} = 400$ GeV. The neutralino decay is assumed to occur via a λ_{122} coupling with a decay length of $c\tau = 300$ mm.

Requirement	N_{vtx}	ϵ_{rel} [%]	ϵ_{abs} [%]
LSP decays	$(2.594\pm0.022) \cdot 10^4$	0±0	100±0
Primary vertex	$(2.489\pm0.022) \cdot 10^4$	95.94±0.07	95.94±0.07
Reconstructed DV	$(5.50\pm0.09) \cdot 10^3$	22.10±0.34	21.21±0.33
Fiducial volume	$(5.27\pm0.09) \cdot 10^3$	95.78±0.32	20.31±0.32
$\Delta_{xy} > 4$ mm	$(5.19\pm0.09) \cdot 10^3$	98.62±0.21	20.03±0.32
$\chi^2/N_{\text{d.o.f.}} \leq 5$	$(5.19\pm0.09) \cdot 10^3$	100±0	20.03±0.32
Material veto	$(3.66\pm0.08) \cdot 10^3$	70.5±0.8	14.12±0.28
Two associated leptons	$(3.27\pm0.07) \cdot 10^3$	89.3±0.6	12.61±0.27
Lepton η, p_{T} requirements	$(3.22\pm0.07) \cdot 10^3$	98.59±0.25	12.43±0.27
Lepton quality criteria	$(3.14\pm0.07) \cdot 10^3$	97.3±0.4	12.10±0.26
Cosmics veto	$(3.09\pm0.07) \cdot 10^3$	98.54±0.24	11.92±0.26
Trigger and filter requirement	$(2.18\pm0.06) \cdot 10^3$	70.5±1.1	8.41±0.22
DV mass	$(2.18\pm0.06) \cdot 10^3$	99.94±0.06	8.40±0.22
Opposite di-lepton charge	$(2.18\pm0.06) \cdot 10^3$	100±0	8.40±0.22

7.6 Signal Predictions

7.6.1 Lifetime Reweighting

Four discrete values of the neutralino decay length have been simulated (see Section 7.2). Signal predictions for arbitrary decay lengths are obtained by interpolation. For a given LSP mean lifetime τ, the proper decay time t follows an exponential distribution

$$f(t|\tau) = \frac{1}{\tau} \exp\left(-\frac{t}{\tau}\right). \tag{7.2}$$

This is used to reweight the simulated samples, produced with a specific lifetime τ_{sim}, to obtain predictions for a new lifetime τ with a weight factor

$$w(t) = \frac{f(t|\tau)}{f(t|\tau_{\text{sim}})} = \frac{\tau_{\text{sim}}}{\tau} \exp\left[-t\left(\frac{1}{\tau} - \frac{1}{\tau_{\text{sim}}}\right)\right] \tag{7.3}$$

for each decay in the simulated sample.

Figure 7.13 illustrates the effect of the reweighting procedure for a Monte Carlo sample

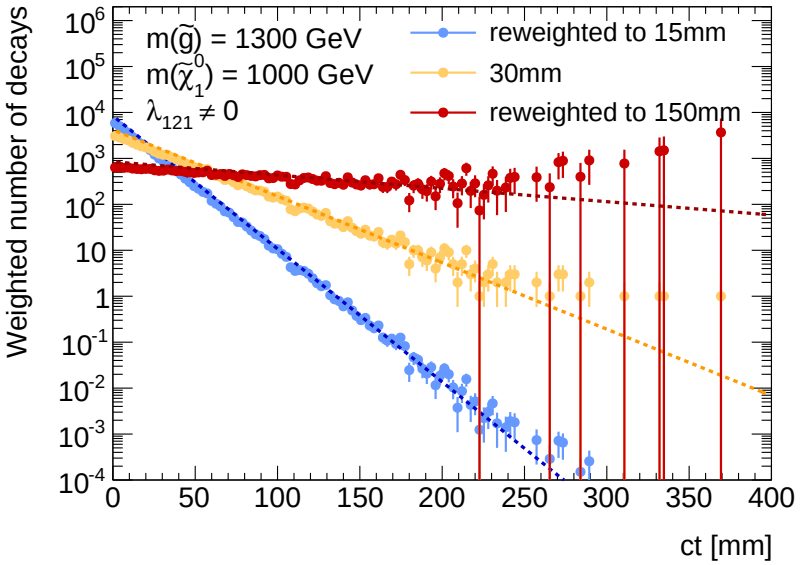

Figure 7.13: Proper decay time distributions of a neutralino LSP with simulated lifetime of 100 ps corresponding to a decay length of 30 mm and after reweighting to decay lengths of 15 mm and 150 mm. The dashed lines represent the ideal distributions predicted by Eq. (7.2).

of $4 \cdot 10^4$ LSP decays with a lifetime of 100 ps corresponding to a decay length of 30 mm. The reweighted distributions reproduce the desired target lifetime spectra in each case. Reweighting to target lifetimes significantly above or below the simulated lifetime increases the statistical uncertainty in the signal prediction, as a small subset of the simulated events is assigned high weights. This is especially problematic when reweighting to higher lifetimes. The example of a 150 mm target lifetime in Figure 7.13 illustrates how individual simulated decays are weighted by factors of 10^3 and more.

Therefore, the four simulated lifetime values of 3 mm/c, 30 mm/c, 300 mm/c and 3000 mm/c were chosen to avoid downward reweighting by more than a factor 10. Reweighting the highest lifetime sample upwards is unproblematic, as the decays that would receive high weights occur outside the fiducial volume and hence do not enter the signal yield.

7.6.2 Systematic Uncertainties

Systematic uncertainties in the calculation of the production cross-sections are the same as for the four-lepton analysis (see Section 6.5) and dominate the error on the signal prediction. In addition, several further uncertainties have been taken into account. The finite number of simulated events results in a statistical uncertainty in the predicted signal efficiency, which is below 7% for most of the lifetime reach with the exception of very short lifetimes ($\tau < 1$ mm/c), where a small number of events are assigned large weights via Eq. (7.3) and the statistical uncertainty in the signal yield can reach 50%.

To take into account a possible dependence of the displaced vertex reconstruction efficiency on the number of pile-up interactions, the simulated events are reweighted based on the mean number of proton-proton interactions per bunch crossing μ to reproduce the mean number of pile-up interaction as found in the data [138]. Uncertainties in the weight factors and the description of the pile-up interactions in the Monte Carlo simulation contribute less than 6% to the overall uncertainty and are never statistically significant.

The lepton trigger efficiencies are determined from data using a tag-and-probe method similar to the technique discussed in Section 4.1 [138]. Scale factors are applied to correct the simulation to reproduce the data. The uncertainties in these scale factors, between 0.8% and 2.1%, result in an uncertainty of less than 5% in the signal prediction for all final states.

Finally, there are uncertainties in the reconstruction and identification efficiencies of leptons from displaced vertices. Cosmic ray muons are used to measure the muon reconstruction efficiency as a function of the transverse impact parameter [138]. The resulting scale factor applied to simulated events has an uncertainty of up to 4%. In the case of electrons, a direct efficiency measurement as a function of $|d_0|$ is not possible due to a lack of processes producing electrons with large transverse impact parameters. Instead, the efficiency is studied as a function of the longitudinal impact parameter z_0 and found to be consistent between data and Monte Carlo simulation. The simulation is assumed to also describe high-$|d_0|$ electrons well, and a conservative uncertainty of 10% is assigned to cover differences in the efficiency as a function of d_0 between different signal samples [138]. The identification of displaced leptons is therefore a dominant source of uncertainty in the signal prediction (see Figure 7.14). For dimuon decays, it is typically around 7%, for decays to one electron and one muon approximately 11% and for decays to two electrons 21%. Tables 7.10 to 7.12 summarise the systematic uncertainties obtained for $c\tau_{\text{LSP}} = 300$ mm for all LSP decay final states for the four gluino-neutralino mass points studied.

Table 7.10: Systematic uncertainties (in percent) associated with the $\tilde{\chi}_1^0 \to ee\nu$ signal yield prediction in the gluino model with different NLSP-LSP mass combinations for 300 mm decay length.

	$m_{\tilde{g}}$[GeV] / $m_{\tilde{\chi}_1^0}$ [GeV], $c\tau_{\text{LSP}} = 300$ mm			
Uncertainty [%]	600 / 50	600 / 400	1300 / 50	1300 / 1000
MC Statistics	12	4	10	3
Pile-up	5	2	5	1
Trigger	4	3	2	2
Electron identification	21	21	21	21
Overall	25	22	24	21

7.6.3 Signal Predictions

Figures 7.15 to 7.17 show the product of acceptance and efficiency of the LSP decay vertex selection for the three flavour final states as a function of $c\tau$. Peak efficiencies of approximately 3–6% for decay lengths $c\tau \approx 10$ mm are reached for boosted light neutralino decays, while around 15% maximum efficiency is obtained for $c\tau = 30$–60 mm for heavy neutralinos. Towards smaller lifetimes, the selection efficiency decreases due

Table 7.11: Systematic uncertainties (in percent) associated with the $\tilde{\chi}_1^0 \to e\mu\nu$ signal yield prediction in the gluino model with different NLSP-LSP mass combinations for 300 mm decay length.

	$m_{\tilde{g}}$ [GeV] / $m_{\tilde{\chi}_1^0}$ [GeV], $c\tau_{\text{LSP}}$ = 300 mm			
Uncertainty [%]	600 / 50	600 / 400	1300 / 50	1300 / 1000
MC Statistics	7	2	7	2
Pile-up	2	1	1	2
Trigger	1	1	1	1
Electron identification	10	10	10	10
Muon identification	3	3	3	3
Overall	13	11	13	11

Table 7.12: Systematic uncertainties (in percent) associated with the $\tilde{\chi}_1^0 \to \mu\mu\nu$ signal yield prediction in the gluino model with different NLSP-LSP mass combinations for 300 mm decay length.

	$m_{\tilde{g}}$ [GeV] / $m_{\tilde{\chi}_1^0}$ [GeV], $c\tau_{\text{LSP}}$ = 300 mm			
Uncertainty [%]	600 / 50	600 / 400	1300 / 50	1300 / 1000
MC Statistics	8	3	8	2
Pile-up	2	3	3	2
Trigger	2	2	2	2
Muon identification	7	7	7	7
Overall	11	8	11	8

to the $|d_0|$ and minimum vertex displacement requirements. Towards higher lifetimes, the efficiency drops again because an increasing number of decays tend to occur outside the fiducial volume of $r_{\text{DV}} < 300$ mm. Model-dependent event selection efficiencies for different couplings are shown in Figure 7.18. They give the probabilities of reconstructing at least one displaced decay in an event where two $\tilde{\chi}_1^0$ decays occur. The event efficiencies ϵ_e are related to the vertex efficiencies ϵ_v by $\epsilon_e = 1 - (1 - \epsilon_v)^2$. Peak values of ϵ_e are up to 30% for a heavy neutralino and up to 10% for a light neutralino. The gluino mass plays a relatively minor role. The efficiencies for the heavy gluino are slightly above the ones for the lighter gluino due to the higher energies of the final-state particles, which lead to an enhances trigger and offline filter efficiency.

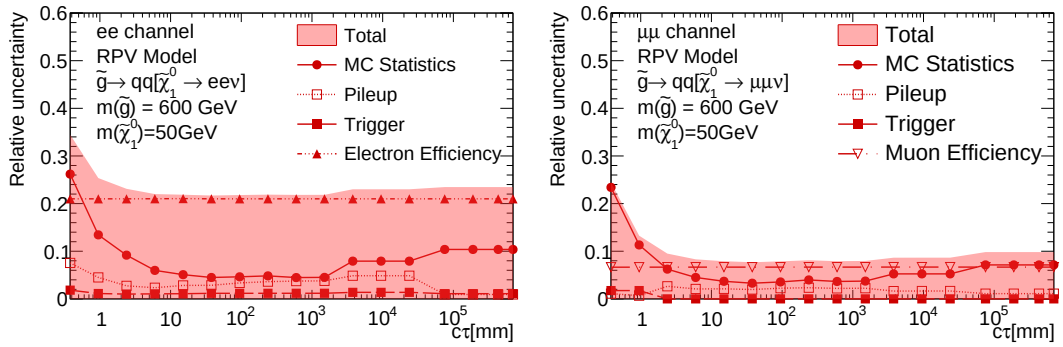

(a) **(b)**

Figure 7.14: Systematic uncertainties in the predicted yields of reconstructed displaced vertices from ee (a) and $\mu\mu$ (b) LSP decays in the gluino model with $m_{\tilde{g}} = 600$ GeV and $m_{\tilde{\chi}_1^0} = 50$ GeV.

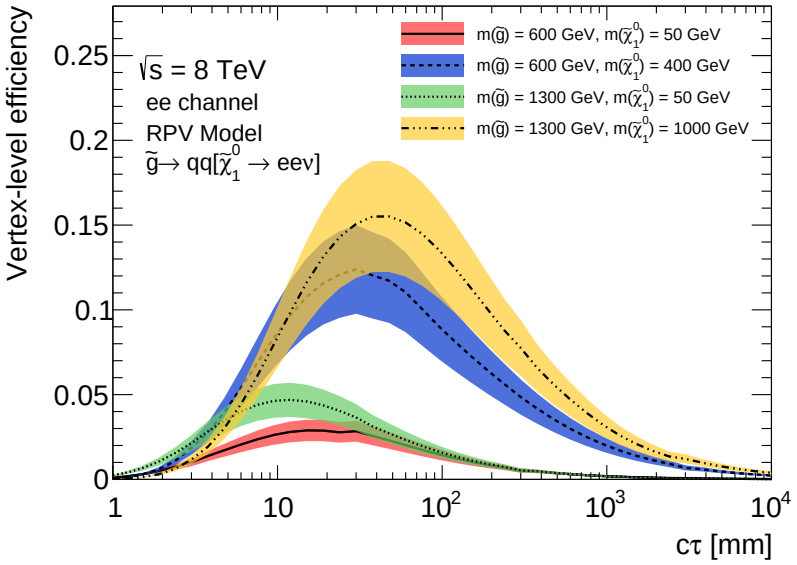

Figure 7.15: Displaced dilepton vertex acceptance times efficiency for $\tilde{\chi}_1^0 \to ee\nu$ decays as a function of the mean neutralino decay length $c\tau$ for the four NLSP-LSP mass combinations studied. The systematic uncertainties are indicated as coloured bands.

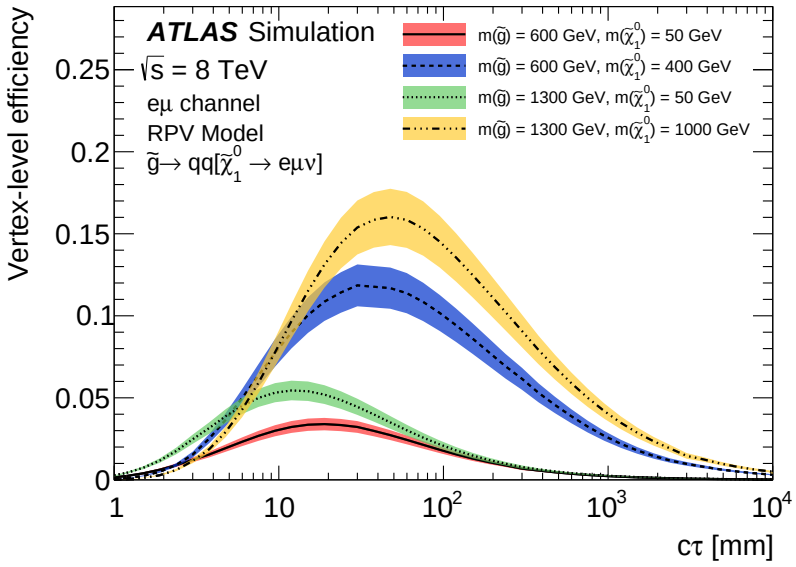

Figure 7.16: Displaced dilepton vertex acceptance times efficiency for $\tilde{\chi}_1^0 \to e\mu\nu$ decays as a function of the mean neutralino decay length $c\tau$ for the four NLSP-LSP mass combinations studied. The systematic uncertainties are indicated as coloured bands

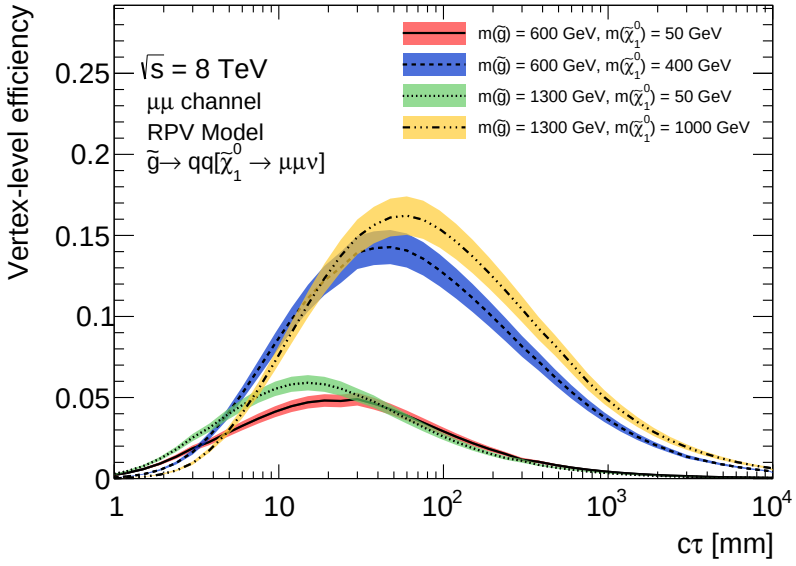

Figure 7.17: Displaced dilepton vertex acceptance times efficiency for $\tilde{\chi}_1^0 \to \mu\mu\nu$ decays as a function of the mean neutralino decay length $c\tau$ for the four NLSP-LSP mass combinations studied. The systematic uncertainties are indicated as coloured bands.

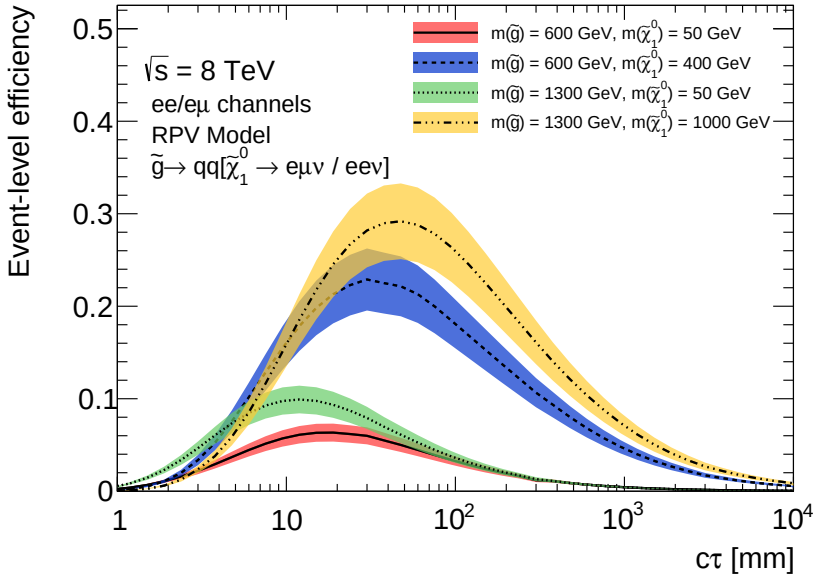

(a)

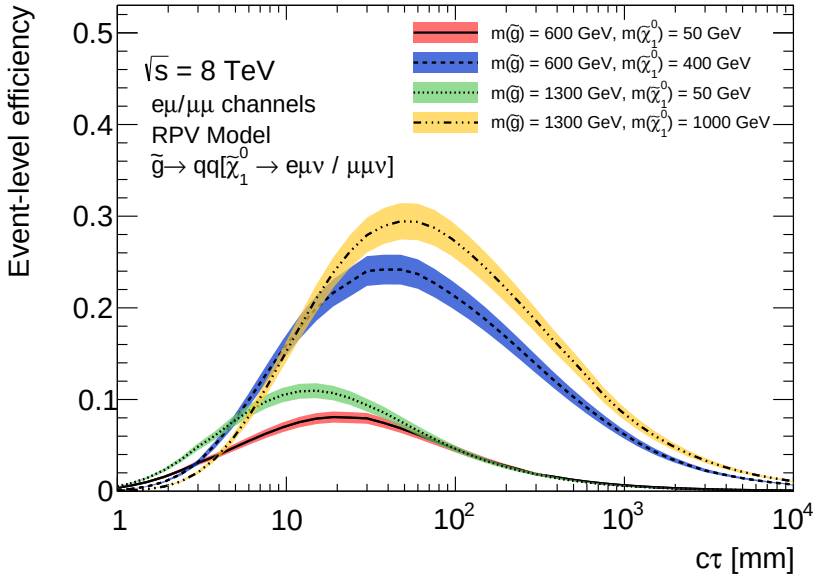

(b)

Figure 7.18: Acceptance times efficiency for pair production of LSPs decaying via $\tilde{\chi}_1^0 \to \ell\ell\nu$ with nonzero λ_{121} (a) and λ_{122} (b) couplings as a function of the mean neutralino decay length $c\tau$ for the four NLSP-LSP mass combinations studied. The systematic uncertainties are indicated as coloured bands.

7.7 Random Crossing Background Estimation

7.7.1 Estimation Method

The dominant background contribution from randomly crossing lepton tracks is estimated by a fully data-driven method. The expected number of displaced vertices N_{DV} resulting from random crossings of lepton track pairs is given by

$$N_{DV} = f_{\mathrm{DV}} \cdot N_{\ell\ell'}, \tag{7.4}$$

where $N_{\ell\ell'}$ $(\ell, \ell' = e, \mu)$ is the number of so-called *seed lepton pairs*, uncorrelated pairs of leptons in an event which fulfil the lepton selection criteria (see Section 7.5) and the requirements for the displaced vertex reconstruction algorithm (see Section 7.4.2). f_{DV} is the so-called *crossing probability*, the probability for an uncorrelated lepton pair to form a displaced vertex passing the signal requirements. To estimate this random crossing probability, lepton tracks from different events are randomly combined to pairs and fitted to a common vertex. The crossing fraction is the fraction of fits resulting in vertices fulfilling all signal criteria. The use of individual vertex fits allows the prediction of differential distributions of vertex properties in addition to the overall number of vertices.

As the leptons in a pair are uncorrelated, azimuthal symmetry is exploited to maximise the statistical precision of the estimate by assuming that every angular separation $\Delta\phi$ between the two leptons in the transverse plane occurs with the same probability. One of the leptons of a random pair is, therefore, rotated through all possible values of the track azimuthal angle parameter ϕ in steps of $\delta\phi = 10^{-3}$, increasing the number of independent track pairs by a factor of $2\pi/\delta\phi \approx 6 \cdot 10^3$.

7.7.2 Vertexing Procedure

The vertices and tracks resulting from the re-tracking procedure and displaced vertex formation are stored in a format with a reduced information content.

The nominal ATLAS vertex reconstruction algorithms cannot process this format and can therefore not be used for performing the vertex fits of the random crossing background estimation. For the same reason, the standard magnetic field maps and detector geometry required to account for material interactions in the track propagation are not available.

A simplified custom vertexing algorithm has therefore been implemented to perform the two-track vertex fit for the random crossing background estimate using the information that is available. Track propagation (see Section 3.3.1) is performed by approximating particle trajectories analytically by helices and assuming a homogeneous magnetic field of 2T along the beam direction in the Inner Detector. This approach ignores material interactions and magnetic field inhomogeneities.

The Billoir fast vertexing algorithm [72] is used to fit vertices by means of an iterative procedure. For a start vertex location $\vec{v}$, an associated χ^2 value according to Eq. (3.11) as well as an improved estimate of the vertex location $\vec{v}' = \vec{v} + \delta\vec{v}$ are determined. Linear approximations of the trajectories with respect to the estimated vertex location are used in the fit. The track momenta $(\theta, \phi, q/p)$ are kept unchanged, reducing the free parameters of the fit to d_0 and z_0. In the local coordinate system with the origin at the estimated vertex location $\vec{v}$, Eq. (3.11) becomes [72]

$$\chi^2 = \sum_i \left(\vec{p}_i - \delta\vec{v}\right)^T W_i \left(\vec{p}_i - \delta\vec{v}\right), \tag{7.5}$$

where $\delta\vec{v} = \vec{v}' - \vec{v}$ is the refinement in the vertex position, $\vec{p}_i$ the point of closest approach of the i-th track to the local z axis and W_i the inverse of the associated covariance matrix of d_0 and z_0 transformed into Cartesian coordinates. Minimising χ^2 yields the vertex refinement $\delta\vec{v}$ [72]

$$\delta\vec{v} = \left(\sum_i W_i\right)^{-1} \left(\sum_i W_i \vec{p}_i\right) \tag{7.6}$$

used for the next iteration. The iteration starts with the primary vertex location. The algorithm either converges with a maximum $\Delta\chi^2 = 0.01$ per iteration or is stopped after 50 iterations. A fit is considered successful if $\chi^2/N_{\text{d.o.f.}} < 5$.

The performance of this approach has been tested using displaced vertices reconstructed in collision data. Tracks associated to displaced vertices identified by the standard displaced vertex reconstruction software (see Section 7.4.2) are used as input to the vertex fitter used for the background estimation. Pairs of non-lepton tracks are used in order to have a signal-free validation sample to test the random crossing background estimate. The results of the fast vertex fitter are compared to the displaced vertex reconstruction in Figure 7.19. In almost 90% of the cases, the fast and standard vertex reconstruction agree within 1 cm and 92% of all tested vertices result in a successful fit by the Billoir fast vertex fitter.

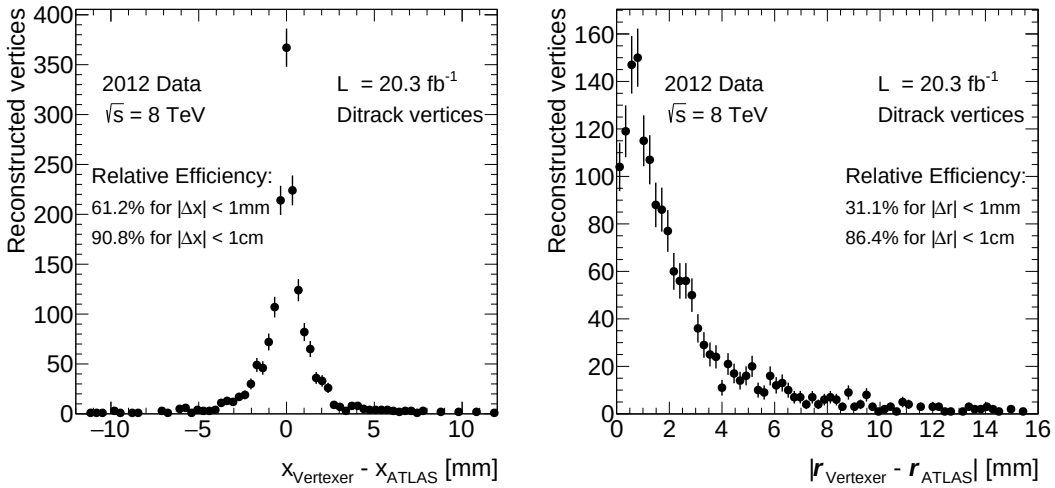

Figure 7.19: Comparison of the helical track propagation and Billoir fast vertex fitting with the displaced vertex reconstruction using the ATLAS software using non-lepton track pairs in the collision data, for the x coordinates (a) and the 3-dimensional locations (b) of the reconstructed vertices.

7.7.3 Irreducible Background Normalisation

For the normalisation of the random crossing background estimate, the number of dilepton pairs $N_{\ell\ell'}$ is needed (see Eq. (7.4)). This is obtained by counting the number of seed lepton pairs in the data (see Section 7.7.1) assuming that the two seed leptons are uncorrelated. The validity of this assumption is tested using the distribution of the azimuthal angle separation $\Delta\phi$ of the two tracks in the seed pair, which should be flat for uncorrelated pairs (see Figure 7.20).

For all track combinations, enhancements at small and large $\Delta\phi$ are observed which indicate correlations between the crossing tracks. To account for this effect, a systematic uncertainty is assigned to $N_{\ell\ell'}$, obtained by comparing the nominal value including all pairs with the number of pairs with $\Delta\phi > 0.5$ rescaled with factor $\frac{\pi}{\pi-0.5}$ and with the number of pairs with $\Delta\phi < \pi - 0.5$, rescaled with $\frac{\pi}{\pi-0.5}$, which explicitly exclude the regions where correlated tracks are seen.

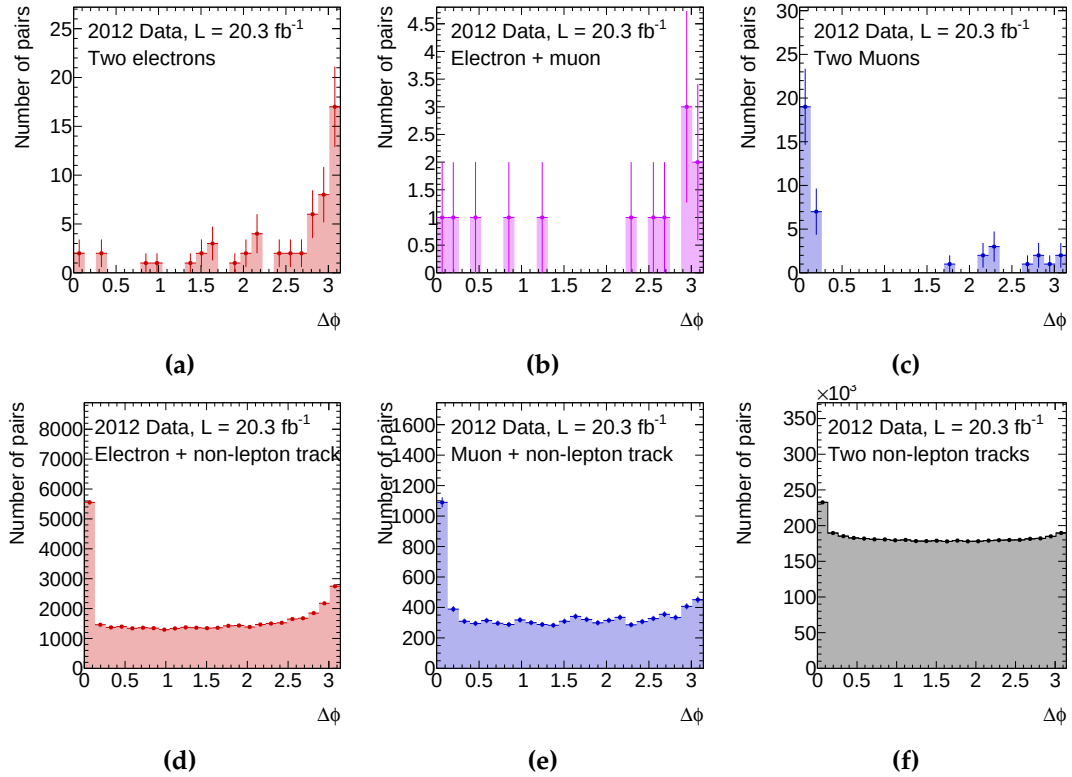

Figure 7.20: Distributions of the azimuthal opening angle $\Delta\phi$ between the two tracks of seed track pairs used to normalise the combinatorial background estimate for combinations of two electrons (a), electron and muon (b), two muons (c), non-lepton track and electron (d), non-lepton track and muon (e) or two non-lepton tracks (f).

7.7.4 Validation of the Estimate

The background estimation technique just described can be tested using collision data by determining the numbers of displaced vertices of two tracks not identified as leptons, of an electron and a non-lepton track and of a muon and a non-lepton track. To enhance statistics, vertex selection requirements are relaxed, removing the opposite charge requirement and the matching to the offline filters and trigger requirements. The minimum transverse momentum requirement on the tracks is also varied (see Table 7.21). Data and prediction agree within 10%. The excellent agreement between data and prediction is also shown in the distributions of the transverse opening angle and the transverse vertex displacement of pairs of non-lepton tracks with $p_{\mathrm{T}} > 10$ GeV in Figure 7.21.

Table 7.14 shows the numbers of displaced vertices with one identified lepton and one

Table 7.13: Numbers of observed and predicted displaced vertices of two non-lepton tracks with relaxed selection criteria in the 2012 data for the validation of the random crossing background estimation. The indicated errors include statistical uncertainties on the crossing probabilities and the systematic error on the number of track pairs discussed in Section 7.7.3.

	2 tracks ($p_T > 5$ GeV)	2 tracks ($p_T > 10$ GeV)	2 tracks ($p_T > 15$ GeV)
$N_{\ell\ell'}$	$(2.29^{+0}_{-0.06}) \cdot 10^7$	$(4.40^{+0}_{-0.07}) \cdot 10^6$	$(1.809^{+0}_{-0.020}) \cdot 10^6$
Crossing prob. f_{DV}	$(3.74 \pm 0.06) \cdot 10^{-4}$	$(4.40 \pm 0.06) \cdot 10^{-4}$	$(4.39 \pm 0.06) \cdot 10^{-4}$
Predicted vertices	$(8.59^{+0.14}_{-0.27}) \cdot 10^3$	$(1.93^{+0.03}_{-0.04}) \cdot 10^3$	795^{+12}_{-15}
Observed vertices	**8742**	**1845**	**726**
Data / Prediction	1.02	0.95	0.91

non-lepton track with and without requiring the lepton to satisfy the single lepton trigger and offline filter requirements. In both cases, the prediction agrees well with the observation. Based on the most significant difference between prediction and observation in these tests, a conservative systematic uncertainty of 15% is applied to the crossing probabilities. Crossing probabilities f_{DV} are found to be on the order of $4 \cdot 10^{-4}$, i.e. two uncorrelated tracks intersect only rarely in the tracker. Nevertheless, these random crossings constitute the dominant source of background in the displaced vertex search in the mass region $m_{DV} > 10$ GeV.

7.7.5 Background Estimate in the Signal Regions

Table 7.15 lists the predicted numbers of displaced random vertices, i.e. the estimated background contributions, in the signal regions. The background is estimated separately for each of the three lepton flavour combinations. As only crossings of two tracks are estimated, there is no overlap between the estimates for the three regions. The result for the flavour-inclusive signal region, therefore, is simply the sum of the individual estimates, taking into account correlated and uncorrelated error contributions. The dominant systematic error is the uncertainty in $N_{\ell\ell'}$ due to the correlations with tracks of small and large opening angles. In all regions, the expected background from random crossings is very small, $O(10^{-3})$. In the analysed data set, no displaced vertices from randomly-crossing lepton tracks are expected.

Table 7.14: Numbers of displaced vertices with one lepton and one non-lepton track in the 2012 data with relaxed selection criteria for the validation of the random crossing background estimation. In the second table, the lepton in the vertex is also required to fulfil the offline filter and trigger criteria. The indicated errors include statistical uncertainties on the crossing probabilities and the systematic error on the number of track pairs discussed in Section 7.7.3.

	$p_T > 10$ GeV	
	electron + track	muon + track
$N_{\ell\ell'}$	$(4.1^{+0}_{-0.4}) \cdot 10^4$	$(8.6^{+0}_{-0.8} \cdot 10^3)$
Crossing prob. f_{DV}	$(4.86 \pm 0.07) \cdot 10^{-4}$	$(3.90 \pm 0.06) \cdot 10^{-4}$
Predicted vertices	$19.8^{+0.03}_{-1.8}$	$3.34^{+0.07}_{-0.32}$
Observed vertices	23	2
	$p_T > 10$ GeV + trigger and filter criteria	
	electron + track	muon + track
$N_{\ell\ell'}$	$(2.09^{+0}_{-0.20}) \cdot 10^4$	$(3.03^{+0}_{-0.22}) \cdot 10^3$
Crossing prob. f_{DV}	$(4.32 \pm 0.06) \cdot 10^{-4}$	$(4.44 \pm 0.07) \cdot 10^{-4}$
Predicted vertices	$9.03^{+0.14}_{-0.86}$	$1.34^{+0.03}_{-0.10}$
Observed vertices	11	0

Table 7.15: Predicted numbers of displaced random vertices in the signal regions for the three lepton flavour combinations and their sum in the 2012 data (20.3 fb^{-1}) with combined statistical and systematic errors. The uncertainty on the final prediction includes the statistical uncertainty of $N_{\ell\ell'}$.

	ee	$e\mu$	$\mu\mu$	Flavour-inclusive
$N_{\ell\ell'}$	$43\ ^{+6}_{-22}$	$7.0\ ^{+1.3}_{-3.4}$	$18\ ^{+0}_{-10}$	n.A.
Crossing probability/10^{-4}	0.23 ± 0.04	3.4 ± 0.5	1.11 ± 0.17	n.A.
Random vertices/10^{-3}	$\mathbf{1.0}\ ^{\mathbf{+0.3}}_{\mathbf{-0.7}}$	$\mathbf{2.4}\ ^{\mathbf{+1.2}}_{\mathbf{-1.8}}$	$\mathbf{2.0}\ ^{\mathbf{+0.6}}_{\mathbf{-1.4}}$	$\mathbf{5.4}\ ^{\mathbf{+1.8}}_{\mathbf{-3.7}}$

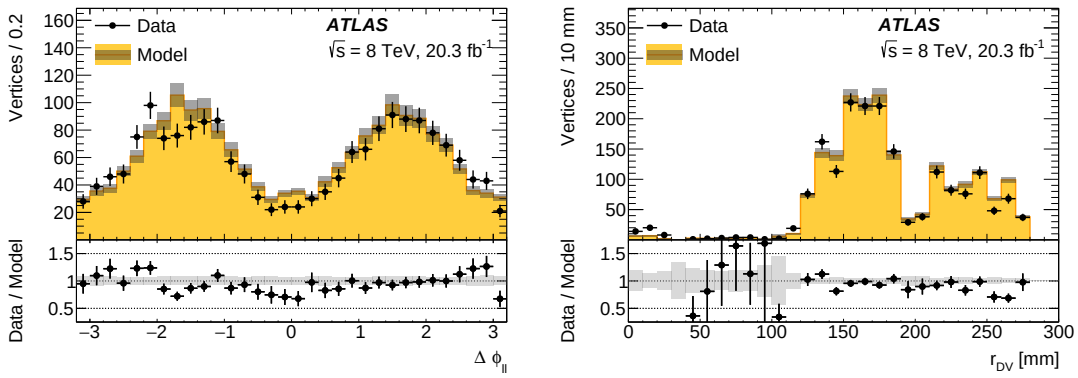

(a) **(b)**

Figure 7.21: Comparison of data and background estimate for vertices of two non-lepton tracks with $p_{\mathrm{T}} > 10$ GeV in distributions of the azimuthal angle $\Delta\phi$ between the tracks (a) and the transverse vertex position (b). Statistical errors are indicated.

7.8 Minor Backgrounds

In addition to the random crossing background, other contributions listed in Section 7.5.1 have been taken into account.

7.8.1 Cosmic Muons

The $\Delta R^{\mathrm{cosmic}}$ variable defined in Eq. (7.1) is used to identify pairs of reconstructed muon tracks pointing in exactly opposite directions as expected from passing cosmic ray muons (see Table 7.6). Dilepton vertices with $\Delta R^{\mathrm{cosmic}} < 0.04$ are rejected. The cosmic muon background is, therefore, studied by requiring $\Delta R^{\mathrm{cosmic}} < 0.04$.

A fraction of the muon pairs selected in this way was found to be inconsistent with the assumption of a single passing cosmic ray muon, due to the impact parameters of the leptons, which should be of identical absolute value for two muons reconstructed from the same cosmic ray. On closer examination, such events were found contain multiple cosmic muons from the same shower traversing the detector simultaneously. As these tracks are parallel, they are not expected to cross in the detector. This was confirmed by the estimation technique for the random crossing background, adapted to this specific situation. The multi-cosmic events are therefore removed from the study presented here, which is intended to investigate the case of a single traversing cosmic muon.

In total 5348 cosmic muon pair candidates are found in the data set, of which 356 form a displaced vertex. Figure 7.22 shows the ΔR^{cosmic} distributions for the pairs in both cases, scaled to the same integral. Both distributions agree very well, indicating that the probability of identifying a displaced vertex is not strongly dependent on ΔR^{cosmic} for $\Delta R^{\text{cosmic}} < 0.01$.

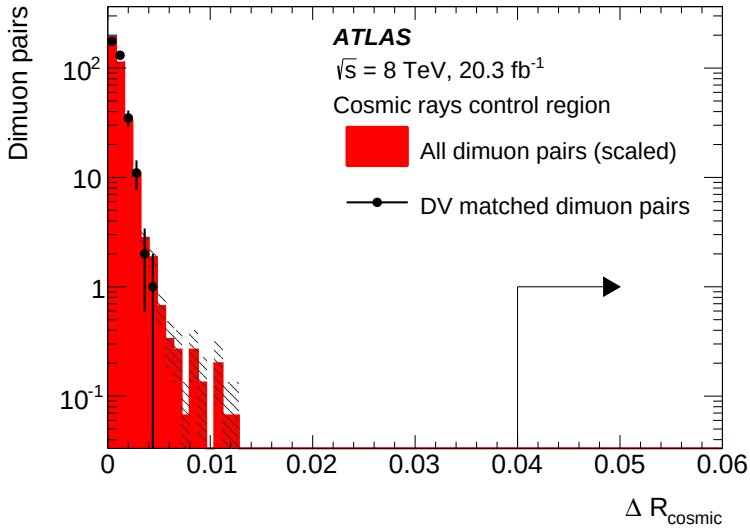

Figure 7.22: Distributions of the ΔR^{cosmic} variable for events rejected by the cosmic muon veto. Dots: muon pairs forming a displaced vertex. Histogram: all muon pairs, rescaled to the number of reconstructed displaced vertices. The signal requirement $\Delta R^{\text{cosmic}} > 0.04$ is indicated.

The distributions fall steeply. No pairs with $\Delta R^{\text{cosmic}} > 0.013$ are observed. Extrapolation of the falling distributions indicates that the residual contribution from cosmic muons above with $\Delta R^{\text{cosmic}} > 0.04$ is negligible.

7.8.2 Hadron Decays

To suppress semileptonic hadron decays, the invariant mass m_{DV} of the tracks at the displaced vertices is used as discriminating variable, requiring $m_{\text{DV}} > 10$ GeV. Figures 7.23 and 7.24 show the invariant mass distribution for vertices with two non-lepton tracks, with a lepton and a non-lepton track and with two muon tracks. The final bin in each distribution includes all vertices found at masses above the range covered by the x axis. No vertices with two electron tracks or with an electron and a muon track with $m_{\text{DV}} < 10$ GeV are observed. In the four cases shown, contributions at low masses

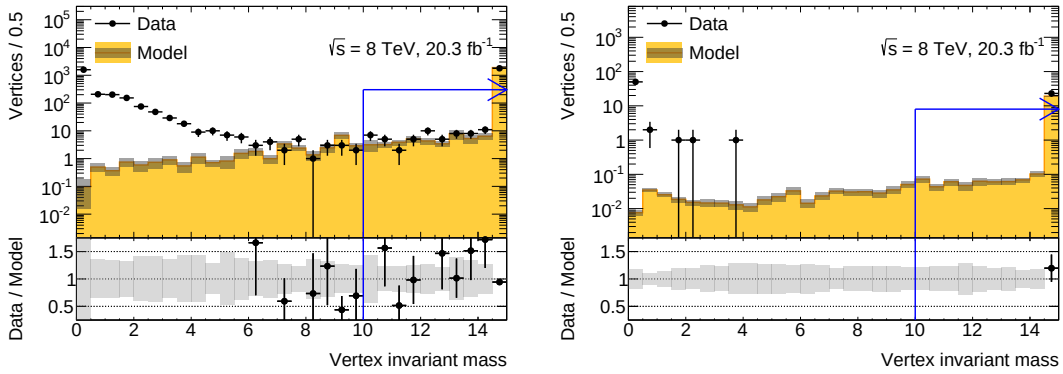

Figure 7.23: Invariant mass distributions for displaced vertices with two non-lepton tracks (a) and with an electron and a non-lepton track (b), without trigger or offline requirements. The estimated random crossing background component is indicated by the shaded histogram, while the data are shown as black dots. The signal requirement $m_{\mathrm{DV}} > 10$ GeV is indicated. The final bin of the histograms indicates the sum of all vertices with masses beyond the range depicted.

not described by the random crossing background estimate are observed which are attributed to hadron decays. In the case of two non-lepton tracks, the random crossing component becomes dominant and fully describes the data above $m_{\mathrm{DV}} = 7$ GeV, such that a contribution from hadron decays becomes negligible in the signal region. In the other cases, no vertices are observed above $m_{\mathrm{DV}} = 6$ GeV and the random crossing background expectation is very small and in agreement with the data for $m_{\mathrm{DV}} > 10$ GeV, indicating that the contribution from hadron decays disappears well before the signal region and is negligible.

7.8.3 Misreconstructed Prompt Decays

Displaced vertices resulting from misreconstructed prompt decays are strongly suppressed by the minimum impact parameter requirements of the vertex reconstruction, the requirement on the vertex fit quality and the minimum separation to primary vertices. The most important candidate process is $Z \to \ell\ell$, due to the large product of cross-section and decay branching ratio of about 1.2 nb per lepton flavour [65, 128]. The number of residual vertices from this source N_{prompt} is estimated as

$$N_{\mathrm{prompt}} = L \cdot \sigma \cdot BR \cdot \alpha \cdot \epsilon_1 \cdot \epsilon_2 \cdot \epsilon_{\mathrm{DV}}, \tag{7.7}$$

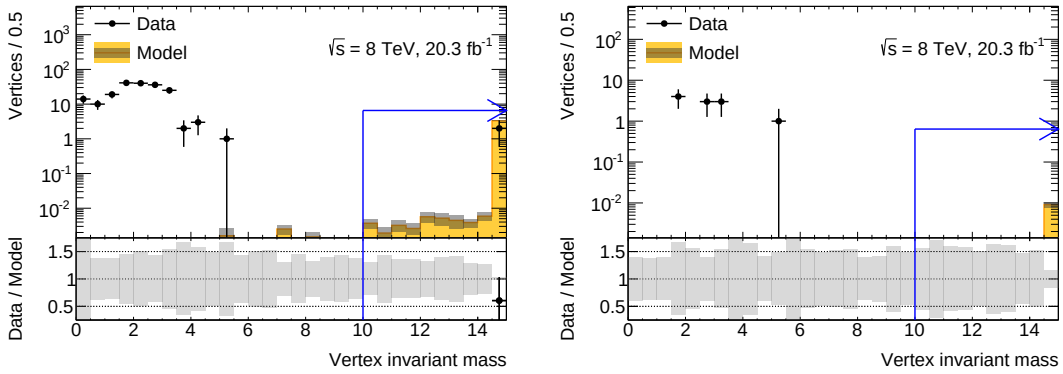

(a) **(b)**

Figure 7.24: Invariant mass distributions for displaced vertices with a non-lepton track and a muon (a) and with two muons (b), without trigger or offline filter requirements. The estimated random crossing background component is indicated by the shaded histogram, while the data are shown as black dots. The signal requirement $m_{\mathrm{DV}} > 10$ GeV is indicated. The final bin of the histograms indicates the sum of all vertices with masses beyond the range depicted.

where $L = 20.3\mathrm{fb}^{-1}$ is the integrated luminosity, σ the Z boson production cross-section, BR the dilepton decay branching ratio of the Z boson, α the kinematic acceptance of the trigger and offline filters for $Z \to \ell\ell$ decays, ϵ_i $(i = 1,2)$ the probabilities for the two leptons from a $Z \to \ell\ell$ decay to pass the track selection criteria of the displaced vertex reconstruction, especially the transverse impact parameter requirement, and ϵ_{DV} the probability for two tracks with high transverse impact parameters originating from a $Z \to \ell\ell$ decay to result in a successful vertex fit.

Using Monte Carlo simulation, the acceptance α is estimated to be about 7% for $Z \to \mu\mu$ and around 5% for $Z \to ee$ decays. The probabilities of leptons from Z decays to pass the impact parameter criteria are estimated using the transverse impact parameter distributions of leptons in Monte Carlo simulated $Z \to ee/\mu\mu$ events. As a cross-check, they are also measured in the data and found to agree within the statistical uncertainties, with values on the order of $10^{-5} - 10^{-6}$ (see Figure 7.25). The vertex reconstruction efficiency for misreconstructed tracks is obtained by inserting track pairs from $Z \to \ell\ell$ decays into the fast vertex fitter used for the random crossing background estimation (see Section 7.7.2) and measuring the fraction of successful vertex fits as a function of the transverse impact parameters of the leptons, resulting in a value of about 10%. The resulting estimate using Eq. (7.7) is $N_{\mathrm{prompt}} \approx 2 \cdot 10^{-5}$ for $Z \to \mu\mu$ and $N_{\mathrm{prompt}} \approx 1.7 \cdot 10^{-4}$ for $Z \to ee$ decays, an order of magnitude below the random crossing background, and

hence considered to be negligible.

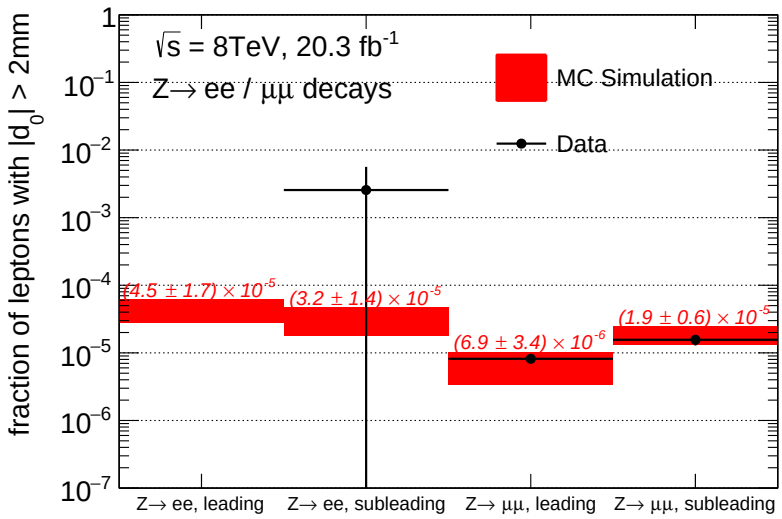

Figure 7.25: Fraction of leptons in $Z \to ee/\mu\mu$ decays passing the $|d_0| > 2$ mm requirement of the displaced vertex track selection for Monte Carlo simulation and data.

7.9 Signal Region Observations and Statistical Interpretation

7.9.1 Signal region Observations

As the background contributions are found to be negligible, only displaced vertices from a signal are expected in the signal regions. Figure 7.26 shows the distribution of observed displaced vertices in the data in comparison with the signal Monte Carlo predictions as a function of the vertex mass and the number of leptons associated with the vertex. The signal regions, corresponding to two reconstructed leptons at the vertex and $m_{\mathrm{DV}} > 10$ GeV, are indicated.

For vertices with no associated leptons, three main contributions are distinguished. At a vertex mass of approximately 400 MeV, the $K^0_S \to \pi^+\pi^-$ resonance is observed. The shift compared to the measured mass value $m_{K^0} = 497.6$ MeV [65] is due to the assumption of massless particles made in the vertex mass calculation – applying a pion hypothesis for the tracks shifts the value to 498 MeV, in agreement with the literature. At high

displaced vertex masses above about 5 GeV, the effect of the particle mass hypothesis becomes negligible. The second contribution is the hadron decay mass spectrum shown in Figure 7.23, which reaches up to about 6 GeV. Finally, at higher masses, the contribution from random crossings is visible, shaped mainly by the transverse momentum requirement of $p_{\mathrm{T}} > 10$ GeV on the tracks.

In the cases where one lepton is associated with the vertex, there is again the contribution from hadron decays at $m_{\mathrm{DV}} < 10$ GeV. An enhancement at the location of the $K^0_S \to \pi^+\pi^-$ resonance indicates misidentified leptons. In the region $m_{\mathrm{DV}} > 10$ GeV, only few vertices are observed with an associated electron, and none with an associated muon, consistent with the random crossing background estimate (see Table 7.14).

No dielectron or electron-muon vertices are found. Four dimuon vertices are observed at vertex masses below 6 GeV outside the signal region, also seen in Figure 7.24. All are close to b-tagged jets and consistent with hadron decays. In the signal regions, no displaced vertices are observed, consistent with the background expectation.

7.9.2 Statistical Interpretation

The above results are summarised in Table 7.16 and analysed using the same statistical methods as the four-lepton search (see Section 6.6). Without the observation of displaced signal vertices, exclusion limits are placed on the signal models.

With negligible expected background, the model independent 95%CL upper limit $N^{95\%}_{\mathrm{BSM}}$ (see Section 6.7.1) is on the order of 3 events, corresponding to a visible cross-section $\sigma^{95\%}_{\mathrm{vis}}$ of about 0.15 fb for all signal channels.

Table 7.16: Observed and expected numbers of displaced signal vertices in the different dilepton channels.

	Exp. SM	**Data**	$N^{95\%}_{\mathrm{BSM}}$	$\sigma^{95\%}_{\mathrm{vis}}$[fb]
ee	$\left(\mathbf{1.0}\ ^{+\mathbf{0.3}}_{-\mathbf{0.7}}\right) \cdot \mathbf{10^{-3}}$	**0**	2.9	0.15
$e\mu$	$\left(\mathbf{2.4}\ ^{+\mathbf{1.2}}_{-\mathbf{1.8}}\right) \cdot \mathbf{10^{-3}}$	**0**	2.9	0.14
$\mu\mu$	$\left(\mathbf{2.0}\ ^{+\mathbf{0.6}}_{-\mathbf{1.4}}\right) \cdot \mathbf{10^{-3}}$	**0**	3.0	0.15

Model-dependent limits are obtained using the signal efficiency measurements discussed in Section 7.6. Upper limits on the number of R-parity-violating neutralino decays in each dilepton final state are shown in Figure 7.27 for the four NLSP-LSP mass combina-

tions studied. These results can be interpreted in other R-parity-violating models with different production cross-sections and neutralino dilepton branching ratios.

For a light neutralino with $m_{\tilde{\chi}_1^0} = 50$ GeV, the strongest limit is placed for a decay length of about 10 mm. The limits become stronger with increasing number of muons in the final state because of the relatively low momentum threshold of the single muon offline filter which enhances the signal efficiency. For $m_{\tilde{g}} = 600$ GeV, the upper limit is on the order of 100 decays to two electrons or one electron and a muon or about 70 decays to two muons, while for $m_{\tilde{g}} = 1300$ GeV, models with more than 60 decays are excluded for all flavour combinations.

For smaller NLSP-LSP mass differences, the strongest limits are reached at higher LSP lifetimes as expected from the lifetime-dependence of the signal efficiency in Figs. 7.15-7.17. The strongest upper limit of 20 decays is obtained for $c\tau \approx 50$ mm. The gluino mass has little influence on this limit. In all cases, the limit becomes weaker towards higher and lower lifetimes as the signal acceptance decreases (see Section 7.6.3).

Equivalent upper limits on the cross-section times LSP decay branching ratio for simplified gluino models with $\lambda_{121} \neq 0$ and $\lambda_{122} \neq 0$ are shown in Figure 7.28. The results for the two coupling choices are comparable with the exception of the limit for $m_{\tilde{g}} = 600$ GeV and $m_{\tilde{\chi}_1^0} = 50$ GeV, where the limit for a λ_{122} coupling is slightly stronger since all decays for this model profit from the higher acceptance of the single muon trigger and offline filter, whereas the dielectron decays in the λ_{121} case do not. For a gluino mass of 600 GeV, decay lengths between 0.5 mm and 40 m are excluded at 95% confidence level for $m_{\tilde{\chi}_1^0} = 50$ GeV assuming a 100% neutralino dilepton branching ratio. For $m_{\tilde{\chi}_1^0} = 400$ GeV, longer lifetimes up to 400 m can be excluded. The lowest excluded $c\tau$ in the latter case is 1 mm.

For higher gluino mass of $m_{\tilde{g}} = 1300$ GeV, the excluded lifetime range shrinks due to the reduced gluino pair production cross-section. The models with small neutralino mass of $m_{\tilde{\chi}_1^0} = 50$ GeV can not be excluded, the strongest limit of about 1.5 fb is attained for $c\tau \approx 1.5$ cm. For a neutralino mass of $m_{\tilde{\chi}_1^0} = 1$ TeV, LSP decay lengths between 1 cm and 4.5 cm are excluded.

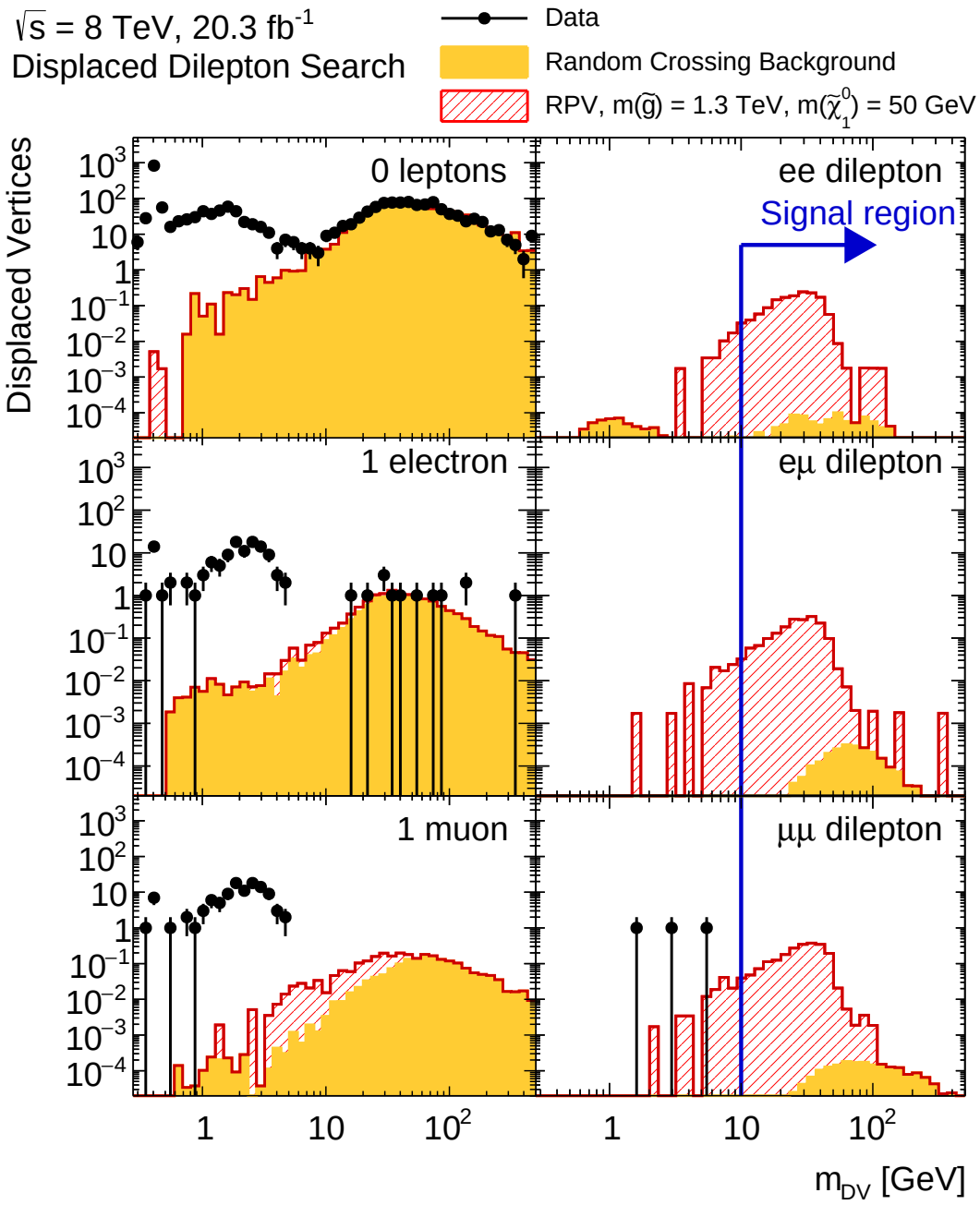

Figure 7.26: Distributions of displaced vertices as a function of the invariant mass m_{DV} for different numbers of leptons associated to the displaced vertices. The signal region corresponds to at least two associated leptons and mass above 10 GeV and is indicated by the blue boundary. The red shaded areas indicate the Monte Carlo expectation for the gluino model with $m_{\tilde{g}} = 600$ GeV and $m_{\tilde{\chi}_1^0} = 50$ GeV, stacked on top of the expected background contribution from random crossings of tracks indicated in yellow, which is expected to fully describe the background for $m_{\mathrm{DV}} > 10$ GeV.

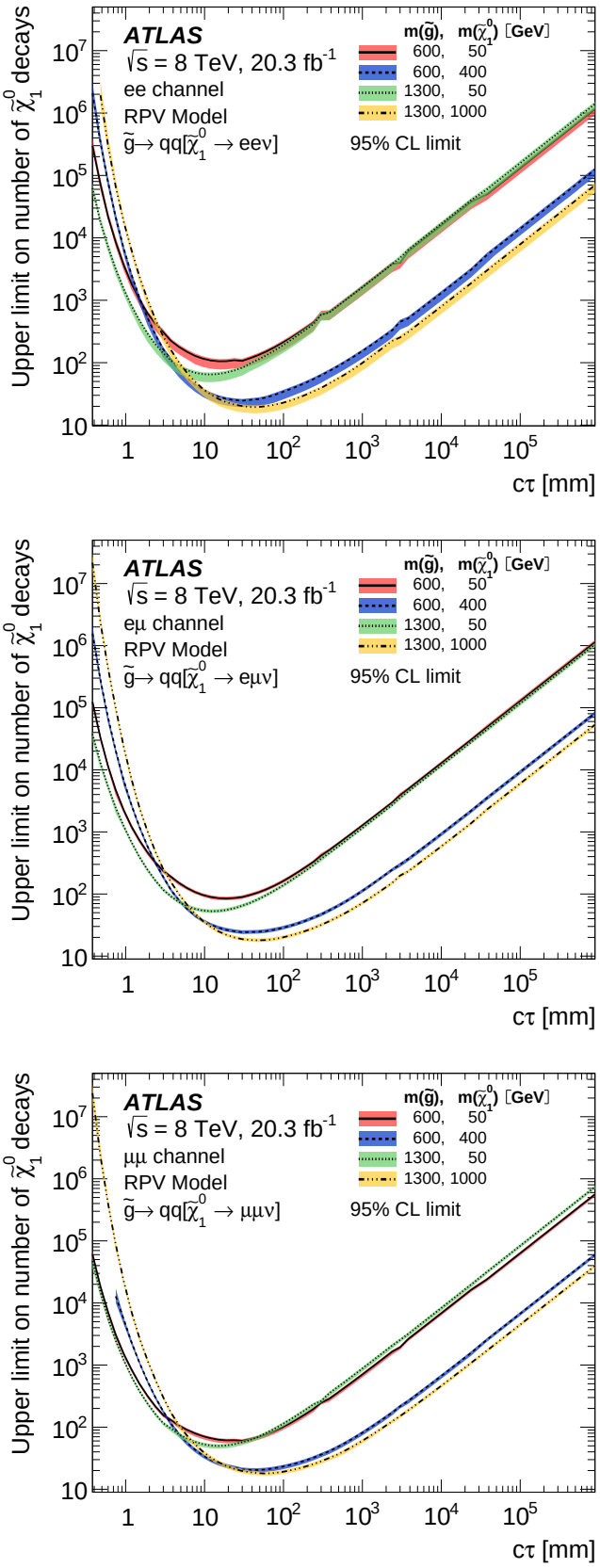

Figure 7.27: 95% CL upper limits on the numbers of R-parity-violating neutralino decays into $ee\nu$ (a), $e\mu\nu$ (b) and $\mu\mu\nu$ (c) final states as a function of the LSP lifetime τ using signal efficiencies determined for the four simplified model NLSP-LSP combinations studied.

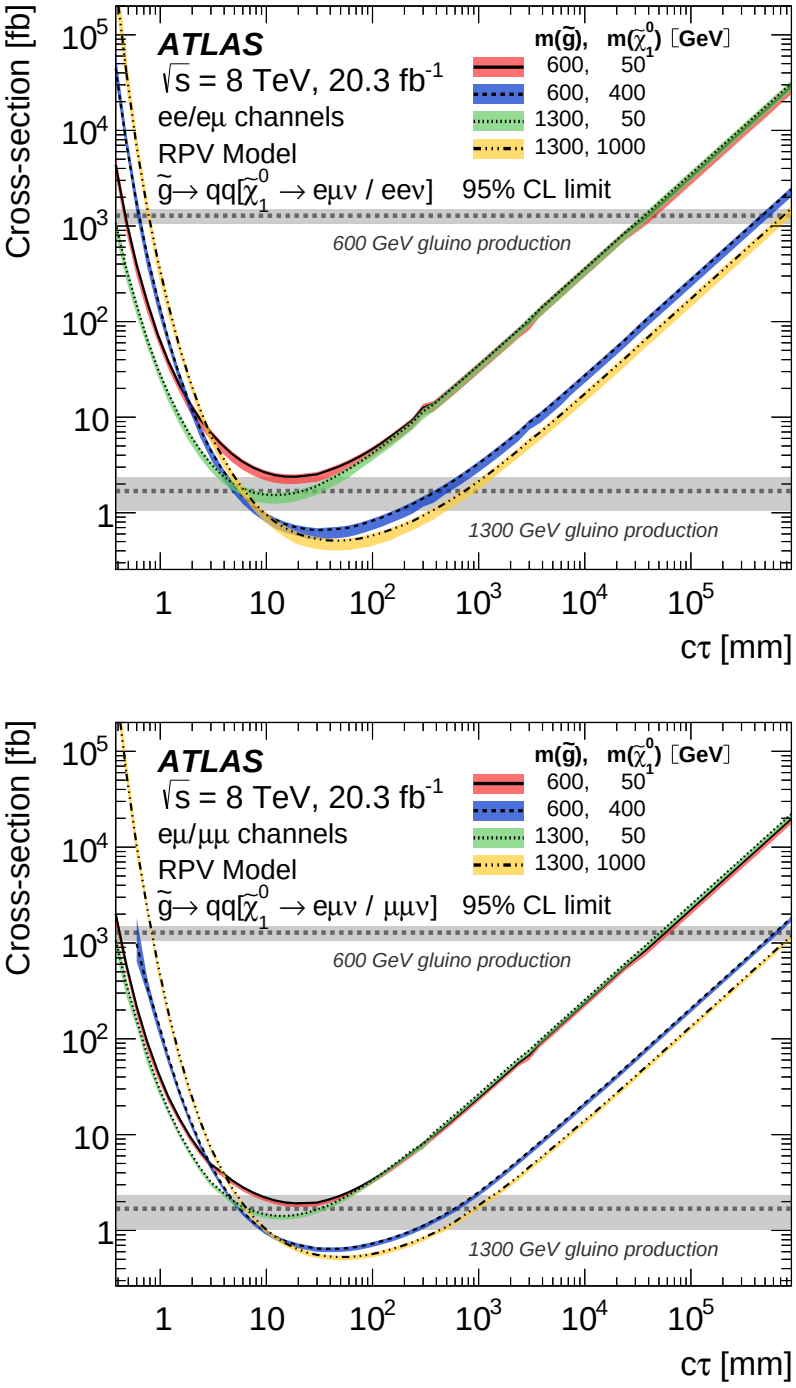

Figure 7.28: 95% CL upper limits on the gluino pair production cross-sections in the simplified RPV model with $\lambda_{121} \neq 0$ (a) or $\lambda_{122} \neq 0$ (b) as a function of the LSP decay length $c\tau$, assuming a 100% inclusive dilepton branching ratio. The theoretical cross-section predictions depending on the gluino mass with their uncertainties are shown as grey horizontal bands.

7.10 Comparison with the Prompt Four-Lepton Search

The simplified model of gluino production was used in the interpretation of both searches described in this thesis. Here, the constraints set by each are compared as a function of the LSP lifetime. The reweighting procedure described in Section 7.6.1 is used to predict the expected signal yield in the four-lepton SR0noZb signal region as a function of the neutralino lifetime for the four NLSP-LSP mass combinations studied in the displaced dilepton vertex search in Figure 7.29. Statistical uncertainties on the acceptance and efficiency are large due to the reweighting with limited Monte Carlo statistics, especially for the light neutralino mass $m_{\tilde{\chi}_1^0} = 50$ GeV. Using the background prediction and number of observed events in the SR0noZb signal region (see Table 6.13), upper limits on the gluino pair production cross-section as a function of the LSP lifetime are derived. Figures 7.30 and 7.31 show these limits in comparison with the limits derived in the displaced dilepton vertex search. Only small differences are observed between the results for an active λ_{121} or λ_{122} coupling. The sensitivity of the four-lepton analysis decreases with increasing neutralino lifetime. The dedicated search for long-lived LSP decays becomes more sensitive for decay lengths longer than 1–2 mm for a light LSP with $m_{\tilde{\chi}_1^0} = 50$ GeV or 3–8 mm for a heavy LSP. If the gluino mass is 600 GeV, the two searches exclude all LSP decay lengths below 400 m (40 m) for neutralino masses of 400 GeV (50 GeV) (see Figure 7.28). For the heavier gluino with $m_{\tilde{g}} = 1.3$ TeV, the excluded decay length regions of the two analyses are disjoint. The prompt four-lepton search is able to exclude decay lengths below about 1.5 mm for $m_{\tilde{\chi}_1^0} = 1$ TeV, while the displaced dilepton vertex search excludes decay lengths between 1 cm and 4.5 cm. For a light LSP with $m_{\tilde{\chi}_1^0} = 50$ GeV, the exclusion by the prompt four-lepton search does not extend into the lifetime range accessible to the reweighting procedure. The strongest limit of the displaced vertex search is a cross-section of 1.5 fb at $c\tau \approx 1.5$ cm, not quite sufficient for an exclusion.

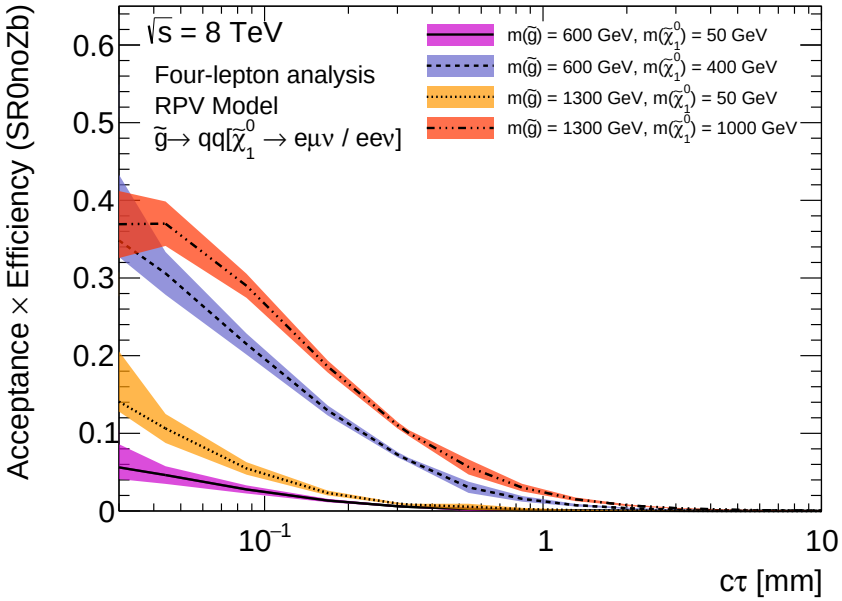

(a)

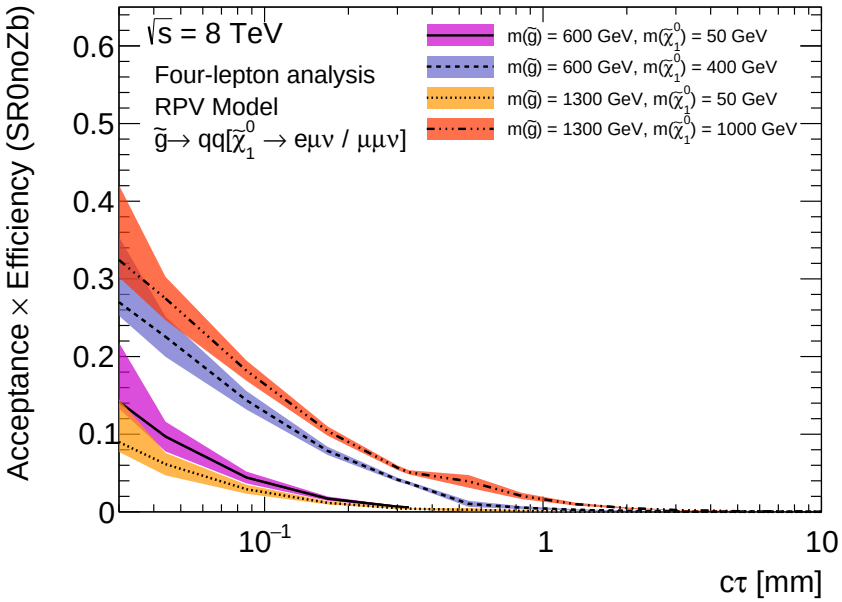

(b)

Figure 7.29: Extrapolated signal acceptance times efficiency of the SR0noZb signal region of the prompt four-lepton search as a function of the neutralino decay length $c\tau$ for the four NLSP-LSP mass combinations in the gluino RPV model studied in the displaced dilepton search, for $\lambda_{121} \neq 0$ (a) and $\lambda_{122} \neq 0$ (b). Statistical errors are shown as filled bands.

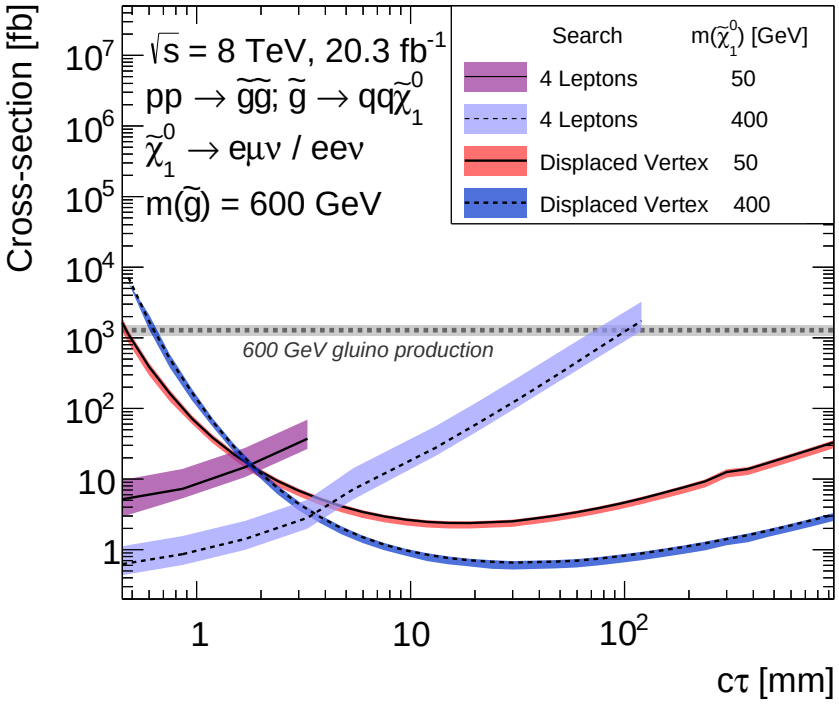

(a)

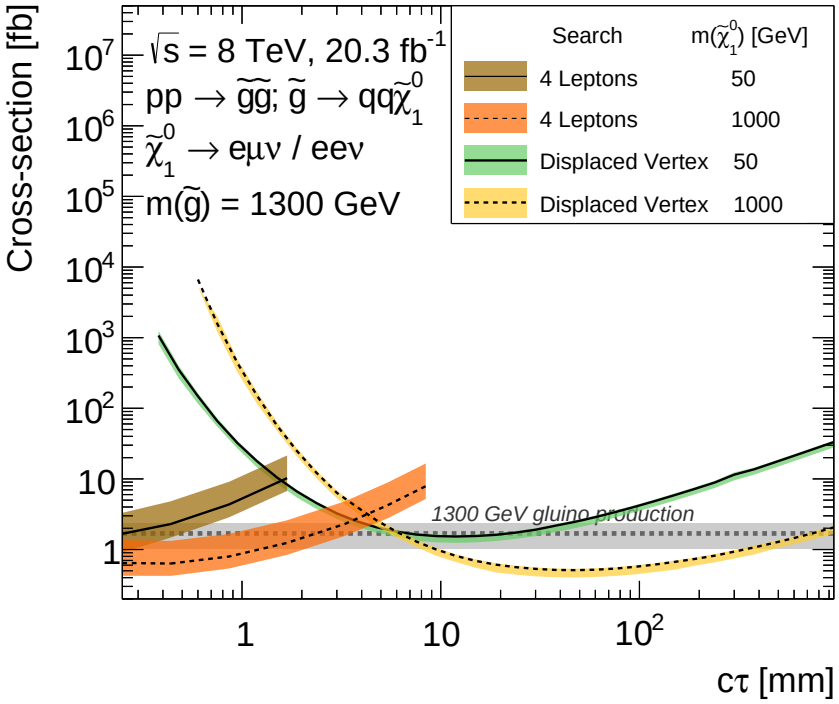

(b)

Figure 7.30: Upper limit on the production cross-section in the simplified RPV model with $m_{\tilde{g}} = 600$ GeV, an active λ_{121} coupling and $m_{\tilde{\chi}_1^0} = 50$ GeV (a) or 400 GeV (b) for the displaced dilepton search and the four-lepton search. The cross-sections predicted by theory are depicted as grey bands.

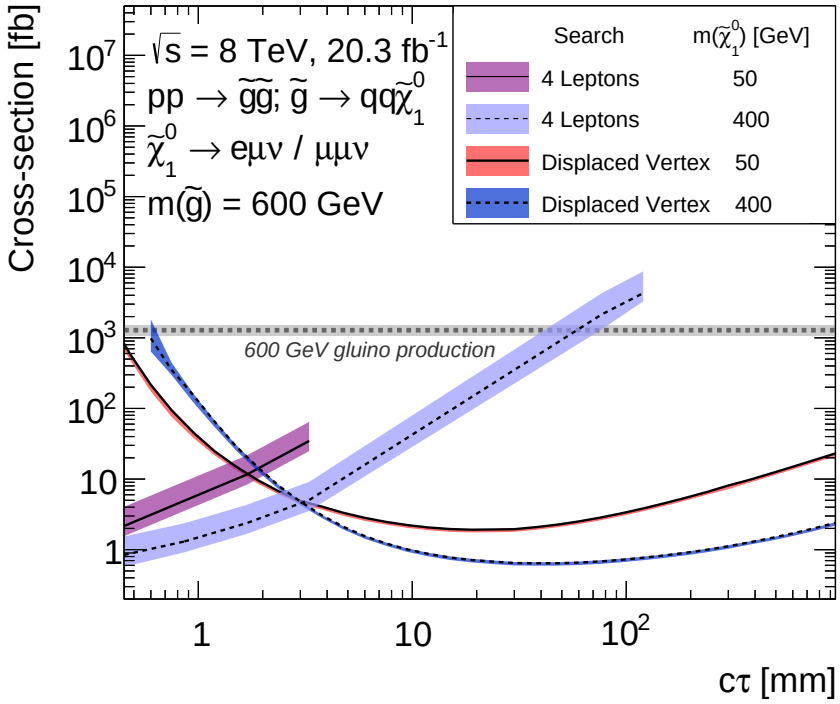

(a)

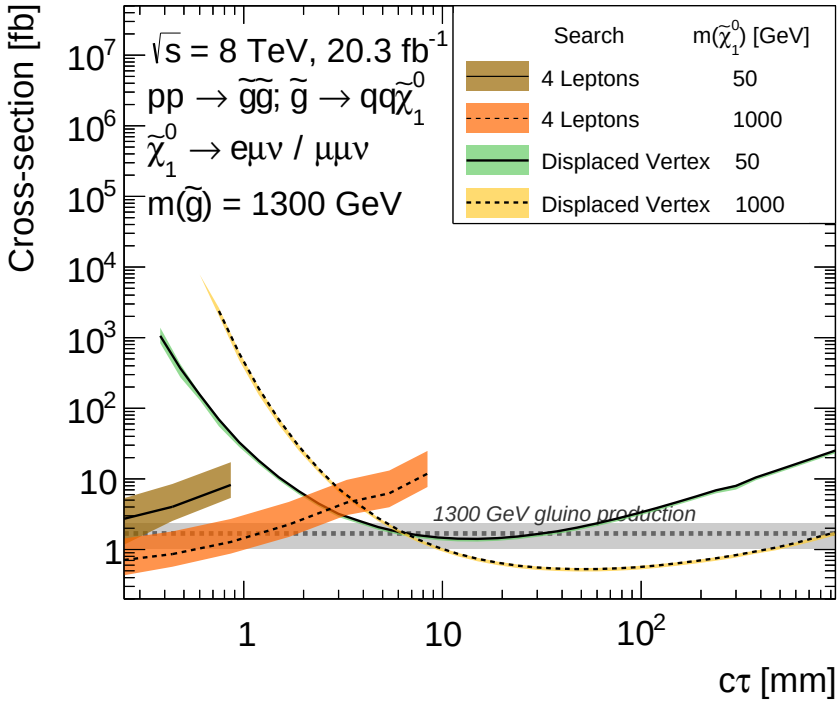

(b)

Figure 7.31: Upper limit on the production cross-section in the simplified RPV model with $m_{\tilde{g}} = 600$ GeV, an active λ_{122} coupling and $m_{\tilde{\chi}_1^0} = 50$ GeV (a) or 400 GeV (b) for the displaced dilepton search and the four-lepton search. The cross-sections predicted by theory are depicted as grey bands.

Chapter 8

Summary

Supersymmetry (SUSY) is a compelling solution to the hierarchy problem of the Standard Model of particle physics. It predicts a superpartner for each Standard Model particle with equal quantum numbers apart from the spin, leading to scalar sfermion partners of the Standard Model fermions and spin-1/2 gaugino and higgsino partners of the gauge and Higgs bosons of the Standard Model, respectively.

As no superpartners with the same masses as the Standard Model particles have been observed, supersymmetry must be broken. In order to provide a solution to the hierarchy problem, masses of the superpartners not larger than about a few TeV are required, motivating searches for supersymmetric particle production at the Large Hadron Collider (LHC), which collides protons at centre-of-mass-energies up to 14 TeV. These searches usually assume the conservation of an additional quantum number, R-parity, which forbids proton decay and requires the lightest supersymmetric particle (LSP) to be stable. However, proton stability can be achieved also by other symmetries than R-parity-conservation. R-parity-violating couplings allow the LSP to decay to Standard Model particles and give rise to signatures not covered by conventional searches for R-parity-conserving supersymmetry.

In this thesis, searches for R-parity-violating decays of the lightest neutralino into two charged leptons and a neutrino are performed using data of the ATLAS experiment taken at $\sqrt{s} = 8$ TeV in 2012. As the neutralinos are produced in pairs at the LHC via R-parity-conserving processes, at least four leptons are produced in such events. Efficient lepton reconstruction, therefore, is vital to these searches. The muon reconstruction efficiency is measured in the data to be greater than 95% with permill precision using

more than 5 million recorded $Z \to \mu\mu$ decays.

If the LSP decays are prompt, a search for events with four charged leptons originating from the primary proton-proton interaction vertex is very effective. The Standard Model background is suppressed by requiring large missing transverse momentum or a large effective mass. The residual background is small, compromised of $ZZ^{(*)}/Z\gamma^{*}$diboson production, top quark pair production in association with a Z boson, triple gauge boson production and Higgs boson production. For final states with hadronically decaying τ leptons, there is an additional background from jets that are misidentified as τ leptons. The number of observed signal events is consistent with the background. Strong exclusion limits on gluino, wino, slepton and sneutrino pair production are derived in the framework of simplified SUSY models. The most challenging scenario is the production of a heavy SUSY particle decaying into a very light LSP, as the boost of the LSP results in soft and/or collimated leptons. The analysis has been improved such that it has become sensitive to LSP masses as low as 10 GeV.

Finite LSP lifetimes have not been considered before in the studied SUSY models. If the LSP decay length exceeds about 1 mm, the final state leptons can no longer be assigned to the primary vertex and the four-lepton search loses sensitivity. A dedicated search for displaced dilepton decay vertices has been developed for such scenarios, which requires reconstruction of the LSP decay vertices in the ATLAS inner tracker. As the standard ATLAS track and vertex reconstruction algorithms are not capable of identifying highly displaced tracks and vertices, the track, lepton and vertex reconstruction had to be repeated using optimised algorithms on a preselected data set. Vertex selection criteria completely suppress backgrounds from cosmic ray muons, semileptonic hadron decays and charged particle interactions with Inner Detector material. The residual background from randomly crossing lepton tracks is estimated from the data using a novel technique and found to be negligible as well. No displaced signal vertices are observed in the data, consistent with this estimation. LSP decays to charged lepton pairs have been excluded for the first time by ATLAS for a wide range of LSP lifetimes in benchmark signal models, considerably strengthening constraints on models of R-parity-violating SUSY.

Appendix A

Supplementary Information to the Four-Lepton Search

A.1 Cross-Sections of Signal and Background Processes

Table A.1 lists the production cross-sections of the irreducible background processes. Higgs boson production cross-sections and decay branching ratios are calculated at NNLO QCD and NLO EW precision with the exception of $t\bar{t}H$, which is known at NLO QCD precision [129].

Table A.2 shows the NLSP pair production cross-sections for the simplified RPV models used in the four-lepton and displaced vertex searches obtained using the programs PROSPINO and NLL-Fast [104–107] with associated errors for electroweak and strong production, respectively. Since the simplified models assume mass-degenerate sleptons and sneutrinos, the flavour-inclusive cross-section is given for these models (see Section 5.3).

Table A.1: Production cross-sections and decay branching ratios for the irreducible background in the four-lepton search.

Process	$\sigma \cdot BR$ [pb]
$ZZ^{(*)} \to 4\ell$	$(7.6\pm0.4) \cdot 10^{-1}$
$t\bar{t}Z \to 4\ell 2\nu b\bar{b}$	$(3.4\pm1.0) \cdot 10^{-3}$
$ZWW^{(*)} \to 4\ell 2\nu$	$(2.3\pm1.2) \cdot 10^{-3}$
$ZZZ^{(*)} \to 4\ell 2\nu$	$(5.0\pm2.5) \cdot 10^{-4}$
(ggF) $H \to 4\ell$	$(5.3\pm0.8) \cdot 10^{-3}$
(VBF) $H \to 4\ell$	$(4.4\pm0.2) \cdot 10^{-4}$
(WH) $H \to 4\ell$	$(1.9\pm0.1) \cdot 10^{-4}$
(ZH) $H \to 4\ell$	$(1.2\pm0.1) \cdot 10^{-4}$
(ttH) $H \to 4\ell$	$(3.6\pm0.5) \cdot 10^{-5}$
(ZH) $H \to \ell^{\pm}\ell^{\mp}q\bar{q}$	$(1.5\pm0.1) \cdot 10^{-3}$
(ttH) $H \to \ell^{\pm}\ell^{\mp}q\bar{q}$	$(4.8\pm0.6) \cdot 10^{-4}$
(ZH) $H \to \ell^{\pm}\ell^{\mp}\nu\bar{\nu}$	$(9.7\pm0.7) \cdot 10^{-3}$
(ttH) $H \to \ell^{\pm}\ell^{\mp}\nu\bar{\nu}$	$(3.0\pm0.4) \cdot 10^{-3}$
(ZH) $H \to \tau^{\pm}\tau^{\mp}$	$(2.6\pm0.2) \cdot 10^{-2}$
(ttH) $H \to \tau^{\pm}\tau^{\mp}$	$(8.2\pm1.1) \cdot 10^{-3}$

Table A.2: NLSP pair production cross-sections in the simplified RPV models as a function of the NLSP mass. For the slepton and sneutrino models, the sum over all (mass-degenerate) lepton flavours is given.

NLSP choice	m_{NLSP} [GeV]	σ [pb]
Wino	200	$(3.8\pm0.2)\cdot10^{-1}$
	300	$(6.8\pm0.5)\cdot10^{-2}$
	400	$(1.8\pm0.1)\cdot10^{-2}$
	500	$(5.4\pm0.4)\cdot10^{-3}$
	600	$(1.9\pm0.2)\cdot10^{-3}$
	800	$(2.8\pm0.3)\cdot10^{-4}$
	1000	$(4.7\pm0.5)\cdot10^{-5}$
Gluino	500	4.5±0.7
	600	1.3±0.2
	800	$(1.5\pm0.3)\cdot10^{-1}$
	1000	$(2.3\pm0.6)\cdot10^{-2}$
	1100	$(9.3\pm2.9)\cdot10^{-3}$
	1200	$(3.9\pm1.4)\cdot10^{-3}$
	1300	$(1.7\pm0.7)\cdot10^{-3}$
	1400	$(7.4\pm3.2)\cdot10^{-4}$
	1700	$(6.6\pm3.8)\cdot10^{-5}$
L-Slepton	75	1.18±0.05
	150	$(8.6\pm0.5)\cdot10^{-2}$
	225	$(1.6\pm0.1)\cdot10^{-2}$
	300	$(4.5\pm0.4)\cdot10^{-3}$
	400	$(1.1\pm0.1)\cdot10^{-3}$
	500	$(3.3\pm0.3)\cdot10^{-4}$
	600	$(1.1\pm0.1)\cdot10^{-4}$
r-Slepton	75	$(4.2\pm0.2)\cdot10^{-1}$
	150	$(3.2\pm0.2)\cdot10^{-2}$
	225	$(6.3\pm0.4)\cdot10^{-3}$
	300	$(1.8\pm0.1)\cdot10^{-3}$
	400	$(4.4\pm0.4)\cdot10^{-4}$
	500	$(1.3\pm0.1)\cdot10^{-4}$
	600	$(4.5\pm0.5)\cdot10^{-5}$
Sneutrino	75	1.36±0.05
	150	$(8.4\pm0.5)\cdot10^{-2}$
	200	$(2.6\pm0.2)\cdot10^{-2}$
	300	$(4.2\pm0.3)\cdot10^{-3}$
	400	$(1.0\pm0.1)\cdot10^{-3}$
	500	$(2.9\pm0.3)\cdot10^{-4}$
	600	$(9.7\pm0.9)\cdot10^{-5}$

A.2 Typical Signal Region Efficiencies and Acceptances

Tables A.3–A.6 list the acceptances, efficiencies and the product of acceptance and efficiency of the most important 0-, 1- and 2-τ signal regions for one typical NLSP mass value for each of the simplified RPV models. As the R-slepton model uses the same simulated events as the L-slepton model, the results are identical between the cases and no separate table is provided.

Table A.3: Acceptances and Efficiencies of the four-lepton signal regions for the simplified RPV model with a wino NLSP with $m_{\tilde{\chi}_1^\pm} = 1.1$ TeV.

		Wino NLSP, $m_{\tilde{\chi}_1^\pm} = 600$ GeV				
	$m_{\tilde{\chi}_1^0}$	10 GeV	50 GeV	200 GeV	400 GeV	590 GeV
$\lambda_{121} \neq 0$ SR0noZb	A	21%	46%	53%	64%	76%
	ϵ	35%	65%	66%	71%	58%
	$A \cdot \epsilon$	7.1%	30%	35%	45%	45%
$\lambda_{133} \neq 0$ SR1noZb	A	2.5%	9.4%	14%	17%	15%
	ϵ	2.2%	14%	29%	26%	26%
	$A \cdot \epsilon$	0.06%	1.3%	4.2%	4.6%	3.8%
$\lambda_{133} \neq 0$ SR2noZb	A	4.2%	7.5%	14%	19%	21%
	ϵ	< 0.01%	6.5%	24%	21%	20%
	$A \cdot \epsilon$	< 0.01%	0.49%	3.3%	4.0%	4.1%

Table A.4: Acceptances and Efficiencies of the four-lepton signal regions for the simplified RPV model with a gluino NLSP with $m_{\tilde{g}} = 1.1$ TeV.

		Gluino NLSP, $m_{\tilde{g}} = 1.1$ TeV					
	$m_{\tilde{\chi}_1^0}$	10 GeV	50 GeV	200 GeV	400 GeV	800 GeV	1090 GeV
$\lambda_{121} \neq 0$ SR0noZb	A	13%	38%	43%	53%	62%	78%
	ϵ	34%	38%	51%	57%	62%	69%
	$A \cdot \epsilon$	4.3%	15%	22%	30%	38%	54%
$\lambda_{133} \neq 0$ SR1noZb	A	0.41%	3.2%	6.8%	10%	14%	18%
	ϵ	0.98%	5.9%	13%	11%	14%	17%
	$A \cdot \epsilon$	0.004%	0.19%	0.89%	1.1%	1.9%	3.0%
$\lambda_{133} \neq 0$ SR2noZb	A	1.9%	3.5%	11%	17%	24%	27%
	ϵ	0.19%	0.69%	8.8%	9.9%	8.3%	12%
	$A \cdot \epsilon$	0.004%	0.02%	0.99%	1.7%	2.0%	3.4%

Table A.5: Acceptances and Efficiencies of the four-lepton signal regions for the simplified RPV model with an L-slepton NLSP with $m_{\tilde{\ell}} = 500$ GeV.

		L-slepton NLSP, $m_{\tilde{\ell}} = 500$ GeV					
	$m_{\tilde{\chi}_1^0}$	10 GeV	50 GeV	100 GeV	200 GeV	300 GeV	490 GeV
$\lambda_{121} \neq 0$ SR0noZb	A	46%	66%	60%	66%	73%	66%
	ϵ	47%	71%	81%	85%	83%	76%
	$A \cdot \epsilon$	22%	46%	48%	57%	61%	51%
$\lambda_{133} \neq 0$ SR1noZb	A	15%	22%	25%	26%	25%	21%
	ϵ	2.9%	23%	45%	58%	63%	34%
	$A \cdot \epsilon$	0.43%	5.1%	11%	15%	16%	7.0%
$\lambda_{133} \neq 0$ SR2noZb	A	8.2%	10%	9.7%	11%	11%	18%
	ϵ	2.0%	19%	44%	64%	72%	26%
	$A \cdot \epsilon$	0.16%	1.9%	4.3%	7.1%	7.6%	4.5%

Table A.6: Acceptances and Efficiencies of the four-lepton signal regions for the simplified RPV model with a sneutrino NLSP with $m_{\tilde{\nu}} = 400$ GeV.

		Sneutrino NLSP, $m_{\tilde{\nu}} = 400$ GeV					
	$m_{\tilde{\chi}_1^0}$	10 GeV	50 GeV	100 GeV	200 GeV	300 GeV	390 GeV
$\lambda_{121} \neq 0$ SR0noZa	A	11%	36%	38%	50%	61%	66%
	ϵ	37%	43%	51%	59%	61%	63%
	$A \cdot \epsilon$	3.9%	15%	19%	28%	38%	42%
$\lambda_{133} \neq 0$ SR1noZa	A	0.09%	2.3%	4.0%	5.9%	8.5%	10%
	ϵ	1.5%	9.3%	22%	19%	21%	21%
	$A \cdot \epsilon$	0.001%	0.21%	0.87%	1.1%	1.8%	2.1%
$\lambda_{133} \neq 0$ SR2noZa	A	0.88%	2.8%	5.4%	9.5%	13%	18%
	ϵ	0.04%	3.6%	11%	20%	17%	18%
	$A \cdot \epsilon$	0.0003%	0.10%	0.58%	1.9%	2.3%	3.2%

A.3 Systematic Uncertainties on the Signal Prediction

Tables A.7 and A.8 summarise the systematic uncertainties in the signal prediction for a selection of typical mass combinations and NLSP choices (see Section 6.5.1).

The experimental systematics are also considered for the irreducible background and treated using a common nuisance parameter.

The simulated reconstruction efficiencies for electrons are corrected using efficiency scale factors (see Section 4). Uncertainties on the scale factor result in a small error of about 3% on the signal region yields. Uncertainties in the calibration constants used to measure electron energies affect the yield at a similar magnitude.

The uncertainties on the muon reconstruction efficiency scale factors are also small (see Section 4) and result in a negligible error of less than one percent on the signal region yield. In addition to the reconstruction efficiency, the resolution of the muon momentum measurement is corrected in the simulation. The correction is accurately determined using Z boson, J/ψ and Υ decays into muon pairs, and residual uncertainties on the muon momentum resolution affect the yields with less than 1%.

The energy calibration and resolution for calorimeter clusters not associated to photons, electrons or jets when calculating the missing transverse energy (see Section 3.3.7) is a further source of a small systematic uncertainty.

Especially in the noZb signal regions relying on a high effective mass, the energy calibration and resolution for jets is one of the more significant experimental systematic uncertainties, resulting in an error of up to 7% on the total yields.

The efficiency of the simulated trigger decision in the signal and irreducible background is assigned a conservative uncertainty of 5%, which directly affects the signal region yields.

The luminosity delivered by the LHC, measured using the technique described in [140], is known at 2.8% accuracy.

Theoretical uncertainties in production cross-sections depend on the production mechanism, ranging from about 5% for electroweak processes up to 100% for strong production. In addition, uncertainties in the prediction of kinematic distributions due to initial state and final state radiation as well as the choice of renormalisation and factorisation scales are estimated at event generator level by simulating large samples of signal decays with variations in the corresponding event generator parameters and comparing the signal

region acceptances. The resulting systematic uncertainty is found to be small, below 5%.

The uncertainty in the parton distribution functions is taken into account by varying the parton distribution functions within their uncertainties and evaluating the effect on the predicted yields. resulting in an error of less than 5%.

Table A.7: Relative Monte Carlo statistical and systematic uncertainties in the yields of the SR0noZa/b signal regions of the four-lepton search for selected signal mass combinations.

	Sneutrino NLSP λ_{122}, SR0noZa $m_{\tilde{\nu}}$ = 300 GeV $m_{\tilde{\chi}_1^0}$ = 100 GeV	Gluino NLSP λ_{121}, SR0noZb $m_{\tilde{g}}$ = 1400 GeV $m_{\tilde{\chi}_1^0}$ = 400 GeV
Monte Carlo statistics	3.8%	3.3%
Electron reconstruction efficiency	1.8%	3.4%
Electron energy calibration and resolution	0.4%	0.4%
Muon reconstruction efficiency	1.0%	0.4%
Muon momentum calibration	0.4%	0.0%
Missing transverse energy (clusters)	0.6%	$< 0.1\%$
Jet energy scale and resolution	3.8%	1.7%
Trigger	$^{+0.6}_{-5.0}\%$	$^{+0.1}_{-5.0}\%$
PDF	$^{+0.9}_{-0.7}\%$	$^{+0.5}_{-0.3}\%$
ISR	2.2%	1.6%
FSR	1.9%	1.0%
Renormalisation / factorisation scale	1.6%	1.1%
Luminosity	2.8%	2.8%
Cross section	7.2%	43.3%
Total	11.3%	43.9%

Table A.8: Relative Monte Carlo statistical and systematic uncertainties in the yields of the SR1noZb and SR2noZb signal regions of the four-lepton search for selected signal mass combinations.

	L-slepton NLSP λ_{133}, SR1noZb $m_{\tilde{\ell}} = 225$ GeV $m_{\tilde{\chi}_1^0} = 100$ GeV	Wino NLSP λ_{133}, SR2noZb $m_{\tilde{\chi}_1^\pm} = 300$ GeV $m_{\tilde{\chi}_1^0} = 100$ GeV
MC statistics	5.7%	22.6%
Electron reconstruction efficiency	3.5%	2.6%
Electron energy calibration and resolution	1.6%	$< 4.8\%$
Muon reconstruction efficiency	0.4%	0.1%
Muon momentum calibration	$< 0.3\%$	$< 4.8\%$
Missing transverse energy (clusters)	0.6%	6.8%
Jet energy scale and resolution	4.8%	7.0%
τ energy calibration	0.5%	$< 4.8\%$
Tau identification efficiency	4.1%	6.3%
Trigger	$^{+1.0}_{-5.0}\%$	$^{+5.4}_{-5.4}\%$
PDF	$^{+0.7}_{-0.7}\%$	$^{+4.0}_{-2.6}\%$
ISR	1.6%	2.3%
FSR	2.7%	2.1%
Renormalisation / factorisation scale	1.7%	2.4%
Luminosity	2.8%	2.8%
Cross section	6.7%	6.6%
Total	13.6%	27.9%

A.4 Validation of Background Modelling

Table A.9: Validation regions defined for the four-lepton search. Three regions veto the presence of a Z boson candidate, similar to the signal regions, while three regions explicitly require the presence of an SFOS lepton pair compatible with a Z boson decay signature. The requirements on missing transverse energy and effective mass are inverted compared to the signal region to enrich backgrounds and suppress a signal.

Validation Region	Light leptons (e, μ)	Tau leptons	Z boson	$E_{\mathrm{T}}^{\mathrm{miss}}$ [GeV]	m_{eff} [GeV]
VR0noZ	≥ 4	≥ 0	Veto	< 50	< 400
VR1noZ	3	≥ 1	Veto	< 50	< 400
VR2noZ	2	≥ 2	Veto	< 50	< 400
VR0Z	≥ 4	≥ 0	Request	< 50	
VR1Z	3	≥ 1	Request	< 50	
VR2Z	2	≥ 2	Request	< 50	

The background estimation procedure is tested using dedicated validation regions defined by inverting the effective mass and missing transverse energy cuts of the signal regions, suppressing the contribution of a potential signal and enriching the backgrounds. In addition, three validation regions additionally invert the Z veto (see Table A.9).

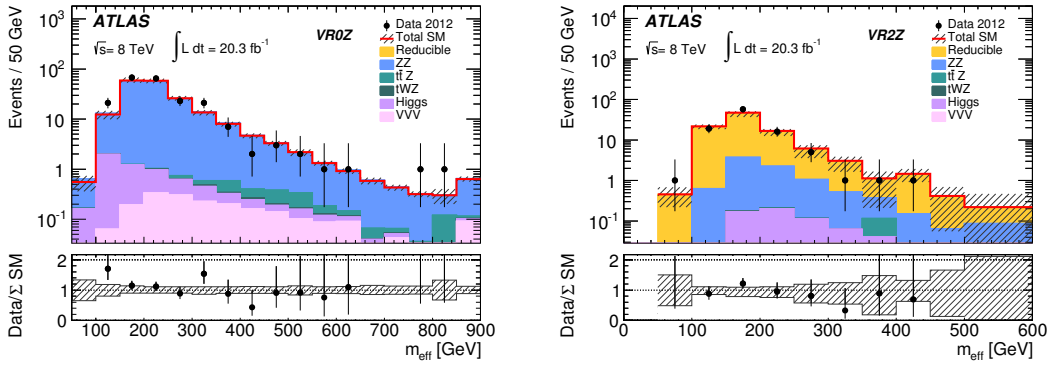

Figure A.1: Examples of effective mass distributions in the VR0Z (a) and VR2Z (b) validation regions of the four-lepton analysis (see Table A.9).

Figure A.1 shows the effective mass distributions for two well-populated validation regions, VR0Z and VR2Z, which are compatible with the predictions for both overall event counts and differential shapes. In Table A.10, the number of predicted background

Table A.10: Background prediction and observation for the six validation regions used in the four-lepton analysis.

	$ZZ^{(*)}/Z\gamma^*$	$t\bar{t}+Z$	VVV	Higgs	Reducible	**Exp. SM**	**Data**
VR0noZ	3.6 ± 0.7	$0.034^{+0.036}_{-0.033}$	$0.090^{+0.032}_{-0.033}$	0.18 ± 0.13	$0.5^{+0.4}_{-0.5}$	$\mathbf{4.4 \pm 0.9}$	**3**
VR1noZ	1.43 ± 0.27	0.033 ± 0.022	0.071 ± 0.029	0.28 ± 0.19	$7.1^{+1.8}_{-1.7}$	$\mathbf{8.9^{+1.8}_{-1.7}}$	**7**
VR2noZ	$1.53^{+0.18}_{-0.17}$	$0.025^{+0.031}_{-0.025}$	0.051 ± 0.020	0.29 ± 0.13	$33.2^{+3.3}_{-7.3}$	$\mathbf{35.1^{+3.4}_{-7.4}}$	**32**
VR0Z	184^{+20}_{-19}	1.2 ± 0.6	2.13 ± 0.33	4.7 ± 3.4	$0.5^{+3.1}_{-0.5}$	$\mathbf{193^{+21}_{-19}}$	**216**
VR1Z	8.8 ± 0.9	0.28 ± 0.11	0.19 ± 0.08	0.63 ± 0.16	21 ± 4	$\mathbf{31 \pm 4}$	**32**
VR2Z	$8.2^{+1.0}_{-1.0}$	$0.09^{+0.12}_{-0.09}$	0.069 ± 0.013	0.61 ± 0.14	90^{+8}_{-22}	$\mathbf{99^{+8}_{-22}}$	**101**

and observed events is listed for all validation regions. As expected given the challenging nature of τ lepton reconstruction, the reducible background plays a major role for all validation regions with τ leptons, while the regions with four light leptons are dominated by irreducible background. In the irreducible case, the only relevant contribution in the validation regions is from the $ZZ^{(*)}/Z\gamma^*$ process – inverted requirements on effective mass and missing transverse energy suppress sensitivity to the rare VVV, $t\bar{t}+Z$ and Higgs boson processes. Therefore, the estimation of these processes is not stringently tested by the validation regions. While for statistical reasons it is not possible to develop dedicated validation regions for such rare contributions using only the data set collected during the 2012 LHC run, future data-taking may allow for the implementation of such regions in upcoming repetitions of the analysis using a larger data set.

However, the observed agreement between observation on collision data and Standard Model expectation in all validation regions does confirm a correct modelling of the $ZZ^{(*)}/Z\gamma^*$ and reducible background components.

Bibliography

[1] ATLAS Collaboration, G. Aad et al., *Observation of a new particle in the search for the Standard Model Higgs boson with the ATLAS detector at the LHC*, Phys. Lett. B **716** (2012) 1.

[2] CMS Collaboration, S. Chatrchyan et al., *Observation of a new boson at a mass of 125 GeV with the CMS experiment at the LHC*, Phys. Lett. **B716** (2012) 30.

[3] L. Evans and P. Bryant, *LHC Machine*, JINST **3** no. 08, (2008) S08001.

[4] Planck Collaboration, P. Ade et al., *Planck 2013 results. I. Overview of products and scientific results*, Astron. Astrophys **571** (2014) A1.

[5] G. Bertone, D. Hooper, and J. Silk, *Particle dark matter: Evidence, candidates and constraints*, Phys. Rep. **405** (2005) 279.

[6] ATLAS and CMS Collaborations, G.Aad et al., *Combined Measurement of the Higgs Boson Mass in pp Collisions at* $\sqrt{s} = 7$ *and 8 TeV with the ATLAS and CMS Experiments*, Phys. Rev. Lett. **114** (2015) 191803.

[7] J. Wess and B. Zumino, *Supergauge transformations in four dimensions*, Nucl. Phys. B **70** no. 1, (1974) 39.

[8] W. Hollik, *Quantum field theory and the Standard Model*, Lectures given at the 2009 European School of High-Energy Physics, Bautzen, Germany, 14-27 June 2009, http://cds.cern.ch/record/1281946.

[9] C. N. Yang and R. L. Mills, *Conservation of Isotopic Spin and Isotopic Gauge Invariance*, Phys. Rev. **96** (1954) 191.

[10] H. Fritzsch and M. Gell-Mann, *Current algebra: Quarks and what else?*, Proceedings of the XVI International Conference on High Energy Physics, Chicago **C720906V2** (1972) 135–165, arXiv:hep-ph/0208010.

[11] H. Fritzsch, M. Gell-Mann, and H. Leutwyler, *Advantages of the Color Octet Gluon Picture*, Phys. Lett. B **47** (1973) 365.

[12] S. L. Glashow, *Partial-symmetries of weak interactions*, Nucl. Phys. **22** no. 4, (1961) 579.

[13] A. Salam and J. C. Ward, *Electromagnetic and weak interactions*, Phys. Lett. **13** (1964) 168.

[14] S. Weinberg, *A Model of Leptons*, Phys. Rev. Lett. **19** (1967) 1264.

[15] S. L. Glashow, J. Iliopoulos, and L. Maiani, *Weak Interactions with Lepton-Hadron Symmetry*, Phys. Rev. D **2** (1970) 1285–1292.

[16] A. Salam, *Weak and Electromagnetic Interactions*, Conf. Proc. C **680519** (1968) 367, originally printed in Svartholm: Elementary Particle Theory, proceedings of the Nobel Symposium held 1968 at Lerum, Sweden.

[17] M. Gell-Mann, *The Interpretation of the New Particles as Displaced Charged Multiplets*, Il Nuovo Cimento **4** (1956) 848.

[18] K. G. Wilson, *Confinement of quarks*, Phys. Rev. D **10** (1974) 2445.

[19] G. Altarelli and G. Parisi, *Asymptotic freedom in parton language*, Nucl. Phys. B **126** (1977) 298.

[20] P. W. Higgs, *Broken symmetries and the masses of gauge bosons*, Phys. Rev. Lett. **13** (1964) 508.

[21] F. Englert and R. Brout, *Broken symmetry and the mass of gauge vector mesons*, Phys. Rev. Lett. **13** (1964) 321.

[22] G. S. Guralnik, C. R. Hagen, and T. W. B. Kibble, *Global Conservation Laws and Massless Particles*, Phys. Rev. Lett. **13** (1964) 585.

[23] N. Cabibbo, *Unitary Symmetry and Leptonic Decays*, Phys. Rev. Lett. **10** (1963) 531.

[24] M. Kobayashi and T. Maskawa, *CP Violation in the Renormalizable Theory of Weak Interaction*, Prog. Theor. Phys. **49** (1973) 652.

[25] Gfitter Collaboration, M. Baak et al., *The global electroweak fit at NNLO and prospects for the LHC and ILC*, Eur. Phys. J. **C74** (2014) 3046.

[26] ATLAS Collaboration, G. Aad et al., *Summary plots from the ATLAS Standard Model physics group*, 04, 2015. https://atlas.web.cern.ch/Atlas/GROUPS/PHYSICS/CombinedSummaryPlots/SM/.

[27] A. D. Sakharov, *Violation of CP in variance, C asymmetry, and baryon asymmetry of the universe*, Soviet Physics Uspekhi **34** no. 5, (1991) 392.

[28] S. P. Martin, *A Supersymmetry primer*, Adv. Ser. Direct. High Energy Phys. **21** (2010) 1, arXiv:hep-ph/9709356.

[29] R. Haag, J. T. Lopuszanski, and M. Sohnius, *All Possible Generators of Supersymmetries of the S Matrix*, Nucl. Phys. **B88** (1975) 257.

[30] S. R. Coleman and J. Mandula, *All Possible Symmetries of the S Matrix*, Phys. Rev. **159** (1967) 1251.

[31] J. Wess and B. Zumino, *A lagrangian model invariant under supergauge transformations*, Phys. Lett. **B49** no. 1, (1974) 52.

[32] N. Sakai and T. Yanagida, *Proton decay in a class of supersymmetric grand unified models*, Nucl. Phys. B **197** no. 3, (1982) 533.

[33] Super-Kamiokande Collaboration, H. Nishino et al., *Search for Nucleon Decay into Charged Anti-lepton plus Meson in Super-Kamiokande I and II*, Phys. Rev. **D85** (2012) 112001.

[34] G. Jungman, M. Kamionkowski, and K. Griest, *Supersymmetric dark matter*, Phys. Rep. **267** (1996) 195.

[35] L. E. Ibanez and G. G. Ross, *Discrete gauge symmetries and the origin of baryon and lepton number conservation in supersymmetric versions of the standard model*, Nucl. Phys. **B368** (1992) 3.

[36] H. K. Dreiner, C. Luhn, H. Murayama, and M. Thormeier, *Baryon triality and neutrino masses from an anomalous flavor U(1)*, Nucl. Phys. **B774** (2007) 127.

[37] J. M. Campbell, J. Huston, and W. Stirling, *Hard Interactions of Quarks and Gluons: A Primer for LHC Physics*, Rep. Prog. Phys. **70** (2007) 89.

[38] M. Bahr et al., *Herwig++ Physics and Manual*, Eur. Phys. J. **C58** (2008) 639–707.

[39] J. C. Collins, D. E. Soper, and G. F. Sterman, *Factorization of Hard Processes in QCD*, Adv. Ser. Direct. High Energy Phys. **5** (1988) 1, arXiv:hep-ph/0409313.

[40] A. Martin, W. Stirling, R. Thorne, and G. Watt, *Parton distributions for the LHC*, Eur. Phys. J. **C63** (2009) 189.

[41] J. Pumplin et al., *New generation of parton distributions with uncertainties from global QCD analysis*, JHEP **07** (2002) 012.

[42] R. D. Ball et al., *Parton distributions with LHC data*, Nucl. Phys. **B867** (2013) 244.

[43] ATLAS Collaboration, G. Aad et al., *Improved luminosity determination in pp collisions at* $\sqrt{s} = 7$ TeV *using the ATLAS detector at the LHC*, Eur. Phys. J. **C73** no. 8, (2013) 2518.

[44] M. Lamont, *Status of the LHC*, J. Phys. : Conf. Series **455** no. 1, (2013) 012001.

[45] ATLAS Collaboration, G. Aad et al., *The ATLAS Experiment at the CERN Large Hadron Collider*, JINST **3** (2008) S08003.

[46] CMS Collaboration, S. Chatrchyan et al., *The CMS experiment at the CERN LHC*, JINST **3** no. 08, (2008) S08004.

[47] LHCb Collaboration, A. Alves Jr et al., *The LHCb Detector at the LHC*, JINST **3** no. 08, (2008) S08005.

[48] ALICE Collaboration, K. Aamodt et al., *The ALICE experiment at the CERN LHC*, JINST **3** no. 08, (2008) S08002.

[49] LHCf Collaboration, O. Adriani et al., *The LHCf detector at the CERN Large Hadron Collider*, JINST **3** (2008) S08006.

[50] TOTEM Collaboration, G. Anelli et al., *The TOTEM experiment at the CERN Large Hadron Collider*, JINST **3** (2008) S08007.

[51] MoEDAL Collaboration, J. Pinfold et al., *Technical Design Report of the MoEDAL Experiment*, CERN-LHCC-2009-006, http://cds.cern.ch/record/1181486.

[52] J.-L. Caron, *LHC Layout*, Sep, 1997. http://cds.cern.ch/record/841573.

[53] *The CERN accelerator complex*, http://cds.cern.ch/record/1621894/. OPEN-PHO-ACCEL-2013-056.

[54] B. Goddard and S. Dubourg, *Proceedings of the 4th Evian Workshop on LHC beam operation*, CERN (2013).

[55] R. Bruce et al., *Baseline LHC machine parameters and configuration of the 2015 proton run*, arXiv:1410.5990 [physics.acc-ph].

[56] ATLAS Collaboration, G.Aad et al., *Total Integrated Luminosity and Data Quality in 2011 and 2012*, 02, 2015. https://twiki.cern.ch/twiki/bin/view/AtlasPublic/LuminosityPublicResults.

[57] ATLAS Collaboration, G.Aad et al., *Number of Interactions per Crossing in 2011 and 2012 data*, 02, 2015. https://twiki.cern.ch/twiki/bin/view/AtlasPublic/LuminosityPublicResults.

[58] ATLAS Collaboration, G. Aad et al., *Measurement of the Inelastic Proton-Proton Cross-Section at $\sqrt{s} = 7$ TeV with the ATLAS Detector*, Nature Comm. **2** (2011) 463.

[59] ATLAS Collaboration, G. Aad et al., *ATLAS detector and physics performance: Technical Design Report, 1*, CERN-LHCC-99-014 (1999).

[60] ATLAS Collaboration, G. Aad et al., *ATLAS detector and physics performance: Technical Design Report, 2*, CERN-LHCC-99-014 (1999).

[61] A. Salzburger, *The ATLAS Track Extrapolation Package*, ATL-SOFT-PUB-2007-005 (2007), http://cds.cern.ch/record/1038100/files/soft-pub-2007-005.pdf.

[62] *Computer generated image of the whole ATLAS detector*, 2008. http://cds.cern.ch/record/1095924.

[63] ATLAS Collaboration, G. Aad et al., *ATLAS central solenoid: Technical Design Report*, CERN-LHCC-97-21 (1997).

[64] ATLAS Pixel Collaboration, G. Aad et al., *ATLAS pixel detector electronics and sensors*, JINST **3** no. 07, (2008) P07007.

[65] Particle Data Group, K.A. Olive et al., *Review of Particle Physics*, Chin. Phys. **C38** (2014) 090001.

[66] ATLAS Collaboration, G.Aad et al., *ATLAS inner detector: Technical Design Report, 2*, CERN-LHCC-97-17 (1997).

[67] ATLAS TRT Collaboration, E. Abat et al., *The ATLAS TRT Barrel Detector*, JINST **3** no. 02, (2008) P02014.

[68] *Computer generated image of the ATLAS Muons subsystem*, 2008. https://cds.cern.ch/record/1095929.

[69] W.Stirling, *Private Communication*, 2015.

[70] ATLAS Collaboration, G. Aad et al., *Performance of the ATLAS Trigger System in 2010*, Eur. Phys. J. C **72** (2012) 1849.

[71] ATLAS Collaboration, G. Aad et al., *Expected Performance of the ATLAS Experiment - Detector, Trigger and Physics*, arXiv:0901.0512.

[72] P. Billoir and S. Qian, *Fast vertex fitting with a local parametrization of tracks*, Nucl. Inst. Meth. **A311** (1992) 139.

[73] G. Piacquadio, K. Prokofiev, and A. Wildauer, *Primary vertex reconstruction in the ATLAS experiment at LHC*, J. Phys. : Conf. Series **119** no. 3, (2008) 032033.

[74] *A computer generated image representing how ATLAS detects particles*, 2013. https://cds.cern.ch/record/1505342.

[75] ATLAS Collaboration, G. Aad et al., *Electron reconstruction and identification efficiency measurements with the ATLAS detector using the 2011 LHC proton-proton collision data*, Eur. Phys. J. **C74** no. 7, (2014) 2941.

[76] ATLAS Collaboration, G. Aad et al., *Electron and photon energy calibration with the ATLAS detector using LHC Run 1 data*, Eur. Phys. J. **C74** no. 10, (2014) 3071.

[77] ATLAS Collaboration, G. Aad et al., *Electron efficiency measurements with the ATLAS detector using the 2012 LHC proton-proton collision data*, ATLAS-CONF-2014-030, 2014, http://cdsweb.cern.ch/record/1706239.

[78] M. Cacciari, G. P. Salam, and G. Soyez, *The Anti-k(t) jet clustering algorithm*, JHEP **04** (2008) 063.

[79] M. Cacciari and G. P. Salam, *Dispelling the N^3 myth for the k_t jet-finder*, Phys. Lett. **B641** (2006) 57–61.

[80] ATLAS Collaboration, G. Aad et al., *Jet energy measurement and its systematic uncertainty in proton-proton collisions at $\sqrt{s} = 7$ TeV with the ATLAS detector*, Eur. Phys. J. **C75** no. 1, (2015) 17.

[81] ATLAS Collaboration, G. Aad et al., *Characterisation and mitigation of beam-induced backgrounds observed in the ATLAS detector during the 2011 proton-proton run*, JINST **8** (2013) P07004.

[82] ATLAS Collaboration, G. Aad et al., *Calibration of the performance of b-tagging for c and light-flavour jets in the 2012 ATLAS data*, ATLAS-CONF-2014-046, 2014, https://cds.cern.ch/record/1741020.

[83] ATLAS Collaboration, G.Aad et al., *Identification of the Hadronic Decays of Tau Leptons in 2012 Data with the ATLAS Detector*, ATLAS-CONF-2013-064, 2013, https://cds.cern.ch/record/1562839.

[84] ATLAS Collaboration, G. Aad et al., *Reconstruction, Energy Calibration, and Identification of Hadronically Decaying Tau Leptons*, ATLAS-CONF-2011-077, 2011, https://cds.cern.ch/record/1353226.

[85] ATLAS Collaboration, G. Aad et al., *Identification and energy calibration of hadronically decaying tau leptons with the ATLAS experiment in pp collisions at* $\sqrt{s}$*=8 TeV*, CERN-PH-EP-2014-227 (2014), arXiv:1412.7086.

[86] ATLAS Collaboration, G. Aad et al., *Measurement of the muon reconstruction performance of the ATLAS detector using 2011 and 2012 LHC proton-proton collision data*, Eur. Phys. J. **C74** no. 11, (2014) 3130.

[87] ATLAS Collaboration, G. Aad et al., *Performance of Missing Transverse Momentum Reconstruction in Proton-Proton Collisions at 7 TeV with ATLAS*, Eur. Phys. J. **C72** (2012) 1844.

[88] ATLAS Collaboration, G. Aad et al., *The ATLAS Simulation Infrastructure*, Eur. Phys. J. C **70** (2010) 823.

[89] M. Dobbs et al., *Les Houches guidebook to Monte Carlo generators for hadron collider physics*. 2004. arXiv:hep-ph/0403045.

[90] T. Sjöstrand, S. Mrenna, and P. Z. Skands, *PYTHIA 6.4 Physics and Manual*, JHEP **05** (2006) 026.

[91] T. Sjöstrand, S. Mrenna, and P. Z. Skands, *A brief introduction to PYTHIA 8.1* , Comp. Phys. Comm. **178** no. 11, (2008) 852.

[92] T. Gleisberg et al., *Event generation with SHERPA 1.1*, JHEP **02** (2009) 007.

[93] G. Corcella et al., *HERWIG 6: An Event generator for hadron emission reactions with interfering gluons (including supersymmetric processes)*, JHEP **01** (2001) 010.

[94] M. L. Mangano et al., *ALPGEN, a generator for hard multiparton processes in hadronic collisions*, JHEP **07** (2003) 001.

[95] J. Alwall et al., *MadGraph/MadEvent v4: The New Web Generation*, JHEP **09** (2007) 028.

[96] J. Alwall et al., *The automated computation of tree-level and next-to-leading order differential cross sections, and their matching to parton shower simulations*, JHEP **07** (2014) 079.

[97] P. Nason, *A New method for combining NLO QCD with shower Monte Carlo algorithms*, JHEP **11** (2004) 040.

[98] S. Frixione, P. Nason, and C. Oleari, *Matching NLO QCD computations with Parton Shower simulations: the POWHEG method*, JHEP **11** (2007) 070.

[99] S. Frixione and B. R. Webber, *Matching NLO QCD computations and parton shower simulations*, JHEP **06** (2002) 029.

[100] GEANT4 Collaboration, S. Agostinelli et al., *GEANT4: A Simulation toolkit*, Nucl. Inst. Meth. **A506** (2003) 250.

[101] ATLAS Collaboration, G. Aad et al., *Performance of the Fast ATLAS Tracking Simulation (FATRAS) and the ATLAS Fast Calorimeter Simulation (FastCaloSim) with single particles*, ATL-SOFT-PUB-2014-001, 2014, https://cds.cern.ch/record/1669341.

[102] ATLAS Collaboration, G. Aad et al., *The simulation principle and performance of the ATLAS fast calorimeter simulation FastCaloSim*, ATL-PHYS-PUB-2010-013, 2010, http://cds.cern.ch/record/1300517.

[103] K. Edmonds et al., *The fast ATLAS track simulation (FATRAS)*, ATL-SOFT-PUB-2008-001, 2008, http://cds.cern.ch/record/1091969.

[104] W. Beenakker, R. Hopker, and M. Spira, *PROSPINO: A Program for the production of supersymmetric particles in next-to-leading order QCD*, arXiv:hep-ph/9611232.

[105] W. Beenakker, R. Hopker, M. Spira, and P. Zerwas, *Squark and gluino production at hadron colliders*, Nucl. Phys. **B492** (1997) 51.

[106] W. Beenakker et al., *Soft-gluon resummation for squark and gluino hadroproduction*, JHEP **12** (2009) 041.

[107] W. Beenakker et al., *Squark and Gluino Hadroproduction*, Int. J. Mod. Phys. **A26** (2011) 2637.

[108] ATLAS Collaboration, G. Aad et al., *Search for squarks and gluinos with the ATLAS detector in final states with jets and missing transverse momentum using* $\sqrt{s} = 8$ *TeV proton–proton collision data*, JHEP **09** (2014) 176.

[109] ATLAS Collaboration, G. Aad et al., *Search for direct production of charginos, neutralinos and sleptons in final states with two leptons and missing transverse momentum in pp collisions at* $\sqrt{s} = 8$ *TeV with the ATLAS detector*, JHEP **05** (2014) 071.

[110] ATLAS Collaboration, G. Aad et al., *Search for top squark pair production in final states with one isolated lepton, jets, and missing transverse momentum in* $\sqrt{s}$ *=8 TeV pp collisions with the ATLAS detector*, JHEP **11** (2014) 118.

[111] ATLAS Collaboration, G. Aad et al., *Search for massive supersymmetric particles decaying to many jets using the ATLAS detector in pp collisions at* $\sqrt{s} = 8$ *TeV*, Accepted by Phys. Rev. D (2015), arXiv:1502.05686.

[112] ATLAS Collaboration, G. Aad et al., *A search for* $B - L$ *R-Parity violating scalar top decays in* $\sqrt{s} = 8$ *TeV pp collisions with the ATLAS experiment*, ATLAS-CONF-2015-015, 2015, https://cds.cern.ch/record/2002885.

[113] ATLAS Collaboration, G. Aad et al., *Search for a Heavy Neutral Particle Decaying to* $e\mu$*,* $e\tau$*, or* $\mu\tau$ *in pp Collisions at* $\sqrt{s} = 8$ *TeV with the ATLAS Detector*, Accepted by Phys. Rev. Lett. (2015), arXiv:1503.04430.

[114] OPAL Collaboration, G. Abbiendi et al., *Search for R parity violating decays of scalar fermions at LEP*, Eur. Phys. J. **C33** (2004) 149.

[115] L3 Collaboration, P. Achard et al., *Search for R parity violating decays of supersymmetric particles in* e^+e^- *collisions at LEP*, Phys. Lett. **B524** (2002) 65.

[116] DELPHI Collaboration, J. Abdallah et al., *Search for supersymmetric particles assuming R-parity nonconservation in e+ e- collisions at* $s^{1/2} = 192$ *GeV to 208 GeV*, Eur. Phys. J. **C36** (2004) 1.

[117] ALEPH Collaboration, A. Heister et al., *Search for supersymmetric particles with R parity violating decays in e^+e^- collisions at $\sqrt{s}$ up to 209 GeV*, Eur. Phys. J. **C31** (2003) 1.

[118] LEP2 SUSY Working group, ALEPH, DELPHI, L3 and OPAL experiments, *Combined results on Rp violation with LLE couplings*, LEPSUSYWG/02-10.1 (2002).

[119] D0 Collaboration, V. Abazov et al., *Search for R-parity violating supersymmetry via the LL anti-E couplings λ_{121}, λ_{122} or λ_{133} in $p\bar{p}$ collisions at $\sqrt{s}$ = 1.96 TeV*, Phys. Lett. **B638** (2006) 441.

[120] Y. Kao and T. Takeuchi, *Single-Coupling Bounds on R-parity violating Supersymmetry, an update*, arXiv:0910.4980.

[121] H. K. Dreiner and G. G. Ross, *R-parity violation at hadron colliders*, Nucl. Phys. **B365** (1991) 597.

[122] ATLAS Collaboration, G. Aad et al., *Searches for heavy long-lived charged particles with the ATLAS detector in proton–proton collisions at $\sqrt{s}$ = 8 TeV*, JHEP **01** (2015) 068.

[123] L. Hehn, *Study of Supersymmetric Extensions of the Standard Model with R-Parity Violation*, Master's thesis, Technische Universität München, 2013.

[124] ATLAS Collaboration, G. Aad et al., *Search for supersymmetry in events with four or more leptons in $\sqrt{s}$ = 8 TeV pp collisions with the ATLAS detector*, Phys. Rev. **D90** no. 5, (2014) 052001.

[125] ATLAS Collaboration, G. Aad et al., *Search for supersymmetry in events with four or more leptons in 21 fb^{-1} of pp collisions at $\sqrt{s}$ = 8 TeV with the ATLAS detector*, ATLAS-CONF-2013-036, 2013, http://cdsweb.cern.ch/record/1532429.

[126] ATLAS Collaboration, G. Aad et al., *Measurements of Four-Lepton Production at the Z Resonance in pp Collisions at $\sqrt{s}$ = 7 and 8 TeV with ATLAS*, Phys. Rev. Lett. **112** (2014) 231806.

[127] A. Kardos, Z. Trocsanyi, and C. Papadopoulos, *Top quark pair production in association with a Z-boson at NLO accuracy*, Phys. Rev. **D85** (2012) 054015.

[128] J. Butterworth et al., *Single Boson and Diboson Production Cross Sections in pp Collisions at $\sqrt{s}$=7 TeV*, ATL-COM-PHYS-2010-695 (2010), https://cds.cern.ch/record/1287902.

[129] LHC Higgs Cross Section Working Group, S. Heinemeyer et al., *Handbook of LHC Higgs Cross Sections: 3. Higgs Properties*, CERN-2013-004 (2013), arXiv:1307.1347.

[130] G. Cowan, K. Cranmer, E. Gross, and O. Vitells, *Asymptotic formulae for likelihood-based tests of new physics*, Eur. Phys. J. **C71** no. 2, (2011).

[131] S. Stern, *Searches for Higgs Boson Decays to Muon Pairs in the Standard Model and in its Minimal Supersymmetric Extension with the ATLAS Detector*. PhD thesis, Technische Universität München, July, 2013. CERN-THESIS-2013-108, MPP-2013-243.

[132] A. L. Read, *Presentation of search results: the CL_s technique*, J. Phy. **G28** no. 10, (2002) 2693.

[133] ATLAS Collaboration, G. Aad et al., *Search for supersymmetry in events with four or more leptons in* 13.0 fb^{-1} *pp collisions at* $\sqrt{s} = 8$ *TeV with the ATLAS detector*, ATLAS-CONF-2012-153, 2012, http://cdsweb.cern.ch/record/1493492.

[134] ATLAS Collaboration, G. Aad et al., *Search for direct production of charginos, neutralinos and sleptons in final states with two leptons and missing transverse momentum in pp collisions at* $\sqrt{s} = 8$ *TeV with the ATLAS detector*, JHEP **05** (2014) 071.

[135] ATLAS Collaboration, G. Aad et al., *Search for the direct production of charginos, neutralinos and staus in final states with at least two hadronically decaying taus and missing transverse momentum in pp collisions at* $\sqrt{s} = 8$ *TeV with the ATLAS detector*, JHEP **10** (2014) 96.

[136] ATLAS Collaboration, G. Aad et al., *Search for R-parity-violating supersymmetry in events with four or more leptons in* $\sqrt{s} = 7$ *TeV pp collisions with the ATLAS detector*, JHEP **1212** (2012) 124.

[137] ATLAS Collaboration, G. Aad et al., *Search for massive, long-lived particles using multitrack displaced vertices or displaced lepton pairs in pp collisions at* $\sqrt{s} = 8$ *TeV with the ATLAS detector*, Submitted to Phys. Rev. D (2015), arXiv:1504.05162.

[138] N. Barlow et al., *Search for long-lived, heavy particles using a multi-track displaced vertex, in pp collisions at 8 TeV centre-of-mass energy, with the ATLAS detector at the LHC*, ATL-COM-PHYS-2014-370, 2014, https://cds.cern.ch/record/1697511, Internal Documentation.

[139] S. Das, *On a New Approach for Finding All the Modified Cut-Sets in an Incompatibility Graph*, IEEE Transactions on Computers **C22** no. 2, (1973) 187.

[140] ATLAS Collaboration, G. Aad et al., *Luminosity Determination in pp Collisions at $\sqrt{s}$ = 7 TeV Using the ATLAS Detector at the LHC*, Eur. Phys. J. **C71** (2011) 1630.

List of Figures

List of Tables